Matériaux bidimensionnels, nanoparticules et leurs hétérostructures pour la nanoélectronique et l'électronique de spin

Louis Donald Mouafo Notemgnou

UNIVERSITÉ DE STRASBOURG

ÉCOLE DOCTORALE DE PHYSIQUE, CHIMIE-PHYSIQUE

Institut de Physique et Chimie des Matériaux de Strasbourg

THÈSE présentée par :

Louis Donald MOUAFO NOTEMGNOU

soutenue le : **04 Mars 2019**

pour obtenir le grade de : **Docteur de l'Université de Strasbourg**

Discipline/ Spécialité : Physique/ Nanophysique

Two dimensional materials, nanoparticles and their heterostructures for nanoelectronics and spintronics

THÈSE dirigée par:

M. Jean-François DAYEN	Maître de conférence, Université de Strasbourg

RAPPORTEURS :

M. Luis HUESO	Professeur, CIC nanoGUNE, Espagne
M. Dominique VUILLAUME	Directeur de recherche, CNRS, IEMN - Lille

EXAMINATEURS :

Mme. Anne BERNAND-MANTEL	Chargé de recherche, CNRS, Institut NEEL - Grenoble
M. Xavier JEHL	Chercheur, CEA - Grenoble
M. Laurent SIMON	Directeur de Recherche, CNRS, IS2M - Mulhouse
M. Bernard DOUDIN	Professeur, Université de Strasbourg

Contents

Remerciements

Le présent manuscrit marque la fin de l'exaltante aventure débutée plus de trois ans plus top et pendant laquelle j'ai appris bien plus que de la physique. Une aventure qui s'est avérée si exaltante grâce à la contribution de nombreuses personnes à qui j'aimerai ici exprimer ma profonde gratitude.

Mes remerciements s'adressent premièrement aux membres de mon jury qui ont accepté d'évaluer mon travail de thèse. Notamment à Bernard Doudin qui, au delà de m'avoir fait l'honneur de présider mon jury, a été d'un apport considérable dans l'accomplissement de ce travail, à Dominique Vuillaume et Luis Hueso pour avoir été rapporteurs de ce travail, à Anne-Bernand Mantel, Xavier Jehl et Laurent Simon pour avoir été examinateurs.

Les mots ne sauraient suffire pour exprimer ma reconnaissance à Jean-François Dayen mon superviseur. De toute évidence, la qualité de ce travail trouve la raison aussi à son constant aiguillage. Depuis le stage de Master à ma soutenance de thèse, tu as fait preuve d'écoute, de conseil cumulativement à une bonne marge de liberté dont tu m'as laissé bénéficier. Des ingrédients qui ont servis à nourrir en permanence ma motivation. J'ai apprécié la simplicité que tu as bien voulu laisser à nos rapports. Toutes ces années, nous avons partagé plus que de la science. Merci!

Merci à Celine Etrillard et Florian Godel qui m'ont transmis les premières dextérités expérimentales à mon arrivé au laboratoire. Ha Florian, que dire de ta sympathie ? Je pense que mon accueil chez toi pendant la semaine passée à Thales restera l'un des moments marquant de cette thèse. J'en profite pour remercier Pierre Seneor pour avoir permis cela. Un merci particulier à mes coéquipiers Guillaume Chaumy et Ulrich Noumbe avec qui l'ambiance si sympathique a toujours rendu agréable la vie de l'équipe, j'ai admiré votre simplicité. Je vous souhaite tout le succès pour la suite des manips. Je tiens également à dire merci à mes collègues de bureau notamment Peter Dune dont j'ai profité de la grande culture scientifique lors nos diverses discussions, Tindara Verduce, Dominik Mtten, Xin Zhang, Léo Colombier pour nos ambiances de bureau et de repas de midi. Une conviviale camaraderie à laquelle j'associe également Etienne Lorchat et François Fermique.

Mes chaleureux remerciements aux autres membres de l'équipe Nano-dispositifs notamment Stephane Berciaux et Bodhan Kundis pour les nombreuses discussions scientifiques mais aussi pour nos fructueuses collaborations. Une mention spéciale à Fabien Chevrier pour son constant soutient technique, à l'équipe STnano : Sabine Siegwald, Romain Bernard et Hicham Majjad pour leur soutient dans les salles eFab et blanche. Romain et Sabine, j'ignore comment vous y êtes parvenus, mais malgré les contraintes sécuritaires, vous avez su rendre le travail en salle blanche quasiment récréatif. Merci également à tout le DMONS et sa secrétaire Véronique Wernher qui a toujours fait preuve d'une sollicitude maternelle. Merci à Mebarek Alouani qui fut mon premier contact à l'institut et qui m'a accueilli dès mon arrivé pour le Master MCN et est resté depuis lors d'un soutient constant. Pendant la thèse, j'ai eu le privilège de représenter mes collègues doctorants au conseil de l'école doctorale 182, ce qui m'a donnée l'opportunité de souvent participer à la commission de sélection pour les bourses doctorales. Ce fut une expérience enrichissante que j'ai effectuée avec un immense plaisir. Merci à Hyves Heny de m'avoir recommandé à cette poste.

Il est bien sûr certain que la réussite de cette thèse doit beaucoup à l'excellent environnement de scientifique de l'IPCMS et à tout son personnel. Mes sincères remerciements à nos collaborateurs du DSI Ovidiu Ersen et Giorgian Milente, à David Halley, Mathieu Bailleul, Martin Bowen, Jacques Faerber et Victor Da costa, avec qui j'ai régulièrement échangé et souvent travaillé. Je tiens aussi à exprimer ma reconnaissance à Laurent Simon, Yannick Dappe et Yan Leroy pour de fructueuses discussions scientifiques qui ont permis de lever le voile sur de nombreux aspects de la thèse.

À toute ma famille à qui je dédie cette thèse, j'exprime ma reconnaissance pour tout le soutient et l'affection qu'elle m'a apportés toute ma scolarité durant. À ma mère, Jacqueline Makoua, je ne trouverais jamais de mots assez forts pour exprimer ma reconnaissance. Trouve en ce travail maman, 'une expression' de mon profond amour. Au moment ou je reçois ce doctorat, le souvenir de mon premier jour d'école reste si présent. Ce fut par un milieu de mâtinée ensoleillé que, teint par la main, ma Grand-mère 'Melhoum Hélène', me conduisit à travers les sentiers du village pour ma première inscription scolaire. Grand-mère, certainement étais-tu loin d'imaginer conduire ton jadis petit homme vers un long périple qui culminerait au Doctorat de physique, trouve en ce travail tout le fruit de ton amour. Que dire de mon papa, Paul Dagobert Notemgnou ? Si j'y suis arrivé c'est certainement grâce tes encouragements et ton soutient constant. Ce mérite est tout aussi tient. Á maman Delphine Djukem, j'exprime ma gratitude, de l'homme que je suis devenu, ta contribution est inestimable. À mes frères et sœurs, j'exprime tout ma fraternité. Je sais votre amour pour moi. À mes amis nombreux, je vous dis à tous et à chacun un grand Merci!.

Chapter 1

General introduction : From 2D nanocrystals to 2D-nD Van Der Waals heterostures

In the years 60s, despite the progress of quantum mechanics setting the main theoretical tools for understanding the behavior of the mater at the 'microscopic' scale, none of what refers to date to nanoscience was existing. In 1959 Richard Feynman, the famous noble prise physicist during his visionary lecture "There is a plenty of rooms at the bottom" highlighting fascinating possibilities affordable by downscaling and illustrating his vision fare beyond his time declared : "In the year 2000, when they look back at this age, they will wonder why it was not until the year 1960 that anybody began seriously to move in this direction" [Feynman60]. Although difficult to estimate to what extent he succeeded in motivating the community, it is certain that in the year 2000 there was no reason to wonder since valuable progress has been done so far following Feynmann's intuition and setting the foundation of what is today known as nanoscience and nonatechnology.

During its earlier years, nanoscience has enabled the emergence of different classes of nanostructures. Depending of the number of dimensions remaining above 100 nm, on distinguishes nanoparticles (0D), nanowires (1D), thin films (2D) and bulk polycrystal and nanocomposites (3D). The prominence of quantum effects at nanometer scale opened numerous of fundamental research fields including nanoelectronic and spin electronics (Spintronics). Already, the earlier progresses have lead to important discoveries such as the Giant Magneto-Resistance (GMR) [Baibich88, Binasch89] and Tunneling Magneto-Resistance (TMR) [Julliere75] in multilayer thin films which favored major advances in magnetic sensing

and data storage industries. Capitalizing the continuous technical progress in nanoelectronics enables the fabrication of devices with continuing decreasing size until the recent argue of the fundamental limit below which quantum tunneling becomes unavoidable in usual device geometry highlighting the need of alternative approachies. In this perspective, the use of layered materials as conductive channel in Field Effect Transistor emerged as promising direction. Also, other classes of devices emerged, such as the Single Electron Devices using nanoparticles (NPs). When NPs become smaller than few tens of nanometers, Coulomb interactions become prominent and induce a charging energy $E_C = e^2/2C$ that can dominate the thermal energy and prevent sequential charge tunneling into the nanoparticle resulting to the so called Coulomb Blockade (CB) effect.

Coulomb interaction energy was first suggested in 1951 to explain the important increase of the resistance in granular metallic film at low temperature [Gorter51]. However, it is particularly in the year 80s that it became technically possible to fabricated nanometer scale tunneling junction owing the observation CB mediated conductance oscillation [Fulton87]. This pioneer experimental realization inspired theoretical developments which have enabled to establish the orthodox theory of CB widely used nowadays to interpret quantum transport experiments in the CB regime [Kastner92]. Implementing ferromagnetic component(s) in a

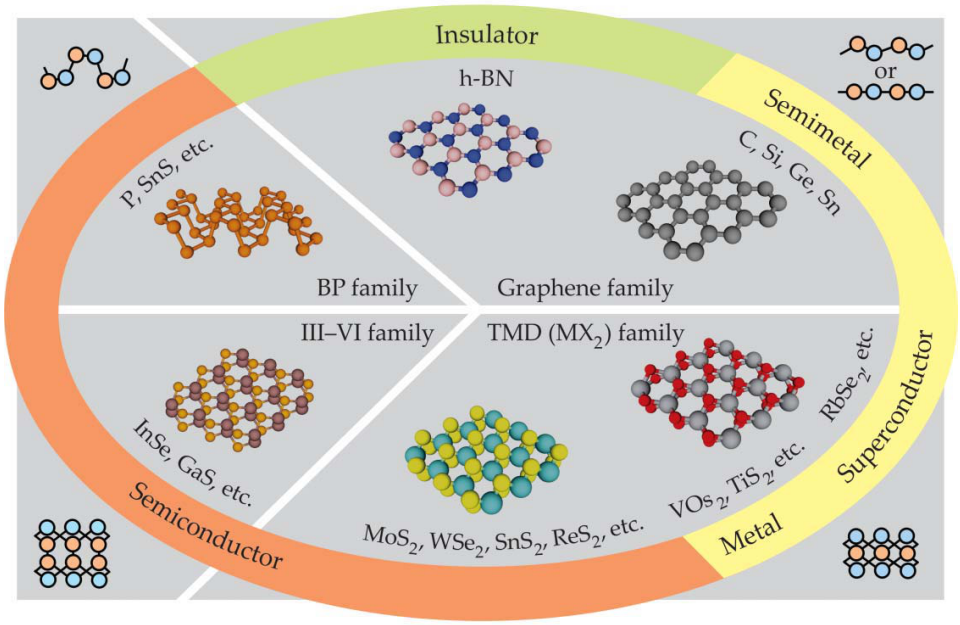

***Figure 1.1** – The large family of 2D materials cover the entire range of electrical properties ranging from insulator to superconductor including semiconductor (mostly III-V), semimetal and metal. It has been enriched in 2018 by the discovery of 2D ferromagnetic materials. Adapted from Ref. [Ajayan16].*

Single electron transistor (SET) sets the conditions for the interplay between CB and spin degree of freedom of electrons resulting to Magneto-Coulomb (MC) effect demonstrated to yield novel magneto-transport property [Shimada98, Seneor07]. SETs are prospected as a serious alternative to Complementary Metal Oxide Semiconductor (CMOS) technology because of low power consumption and high speed performances with foreseen applications as very

sensitive sensors [Seneor07], memories, multilogic devices [Kastner92] and in nanometrology and quantum computing [Nazarov09]. The later holding the promise to revolutionize the information and communication technology. Unfortunately, reliable and reproducible device fabrication approach remains a major bottleneck of nanoelectronics and nanospintronics and SETs stay at the stage of laboratory. Indeed, contacting and patterning a single NPs with the required nanometer scale precision is a very complicated technological challenge. Meanwhile, single electron features are smeared out in large-scale devices with potentially thousands of NPs contacted having a size dispersion and thus different electronic properties. It is thus essential to develop new materials and/or device concepts circumventing those difficulties. In this perspective, graphene and related 2D transition Metal dichalcogenide (TMDs) of chemical formula MX_2 (Where M is a transition metal e.g. Mo, W and X a chalcogene e.g. S, Se, Te...) are of paramount importance. On one hand, they offer the possibility of fabricating Field Effect Transistors (FET) which the ultimate atomic thick channel, on the other hand, they provide a perfect platform for the growth of self-assembled NPs with similar electronic properties.

Driven by the isolation of the single carbon atomic thick material (graphene) in 2004 [Novoselov04], a frenzy of research activities have led to the isolation of many other layered materials [Radisavljevic13] resumed in Fig.10.3. Today, the large family of 2D materials covers a wide range of physical properties including insulators, semiconductors, metals, semimetals and superconductors [Ajayan16] and also the recently discovered 2D ferromagnetic materials [Gong17, Huang17]. More importantly, 2D materials are extremely sensitive to external stimuli such as electric and magnetic field making them ideal candidates for electronics, optoelectronics [Novoselov16, Liu16] and spintronics [Dankert17a, Piquemal-Banci17] applications. Furthermore, the passivated dangling bonds free-surface of 2D materials offers the possibility to stack them into 2D-2D Van der Waals heterostructures (VdWh) [Jariwala16, Liu16] without suffering the problem of lattice mismatch contrary to traditional epitaxial multilayer heterostrures widely present in the industrial applications and for which Alferov received a noble price for his related activities [Alferov01]. Interestingly, VdWh are not limited to 2D-2D stacking. Any passivated free surface dangling bond system interacts with other materials through non covalent bonds[Jariwala16]. Hence, graphene and TMDs interact with other n-dimensional materials (n = 0, 1, 3) to form the so call mixed dimensional VdW-h (MD-VdW-h) summarized in Fig.10.4. MD-VdW-h are under intensive investigations since their have shown promising prospect for important applications in a large number of areas and particularly electronics and optoelectronics [Jariwala16, Liu16]. The Thomas-Fermi screening length λ_{TF} expressing the penetration of the electric field in a given material is expected to exceed few layers, owing the possibility of modulating the electrical properties of the n-dimensional nanoobjects sitting under the 2D materials (Fig.10.4). These combined features set suitable conditions for developing new devices concept using MD-VdW-h.

In this general context, my PhD projet aims to develop alternative approaches for fabricating novel nanodevices for nanoelectronics and nanospintronics applications tak-

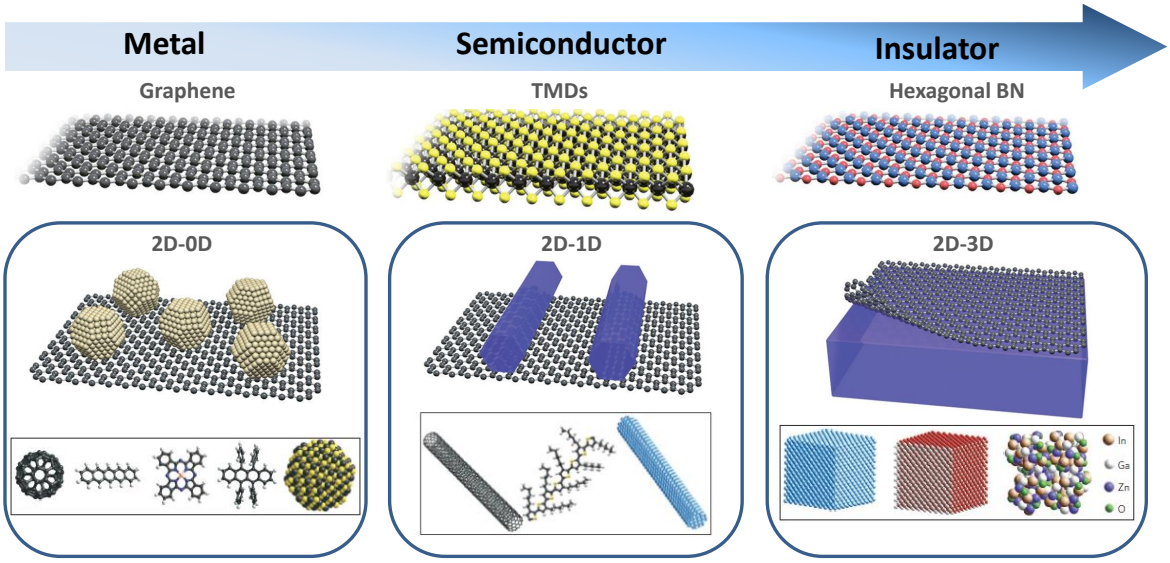

Figure 1.2 *– The reported MD-VdW-h consists of the interaction of 2D material with material of other dimensionality : 0D (Nanoparticles, dispersed molecules, fluorine C_{60}), 1D (Nanowire and nanotube), 3D (2D material interact with bulk substrate and other bulk materials). Adapted from Ref [Liu16, Jariwala16].*

ing advantage of low dimensional nanocrystals including nanoparticles and 2D layered materials such as Graphene and semiconductor TMDs (SC-TMDs). Then, to investigate the fundamental processes governing their transport and magnetotransport properties. In particular, we demonstrated novel SET geometry consisting of 2D-0D Mixed dimensional van der Waals heterostructures and we succeeded to implement the magnetic fictionalization of these devices thanks to the MC effect. In addition, we fabricated and conducted a comprehensive studied of the transport properties of FET using a bilayer $MoSe_2$ as channel for charge transport. We also addressed the transport and magnetotransport properties of Lanthanum Strontium Magnetite Oxide (LSMO) nanoparticles trapped into high aspect ratio nanotranches and observed an exceptionally large magnetoresistance at low temperature. In this manuscript, I develop the main results of each of these aspect of the work.

This thesis manuscript is organized in 10 chapters including the present chapter dedicated to the general introduction.
In **Chapter**2, I present an overview of the structural and electronic properties of Graphene and Semiconducting TMDs. I review the recent advances in the fabrication methods of Graphene, SC-TMDs and MD-VdWh based devices for nanoelectronics and nanospintronics.

In **Chapter**3, I review the transport processes taking place in Graphene and SC-TMDs FETs. In addition, I present the orthodox theory of CB which governs the transport of charges in SET and I detail the mechanisms sustaining the interplay between CB and spin degree of freedom of electrons so called the Magneto-Coulomb (MC) effect governing the magneto-transport properties of SEDs.

In **Chapter**4, I present our experimental methods for sample fabrication and our set-up

for transport characterization. In particular, I detail our fabrication method of 2D-0D MD VdWh consisting of graphene or MoS_2 used as a template for the growth of a thin Al layer resulting to self-assembled Al nanoparticles which, after oxidation, adopt a core-shell structure with metallic Al core embedded into alumina matrix providing thus a configuration suitable for single electron transport processes.

The **Chapter**5 presents the transport measurements of 2D-0D Al-AlOx/Graphene MD-VdWh based SET. We demonstrate that, tunnel junction integrating Al-AlOx/Graphene heterostructures present transport properties characteristic to single electron processes with remarkable Coulomb staircases in the I-Vsd characteristics and Coulomb oscillation of the differential conductance resulting from the CB effect of the nanoparticles. A vertical electric field applied at the back $p^{++}Si/SiO_2$ gate efficiently modulates the Coulomb levels of the supporting NPs through the underneath graphene flake resulting to gate voltage dependent current oscillation. The conductance spectroscopy presents Coulomb diamond patterns characteristic to SETs.

The **Chapter**6 presents low temperature spintronics properties of the 2D-0D Al-AlOx/Graphene MD-VdWh based SEDs. We show that the magnetization orientation of a single ferromagnetic electrode enables to tune the electric charge experienced by the core Al of the NPs thanks to the anisotropic magneto-Coulomb (AMC) effect originating from spin-orbit coupling within the ferromagnetic electrode. This modulates the resistance of the devices resulting to a spin valve-like magnetoresistance signatures without requiring a spin coherent tunneling.

In **Chapter**7, we report on tunable Metal/$MoSe_2$ interface charge transport in a bilayer $MoSe_2$ FET using a Ti/Au contacts. We observed that the modulation of Ti/$MoSe_2$ interface energy band profiles by the combined effects of temperature, gate and source-drain voltages enables to elucidate a complete map of the interface charge injection mechanisms including the observation of Fowler-Nordheim tunneling in SC-TMDs based FETs.

In **Chapter**8, we report on the transport properties of 2D-0D Al-AlOx/MoS_2 based SET. The low temperature conductance measurements present Coulomb oscillations superimposed to the field effect characteristics intrinsic to the MoS_2 channel. The conductance stability diagram presents remarkable Coulomb diamonds patterns which are characteristic features of SET.

In **Chapter**9, we report the magnetotransport properties of 20 nm ligand-free $La_{0.67}Sr_{0.33}MnO_3$ perovskite nanocrystals of nearly perfect crystalline quality. We demonstrated that these nanocrystals exhibit a core-shell magnetic structure with a ferromagnetic core embedded into a magnetically dead layer at extremely tinny chemically shell. We observed an exceptionally large magnetoresistance at low temperature essentially driven by shell magnetization of the nanocrystals independently of the spin polarization of their ferromagnetic core. This work reveals the way the nanoscale impacts magnetotransport in this material widely used as electrode in hybrid spintronic devices.

The **Chapter**10 presents the general conclusion to this work and outlines several important perspectives.
In appendix A, I discuss the notion of quantum capacitance which is important when addressing the gating of low dimensional systems. I provide its derivation in the case of graphene.
In appendix B, I present the derivation of the I(Vsd) formula across the metal/semiconductor interface Schottky barrier in the 3D and 2D model as applied to SC-TMDs FETs.
An additional section dedicated to the detailed summary of the thesis in French closes this manuscript.

Chapter 2

Introduction to graphene, semiconductor TMDs and related Van der Waals heterostructures

The electronic properties of materials are in general correlated with their structural properties. In graphene [Novoselov04] and semiconducting transition metal dichalcogenides (TMDs) [Wang12] such a correlation is more pronounced due to quantum confinement induced by their layered nature. Hence, their electronic properties depend directly on their thickness i.e. the number of monolayer composing the 2D nanocrystal. In addition, the properties of any types of Van der Waals heterostructures (VdWh) [Jariwala16, Liu16] are closely related to those of 2D crystals involved and by mutual quantum interactions that can provide additional properties. In this chapter, I present the structural and electronic properties of graphene and TMDs, then I review the fabrication methods of VdWh with particular emphasis on MD-VdWh for device applications in nanoelectronics and optoelectronics and spintronics.

2.1 Graphene

2.1.1 Crystal structure

Graphene (Gr) is the thinnest material ever reported. It consists of a two dimensional organization of carbon atom in honeycomb lattice as illustrated in Fig.2.1(a). In such an atomic organization, not all the atoms are equivalent in a crystallographic point of view since they can not all be connected one another with a Bravais lattice vector. The atoms of a Gr plane can

thus be divided into two families labeled as family A (grey filled circles) and B (red filled circles). The atoms in each of these families are equivalent, which means they can be connected by a Bravais lattice vector. In each family the atoms are organized in triangular lattice and it is impossible to connect an atom of family A to the other of family B with a vector of the Bravais lattice (Fig.2.1.(a)). Any atom of the family A has three nearest B atoms neighbors respectively at 0°, 120° and 240° while any atom of family B have its atoms A nearest neighbors at 60°, 180° and 300°. Therefore, Gr lattice is commonly described as two triangular sublattices consisting of atoms A and B. It can as well be described by a single triangular lattice with basic component consisting of a couple of nearest atoms A and B. In the following we keep the former description for which the basic vectors of the primitive unit cell are given by $\boldsymbol{a_1} = \frac{a}{2}(3, \sqrt{3})$ and $\boldsymbol{a_2} = \frac{a}{2}(3, -\sqrt{3})$. Also, the three vectors connecting an atom B to its nearest neighbors are given by $\boldsymbol{\delta_1} = \frac{a}{2}(1, \sqrt{3})$, $\boldsymbol{\delta_2} = \frac{a}{2}(1, -\sqrt{3})$ and $\boldsymbol{\delta_3} = -a(1, 0)$ (Fig.2.1(a)). Each atom independently of the family is coupled to each of its three nearest neighbors with a single covalent bond (σ) and an additional π type covalent bond with the third nearest neighbor (see section2.1.2). Hence, the distance between two neighboring atoms A and B is $a = 1.42\,\text{Å}$ which represents roughly the mean of simple C-C bond length ($a = 1.47\,\text{Å}$) and double C-C bond ($a = 1.35\,\text{Å}$). Given the definition of the reciprocal space $\boldsymbol{a_i b_j} = 2\pi\delta_i j$, ($\delta_i j = 1$ if $i = j$;

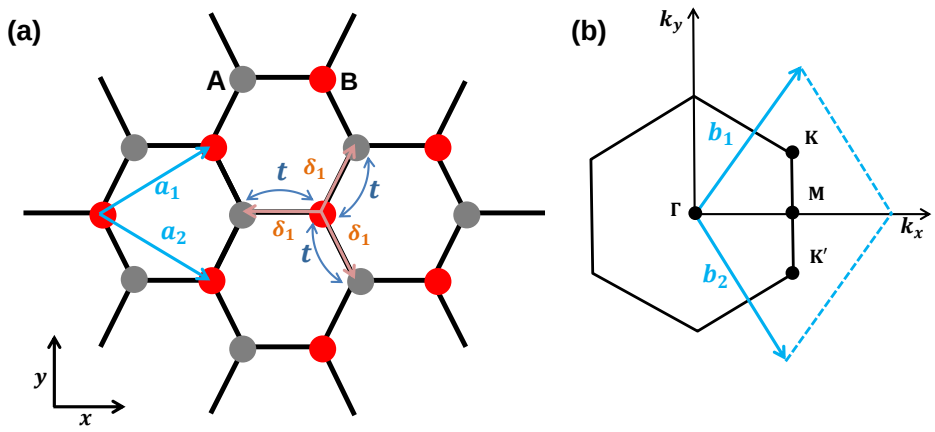

Figure 2.1 *– (a) Honeycomb lattice structure of Gr composed of a triangular lattice with a basis of two inequivalent carbon atoms, A and B.* $\boldsymbol{a_1}$ *and* $\boldsymbol{a_2}$ *are the primitive unit vectors. The vectors* $\boldsymbol{\delta_1}$, $\boldsymbol{\delta_2}$ *and* $\boldsymbol{\delta_3}$ *connect an atom B to its three nearest neighbors A. Electron can hope from a given carbon atom to one of its three nearest neighbor with a hopping parameter t. (b) The first Brillouin zone.* $\boldsymbol{b_1}$ *and* $\boldsymbol{b_2}$ *are the basis vectors of the reciprocal lattice. High symmetry points are indicated with black dots and labeled.*

0 if $i \neq j$, one deduces the corresponding basis vectors of the reciprocal lattice $\boldsymbol{b_1} = \frac{2\pi}{3a}(1, \sqrt{3})$ and $\boldsymbol{b_2} = \frac{2\pi}{3a}(1, -\sqrt{3})$. The first Brillouin zone (FBZ) is hexagonal and characterized by four high symmetry points indicated by Γ, M, K and K' (Fig.2.1(b)). As consequence of its hexagonal symmetry, the six high symmetry points at the corners of the FBZ are separated into two families of equivalent points connectable by a reciprocal Bravais vector and denoted K and K'. Since minimum of conduction band and the maximum valence band of Gr are located at K and K' points, they play an essential role in the electronic properties of Gr as will be seen in the next section.

2.1.2 Electronic properties

Band structure

In the atomic ground state, the electronic configuration of a carbon atom is $1s^2 2s^2 2p^2$. The two inner 1s electrons close to the nuclei are not concerned by chemical bonds or reactions contrary to the four outer 2s and 2p electrons. In general, before to get involved into chemical bonds with any other atom, a carbon atom undergoes a slight excitation which modifies its orbitals. One electron moves from the 2s orbital to the only empty 2p orbital, let say the $2p_z$ orbitals. Therefore, each of the four 2s, $2p_x$, $2p_y$ and $2p_z$ orbital becomes filled with one lone pair electron. Thus, the single $|2s\rangle$ state undergoes quantum superposition with 1, 2 or the 3 $|2p\rangle$ states to form sp^n hybridation states of the "excited" carbon atom essential for covalent bonds which most often determine the physical properties and the symmetry of the resulting carbon based compound. As illustration, the gaseous compound of the geometrically linear acetylene molecule results from the sp^1 hybridation of carbon atom while the sp^3 hybridation of carbon leads instead to covalent bonds oriented to the vertexes of an octahedron and results to octahedral molecules such as methane. In addition, the sp^3 hybridation of carbon is responsible for the formation of diamond which is one of the hardest material with the lattice structure consisting of two interpenetrating face-center-cubic lattices.

The Gr structure results from sp^2 quantum superposition of the lone 2s orbital with two 2p orbitals ($2p_x$ and $2p_y$) to form three sp^2 planar hybridized orbitals having 120° mutual angle. The remaining unhybridized $2p_z$ is oriented perpendicular to the plan of sp^2 hybridized orbitals. The sp^2 hybridized states of the adjacent atoms intensively overlap to form σ covalent bond ground states and excited σ^* antibonding states. The σ bond states are fully occupied by the electrons involved whereas its corresponding excited σ^* antibonding states remain unoccupied. Likewise, the unhybridized $2p_z$ slightly overlap to form π bonds occupied, and its corresponding π^* unoccupied antibonding states. These molecular orbital: σ, σ^* and π^*, π which form only discrete states for a small number of carbon atoms, merge into energy bands when extended the whole Gr lattice. First principle calculation of the electronic band structure of Gr have revealed the σ and σ^* bands to be very energetic and more than 10 eV fare from the Fermi energy located at K and K' points (Fig.2.2(b)). Hence, only π and π^* bands are present at Fermi energy in the vicinity K and K' and thus determine the electronic properties of Gr at low excitation energy [Fuchs08].[1] Therefore, to describe the electronic properties of Gr it is sufficient to consider only the π and π^* electronic bands. The first precise description of the π and π^* bands in graphite has been proposed by Wallace in 1947 [Wallace47] using a tight-band model. This approach has so fare been adapted to describe the π and π^* bands in Gr [Charlier07, Cresti08]. In this model, an electron of the p_z orbital with a spin $\mathbf{s}$ ($s = \uparrow, \downarrow$) can hope from a carbon atom indexed $\imath$ of the sublattice **A** to one of its three nearest neighbor of sublattice **B** with an hopping integral $t \approx 2.8$ eV. Hence, if one defines two creation operators

[1] The operation of the devices in nanoelectronics and spintronics is in general limited to low energy regime such that the stimuli on the devices are limited to the excitation of π and π^* electrons.

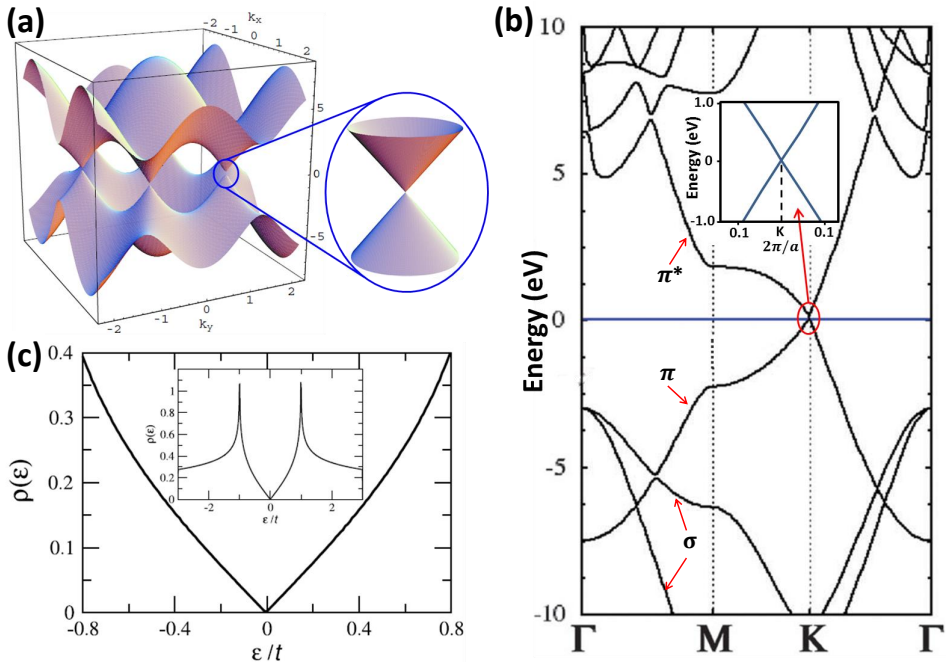

Figure 2.2 *– Dispersion relation of Gr calculated using a first nearest neighbor tight-binding model. (a) 3D plot of dispersion relation. The valence and conduction bands touch each other at the six corners of the FBZ. The highlighted region (in blue) at the vicinity of a Dirac point shows a conical shape illustrating the linearity of the dispersion relation. adapted from [Peres07]. (b) Band structure along Γ – M – K – Γ. The insert presents the linear behavior up to 1 eV. adapted from [Miró14, Terrones10].(c) The DOS as function of the energy (in unit of the hopping energy t) presenting a perfectly linear behavior reminiscent electron-hole symmetry in Gr. The linear behavior ρ(E) =| E | is apparent close to the neutrality point. The inset presents the behavior per unit cell. adapted from [Castro Neto09a].*

of a spin **s** electron on $\imath$ and $\jmath$ atoms of the sublattices **A** and **B** by $a^+_{i,s}$ and $b^+_{i,s}$ respectively, the tight-binding Hamiltonian is given by Eq.2.1 [Cresti08, Castro Neto09b].

$$H = -t \sum_{<i,j>,s} (a^+_{s,i} b_{s,j} + b^+_{s,i} a_{s,j}) \tag{2.1}$$

A convenient choice of the analytical expression of the tight-binding eigenfunctions in the form of a spinor, whose components correspond to the amplitudes on A and B atoms within the unit cells, enables to reduce this Hamiltonian to a simple quadratic off diagonal matrix in the **k**-space representation [Cresti08].

$$\hat{\mathbf{H}}_k = \begin{bmatrix} 0 & f(\boldsymbol{k}) \\ f^*(\boldsymbol{k}) & 0 \end{bmatrix} \quad ; \quad f(\boldsymbol{k}) = -t \sum_{l}^{3} \exp i \vec{\boldsymbol{k}} . \vec{\boldsymbol{\delta}_l} \tag{2.2}$$

$\boldsymbol{\delta}_l$ represent the vectors connecting **A** type sites to the three nearest **B** type sites (Fig.2.1). The diagonalisation of the 2×2 matrix of Eq.2.2 provides the dispersion relation of the π and π^* bands as given in Eq.2.3.

$$E_{\pm}(\boldsymbol{k}) = \pm t[3 + 2\cos(\sqrt{3}k_y a) + 4\cos\left(\frac{\sqrt{3}}{2}k_y a\right)\cos\left(\frac{3}{2}k_x a\right)]^{1/2} \tag{2.3}$$

$\boldsymbol{k}(k_x, k_y)$ denotes the electron wave vector.

This dispersion relation is plotted in Fig.2.2.(a). The lower valence band is symmetric to the upper conduction band with respect to the zero-energy plane containing the six degeneracies points where the two energy bands touch each other. These degeneracy points correspond to the six corners of the FBZ ($\boldsymbol{K}$ and $\boldsymbol{K'}$). It is worth noticing that there is a conceptual difference between the $\boldsymbol{K}$, $\boldsymbol{K'}$ points and the degeneracy points where the two bands get in contact. The latter can move away from $\boldsymbol{K}$ and $\boldsymbol{K'}$ if the hopping parameter becomes anisotropic due for instance to mechanical strain [Hasegawa06]. The honeycomb lattice giving rise to two carbon atoms per unit cell, and contributing each with one electron to the π band, the lower valence band is completely filled whereas the the upper conduction π^* band is completely empty [Castro Neto09a]. This results to the Fermi energy situated at the degeneracy points of the two bands which are thus chosen to be the zero origin of energy. Let remind that in semiconductors, the completely filled valence band is separated from the conduction band by a forbidden energy band (the gap) such that the conduction band is empty at absolute temperature whereas at finite T, electrons are thermally excited therein leading to an effective non zero intrinsic carrier density. This contrasts with the metal whose valence and conduction bands overlap such that electrons are present in the conduction band even at absolute T. The hypothetic band structure of Gr with no forbidden energy gap but also empty conduction band at absolute temperature situates it in between this two common classes of materials. Therefore, Gr is classified as a ***semimetal***. By definition, semimetal refers to materials for which the valence and the conduction bands just slightly overlap. This is strictly speaking not the case for monolayer Gr contrarily to bilayer and thicker Gr as will be described later. It is important to note that although $\boldsymbol{K}$ and $\boldsymbol{K'}$ are not crystallographically equivalent, they are indeed energetically equivalent since the dispersion relation is identical at their vicinity. Thus, in Gr, an electron at the vicinity of the Fermi level can occupy a state either at $\boldsymbol{K}$ or at $\boldsymbol{K'}$. This confers to them in addition to the spin, a supplementary degree of freedom refereed to as the **valley degree of freedom**.

Linear dispersion relation : the massless Dirac fermions

At the vicinity of $\boldsymbol{K}$ and $\boldsymbol{K'}$, i.e. at low energy limit ($\left|E(\vec{k})\right| < t$), the electron wave vector can be written as $\vec{k} = \vec{K} + \boldsymbol{\kappa}$, with $|\boldsymbol{\kappa}| \ll |\boldsymbol{K}| \sim 1/a$ (or $|\boldsymbol{\kappa}|a \ll 1$).[2] Hence, the first order Taylor expansion of the dispersion relation in $\boldsymbol{\kappa}.a$ yields a linear dependency of the energy with $\boldsymbol{\kappa}$ (Eq.2.4) regardless to the $\boldsymbol{K}$ and $\boldsymbol{K'}$ valley.

$$E_{\pm}(\boldsymbol{\kappa}) = \pm\hbar v_{\mathrm{F}}|\boldsymbol{\kappa}|, \quad \text{with } v_{\mathrm{F}} = \frac{3ta}{2\hbar} \approx 1 \times 10^6 \text{ m s}^{-1}. \tag{2.4}$$

Here, v_{F} denotes the Fermi velocity. This linear dispersion relation of Gr is reminiscent of the solution of Dirac's equation for relativistic particles $E = \pm\sqrt{p^2c^{*2} + m^{*2}c^{*4}}$ which in the limit of ultra relativistic particles ($m \to 0$) yields a simple linear expression $E = \pm pc^*$ in analogy with

[2] It can be considered also the equivalent relation for $\vec{K'}$, $\vec{k} = \vec{K'} + \boldsymbol{\kappa}$ with $|\boldsymbol{\kappa}| \ll \left|\boldsymbol{K'}\right| \sim 1/a$.

Eq.(2.4) for $c^* = \frac{\sqrt{3}a}{2\hbar}t$ and $p = \hbar|\boldsymbol{\kappa}|$ [Peres07, Avouris10, Das Sarma11, Castro Neto07]. For this reason, $\boldsymbol{K}$ and $\boldsymbol{K'}$ are called "Dirac points" in the vicinity of which electrons in Gr are considered to be massless. However, the latter consideration has no a strict fundamental meaning. Indeed, at the vicinity of Dirac points electrons have been reported not to be strictly massless. They process a small but non vanishing effective mass that can be as small as $0.007m_0$ in monolayer Gr, m_0 is the free electron mass[3] [Novoselov04, Zhang05b]. The well known condensed matter physics definition of the effective mass $m^* = \hbar/(\frac{\partial E}{\partial k^2})$ [Mathieu09] assumes a parabolic dispersion relation and is not appropriated for linear dispersion relation as it would lead to the divergency of the effective mass. To circumvent this divergency, an alternative definition of effective mass has been adopted in Gr using cyclotron mass.[4] In a perpendicular constant magnetic field, carriers in 2D electrons gas propagate on close trajectories that can be considered circular in ideal conditions. The effective mass of cyclotron electrons in semi-classical approximation in given by $m^* = \frac{1}{2\pi}(\frac{\partial A(E)}{\partial E})_{E=E_F}$ [Ashcroft76, Castro Neto09b] where $A(E) = \pi k(\vec{E})^2$ is the area enclosed by the orbit in $\vec{k}$ space. The linear dispersion relation leads to the effective mass of charge carriers in Gr proportional to the square root of carrier density $m^* = \frac{\pi}{v_F}\sqrt{n}$ [Castro Neto09a]. The experimental observation of such effective mass dependency have been reported [Novoselov04, Zhang05b] in Gr. These reports also highlighted that from $m^* = 0.04m_0$ at high carrier density, the effective mass drops to $0.007m_0$ near the Dirac point without vanishing completely at finite temperature. Due to the linear dispersion relation, the density of state in Gr also presents a perfectly linear dependence with energy for both holes and electrons at the vicinity of the neutrality point (Fig.2.2.(c)).

Multilayer graphene

The electronic structure of multilayer Gr deviates from that of monolayer and depends on the number of layers and the stacking order. For bilayer Gr, one distinguishes two main stacking orders. The AA stacking in which the carbon atoms of the upper layer sit on top of those of the bottom layer. This type of bilayer stacking is rarely encounter, since it is unstable and experimentally difficult to distinguish from monolayer[Liu09]. It has however been experimentally observed [Liu09]. The most stable bilayer stacking also the most studied Gr is the AB stacking within which half of the atoms of the upper layer sit on top of the atoms of the bottom layer while the other half sit at the center of the hexagons formed by the atoms of the bottom layer (Fig.2.3.(a).). In this condition, the upper layer can be considered to be translated with respect the bottom layer by one of the three joint vectors $\boldsymbol{\delta_i}$. In bilayer Gr containing four atoms per unit cell, additionally to the in plane carbon-carbon electron hopping in each layer, inter layer electron hopping occurs and quantified by a second hopping parameter $t_\perp$ [Das Sarma11] which depends on the relative position of the atoms involved.

[3] With a strict consideration of absolute zero mass for electrons, it could have been fundamentally complicated to define the mobility of charge carriers in Gr which in this case would diverge.

[4] Another interesting approach based on particle-wave duality is discussed by Viktor Ariel and Amir Natan resulting to a formula compatible with cyclotron trajectory of carriers and argued to be a general formula for m^* applicable regardless to the type of dispersion relation either parabolic or linear.

The tight binding model can thus be adapted to study the electronic structure of bilayer Gr. In the case of AB stacking, considering only the most prominent processes, the inter layer hoping parameter is $t_\perp = 0.4eV$ [Das Sarma11]. For small wave vector satisfying $\hbar v_F \left|\vec{k}\right| \ll \left| t_\perp \right.$ [Das Sarma11], the bilayer dispersion relation satisfies a common quadratic equation $E = \pm\frac{\hbar^2 k^2}{2m}$ where $m = t_\perp / 2v_F^2$ (Fig.2.3.(b)). The signs ± denote the conduction and valence band which effectively overlap (but just slightly) at Dirac point [Terrones10] as expected for perfect semi-metal in contrary to Gr. The stacking structure of trilayer Gr depends on that of bilayer.

Any trilayer Gr involving AA bilayer stacking has been reported. In AB bilayer, if we assume the upper layer to be translated by either δ_i with respect to the bottom layer, the third layer can as well be translated by δ_i or $-\delta_i$ compared to the second layer. For $-\delta_i$ translation of the third layer, its atomic sites coincide with those of the first layer resulting to ABA or Bernal stacking. For δ_i translation instead, the atomic configuration of the first layer is not recovered and the stacking is reported as ABC or rhombohedral. The trilayer band structure can be described as a combination of both monolayer and bilayer band structures taken independently. This means that its consists of a bilayer quadratic dispersion relation superposed to a Dirac like linear dispersion relation of monolayer (Fig.2.3.(c)). The stacking structure of four an ticker multilayer is resumed in three cases including the ABA (Bernal), the ABC (rhombohedral) stacking and a disordered stacking with no discernible order known as the turbostatic stacking. Similarly, the band structure of multilayer Gr exhibits a bi or trilayer like behavior for even and odd number of layers respectively and gets closer to the bulk graphite band structure with increasing thickness. It is important to note that not only the translation

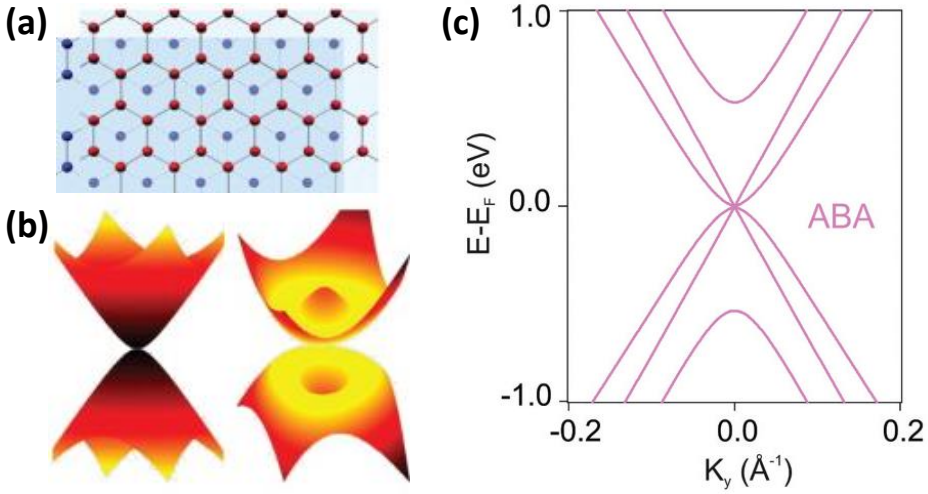

Figure 2.3 *– (a) Schematic of AB bilayer stacking Gr. The red and blue layer represents the and bottom layers respectively. (b) Gapless parabolic band structure of bilayer Gr (left). An applied perpendicular electric field induces a gap opening (right). (c) Trilayer band structure with a superposition of a linear monolayer and parabolic bilayer like dispersion relations. Adapted from [Lau12](a, b) and [Coletti13] (c).*

of layers is important in the multilayer Gr stacking. Their mutual-rotation is to be considered as well. In bilayer, the two layers can be rotated by an angle $\phi = \frac{\vec{a_1}}{\left|\vec{a_1}\right|}\frac{\vec{a_1}}{\left|\vec{a_1}\right|}$ where $\vec{a_1}$ is the lattice vector of the bottom layer and $\vec{a_1'}$ its equivalent in the top layer. When this angle fulfils

certain remarkable conditions, one obtains a moiré pattern reproducing a honeycomb like lattice structure with a larger unit cell. Recent experiments show that such a twisted bilayer Gr with an angle $\phi = 1.1°$ reported as 'magic angle' presents an electronic structure exhibiting a flat band near Fermi energy [Cao1805, Cao18]. This flat band results in correlated insolating state at half filling. Upon electrostatic doping, the twisted bilayer Gr moved from correlated insulating states to exhibit zero resistance state [Cao1805, Cao18]. Due to the absence of gap in their band structures, single or few layers Gr based FET exhibit a modest on-off current ratio which represents an important disadvantage for electronic applications. To circumvent this limitation, experimental efforts has been developed to induce a gap in Gr band structure. A successfully demonstration of 130 meV gap has been reported in bilayer Gr upon application of a perpendicular electric field [Xia2010], a modest value however compared to the theoretical prediction of 250 meV (Fig.2.3.(b)). Today, this direction seems to have slowdown with the emergence of layered semiconductors exhibiting wide range of band gap appropriate for various types of electronic and optoelectronic applications. In the following section we detail the structural and electronic properties of layered semiconductors and particularly semiconductor transition metal dichalcogenides.

2.2 Semiconducting transition metal dichalcogenides

Transition metal dichalcogenide (TMD) refers to a large family of materials of chemical formula MX_2 where M is a transition metal element from group IV to X of the periodic table of chemical element [Chhowalla13, Wang12, Ajayan16, Li17] and X is a chalcogen element of group XVI (S, Se, Te) [Chhowalla13]. Similar to Gr, they exhibit layered structure with a strong intra-layer covalent bonds between atoms which drastically contrast with the weak Van der Waals inter-layer coupling. This makes possible the isolation of one or few layers TMD from the bulk crystal by exfoliation. A monolayer TMD consists of 3 atomic plans of form X-M-X such that a transition metal atomic plan is sandwiched between two chalcogen atomic plans. The large possibility of combination of transition metal atoms with chalcogen atoms in MX_2 stoichiometry, give rises to a large variety of TMDs with diverse electronic structures and completely different electrical properties. Hence one distinguishes insulators, semiconductors [Wang12, Chhowalla13], metals, semimetals and superconductors[Yang17, Ajayan16, Li17]. These electronic properties are essentially controlled by the occupation rate of the non-bonding d orbitals of M atoms [Schmidt15] by electrons. This electronic occupation rate of the non-bonding d orbitals of M atoms differ in TMDs depending on the group of the transition metal and determines the spatial coordination geometry of the later and hence the crystal structure of TMDs to which their electronic structures are closely related.

2.2.1 Crystal structure of semiconducting TMDS

The transition metal's coordination can be either trigonal prismatic or octahedral resulting to a variety of polymorph and polytype phases. The three frequently encounter poly-

morphs are the hexagonal phase (2H), the trigonal phase (1T) and the rhombohedral phase (3R) [Chhowalla13]. The digits preceding the letters H, T and R indicate the number of X-M-X layer in the unit cell. Indeed, in hexagonal polymorphic phase, two monolayers MX_2 are required to form the primitive cell. To distinguish from few layers or bulk, the nomenclature adopts the notation (1H) when referring to a monolayer TMD in hexagonal polymorphic phase. The trigonal phase requires only one monolayer to form the primitive cell no matter the thickness. The same, rhombohedral polymorph exists only in three layers and thicker samples. Metallic TMDs composed of group IV and V such as TaS_2 and TiS_2 are thermodynamically stable in 1T phase contrary to their semiconductor counterpart such as MoS_2, $MoSe_2$ and WS_2 stable in 2H phase [Chhowalla13, Kappera14b, Li17]. The 1T metastable metallic phase in MoS_2, $MoSe_2$ and WS_2 requires a relatively high activation energy of approximately 1 eV to relax back into the semiconducting 2H phase [Voiry13, Kappera14a]. Furthermore, engineering the occupation of the non-bounding d-orbital of the M atom by chemical or electrostatic doping enables inducing a transition from the stable 2H phase to the metastable 1T phase which have important application in nanoelectronic for contact resistance engineering [Kappera14a].

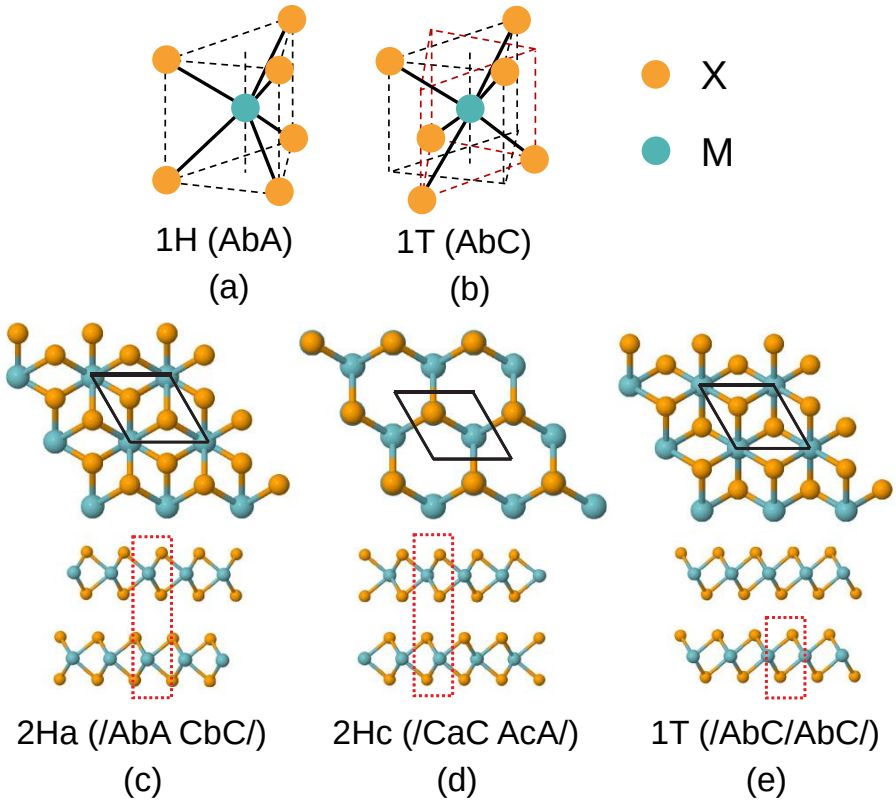

Figure 2.4 *– Transition metal atom coordination for (a) trigonal prismatic (H) and (b) octahedral (T) polymorph. The blue and orange spheres represent the transition metal and chalcogen atoms respectively. Top and side views of (c) 2Ha, (d) 2HC and (e) 1T bulk polytypes. The primitive cells are highlighted by black rhombuses in the top views and red dashed squares in the side views. The primitive cells of 2H and 1T polytypes contain six and three atoms respectively. The stacking orders are indicated in brackets. Adapted from Ref. [Ribeiro-Soares14].*

In regard to their geometrical organization, the atoms in each of the three monoatomic layer constituting a monolayer MX_2 TMDs have a triangular organization comparable to the Gr sublattices (see section2.1.2). Only the vertical intra-layer arrangement differentiate the (1H) and more generally the (2H) polymorphic phase to the (1T) polymorphic phase (Fig.2.4.(a,b)). The hexagonal 1H polymorph (also refereed as trigonal prismatic phase) results from a trigonal prismatic coordination of the transition metal atoms M with its six chalcogen nearest neighbors half distributed in the top and bottom chalcogen plan. The chalcogen atoms of the top and bottom layer are vertically aligned along the z-axis resulting to AbA stacking sequence of monolayer MX_2. A and b refer to chalcogen and transition metal atoms respectively (Fig.2.4.(a)). The 2H TMDs (thickness superior to one MX_2 layer of trigonal prismatic polymorph) exist in two forms with different stacking symmetries [Ribeiro-Soares14] reported as 2Ha and 2Hc (Fig.2.4.(c,d)). The 2Ha polytype reported for group V based TMDs such as $Nb(S,Se)_2$ and $Ta(S,Se)_2$, corresponds to /AbA CbC/ stacking sequence in which all the transition metal atoms align in the z-direction as presented in Fig.2.4.(c). The 2Hc polytype stable in group VI based semiconducting TMDs including $Mo(S,Se)_2$ and $W(S,Se)_2$ corresponds to /CaC AcA/ stacking sequence where each transition metal atom is vertically aligned with the two chalcogen atoms of the subsequent layer (Fig.2.4.(d)). The 3R polymorphic phase often present in chemically synthesized MoS_2 corresponds to the stacking sequence of /AbA CaC BcB/. The 1T polymorph or octahedral phase

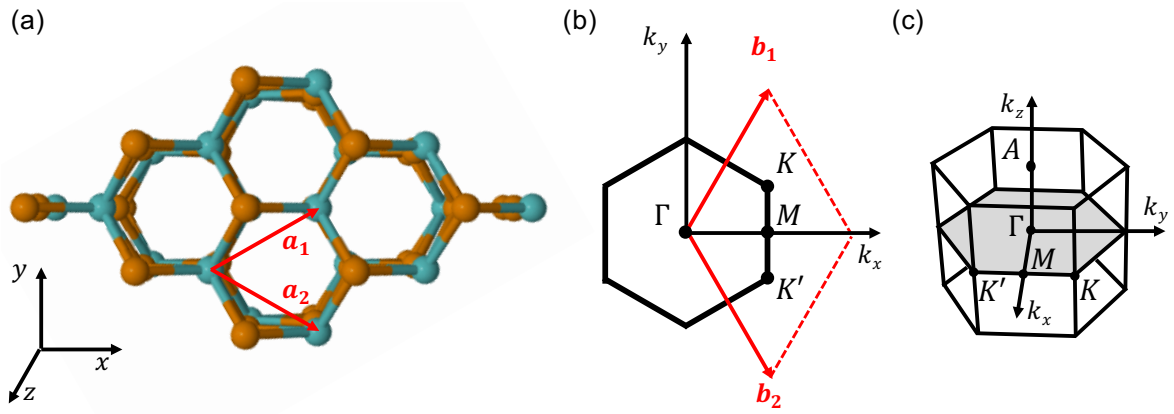

Figure 2.5 *– (a) Top view of 2Hc TMDs. $\boldsymbol{a_1}$ and $\boldsymbol{a_2}$ are the in-plane primitive unit vectors. (b) Corresponding first Brillouin zone. $\boldsymbol{b_1}$ and $\boldsymbol{b_2}$ are the in-plane reciprocal primitive unit vectors. The main four points are labeled: Γ, K, K′ and M. (c) Three-dimensional first Brillouin zone of bulk 2Hc TMDs. In addition to the four points depicted in (b), there is a fifth point labeled A. Adapted from [Froehlicher16].*

results from octahedral coordination of the metal atoms with its six nearest chalcogens of the two chalcogen layers still organized as in the 1H polymorph but rotated with respect to each other relatively to a vertical axis containing the transition metal atoms. Hence, the chalcogen atoms of both layer are not anymore aligned along the z-axis resulting to AbC stacking sequence (Fig.2.4.(b)). Consequence of the trigonal atomic organization, the Bravais lattice as well as the subsequent FBZ are hexagonal with the basis vectors $(\boldsymbol{a_1}, \boldsymbol{a_2})$ and $(\boldsymbol{b_1}, \boldsymbol{b_2})$ respectively (Fig.2.5(a, b)). It results two set of inequivalent points K and K' located at the vertexes of FBZ with a direct consequence of introducing a double valley degeneracy. The

FBZ presents four high symmetry points at its center Γ, middle of its edges (M) and its vertexes (K, K') (Fig.2.5(b)). For bulk TMDs, the FBZ becomes hexagonal prismatic with an additional high symmetry point (A) located on the same vertical with the Γ point at half high of bulk FBZ.

2.2.2 Band structure : Indirect-to-direct bandgap transition

The electronic structure of TMDs depends both on the occupation of d orbitals and the coordination of the transition metal atoms. In 2H and 1T TMDs (1H and 1T in case of monolayer), the non bonding d bands are located within the gap defined by the bonding σ and antibonding σ^* bands of M-X bonds [Chhowalla13] (Fig.2.6.(a,b)). In trigonal prismatic coordination (2H) polymorph, the d orbitals of the transition metal split into three groups. Successively the highest $d_{xz,zy}$ and intermediate $d_{x_2-y_2,xy}$ double degenerated orbitals and the non degenerated d_{z^2} orbital[5] situated 1.0 eV below the intermediate orbitals [Chhowalla13] (Fig.2.6.(a,b)). In group VI based 2H TMDs such as MoS_2 and $MoSe_2$ the lowest energy d_{z^2} orbital is completely filled with the two non-bonding electrons of Mo atom resulting to a semiconducting behavior (Fig.2.6.(a)) [Schmidt15]. In octahedral coordination of transition metal (1T phase) its d orbitals are modified to form two groups. The higher energy double degenerated $d_{x_2-y_2}$, d_{z^2} orbitals (e_g) and the lower triple degenerated $d_{xy,xz,zy}$ (t_{2g}) orbitals (Fig.2.6.(b)). Since only two electrons populate the lower energy t_{2g} orbitals, they remain partially filled. This consequently fixes therein the Fermi level and induces therefore the metallicity of the 1T TMDs. From the structural unit to the entire crystal, the orbital energy levels merge into bands. The Fig.2.6.(c) presents first principle calculation of the band structure of the 2H MoS_2 from bulk to monolayer [Splendiani10]. They present a typical semiconducting structure with and indirect band gap of $\sim$ 1 eV between the valence band maximum and the conduction band minimum situated respectively at Γ point and at the middled of Γ–K segment.

In TMDs, the quantum confinement becomes increasingly prominent as the number of layer decreases affecting their band structures. From their initial indirect gap band structure, the group VI based semiconducting TMDs (Mo,W)$(S,Se)_2$ undergoes a transition to a direct bandgap in monolayer at K point due to the absence of interlayer orbital interactions [Schmidt15]. In general, this transition is accompanied by an increase of the bandgap. For MoS_2, it increases to 1.8 eV (Fig.2.6.(c)). The indirect-to-direct band gap transition induces an important enhancement of the photoluminescence in monolayers of Mo$(S,Se)_2$ and W$(S,Se)_2$ whereas only a weak emission is observed in their multilayer counterpart [Chhowalla13] since the interband transition required and additional momentum (Fig.2.6.(d)). The group symmetry of TMDs also changes with their thicknesses [Ribeiro-Soares14]. The inversion symmetry presents in bulk or in odd number of layer thick samples is broken in monolayer or even number of fewlayer thick Mo$(S,Se)_2$ and W$(S,Se)_2$ [Chhowalla13, Yang17, Zeng13, Zhang14b, Zeng12]. In monolayer MoS_2 for example, such inversion symmetry breaking combines with strong spin-orbit coupling (SOC)

[5] The spin degeneracy is not taken into account here.

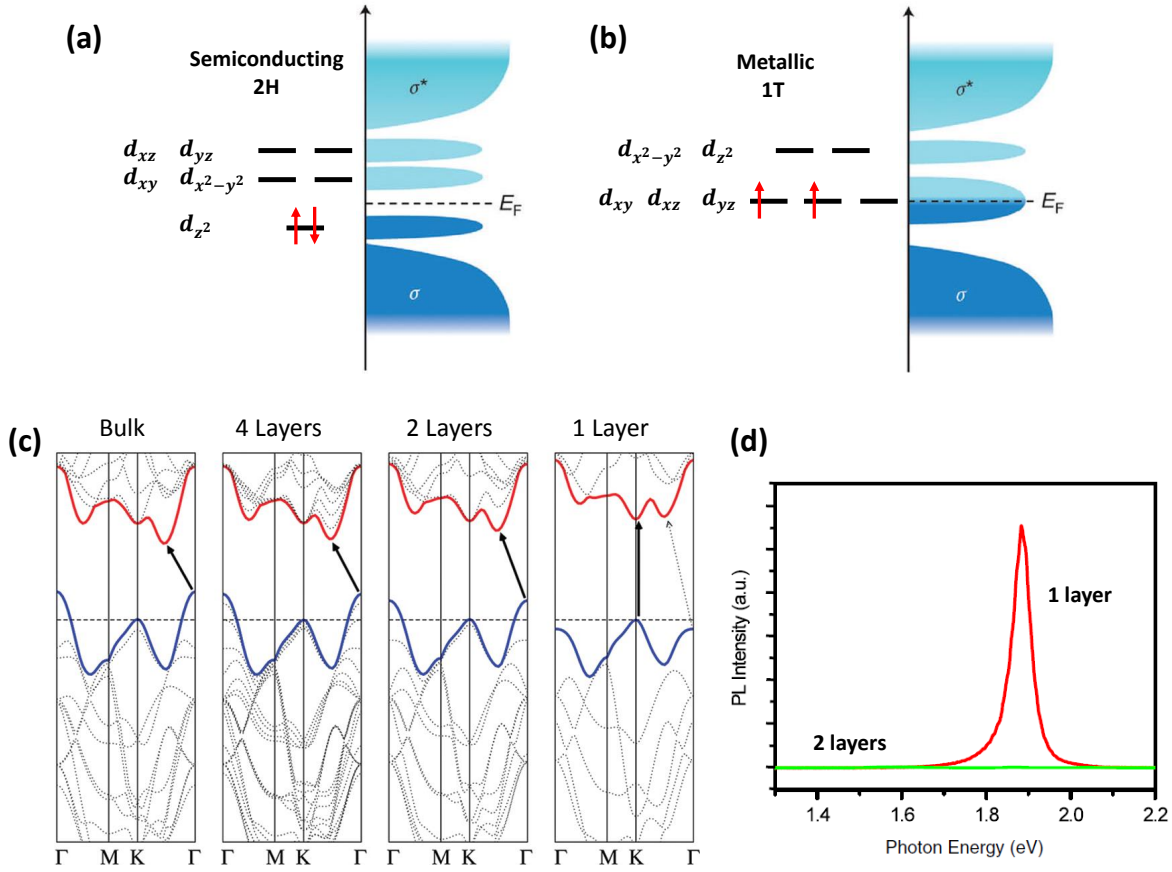

Figure 2.6 *– Band structure of semiconductor TMDs. Qualitative schematic illustration of the disposition and the filling of d orbitals located within the bandgap between the bonding σ and antibonding σ* bands in both 2H (a) and 1T phase (b). Adapted from [Chhowalla13] and [Schmidt15]. (c) The band structure of bulk, four layers (4L), bilayer (2L) and monolayer (1L) MoS_2 presenting an indirect to direct band gap transition. Adapted from[Splendiani10]. (d) Photoluminescent of suspended monolayer and bilayer MoS_2. Adapted from[Mak10].*

produce an out-of-plane valley dependent electron spin polarization at K and K' point. First principle calculations and photoluminescent experiments with left/right circular polarized light revealed such a spin valley polarization to be up to +30% and −30% at 10 K for spin up (K) and spin down (K') respectively [Zeng12]. The dangling bond free surface passivation of layered materials offers the possibility to restack them into all 2D-2D VdWh [Novoselov16] or to coupled them to other low dimensional nanostructures including nanoparticles (0D), nanowires (1D) and polycrystalline thin films and bulks (3D) to form a class of heterostrustures recently reported as 2D-nD (n = 0, 1, 2) mixed dimensional Van der Waals heterostructures (MD-VdW-h) [Jariwala16, Liu16] (see chap. 1). This enables to take benefit of cooperative properties expected to emerge from heterostructures likely leading to novel applications. In the following section, we detail the prospect of VdWh for optoelectronics, nanoelectronics and nanospintronics and review the fabrication methods of TMDs, VdWh and MD-VdWh based devices.

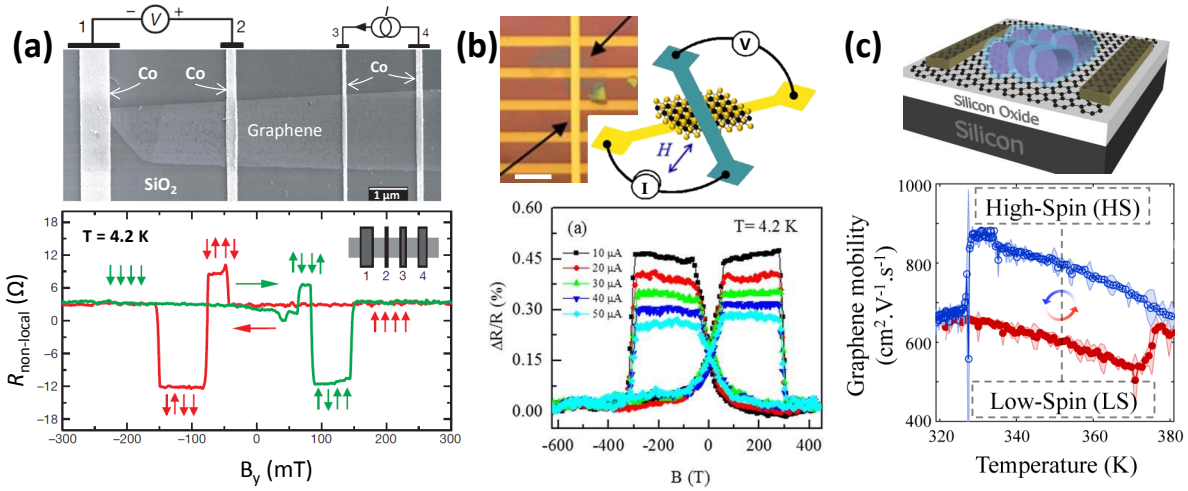

Figure 2.7 – MD-VdWh for spintronic applications. *(a) Lateral Spin valve device based Single-layer Gr exfoliated on SiO_2 substrate (top panel). Non-local spin valve signal of the device at 4.2 K (Bottom panel). The current is injected from electrodes 3 and 4 and the coherent spin diffusion detected by 2 and 1. Adapted from [Tombros07]. (b) Vertical NiFe/WS_2/Co MTJ device. Optical image (the scale bar is 10 µm) and sketch of the junction presenting the device configuration with the WS_2 flake exfoliated on a prepatterned NiFe electrode (top panel). The reported TMR spin signal (bottom panel). Adapted from [Piquemal-Banci17]. (c) Thermal memory signal of a device consisting of spin cross-over molecule film on Gr layer (bottom panel). The top image shows the schematic of the device. Adapted from [Dugay17].*

2.3 Van Der Waals heterostructures

Passivated dangling bond free surfaces are chemically inert and any materials either 2D or non-2D are expected to adhere with layered materials primarily through non covalent weak Van der Waals interactions [Jariwala16]. The extensive library of 2D materials and other low dimensional nanostructures with a wide range of properties offers the possibility to realize various types of heterostructures based devices with diverse geometries suitable to access new fundamental properties. Compare to bulk, atomically thin 2D materials exhibit low density of states rending them transparent to the applied electric field normal to the 2D plane. This makes feasible the modulation of the heterojunction interfaces of MD-VdWh with an applied vertical electric field as well as the electric properties of nD nanocrystals standing on the surface of 2D material. This represents the main reason sustaining the prospect of layered materials and VdWh for diverse applications in nanoelectronics, optoelectronics and spintronics. Yet, VdWh and MD-VdWh have enabled to realize FETs, tunneling FETs, phototransistors [Jariwala16, Liu16, Novoselov16, Wang12], high performance lateral and vertical spin valve devices [Piquemal-Banci17, Feng17]. Since 2D-1D and 2D-0D present a large surface to volume ratio resulting to an important density of active sites for chemical reactions, MD-WdV-h are widely used for catalyst and gas sensing applications [Gong18].

2.3.1 2D materials based devices

The physics and engineering of 2D material based solid state devices is sustained by a combination of requirements that may seems obvious while nothing guarantees them in principle.

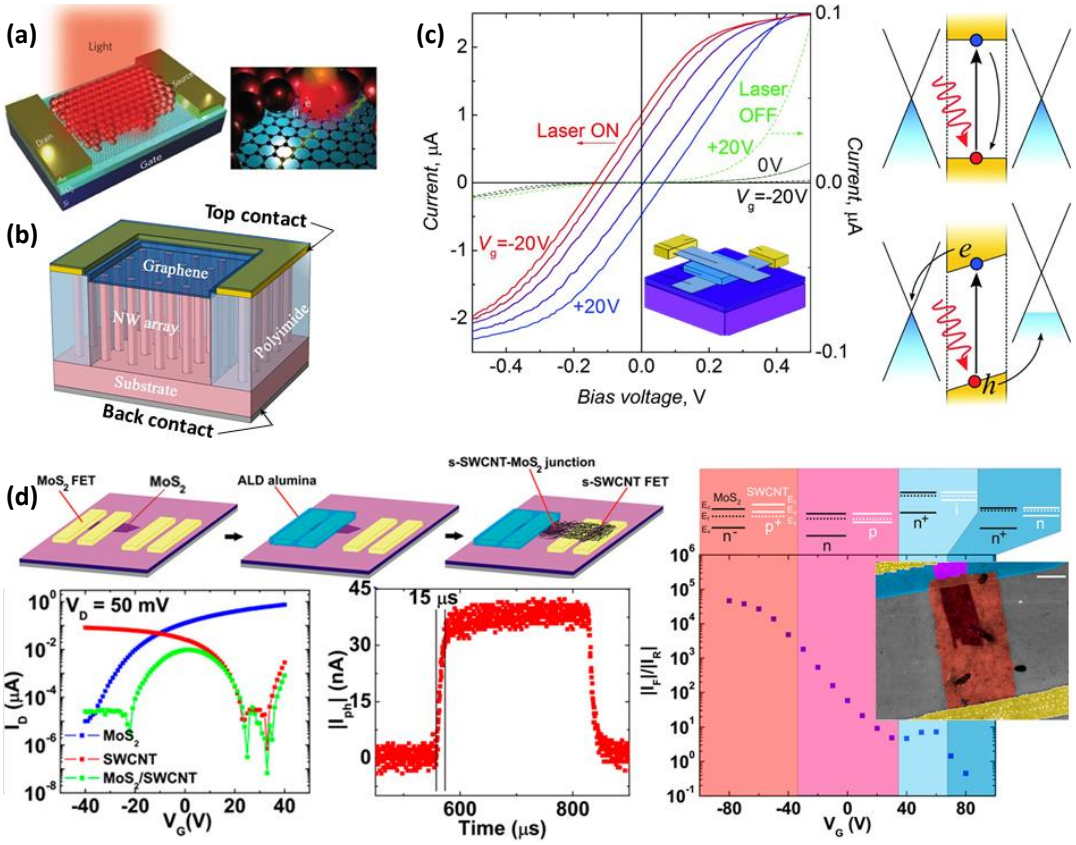

Figure 2.8 – Optoelectronic applications of MD-VdWh. *(a) Schematic of 0D-2D based PbS quantum dot/Gr [Konstantatos12] and (b) 2D-1D based Gr/vertically standing GaAs nanowires [Gong18] optoelectronic devices. (c) 2D-2D heterostructure consisting of Gr/Ws_2/Gr for optoelectronics. Gate tunable I-V characteristics with and without illumination. The insert shows the schematic of the devices (right panel). Heterostructure band diagram without (top) and with (bottom) a built-in electric field to separate the photogenerated electron-holes pairs (right panel). Adapted from[Britnell13]. (d) A completed 1D-2D FET and phototransistor experiment showing (from top to down and right to left) the device fabrication steps including the exfoliation of MoS_2 and electrodes patterning. Protection of MoS_2 FET with alumina. Sorting of SWCNTs on the free part of MoS_2 to make both SWCNTs/MoS_2 p-n junction and SWCNTs FETs. The transfer curves of the devices. The photodiode response of the SWCNTs/MoS_2 junction and Gate dependent forward-to-reverse current ratio (Ion/Ioff). The labels at the top show the corresponding gate rectification band diagrams for the SWCNT/SL-MoS_2 p-n heterojunction. The insert the colored scanning electron image of the p-n junction. Adapted from [Jariwala13].*

First, the 2D materials have to sufficiently stick on the substrate to enable subsequent fabrication steps often including immersion (usually accompanied with agitation) in various types of solvents and acid during the processing. Second, the possibility to identified the sheet of 2D material on an insulator substrate by simple optical contrast. The latter fact combine with the possibility to growth 3D metallic film (often used as electrodes) on 2D materials fulfilling the mentioned indispensable requirements of surviving to the subsequent processing steps favored the rapid expansion of 2D materials based solid state devices. Thanks to such a combination of factors, the first Gr based FET was reported in 2004 [Novoselov04] followed in 2011 by the first MoS_2 based FET [Radisavljevic11] have set the foundation of what constitutes to date a major branch of condensed matter physics and engineering.

Under optical illumination of the semiconductor channel, certain chemical bonds are broken and electrons are excited into the conduction band inducing holes in valence band. An applied DC bias to the electrodes splits the so photogenerated excitons and produces a gate modulable photocurrent through such phototransistor devices. Yin *et al.* [Yin11] provided the first demonstration of single layer MoS_2 phototransistor with 50 ms response time and a photoresponsivity of 7.5 mA/W. A value one order of magnitude exceeding those reported on Gr based phototransistor [Xia09a, Xia09b]. Lateral spintronic devices with magnetic electrode contacting the Gr sheet used as spin diffusion channel were also demonstrated [Feng17]. Indeed, thanks to limited carrier scattering source and low SOC, lateral Gr based spintronic devices demonstrated a long spin diffusion length of $2\mu m$ for exfoliated Gr [Tombros07] using Al_2O_2 tunnel barrier (Fig.2.7.(a)). Similar experiment recently reported a longer spin diffusion length up to 6μm together with a MR ratio of 20% at room temperature with CVD Gr [Kamalakar15] using TiO_2 tunnel barrier. This demonstrates the prospect of Gr for long-distance spin communication in 2D-3D VdW-h. Such coherent spin injection and detection turned to be very difficult to realize in lateral spin valve device made of TMD materials due to high TMDs/Metal contact resistance and large SOC preventing long distance spin coherent propagation. However, recent experiments with two terminals spin valve devices with MoS_2 channel revealed 1% MR [Liang17, Dankert17b].

Vertical magnetic tunneling junctions (MTJs) have also been reported using different 2D materials including Gr, SC-TMDs or h-BN as tunnel barrier [Piquemal-Banci17, Dankert17a]. In the case of TMDs, vertical MTJs demonstrated better results compare to their lateral homologous (Fig.2.7.(b)). The advantage of 2D materials in vertical MTJ devices is many folds : First, the atomically control of the thickness of the tunnel barrier in contrary to the commonly used thin oxide film deposited by physical vapor deposition technics [Piquemal-Banci17, Dankert17a]. Second, 2D materials favor the spin filtering at their interfaces [Godel14] and they passivate the surface of magnetic injectors or detectors their in contact with against oxidation usually detrimental for spin valve devices [Piquemal-Banci17].

2.3.2 2D-2D Van Der Waals heterostructures

The encapsulation of Gr in h-BN prevents it from extrinsic sources of scattering such as substrate roughness or impurities and water molecules adsorbed during the sample processing which are detrimental for its properties. This enables to achieve high mobilities reaching 200000 $cm^2V^{-1}s^{-1}$ in Gr FET [Mayorov11]. Gr/h-BN heterostructures based vertical tunneling transistor have also been reported (Fig.2.9.(a)) [Wang16, Pisoni18]. In such devices, the tunneling of charges is assisted either by phonon resulting from gate induced lattice vibration or by resonant tunneling trough discrete energy states of the impurities present in the h-BN tunneling layer [Chandni16]. Likewise, SETs fabricated by gate depleted quantum dot in 2D electron gases (2DEGs) such as sc-TMDs and Gr utilizing h-BN as gate dielectric were recently reported [Wang18a, Pisoni18]. This opened new perspective in mesoscopic physics of 2DEGs in CB regime with better defined systems compared to MOSFET and GaAs based quantum

well geometries which have sustained this frontier since three decades [Das Sarma11]. In optoelectronics, a repeating stack of 2D TMD semiconductors/h-BN constitutes stable quantum well with negligible leakage demonstrating efficient electron to photon conversion within the active semiconductor TMD layers when an electric field is applied perpendicular to the stack. Light emitting diodes (LEDs) consisting of such heterostructures have shown quantum efficiency reaching 20% at room temperature [Novoselov16] comparable to organic LED and state of the art GaAs based quantum well LED. The Fig.2.8.(c) presents an example of Gr/WSe_2/Gr phototransistor together with the photogenerated electron-hole splitting mechanism [Britnell13].

2.3.3 2D-1D Van Der Waals heterostructures

Nanowires can either be monodispersed on the Gr template or deposited as thin film [Jariwala13]. 2D materials have been successfully transferred on an array of vertically standing nanowires (Fig.2.8.(b and d)) [Jariwala16, Gong18, Wu17]. In any case, the diffusion of electrons in Gr induces a strong built-in field at the nanowire/Gr interfaces which splitted the carriers photogenerated in the active semiconducting nanowire and the holes are collected and rapidly transported to the leads by Gr thanks to its high mobility [Gong18]. Photodetectors made of Gr transferred on vertically standing GaAs nanowires (Fig.2.8.(b).) demonstrated 71 μs photoresponse time that is faster than the 120 ms reported on ZnS nanowires thin film deposited on Gr [Wu17, Gong18]. Vertical p-n heterojunctions consisting of p-type semiconducting SWCNTs thin film sorted on the n-type monolayer MoS_2 have also been fabricated and demonstrated to work both as logic gate FET and photodiode [Jariwala16]. Interestingly, the splitting rate of the photogenerated carriers within the interface p-n junction was demonstrated to be highly sensitive to the electric field leading to 5 orders of magnitude gate modulation of the photocurent with fast responsivity less than 15 μs (Fig.2.8.(d)). More importantly, both the underneath MoS_2 layer and the supporting CNT film was highly sensitive to the electrical gate doping. Thus, the observed modulation of the photocurent was explained by the significant change of the heterojunction from the n^--p^+ state with very efficient separation capability of the photogenerated excitons at high negative voltage to the weakest separation capability state p^+-n state at high positive voltage [Jariwala16] (Fig.2.8.(d)). This is the most obvious illustration of the possibility offered by MD-VdWh to modulate the electric properties of both 2D material template and the above sorted nanostructures. A property at the core of this thesis.

2.3.4 2D-0D Van Der Waals heterostructures

2D-0D VdW-h phototransitors follow the same logic as their 2D-1D counterparts. The photogenerated excitons are splitted by the interface built-in field and holes are collected and transported to the leads by the Gr template. Semiconductor PbS quantum dots/Gr phototransistors demonstrated photoresponsivity of about 10^7 AW^{-1} [Konstantatos12] which is the highest reported value on Gr based photodetectors (Fig.2.8.(a)). A report on Gr/C_{60} thin

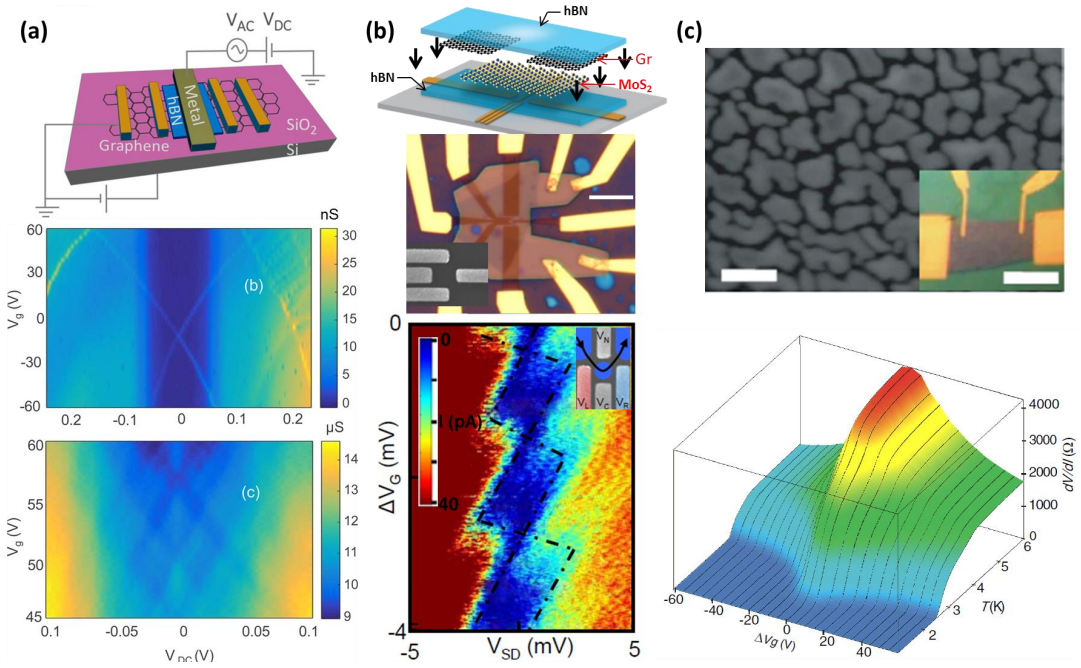

Figure 2.9 – Electronic transport applications of MD-VdWh. *(a) Phonon and defect assisted tunneling in Metal/hBN/Gr junction (top panel). The intermediate panel presents phonon assisted conductance map. The bottom panel presents Coulomb diamonds featured defect assisted conductance. Adapted from [Chandni16]. (b) hBN/Gr/MoS_2/hBN VdW-h transferred on prepatterned local gate electrodes for electrostatically defined quantum dot (top panel). The intermediate panel shows the optical image of the device. The inset is the SEM image. The bottom panel presents conductance color map with the Coulomb diamond patterns. The right insert is the electrostatically induced quantum dot. Adapted from [Wang16]. (c) Scanning electron micrograph of Sn islands morphology on Gr together with the optical image of the device (top panel), the scale bars are 100 nm for the main image and 10 μm. The bottom figure represents the temperature and gate dependent resistance. Adapted from [Kessler10].*

film FET and photoransistor demonstrated a gate tunable interface barrier resulting to 5 orders of magnitude on/off ratio and exponential gate dependent photocurrent [Parui15]. The decoration of MoS_2 with 3D bulk PbS micron scale plates[6] provided the first demonstration of infrared optoelecronics [Wang18b]. 2D materials are also sensitive to other types of fictionalization with decorating 0D nanostructures suitable for other possible applications. Non percolating tin (Sn) superconductor nanoparticules (NPs) deposited on Gr revealed to efficiently doped the Gr substrate up to inducing a long-range superconducting correlation [Kessler10, Allain12]. This enabled to observe a zero resistance response in the transport properties of NPs-Sn/Gr base device below 2.5 K (Fig.2.9.c.). The functionalization of Gr with spin cross-over molecules (i.e. molecules exhibiting bi-stable spin memory state sensitive to different external stimuli including temperature) enabled the fabrication of thermal memory devices. The memory operation been mediated by the switching of the spin state of the molecular thin films affecting the resistance of the underneath Gr [Dugay17] (Fig.2.7.c.).

The non exhaustive examples of VdWh and MD-VdWh based devices reported above demonstrate that up to now, any demonstration of 2D-0D MD-VdWh based SET have been

[6]The PbS nanoplates involved are mostly bulk such that the MD-VdWh is of type 2D-3D. It is mentioned here because the mechanism of carriers photogeneration is similar to those of 2D-0D.

reported. Though, this geometry represents an intuitive alternative to the challenging fabrication processes required for realizing such types of nanoelectronic devices. The above reviewed VdWh and MD-VdWh based relied on different fabrication approaches. In the following section, we provide an overview of these approaches which set the baseline for critical description of our methods presented in chap.4.

2.4 Fabrication methods of layered materials and VdWh

The fabrication of VdWh and MD-VdWh combines the distinct methods adapted to their individual components and that follow either a bottom-up or a top-down approach. The top-down approaches such as mechanical or chemical exfoliation consists to separate few or a single layer from bulk layered materials while braking the weak van der Waals interlayers adhesion energy calculated to be $\sim 2eV/nm^2$ in graphite requiring a weak force of about 300 nN/μm^2 to peel different layers [Zhang05a]. The bottom-up approach instead, relies on chemical synthesis method such as chemical vapor deposition (CVD), atomic layer deposition (ALD) or molecular beam epitaxy (MBE). Combined to these approaches adapted to layered materials one has also to consider the methods adapted for nanowires/nanotubes, NPs and molecules. These include chemical synthesis and drop casting, self assembly, thermal evaporation and different physical growth technics appropriate for nanoparticles.

2.4.1 Top-down methods : Exfoliation of layered materials

Mechanical exfoliation : As simple as it seems to be, the mechanical exfoliation consists of peeling from a peace of pristine bulk layered crystal (graphite, TMDs,...) a mono or few layers using an adhesive tape. The so exfoliated layer(s) are then transferred onto a supporting substrate, usually insulator such as Si-SiO_2 as it enables their identification by simple optical contrast to other type of substrate. This method is also referred as dry exfoliation in opposition to wet chemical exfoliation done in solution (section below). It was first proposed by Novoselov et al.[Novoselov04] in their pioneering work on Gr. It is well adapted for fundamental research because of its relative simplicity and high success rate for obtaining large flakes up to 100 microns. Most of the devices presented in this thesis are fabricated using this method. More details are provided in chap.4.

Chemical exfoliation : Chemical exfoliation or wet exfoliation of SC-TMDs involves the intercalation of different chemical species (often ions) in between the layers in order to fade the weak interlayer Van der Waals forces allowing the layer to be exfoliated in liquid [Wang12]. In order to do so, a powder of TMDs is submerged into a solution containing the appropriate chemical species such as n-butyllithium for lithium intercalation [Wang12]. After lithiation (incorporation of lithium ion) that can last more than a day, the material is exposed to water which undertakes a vigorously chemical reaction with Li involving H_2 gas and separate the layers under sonication [Nicolosi13]. The exfoliated nanosheets usually have to be stabilized against reaggregation or sedimentation by solvatation or by steric (i. e. electrostatically in-

duced repulsion of the layer due to adsorption of molecule from the solution). This method results to gram scale quantities of submicron size monolayers [Wang12]. However, the electronic structure of the exfoliated sheets differs from that of pristine bulk. For MoS_2 for example, the 2H semiconductor phase is often changed into 1T metallic phase requiring a thermal treatment to be restored. An alternative faster method reported concerns the intercalation of lithium in a controllable manner with an electrochemical cell containing a lithium fuel anode, followed also by sonication exfoliation in water. This method was demonstrate to work for both semiconducting TMDs and Gr [Wang12]. However, water is not an efficient ultrasonication solvent for Gr exfoliation and many progress have been done to find alternative, 5 μm large size monolayer Gr sheet have so far been reported [Nicolosi13].

Top down methods and particularly mechanic exfoliation provides comfortable flexibility and simplicity as well as clean and perfectly crystalline nanocrystals. It is thus suitable for lab applications for the purpose of device fabrication. However, the size and thickness of the exfoliated layers result from a completely random process and thus not reproducible. Therefore it is not suitable for industrial applications which request alternative synthesis methods enabling large scale production.

2.4.2 Bottom-up methods : CVD and derivatives

Chemical Vapor Deposition (CDV) is a method suitable for large scale growth of 2D layered materials with controlled thickness an lateral size. A successful demonstration of ≈ 1.5 inch wafer crystalline Gr was reported using this method. CVD synthesis of 2D TMDs consists of thermal co-evaporation in a quartz tube of a transition metal and a chalcogen precursor into a vapor phase. This vapor is then transported by an inert gas flux of Ag or H_2 to a nearby target substrate where they react directly to form a TMDs (Fig.2.10.(a)). The frequently used precursors for transition metal elements are trioxides of transition metal such as MoO_3 and WO_3 for Mo and W respectively while solid powder of chalcogens are the frequent chalcogen precursors (e.g. S or Se) [Song17, Choi17]. In a CVD experiment, number of parameters have to be optimized. The substrate which is debated to or not to request different chemical treatments or simple plasma oxygen treatments to favor the adsorption of reactive elements (M ad X) [Song17] favorable for large size TMDs (Fig.2.10.(g, h)). Although being the limiting factor in a CVD experiment since it is defined by the melting point of the precursors sources, the deposition temperature has to be optimized in order to avoid extreme situations. Higher temperature deposition induces 3D island growth process consequence of high surface diffusion of adatoms moving necessarily to most energetically favorable sites. Lower temperature instead leads to amorphous or polycrystalline film due to adatoms not having enough kinetic energy to diffuse to the lowest potential energy sites needed for large area monolayer growth. High quality 2D materials growth requires also optimizing the atomic gas flux to a sufficiently high vapor pressure to ensure the mixture of atomic gases and transport of the atomic species to the substrate while avoiding unnecessary chemical reactions during the transport [Choi17]. CVD enables achieving crystalline monolayer TMDs reaching

millimeter size $MoSe_2$ [Song17]. Interestingly, other transition metal precursors ($(Mo(CO)_6$, $MoCl_5$) enabled successful growth of centimeter crystalline mono and few layers MoS_2 and $MoSe_2$ [Song17, Choi17, Kranthi Kumar15].

Two steps methods: An interesting attempt for large scale production of TMDs has been developed consisting to two steps process. A very thin layer of transition metal is pre-deposited on the substrate using common physical growth method such as Ebeam evaporation or sputtering. Follows then by a chalcogenization in a CVD facility at high temperature resulting to TMDs layer with a thickness determined by that of the pre-deposited layer. Alternatively, the first step can involve instead a pre-deposition of transition metal precursor such $(Mo,W)O_3$ or $(NH_4)_2MoS_4$ on the substrate using either thermal evaporation, atomic layer deposition (ALD) or physical vapor deposition (PVD). In this case, the precursor directly reacts in the CVD system with sulfur during the second step yielding $(Mo,W)S_2$. This approach enables wafer-scale synthesis of TMDs which is an important step stone toward industrial production [Song17].

MOCVD : Other variant to CVD methods has been developed namely metal organic CVD (MOCVD) with the same principle as standard CVD described above. The only difference is that all the precursors are organo-metallic gas selected to exhibit high equilibrium vapor pressure near room temperature and was all introduced to the furnace in gas phase (Fig.2.10.(i)). The approach enabled successful growth of MoS_2 monolayer on a completely 4 inch ($\sim$ 11 cm) SiO_2/Si wafer [Kang15] (Fig.2.10.(i)). This made possible batch wafer fabrication of monolayer MoS_2 FET which demonstrated appreciable mobility of 30 $cm^2V^{-1}s^{-1}$ and 10^6 on/off ratio at room temperature [Kang15] (Fig.2.10.(j)). Note that uniform TMDs film are possible alternative for single or few layer thick TMDs when targeting large scale production and can be obtained by simple epitaxial growth the same as for any other material [Song17].

2D-2D heterostructures : Different methods exist to assemble layered materials into all-2D based VdWh. All of which derivative from the above described methods as resumed in ref.[Novoselov16, Liu16]. The frequently used method in research remains the direct micro-mechanical stacking (or transfer methods). It offers the same flexibility as the mechanical exfoliation. Simply seeking, different layered materials are exfoliated down to mono or few layers. Then, layer by layer stacking to form VdWh thanks to different dry or wet transfer technics [Novoselov16, Liu16]. The same as mechanical exfoliation, this method is not adapted for mass production. Alternative to mechanical transfer is the direct sequential growth of different 2D crystals using either CVD of epitaxy [Novoselov16, Liu16]. It is sometime advantageous to combine CVD and mechanical transfer. In this case, the first layer is mechanically transfer and the subsequent layer is growth by CVD [Novoselov16].

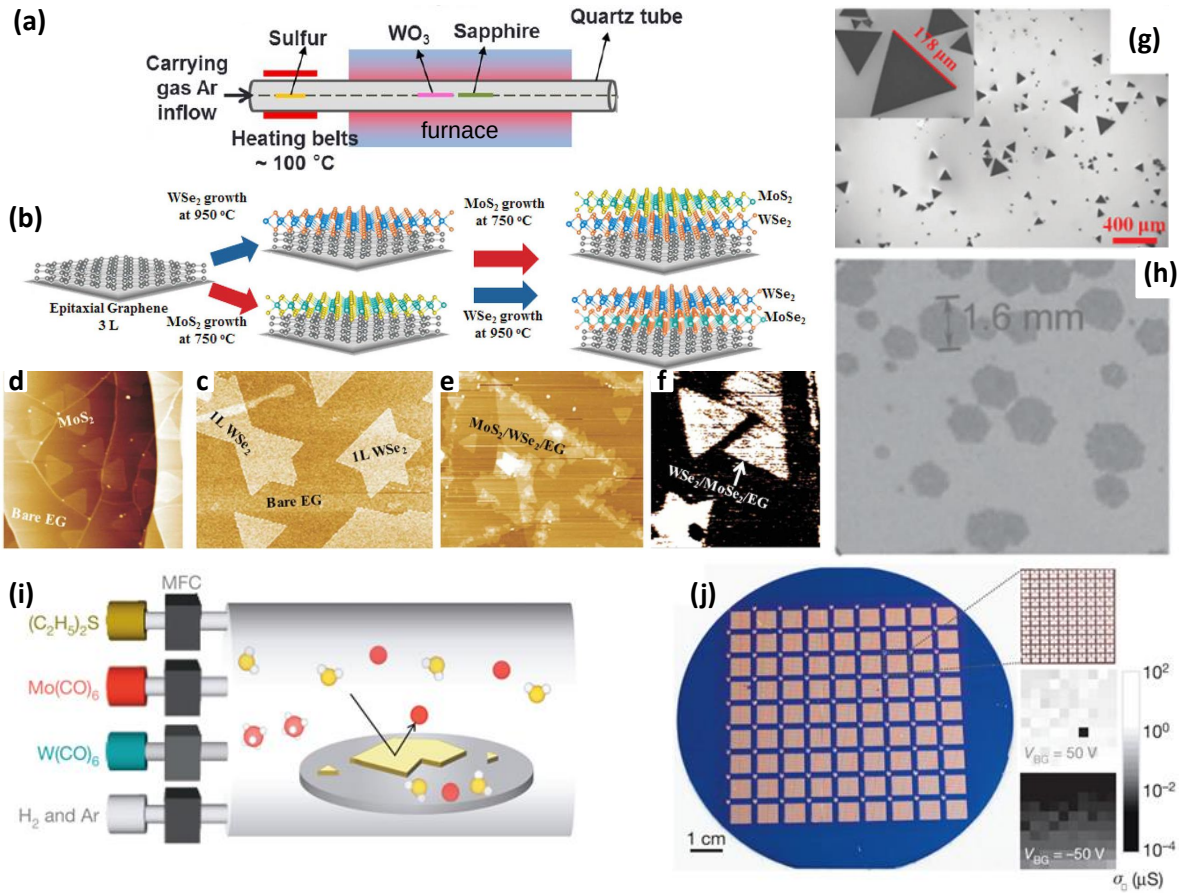

Figure 2.10 – *CVD fabrication method for layered materials and VdW-h. (a) Experimental Setup. (b) Schematics of the CVD growth of three layers VdWh. (e to f) AFM images of MoS_2/Gr, WSe_2/Gr, and MoS_2/WSe_2/Gr heterostructures respectively. (b) to (f) adapted from [Novoselov16]. (g and (h) Morphology of a millimeter scale $MoSe_2$ (b), (g) and (h) adapted from [Song17] (i) MOCVD setup. (j) Full 4 inch wafer MoS_2 monolayer FET with 10^6 Ion/Ioff ratio at room T. Adapted from [Kang15].*

2.4.3 Fabrication of MD-VdW-h

2D-0D and 2D-1D VdW-heterostructures : The fabrication of 2D/Nanoobjects VdWh systematically relies on a two steps approach for simple reasons of feasibility. In the first step, the 2D crystal and the nano-objects (nanoparticles, molecules, nanowires, CNT) are synthesized separately such that each component can be well controlled (shape, size, composition, crystallinity) using their already well established fabrication or synthesis routes. In a second step, the nanobjects are dispersed onto the 2D crystal surface using different methods including thermal evaporation for small organic molecules [Jariwala16], simple drop casting [Robin16, Federspiel15] and spin-coating [Raja16] for nanoparticles and nanowires and dip-coating for polymeric materials from solution [Jariwala16]. It is to be notice that in some case, it is the 2D materials that is transfer onto the nano-object such as in the case of free standing wires [Gong18]. Solution phase layer by layer assembly and wet transfer technics have also been utilized to decorate 2D materials with pre-synthesized 0D[Konstantatos12, Kufer15] and 1D[Jariwala13] nano-oblects respectively.

A second fabrication approach for 2D-0D heterostructures relies on direct growth of NPs over the surface of 2D crystals. This approach is widely used to growth self-assembled of various metallic NPs onto Gr surface by CVD on metal [Pan09, Sicot10]. Examples of optoelectronic and nanoelectronic devices using this approach includes the previously mentioned demonstration of Gr/Sn heterostructure based superconductive material [Kessler10, Allain12] or PbS/MoS_2 based photodetectors[Wang18b] both obtained by thermal evaporation of Sn and PbS nanoclusters respectively on CVD Gr transferred on SiO_2 and MoS_2 exfoliated on SiO_2. In the case of Gr, the growth mechanism of self-assembled metallic NPs differs depending on the Gr's supporting substrate. In the case of metallic substrate, the moiré pattern resulting from the meshing of the Gr and the metal lattices induces favorable sides. Hence, during the growth od a given metal, NPs nucleate preferentially at the moiré unit cells and growth thanks to the Stranski-Krastanov or 3D mechanism resulting to a self-organized ensemble of NPs on the Gr surface [Pan09, Sicot10]. In the case of Gr on insulating substrate instead, the self-assembly of nanoclusters is favored by the high diffusion rate of metal atoms which enables their diffusion to the most energetically favorable sites once adsorbed on the Gr surface resulting similarly of 3D islanding of self-assembled nanoclusters [Kessler10, Allain12]. In all these fabrication methods, the size of the cluster can be controlled with the thickness of the deposited materials. This is quite interesting as it makes this method appropriated for different types of applications including those requesting very small nanoclusters such and transport application in Coulomb blockade regime.

2.5 Conclusion

We have provided detailed descriptions of the structural and electronic properties of graphene and semiconducting TMDs. This broad range of properties can be summarized for graphene by a honeycomb hexagonal lattice originating from sp^2 hybridized carbon atoms. This structural organization favored a delocalization of $2p_z$ electrons which can hope between neighboring carbon atoms resulting semi-metallic behavior with linear dispersion relation comparable to massless Dirac fermions. Regarding semiconducting TMDs, they crystallize into hexagonal lattice with different polymorphic phases including the stable 2H semiconductor phase and a meta-stable metallic 1T phase that they adopt under specific conditions such as intensive doping. Their band structure exhibits transition from indirect to direct band gap when they are exfoliated down to a single layer. The interesting properties of Graphene and SC-TMDs have stimulated intensive development in nanoelectronics, optoelectroncis and spintronics illustrated by numerous of examples. Despite these abundant activities, there is to date no reports highlighting the prospect of MD-VdWh in general and 2D-0D VdWh in particular for quantum transport in the Coulomb blockade regime, which is one of the main objectives of this thesis.

Chapter 3

Transport processes in low dimensional systems

The investigation of the transport mechanisms at play in quantum devices is of paramount importance for both fundamental and applicative reasons. It enables the understanding the processes governing the functioning of the devices and thus indicates the possibilities of their optimization and better design. This thesis focusses specifically on the design and study of Field Effect Transistor (FET) using Graphene, $MoSe_2$ and MoS_2 as channel, Single Electron Transistor (SET) consisting of Graphene-AlOx or MoS_2-AlOx 2D-0D VdW-h and also spintronic devices using either Graphene-AlOx SED geometry or LSMO nanoparticules trapped into nanotranches. In this chapter, we provide the theoretical tools that will sustained the discussion of the results presented in the following chapters. We first present the transport mechanism in graphene and SCs-TMDs based FETs, then the orthodox theory of Coulomb blockade (CB) governing the transport in SET and the Magneto-Coulomb effect sustaining the magnetotransport SED integrating ferromagnetic components due to the interplay between CB and the applied magnetic field.

The notion of Field Effect. The word transistor derives from : transfer and resistor. It refers to a three-terminal device within which the resistance between two terminals is controlled by the third terminal (the gate) through an electric field effect. To capture the notion of field effect, let us consider for the sake of simplicity, a transistor consisting of a piece of metal as conducting channel having a length L, a width w and a depth h contacted by two electrodes : the source (S) and drain (D) and connected to the gate electrode through a capacitor C_g (C_g is a capacitance per unit surface). Under an applied source-drain bias V_{sd}, the channel can be reduced to a simple resistance and the Ohm's conductance $G = \mu \frac{w}{L} e n_v h$ is proportional to the surface carrier density $n = n_v \cdot h$. Here μ is the mobility of charges carriers, n_v their density per

unit volume and e the elementary charge. An applied voltage to the gate electrode induces an additional surface carrier density $n_g = \frac{C_g V_g}{e}$ in to the channel and the conductance formula is modified consequently to $G = \mu \frac{w}{L} e(n + n_g)$. Therefore, the gate electric field noticeably affects the conductance of the channel only if $V_g \succ \frac{enh}{C_g}$. For metallic channel with a high density of carriers usually in the order of $n \sim 10^{22} cm^{-3}$, this requests a gate voltage of about 10^4V. In semiconductor however, or and more generally low DOS systems such as Gr and SC-TMDs where the intrinsic carrier density is often lower than dopants density and usually in the range of $10^{12} cm^{-2}$ to $10^{13} cm^{-2}$, the required gate voltage for a substantial modulation of the channel conductance get reduces below a volt that is quite reasonable for applications.

3.1 Graphene based Field Effect Transistor

In FETs with Gr channel (GFET), an applied electric field directly affect its Fermi energy through doping and thus its transport properties. In general the expression of the density carriers (electron n and holes p) in semiconductors is given by : [Ashcroft76].

$$n = \int_{E_c}^{+\infty} f(E) g_c(E) \mathrm{d}E \quad and \quad p = - \int_{E_v}^{+\infty} [1 - f(E)] g_v(E) \mathrm{d}E, \tag{3.1}$$

Where, $g_c(E)$ and $g_v(E)$ are the density of states in the conduction and valence bands respectively. $f(E) = [1 + \exp((E - \mu)/k_B T)]^{-1}$ the Fermi-Dirac distribution at a temperature T. Because of the perfectly symmetric linear dispersion relation for electron and hole in Gr (see section2.1.2), $g_c(E) = g_v(E) = g(E) = \frac{2E}{\pi(\hbar v_F)^2}$. Hence, the electron density n is identified to that of holes with simply a sign difference. Given, that both the maximum valence band E_v and the minimum conduction band E_c are equal to zero, applying the Eq. 3.1 to Gr at absolute temperature yields a square root dependency of the Fermi energy with the carrier density n.

$$E_F = \mathrm{sgn}(n) \hbar v_F \sqrt{\pi |n|}, \tag{3.2}$$

Where sgn is the sign function. In practice, as T increases from the absolute value, E_F is not much affected and still reasonably defines the chemical potential of Gr [Li11b]. More importantly, the graphene's Fermi energy E_F is always situated in a permitted band due to its semi-metallic nature. Thus, it can be continuously displaced from the conduction to valence band through the Dirac neutrality point. Hence, both holes and electrons participate to electric transport and the electric conductivity of Gr exhibits an ambipolar behavior and a linear dependency $\sigma = \mu_n ne$ with the density of carriers (or gate voltage) (Fig.3.1.(a)) [Novoselov04, Castro Neto09b]. σ increases with the density of carriers either holes in negative Vg or electron in positive Vg. The minimum conductivity is achieved at the Dirac neutrality point where the density of carrier vanishes. In Fig.3.1.(a) it takes place almost at Vg = 0. This is characteristic of pristine samples with negligible extrinsic doping. Indeed, the position of the Dirac point in the transconductance of Gr is a direct indication of its doping. In doped samples, its is away from Vg = 0. The more distant it is from Vg =

0, the more doped is graphene. For p-doped sample it is situated in positive Vg while for n-doped sample it is negative Vg range. The Fig.3.1.(b) illustrates the effect of extrinsic doping of potassium atoms on Gr.

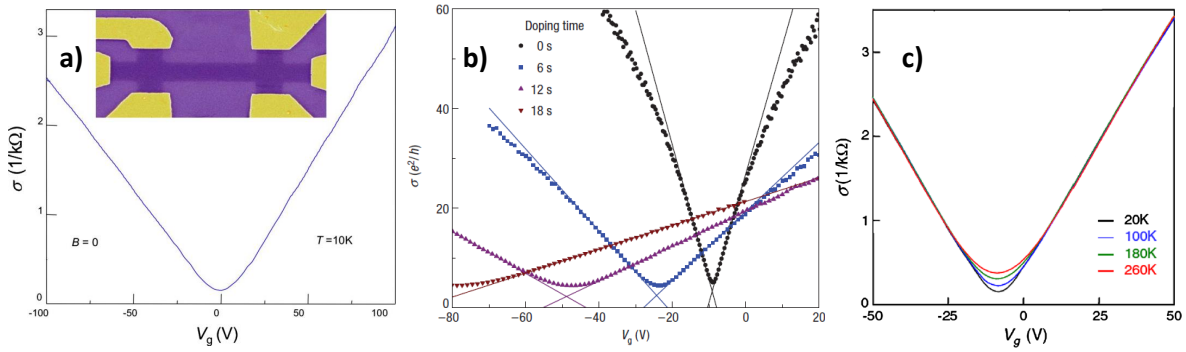

Figure 3.1 *– (a) Linear dependency of Gr's conductivity with V_g at 10 K. Adapted from [Castro Neto09b]. The inset presents the corresponding device geometry. (b) The behavior of the conductivity of Gr with extrinsic potassium atoms doping. 0 seconds corresponds to the sample without potassium ions deposition. 6 s, 12 s and 18 s correspond to potassium deposition duration. (c) Bilayer Gr conductivity at different temperatures. (b-c) Adapted from [Das Sarma11].*

The assumption admitted here concerning the electrostatic doping of Gr ($n_g = \frac{C_g V_g}{e}$) although correct has to be consider with some precision. In principle, the quantum capacitance has to be taken into account. We provide in appendix.A its physical origin and derivation. To resume, it originates from the fact that the new carriers provided by gating to be accommodated in the Gr channel require additional energy to occupy available states higher in energy, the lower energy states being occupied yet by the carriers originally present in the channel. This extra energy requires for electrons or holes to be injected into the channel is seen as an additional capacitance (of quantum origin) in series to the geometrical gate capacitance C_g. This is not specific to Gr, it is a general property low DOS systems, such as 2D electron gas in MOSFETs, semiconductors quantum well or 2D semiconductor TMDs. In the particular case of GFET, the quantum capacitance relates to carriers density by Eq.3.3 (see Appendix.A).

$$C_Q = sgn(n)\frac{e^2}{\hbar v_v \sqrt{\pi}}\sqrt{n} = \frac{e^2}{2}g(E_F) \tag{3.3}$$

This equation predicts the vanishing of the quantum capacitance at Dirac point. This was not confirmed by experiment. Instead, a non vanishing minimum value of $C_{Q,min} = 0.8\mu F cm^{-2}$ was reported and was attributed to the impurities carrier density induced by local potential fluctuation of the substrate remaining non-zero at the Dirac point and not taken into account by the theory describing the Eq.3.3 [Fang07, Fernández-Rossier07, Das Sarma11]. Beside this, both theory and experiment confirm the quantum capacitance of Gr to be in the order of few ten $\mu F cm^{-2}$ for devices with very thin gate oxide or even not separation between the gate and the Gr flake such as in electrolyte gating [Xia09a, Fang07, Fernández-Rossier07]. However, for exfoliated Gr on SiO_2/Si substrate with 300 nm thick oxide, the electrostatic gate contribution is much larger than the quantum contribution to the gate capacitance which is thus complectly negligible [Das Sarma11, Fernández-Rossier07].

3.1.1 Characteristics of GFETs

From Fig.3.1 an optimistic ratio between the maximum and minimum field effect conductivity of Gr of about 30 [Novoselov04, Avouris10], which is quite low to guarantee application for logic FETs at room temperature. Such a low on/off ratio is characteristic of materials with no band gap or a band gap smaller than the thermal excitation energy K_bT. Logic circuit application requires an I_{on}/I_{off} ratio larger than 10^4 implying a minimum band gap of 400 meV at room T [Avouris10, Wang12]. Many strategies were developed to introduce a band gap in Gr. 400 meV band gap was successfully obtained resulting to $I_{on}/I_{off} = 10^7$ on nanoribbons quantum confined Gr with 10 nm width fabricated by chemical exfoliation not compatible for nanoelectronic application [Li08] (see section2.4). Quantum confinement of Gr by lithography patterned close electrodes (up 24 nm) unfortunately produced an I_{on}/I_{off} ratio less than 100 [Han07]. Moreover, these quantum confined Gr nanoribbons based FETs exhibit a high off current due to edge roughness and do not guaranties an acceptable minimum static power dissipation [Avouris10, Wang12]. Effort introducing a band gap in bilayer graphene by applying a perpendicular electric field did not succeeded in achieving a value sufficient for reliable application, only 250 meV was obtained under 100 V [Zhang09] (see section2.1.2). Although been detrimental for logic circuit applications, GFETs are suitable for other types of applications. In particular, the good transconductance, the high mobility and the mechanical stability of Gr make GFETs appropriate for radio frequency (rf) analog electronics where the switch-off of the device is not necessary [Avouris10].

3.1.2 Transport mechanism of in mono and few layers graphene

Ballistic transport regime : The perfect regularity of the crystallography structure of Gr consolidated by the strong sp^2 chemical bonds provides the ideal conditions for carriers to propagate with a large mean free path and negligible scattering deflecting their trajectories in pristine Gr. This favors a ballistic type of transport mechanism in Gr particular at low carrier density. In ballistic regime, carriers propagate at constant velocity v_F between two consecutive collisions with a mean free path reaching a micrometer [Mayorov11]. Scattering are negligible when the effective channel length is comparable to the mean free path (quite often the case in GFETs) and the conductivity increases linearly with n (Fig.3.1) (a part from the close vicinity of the Dirac point). Already in their pioneering contribution, Novoselov et al. reported carriers mean free path of $0.4\mu m$ for Gr on SiO_2 [Novoselov04]. Later, the encapsulation of Gr in hexagonal hBN permitted to achieve a mean free path superior to $3\mu m$ at low temperature [Mayorov11]. One characteristic of Gr is its non zero minimum conductivity at Dirac point (Fig.3.1) [Novoselov04, Novoselov05]. This follows theoretical predictions that in the ballistic regime, although the carrier density vanishes at the vicinity of the Dirac point, the conductivity of Gr converges to ballistic conductance minimum limit of $G_{min} = 4\frac{e^2}{\pi h}$ (4 stands for valley and spin degeneracy) [Castro Neto09b, Das Sarma11]. However, experiments are never carried out at the theoretical limit of absolute T. In addition, as already mentioned it always remains some extrinsic impurities density making the minimum conductivity often

much larger than the minimum predicted value [Tan07, Das Sarma11].

Diffusive transport regime : When the scattering of carriers becomes important, the transport process in Gr changes from ballistic to diffusive mechanism. This happens when the effective channel length exceeds the mean free path or when the density of impurities becomes important[Das Sarma11]. Theoretical development based of the general Boltzmann transport theory in semiclassical regime demonstrated the conductivity of Gr in presence of scattering to be given by [Castro Neto09b, Das Sarma11].

$$\sigma = \frac{e^2 v_F^2}{2} \rho(E_F) \tau(E_F) \tag{3.4}$$

Where τ is the transport scattering time of carriers.
They are three different sources of scattering in Gr [Castro Neto09b, Das Sarma11]. The long range scattering which consists of randomly distributed Coulomb impurities such as local gate potential fluctuation of the substrate and intentional or unintentional charged impurities doping. The short range scattering comprised of neutral point defects or C atom vacancies, phonon scattering due to lattice vibration and finally e-e interaction at very high doping regime. Phonon scattering was counter intuitively demonstrated not to affect much the transport in Gr (Fig.3.1.(c)). The transport mechanism in Gr in diffusive regime is essentially explained by long and short range scattering. At low density of carriers and in presence of charged impurities scattering, the transport scattering time τ is proportional to the square root of carrier density ($\tau \propto \sqrt{n}$) and Eq.3.4 yields the usually observed linear dependency with $\sigma \propto n$ (Fig.3.1.(a,c))[1]. As n increases, charged impurities scattering sources are progressively screened by the 2DEGs. Thus, short range scattering become dominating (at high Vg) limiting the mobility of Gr. Consequently, its conductivity undergoes a sublinear behavior (Fig.3.4.(b)) [Chen, Das Sarma11]. The total conductivity (or resistivity) can be written as a sum of two contributing terms : $\sigma = \sigma_L + \sigma_S$ where the long range scattering term σ_L is proportional to n and the short range term σ_S independent of n [Morozov08, Chen]. Therefore, after extracting σ_S contribution, one recovers the linear behavior of σ_L with n.
In bilayer Gr, although the dispersion relation is not anymore linear. However, the global behavior of the conductivity is not much different from the monolayer case [Das Sarma11, Morozov08]. Indeed, the Fermi energy of few layer Gr remains tunable by doping and can be as well continuously displaced from the conduction to the valence band as in the monolayer. It results a qualitatively comparable n dependency of the conductivity (Fig.3.4.(c)).

Temperature dependent transport : The effect of temperature on the Gr's conductivity (or the mobility) have been intensively studied [Tan07, Morozov08]. The transport behavior of a monolayer Gr with temperature exhibits a typical metallic behavior (Fig.3.2.(a)). However, contrary to metal for which the conductivity is essentially limited by the increase of phonon

[1] In this context, one may conclude that charged impurities scattering are not detrimental for the mobility of carriers at low doping regime which favors the ballistic mechanism. The threshold carrier density for a transition to diffusive regime is often not clear.

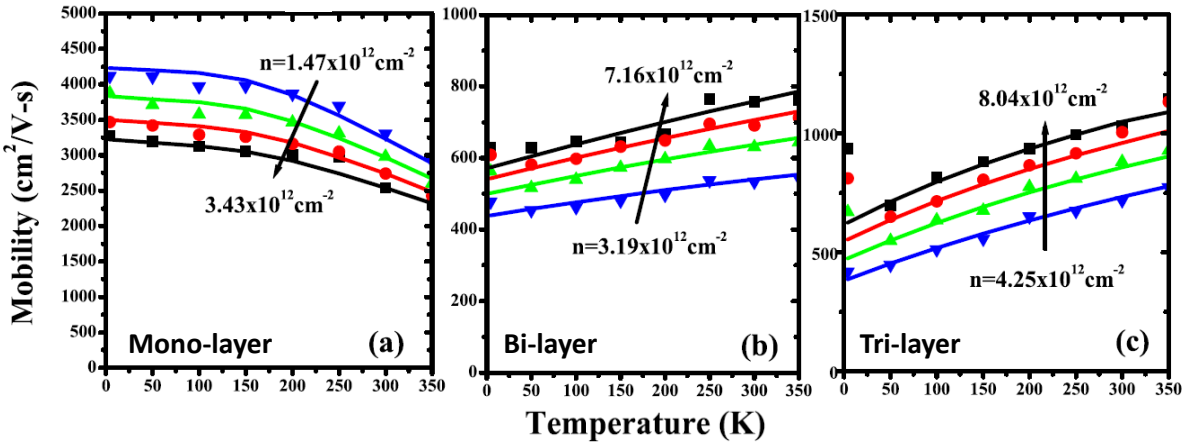

Figure 3.2 *– Temperature dependence of the mobility of single layer graphene (a), bilayer graphene (b) and tri-layer graphene (c). Adapted from [Castro Neto09b].*

scattering rate with increasing temperature, intrinsic phonon scattering have limited effect on Gr conductivity even at room T [Morozov08, Das Sarma11]. To explain the conductivity (mobility) decrease with increasing T, the main reason invoked is the substrate surface polar phonon scattering [Zhu09, Chen, Das Sarma11]. In contrast to monolayer, the mobility of bi(tri)layer Gr increases with temperature just as in semiconductor but for a totaly different reason. Indeed, in bilayer and thicker Gr, the electric field of substrate surface polar phonon is effectively screened and the mobility is dominated instead by Coulomb and neutral points impurities scattering. The former dominates with positive effect at low carrier density and the latter becomes prominent at high n with negative effect resulting to the increase of the mobility with T (Fig.3.2.(b,c)) [Zhu09].

3.2 Semiconducting TMDs based Field Effect Transistor

The Fermi level of SC-TMDs as for any other semiconductor is situated in the forbidden band. Thus, the Metal/SC-TMDs contact induces a potential barrier known as contact Schottky barrier that charge carriers have to overcome to be injected from metal to TMDs and vice versa. The transport characteristics in Schottky interface based devices are completely determined by the interface injection mechanisms. Their description requires the understanding of the structure of the Schottky interface barrier.

They are three ingredients determining the electric contact formation at the interface of two materials [H. Mathieu09]. (i). The vacuum level is the same for all materials and serves as reference level (Fig.3.3.(a)). (ii). At the interface, electrons diffuse to the material with higher extraction energy (work function) ϕ and the conduction band bends consequently (Fig.3.3.(b)). (iii). At equilibrium, the Fermi levels are aligned through out the heterojunction. Assuming $\phi_{sc} \succ \phi_m$ the interface energy profile formation is given on Fig.3.3. In Fig.3.3.a, metal and the semiconductor are isolated. When they get in contact, electrons diffuse from metal to semiconductor and compensate the acceptors. It results in the semiconductor close to the interface an accumulation region of negatively charge carriers and an equivalent positively

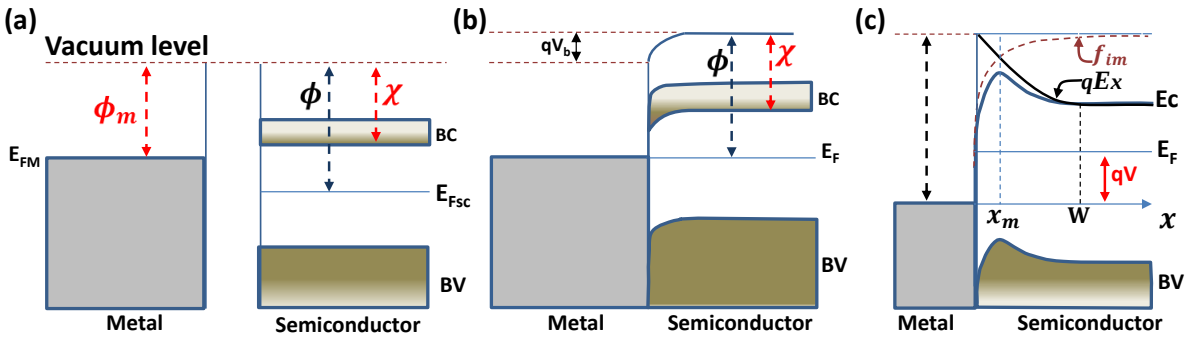

Figure 3.3 *– Metal/Semiconductor interface energy profile formation. (a) The two materials are isolated. (b) They are in contact, electron diffuse into the semiconductor until the equilibrium with the alignment of the Fermi energy of both materials. Near the interface where more electrons are accumulated in semiconductor, the conduction band of the semiconductor bends downward. The distance from the Fermi energy to the conduction band reduces close to the interface. It results at equilibrium an interface Schottky barrier given by $q\phi_b = e\phi_m - e\chi$. (c) Interface energy-band diagram incorporating the interface Schottky barrier lowering due to image charge effect.*

charged region of depleted electron in the metal close to the interface. Since the metallic DOS in the order of 10^{22} cm^{-3} is much larger than the acceptor density within the semiconductors (between 10^{16} and 10^{18} **for bulk semiconductor**), the extra charge essentially accumulate at the metal interface while in the semiconductor, it is spread over the bulk on distance W perpendicular to the interface plane known as the space charged region (SCR). It results an interface potential difference V_b which progressively increases and equilibrated the diffusion forces at the equilibrium when the Fermi levels of both the metal and semiconductor get aligned. Admitting that all the N_a acceptors are compensated, the total charge induced in the SCR is $\rho(x) = -eN_a$ $(0 < x < W)$. Over the SCR (W < x), $\rho(x) = 0$. Integrating the poisson equation under these limit conditions enables deducting both the potential profile (Eq.3.5.(a)) in the SCR and the width W of the SCR (Eq.3.5.(b)).

$$V(x) = \frac{eNa}{\varepsilon_{sc}}(Wx - \frac{x^2}{2}) \quad (a); \qquad W = \sqrt{\frac{2\epsilon_{sc}}{eNa}V_b} \quad (b) \tag{3.5}$$

Here, Eq.3.5.(b) is obtained from Eq.3.5.(a) by expressing the interface voltage as potential deference $V_b = V(x = 0) - V(x = W)$. When a forward bias is applied to the system, the SCR's width becomes $W = \sqrt{\frac{2\epsilon_{sc}}{eNa}V - V_b}$. This interface configuration is more often encounter at metal/2D SC-TMDs interfaces [Allain15]. These formula are adapted from the more pedagogical case where the interface voltages V_b results from the depletion of charge within the semiconductor leading to a space charge region of uncompensated donors well described in text books [Sze81, H. Mathieu09].

3.2.1 Schottky effect at metal/semiconductor interface

The equilibrium interface energy barrier resulting from interface charge diffusion and the subsequent semiconductor band bending described above is given for an n-type semiconductor by $q\phi_b = e\phi_m - e\chi$ (Fig.3.3.(b)). ϕ_m and χ are respectively the metal work function and

the electron affinity of the semiconductor. Under applied voltages (dc and gate), the energy bands of the semiconductor are affected and the energy barrier deviates from this value which becomes valid only at flat band. An accurate estimation of the interface barrier requires taking into account the potential barrier lowering due to a combined effect of both image force an the applied electric field known as the Schottky effect [Sze81]. Indeed, for an electron placed at a distance x from the metal (i.e. within the semiconductor), a positive image charge is induced within the metal and exerts and additional attractive force to the electron. Two forces act thus on the electrons : The image force ($f_{im} = -q^2/4\pi\epsilon_{sc}(2x)^2$) and the electric force ($f_e = qEx$) due to the applied field $\vec{E}$. The resulting total electric potential of the electron is the integral of the potential of the two forces and evolves with the distance x from the interface (Fig.3.3.(c)). Its maximum is reached at a finite distance x_m from the interface with an effective barrier-lowering of $\Delta\phi = (q\left|\vec{E}\right|/4\pi\varepsilon_{sc})^{1/2}$.

The electric field dependence of both the band bending width W and potential barrier high $\phi_b - \Delta\phi$ demonstrates the possibility of modulating the band configuration in a FETs thanks to the DC bias. This has to be combined with the effect of the gate electric field which induces electric doping of the semiconductor contributing to further band modulation. In general, the effective energy barrier that carriers have to overcome to access the channel is given by $E_a = q\phi_b - (E_c^\infty - E_c^0)$ [Allain15]. Where $E_c^\infty - E_c^0$ is the difference between the conduction band minimum far from (E_c^∞) and at the interface (E_c^0). At flat band, this term is nil and the interface activation energy E_a gets reduce to the effective Schottky barrier height[2]. Two distinct mechanisms, namely the thermionic emission and the field assisted quantum tunneling govern the transport of charges across metal/semiconductor interface and can be unveiled by the band modulation thanks to the mutual effects of dc bias and gate voltage. This will be at the core message of chap.7 presenting our experimental results on the transport properties in bilayer $MoSe_2$ FET. The thermionic emission is likely expected at higher temperature due to thermal excitation of charges across the interface barrier while the field assisted charge tunneling or the direct tunneling (DT) most likely occurs at lower temperature (or higher voltages range regardless to the temperature).

Thermionic emission at metal/Bulk semiconductor interface : the 3D model In appendix.B we provide the detail theoretical derivation of the thermionic emission mechanism following the approach of developed in [H. Mathieu09, Sze81]. For bulk semiconductors, in the quite often functioning condition of $qV \gg k_BT$, the term $\exp(\frac{qV}{kT})$ is much large compare to 1 and the current-voltage characteristic is given by Eq.3.6.

$$Isd = AA^*T^2 \exp(\frac{E_a}{k_BT})\exp(\frac{qV}{kT}) \tag{3.6}$$

where A is the contact area and A^* the effective Richardson constant for 3D bulk materials. Often, FET consists of two Schottky diodes connected back to back in series at the

[2]The interface activation energy E_a has not to be confused with the activation energy of the hopping transport process intrinsic to the semiconductor

source and drain and the Eq.3.6 refers to source-drain voltage. This equation is commonly used to study the electric characteristic of 3D bulk semiconductor based CMOS FETs and diodes in thermionic regime [Sze81]. The properties of SC-TMDs presented in the chap.2 highlighted that quantum confinement prominent in few layer thin sheets is substantially altered in thicker sheet and their properties get closer to that of a bulk. The Eq.3.6 is thus adapted to study the electric characteristics of multilayers and thicker TMDs based FET [Allain12, Song17].

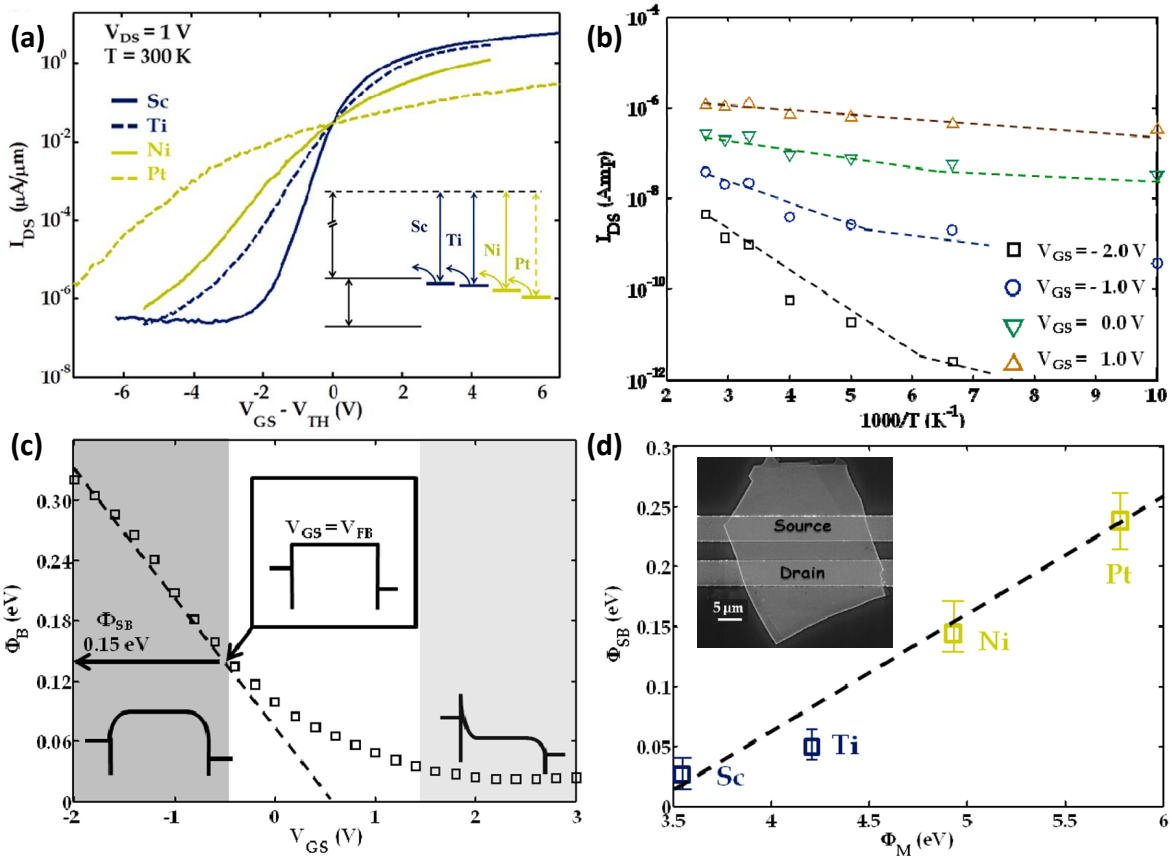

Figure 3.4 *– Characteristics of bulk MoS_2 based FET. (a) The transfer curves for different metal contacts in log scale. (b) Analysis of the interface activation energy. (c). Interface activation energy dependence with the gate voltage. The deviation from the linearity happens at flat band. (d) Schottky barrier high for different metals. Adapted from [Das13b].*

Das et al. investigated the injection mechanisms in multilayer MoS_2 FET with different metal contacts (Pt, Ni, Ti, Sc) [Das13b] which unanimously demonstrated an n-type unipolar behavior (Fig.3.4). They argued that the representation of their data in terms of $log(Isd)$ v.s. $\frac{1000}{T}$ for different gate voltages exhibits a linear behavior (Fig.3.4.(b)) and analyzed the slope based on Eq.3.6. The Fig.3.4(c) presents the resulting Vg dependence of the activation energy E_a for the Ni contact. For sufficiently negative Vg (low n doping) where thermionic emission most likely dominates the source-drain current, E_a (denoted as Φ_{SB} in Fig.3.4.(c)) depends linearly on Vg. However, when direct tunneling becomes relevant, the E_a deviates from linearity starting at the flat band where the activation energy is equal to the Schottky barrier denoted as Φ_{SB} in Fig.3.4.(d). The Fig.3.4.(d) resumes the SBH for different metal

contacts demonstrating that Ti and Sc are the best metal electrode for MoS_2 FET.

Although this approach proposed by Das et al. [Das13b] provided important insight into the understanding of the injection mechanism across Metal/MoS_2 interface and inspired most of the subsequent works, important criticisms emerge regarding the extraction method for E_a (Φ_{SB} in their case). From Eq.3.6, $log(I_{sd})$ is strictly speaking not expected to be a linear function of $\frac{1000}{T}$. In addition at $V_{sd} = 1V$ where the analysis has been carried out, the band diagram configuration is expected to be highly affected given that the voltage drop takes place preferentially at the interface and the SB considerably altered. The consequence of these cumulative incontinencies could explain the relatively low value of Φ_B inferior to 50 meV. More accurate approach for Schottky barrier analysis in multilayer was proposed by Dankert et al. [Dankert14] (Fig.3.5.(a)). They studied two different device geometries. One with Co electrode directly contacting the ML MoS_2 flake and the other integrating a TiO_2 tunnel barrier between the Co electrode and the ML flake. Instead of $ln(Isd)$ v.s. $\frac{1000}{T}$, they plotted the data in terms of $ln(\frac{I_{sd}}{T^2})$ v.s. $\frac{1000}{T}$ which is clearly linear with a slope given by $S \propto \frac{E_a}{k_B} + \frac{qVsd}{k_B}$ (Fig.3.5.(a)). Thus, for a given Vg, plotting the slopes extracted from the Arrhenius plot provides the activation energy when extrapolating the curves to the zero Vsd value. Reporting all the values obtained for different Vg values onto a single plot (E_a v.s. Vg) enables extracting the SBH ϕ_B at the flat band. They obtained $\phi_B = 121meV$ for Co/MoS_2 interface while for Co/TiO_2/MoS_2 interface it was reduced to $\phi_B = 27meV$.

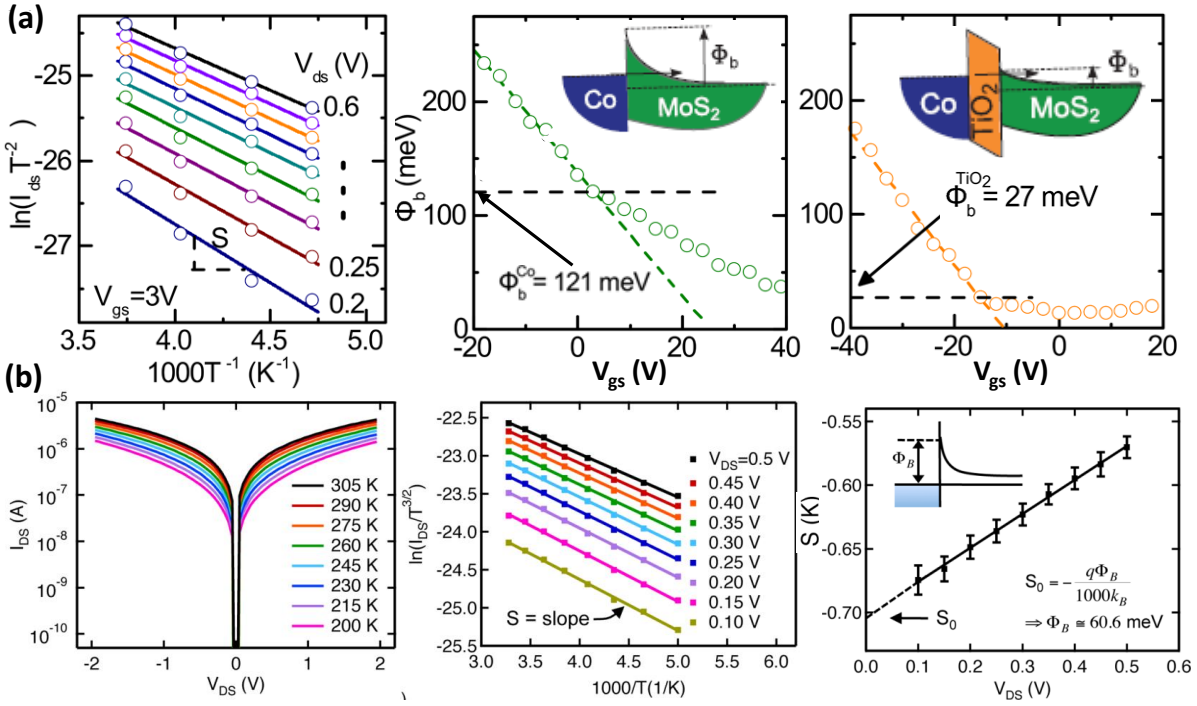

Figure 3.5 *– Schottky barrier characterization of multilayer and monolayer MoS_2 FET. (a) From left to right : the Arrhenius representation of experimental data, the activation energy dependency with Vg. The inset shows the energy band profiles. Adapted from [Dankert14]. (b) From left to right : the I-V characteristics, the Arrhenius representation in 2D model and the linear dependence of the slope. Adapted from [Chen13].*

Thermionic emission at metal/confined SCs-TMDs : the 2D model In few layer thin SC-TMDs, quantum confinement freezes the motion of carriers in the Z direction and the channel is reduced to a 2D electron gas. The derivation of the thermionic current has to be reconsidered taking into account the specificity of 2DEG. In appendix.B we provide the details of the calculation. Thus, in the condition of $qV \gg k_BT$, $\exp(\frac{qV}{kT}) \gg 1$ and the thermionic current across a Schottky metal/2D semiconductor contact interface becomes :

$$Isd = AA^*_{2D}T^{3/2}\exp[-(\frac{E_a - qV}{k_BT})] \tag{3.7}$$

A^*_{2D} the effective 2D Richardson constant.
The Arrhenius representation of Eq.3.7 $ln(\frac{I_{sd}}{T^{3/2}})$ *v.s.* $\frac{1000}{T}$ is expected to exhibit a linear dependence. The method adopted by Dankert et al. presented above was inspired by Chen et al. [Chen13]. Indeed, following the proposal of Das et al [Das13b] on multilayer MoS_2 with the mentioned inconveniences Chen *et al.* proposed an improved methodology for SB extraction for monolayer MoS_2 FET [Chen13]. Based on Eq.3.7, they used $ln(\frac{I_{sd}}{T^{3/2}})$ *v.s.* $\frac{1000}{T}$ instead of $ln(I_{sd})$ v.s. $\frac{1000}{T}$ (Fig.3.5.(b)). However, they directly attributed the intercept of slope curves (S v.s. Vsd) to the SBH which is also an inconvenience. From the above discussion it likely represents a particular value of E_a for the given Vg value at which it is extracted. It is not certain that this Vg value corresponds to the flat band. Despite this inconvenience (later corrected by Dankert et al [Dankert14] Fig.3.5.(a)), they also successfully demonstrated that an integration of MgO tunnel barrier considerably alter the interface SBH up to 80% [Chen13]. This interest of using ferromagnetic electrodes with spin tunneling barrier is not fortuitus. It demonstrates the effort of realizing spin valve device with SC-TMDs with ultimate goal of combining both logic gate switch and spin memory in a single devices targeting the hope of Spin-FET.

3.2.2 Direct tunneling regime

In addition to the thermionic emission, different quantum tunneling regimes are likely to take place trough the metal/semiconductor interface energy barrier as is being modulated by the applied voltages and may becomes the dominant mechanism contributing to the current in some excitation range. It is the case either at high Vsd and Vg or at low temperature when thermal energy becomes negligible. In such regimes, the interface energy barrier height becomes irrelevant contrary to its shape. Particularly its width becomes the key parameter determining the transmission of carriers [Sze81, Simmons63]. The theories describing the tunneling processes across a potential barrier primarily adapted to Metal/insulating/Metal (MIM) or Metal/insulating(or oxide)/semiconductor (MIS or MOS devices) [Sze81, Simmons63] (Fig.3.6) are thus adapted to describe the transport of SC-TMD based FETs in direct tunneling regime. The insulating barrier in this case is represented by the interface barrier width W resulting from band bending ($E_c^{\infty} - E_c^0$). Since it can be strongly modulated by both Vsd and Vg (Eq3.5), it is expected different direct tunneling regime depending on the voltages range. At moderated voltages ($eVsd < E_a$) and Vg inferior to the

flat band voltage $Vg < V_{FB}$ and given the requirement with the T is fulfilled, the current exhibits a simple linear dependency with Vsd, $Isd \propto V_{sd} exp[-kd\sqrt{E_a}]$, with $k = 4\pi\sqrt{2m^*}/h$ and d the barrier width. This transport regime often leads to misinterpretation of experimental data attributing such the linearity to Ohmic contact instead of direct tunneling [Das13b]. At higher voltages $eVsd > E_a$, the tunnel barrier adopts a triangular shape reducing considerably the width of the tunnel barrier, the tunneling becomes highly field assisted and the current adopts the Fowler-Nordheim form given by Eq.7.3 [Sze81, Simmons63].

$$Isd \propto V_{sd}^2 exp(-k^{'} dE_a\sqrt{E_a}/V_{sd}) \quad ; \quad k^{'} = 8\pi\sqrt{2m^*}/3qh \tag{3.8}$$

Representing Eq.3.8 as $ln(\frac{Isd}{Vsd^2})$ v.s. $\frac{1}{Vsd}$ gives a straight line, which is the experimental signature of Fowler-Nordheim (FN) tunneling (Fig.3.6.(a)). This mechanism is quite common in MIM, MIS and MOS devices [Sze81, Simmons63, Ranuárez06] but so far not yet demonstrated in SC-TMDs FET. Direct tunneling and FN tunneling have also been reported MIM devices with single or few molecules trapped into a few nanometers gap obtained by electromigration fractionation of a continues Au nanowire (Fig.3.6) [Beebe06, Song09].

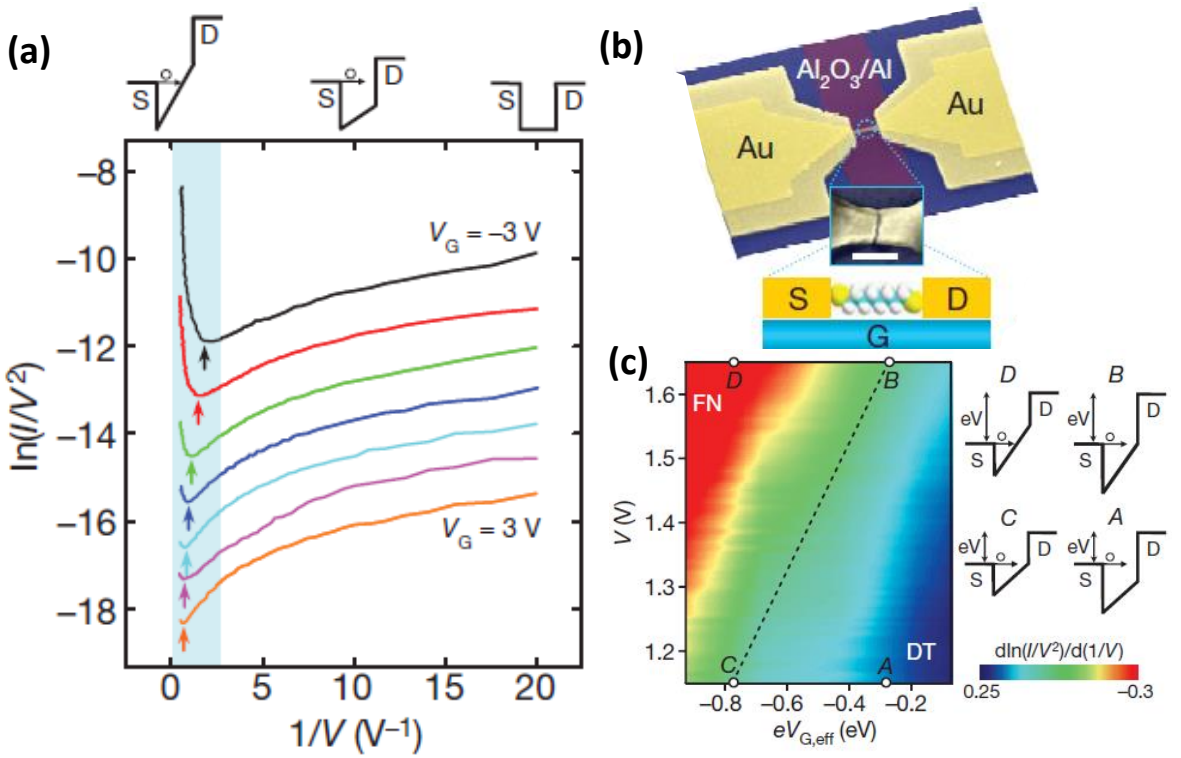

Figure 3.6 *– Tunneling processes in Metal-molecules-Metal (MIM) devices. (a) I-Vsd characteristics plotted in FN forms ($ln(\frac{Isd}{Vsd^2})$ v.s. $\frac{1}{Vsd}$). The top drawing present the energy band configuration across the devices in transport regime. (b) The geometry of the MIM device fabricated by electromigration break junction technics. (c) The color plot representation of the data in the form appropriated to highlight the FN and DT regimes. The the right drawing are the energy band configurations across the devices at the corresponding points of the map (A, B, C and C). Adapted from [Beebe06, Song09].*

3.3 Mobility of SC-TMDs in FETs

3.3.1 The field effect mobility

The field effect mobility is extracted from the 2 terminals transfer curve (Isd v.s. Vg) using the formula $\mu_{FE} = (\frac{dIsd}{dV_g})\frac{L}{C_g V_{sd} l}$. Therefore it is expected to be strongly affect by the interface contact resistances. Indeed, the interface SB represents the main detrimental source to μ_{FE} limiting it in the range of $10^{-1} - 10^{2} cm^2 V^{-1} s^{-1}$ [Radisavljevic11]. Many studies demonstrated that the reduction of the SBH is always accompanied by the subsequent increase of μ_{FE}. As illustration, when Dankert et al integrated a TiO_2 tunnel barrier at Co/MoS_2 interface reducing the SBH by a factor of 5. They observed that μ_{FE} increased by almost the same factor passing form 12 $cm^2 V^{-1} s^{-1}$ for Co/MoS_2 interface to 76 $cm^2 V^{-1} s^{-1}$ for Co/TiO_2/MoS_2.

3.3.2 Intrinsic mobility of SC-TMDs : High T phonon scattering

To access the intrinsic mobility of TMDs sheets and capture the transport mechanism intrinsic to SC-TMDs, non local measurements are required to avoid the effects of contacts resistances. Schmidt et al. [Schmidt15] summarized in a single plot the mobility values of SC-TMDs reported in the literature before 2015. They sorted the data by thicknesses, supporting substrates and measurement temperatures. They noticed that similar to field effect mobility, the mobility of SC-TMDs are spread over 3 order of magnitudes even for measurements conducted in similar conditions. They attributed it to subtle differences in experimental conditions (differences in the material quality, device fabrication and configurations and measurement conditions). All of which are known to influence the device performances. In any case, universal tendencies were clearly reported. The Low temperature intrinsic mobilities of SC-TMDs were noticed to be significantly larger compare to room temperature values contrarily to the field effect mobility which follows opposite trend due to the increase of contact resistance with decreasing temperature. The increase of the intrinsic mobility of SC-TMDs with decreasing temperature is an indication that phonon scattering is the dominant factor limiting the carrier mobility at rom T. Indeed, Kaasbjerg *et al.* demonstrated using first principle calculations that, the mobility of MoS_2 is predominantly limited in high temperature range (> 100 K) by phonon scattering with maximum achievable room temperature value of $417 cm^2 V^{-1} s^{-1}$ [Kaasbjerg12]. They also demonstrated that as the temperature decreases in the range of 300 K to 100 K, the mobility increases following a power law $T^{-\gamma}$, γ being the phonon damping factor (Fig.3.7). All the experimentally reported temperature dependent mobilities of different SC-TMDs verified this tendency (with different phonon damping factor γ) (Fig.3.7). This provides a clear confirmation that phonon scattering are the main limiting factor of the mobility of carriers at high T [Radisavljevic11, Das13b, Chamlagain14, Schmidt15, Yu16, Song17]. In lower temperature regime, a model developed by the same authors suggested a T^{-4} trend of the mobility and predicted a mobility exceeding 10^5 below 10 K considering phonon scattering as the only limiting factor [Kaasbjerg13]. However, experimental data do not sup-

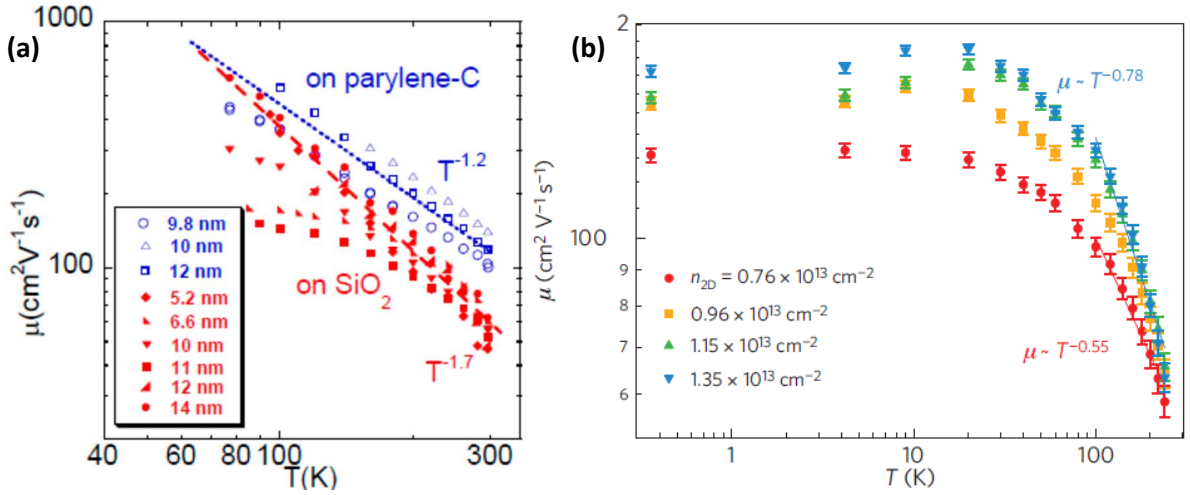

Figure 3.7 *– Temperature dependence of the mobility of SC-TMDs fitted with $T^{-\gamma}$ law. (a) Multilayer $MoSe_2$ on SiO_2 (solid symbols) and on parylene-C (hollow symbols). Adapted from [Chamlagain14]. (b) Monolayer MoS_2 on SiO_2. Adapted from [Radisavljevic11].*

port this prediction. Instead they unanimously demonstrate that in the low temperature regime the mobility keeps increasing with decreasing T and saturate at values below 10^3 $cm^2V^{-1}s^{-1}$ [Radisavljevic11, Das13b, Chamlagain14, Schmidt15, Yu16]. This demonstrates that phonon scattering are not the limiting factor of the mobility of SC-TMDs in the low temperature regime. In this temperature ranges, short and long range scattering are expected to play a dominant role.

3.3.3 Low temperature Mobility : Short and long range scattering

The review from Schmidt et al. highlighted not an important difference between the mobilities of the mechanically exfoliated or CVD grown SC-TMDs. This suggests that grain boundaries presumably important in CVD samples play only a minor role compare to sulfur vacancies point defects present in both exfoliated and CVD grown SC-TMDs nanocrystals[Chamlagain14, Schmidt15]. In addition, the mobility of SC-TMDs has been demonstrated to decrease with decreasing number of layers limited by the random distributed charged impurities due to local gate potential fluctuation of the SiO_2 substrate influencing more strongly the thinner layers [Li13, Chamlagain14]. Further more, the devices fabricated on SiO_2 substrate with pre-coated PMMA known to exhibit less charged impurities or Palylene-C known to screen the field of the charge impurity of the SiO_2 substrate demonstrated improved carrier mobilities compare to those fabricated straight on SiO_2 (Fig.3.7.(a)) [Chamlagain14, Schmidt15]. Furthermore, encapsulating the devices channel with PMMA or h-BN was argued to modified its dielectric environment reducing the effect of the substrate charged impurities resulting to an improved mobility [Song17, Schmidt15]. These arguments indubitably point out the charged impurities as the main carriers scattering source in SC-TMDs at low temperature.

3.4 Transport mechanism in SC-TMDs : The hopping processes

In disordered systems consisting of randomly distributed localized charge impurities such as SC-TMDs as has emphasized the previous discussion, the conduction is essentially driven by hopping [Shklovskii84]. In such systems, each localized charged impurity induces a set of discrete states within the gap of the semiconductor. More than one electrons can occupied the discrete localized states of a single impurity and the Coulomb interaction between these on-site electrons is non negligible given their proximity. A simple description of such systems is based on the Mott model [Shklovskii84]. It assumes an ideal system consisting of an ensemble of impurities with the same Coulomb interaction potential $U(\vec{r_j})$ regularly distributed on impurities sublattice embedded in the main lattice of the matrix material. We assume the impurities sublattice parameter to be b_0. When considering the entire impurity lattice, the individual discrete energy levels merge into impurities bands (Fig.3.8.(a)). Assuming 2 electrons per site and U_0 the average on-site electron-electron interaction energy, the properties of the system evolve with the distance b_0 between neighboring impurities. When b_0 is very large, the individual discrete states are very localized. It results two distinct narrow bands separated by a forbidden gap of width U_0 (Fig.3.8.(a)). The material is in an insolating state. However, when b_0 decreases, the impurities bands start spreading, reducing thus the gap. It exists a critical value of b_0 below which the band overlap and the material undergoes a transition toward metallic state (Fig.3.8.(a)). It is the Mott transition [Shklovskii84]. The model can be complexified to make it closer to the reality by assuming a random distribution of impurities potential. For simplicity, the random distribution of impurities potential energy ε_j are assumed to remain within an interval $\pm\frac{E}{2}$ around an average value. In this condition, the properties of the system depend on the parameter $\pm\frac{E}{I}$ with I representing the overlap integral of impurities states. For large values of $\pm\frac{E}{I}$, the impurities states are very localized, the system is in an insolating state. When $\pm\frac{E}{I}$ decreases, the states are delocalized within the insolating gap. It exists a critical value at which the delocalization recovers the entire forbidden gap (Fig.3.8.(a)) resulting to the Anderson type of transition of the system toward metallic state[3].

In semiconductors, the conduction mechanism strongly depends on the carrier density i.e. the position of the Fermi energy. From the insulating state with E_F located within the gap, modulating the carriers density enables realizing partial inversion layer with the Fermi level surrounded by randomly distributed localized states due to the "oscillatory" structure of the conduction band edges (Fig.3.8.(d), right panel)[4]. This makes SC-TMDs FET and more historically CMOS devices such as MOSFET suitable systems to study Mott-Anderson metal-to-insulator transition. From its position close to the conduction band edges where E_F is surrounded by random localized states, a continuous doping progressively moves higher the E_F

[3] None of these model is valid for 1D systems where any even though small energy fluctuation turns the 1D conductor into insulator

[4] This means that the localized states are not exclusively from extrinsic origin and may result from the intrinsic band configuration of the material Fig.3.8.(d).

and the surrounding states become more and more delocalized [Schmidt15] (Fig.3.8.(d),right panel). Further doping takes E_F deep in the conduction band leading to insulator to metal transition [Shklovskii84, Schmidt15].

Numerous of contributions have investigated both temperature and carrier density dependency of conductivity (or resistivity) of SC-TMDs [Schmidt15] (Fig.3.8.(b-f)). At low density, the Fermi energy lies within the gap and SC-TMDs are in insulating state with no carriers contributing to the transport(Fig.3.8.(b)) [Schmidt15]. For n-type SC-TMDs, positive Vg brings their Fermi energy to the conduction band edges (Fig.3.8.(d)) where it is effectively surrounded by random distributed states. Depending on the delocalization extent of such states, low temperature transport can be understood in the framework of percolation theory. In this theory, the sublattice of the random states is modeled as a network of random resistances. When the states are strongly localized (i.e. E_F in the gap) the conductance is given by $\sigma \propto \exp(\xi(r))$, $\xi(r) = \varepsilon/kT$. ε the distance from the E_F to the minimum of the conduction band [Shklovskii84]. In this strongly localized regime, with $\varepsilon \gg kT$, $\xi(r)$ below a critical value ξ_c, the resistance of the system goes to infinity ($\sigma \to 0$) (Fig.3.8.(c)). In contrast, above ξ_c a percolating hoping channel is established in the resistance network (Fig.3.8.(b)). As ξ progressively increases more percolating parallel channels emerge in the material and the conductance obeys to the power law [Shklovskii84, Chen15b] (Fig.3.8.(b)).

$$\sigma(\xi) \propto (\xi - \xi_c)^b \quad , \quad b > 0 \tag{3.9}$$

This behavior usually observed in MOSFET devices with $\xi = n$ [Das Sarma11] has been observed in MoS_2 as well (Fig.3.8.(c)) [Chen15b].

For $\xi > \xi_c + 1$ the total resistance of the material becomes limited by the most resistive channels and the conductance takes the expression $\sigma \propto \sigma_0 \exp(\xi_c)$ and does not increase anymore with new percolating channels. In low the temperature regime, the tunneling (hopping) probability between the neighboring states of the randomly distributed impurity states around the Fermi level is much smaller than the tunneling probability between the only few more distant states with energies close to E_F. The transport is thus mediated by hopping with a length determined by the balance between the distance to the more favorable states and the energy levels of the closer states. This is known as variable range hopping (VRH). The conductivity increases with temperature following the general formula expressed in Eq.3.10 [Schmidt15] (Fig.3.8.(c)).

$$\sigma(T) \propto AT^m \exp[-(\frac{T_0}{T})^{1/(d+1)}] \tag{3.10}$$

Where d is the dimension of the system (= 2 for monolayer layers SC-TMDs) and m an empirical parameter often equals to 0.8. At high temperature regime, the hopping probability between the state becomes similar and the conduction is driven by thermally activated nearest neighbor hoping [Schmidt15]. The T dependency of the conductivity becomes:

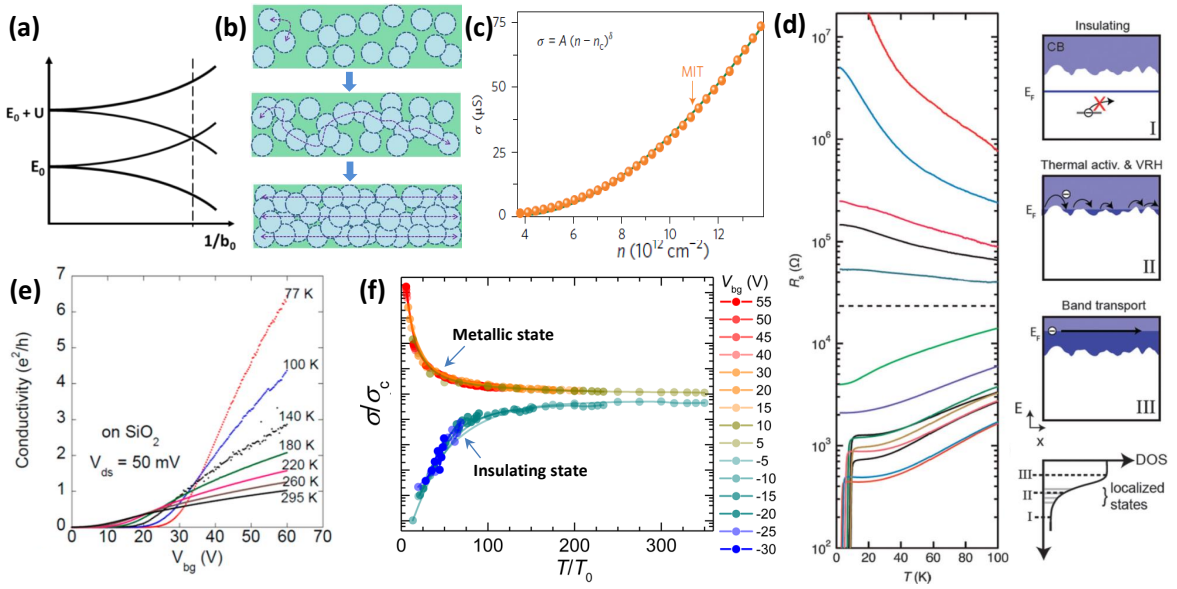

Figure 3.8 *– Transport mechanism in semiconductors: the case of SC-TMDs . (a) Energy band of impurities. (b) Schematic of doping induced percolating conductive channels resulting to MIT as the electron density increase (from top to bottom). The circles denote isolated carrier puddles. (c) Conductivity dependency with the carrier density. The arrow highlights the critical point for MIT. (b-c) Adapted from [Chamlagain14]. (d) The right schematic represents the energy band modulation in MoS_2 by doping and the corresponding transport mechanism. At the left, the corresponding T dependency of the resistivity for progressive doping (from top to bottom). One observes a transition from the insulating state (decrease of the resistivity) at low doping regime to a metallic state (increase of the resistivity) at intermediate doping regime to a superconductive state (the resistivity vanishes at low T) at high doping regime. Adapted from [Schmidt15]. (e) Conductivity dependence of $MoSe_2$ with both doping and T. The transition takes at the vicinity of quantum conductance. Adapted from [Chamlagain14]. (f) Scaling analysis of the renormalized conductivity of ReS_2 demonstrating metallic and insulating branches. Adapted from [Pradhan15].*

$\sigma(T) \propto \sigma_0(T)\exp[-(\frac{E_a}{k_B T})]$. From this hopping regime, further doping moved the Fermi energy deep in the conduction band and SC-TMDs undergo a transition to a metallic regime characterized by the decrease of conductivity with increasing T [Schmidt15, Yang17] (Fig.3.8.(c)). By assuming the localized states originating essentially from the minimum conduction band edge close to which E_F is dragged by doping, we implicitly assume the material depleted from extrinsic source of doping. Note that, abundant presence of such doping may introduce within the gap sufficiently random distributed states close to E_F to induced transport by VRH without the need to drag E_F at the vicinity of minimum conduction band edge. However, such types of defects are negligible in SC-TMDs.

3.4.1 Metal to insulator transition in SC-TMDs

Several contributions have reported on the MIT in monolayer and few layer SC-TMDs [Radisavljevic13, Pradhan15, Chamlagain14, Schmidt15, Yang17] (Fig.3.8.(b-d)). The transition takes place when the conductivity get closer to the minimum theoretically predicted metallic conductivity (the quantum conductivity (e^2/h)) (Fig.3.8.(d)). This violates the scaling theory of localization which, based on non-interacting electronic systems predicted that a minimum metallic conductivity can not be achieved in 2D systems [Radisavljevic13,

Pradhan15]. MIT in SC-TMDs is debating to be of two distinct origins. First, it is argued to result from a percolation type of transition driven both by disordered states and strong electron-electron interaction in SC-TMDs 2DEGs as described above [Radisavljevic13]. In this consideration, the strength of $e-e$ correlation is characterized by the dimensionless Weigner-Seitz radius (r_s) defines as the ratio between the $e-e$ Coulomb interaction energy U_c and their kinetics energy (the Fermi energy E_F).

$$r_s = \frac{U_c}{E_F} = \frac{g_v m^* e^2}{4\pi\epsilon\hbar^2\sqrt{\pi n_{2D}}} \tag{3.11}$$

For $r_s \ll 1$, the confined 2D SC-TMDs is in non interacting regime and experiments support the scaling theory of localization which predicts the system to be in the insulating state [Radisavljevic13, Pradhan15, Chamlagain14, Schmidt15, Yang17]. In strong interacting limit however, ($r_s \gg 1$) the prediction of the scaling theory of localization are not valid anymore. The 2DEGs are in weak disordered regime and the SC-TMDs exhibits a metallic state [Radisavljevic13, Chamlagain14, Schmidt15]. This description contrasts a bit with a second approach that study the MIT in SC-TMDs by means of a scaling analysis of conductivity as function of T and carrier density n_{2D} [Pradhan15] (Fig.3.8.(d)). In this case, the MIT was argued to be a second order[5] quantum type of transition essentially driven by temperature an electronic doping [Pradhan15]. In this case conductivity near by the critical doping density is predicted to exhibit a universal power law dependency with T. Furthermore, the conductivity is expected to follow a power dependence with T on both the insulating and on the metallic sides of the transition with the same exponent even away from the critical doping density [Pradhan15]. Such a behavior has been argued to be reported in 2D ReS_2 semiconductor [Pradhan15]. However, future contributions on MIT in disordered system such as SC-TMDs will likely contribute settle this debate regarding the type of transition.
Despite the important number of contributions on layered materials as review in this chapter and the previous, many efforts are still to be done to ascertain benefiting most of the urge possibilities offers by this materials in both the applicative and fundamental points of view. In the rest of this chapter, I will present the orthodox theory of Coulomb blockade which sustained the electronics transport in SEDs.

3.5 Transport mechanism in Coulomb blockade regime

Let consider an isolated metallic nanoisland with a small enough size ($\sim 10nm$). Its closely packed electron cloud induces a sufficiently important Coulomb repulsion inducing a charging energy E_C that can dominate the thermal energy and prevents sequential charge tunneling into the island. Assuming that such an island is coupled to a source and a drain electrodes through tunnel junctions characterized by the capacitances C_D, C_S and resistances R_S, R_D and to a gate trough a capacitance C_g (Fig.3.9.(a)). At low temperature ($K_BT \ll E_C$), if the energy supplied by the applied bias remains small than the charging energy (eVsd $< E_C$) no

[5] Occurring without the divergence of physical quantities at the critical point.

electron can tunnel onto or out of the nanoisland, no current flows trough the device. It is the so call Coulomb Blockade (CB) regime (Fig.3.9.(c)). This is illustrated by the central gap in the theoretical I-Vsd characteristics of Fig.3.9.(b). In contrast, if the energy supplied is sufficient to overcome the CB barrier, one electron tunnels into or out of the central island leading to one electron current flowing trough the device. The incoming electron adds a new charging energy that prevents another electron to tunnel onto to the dot [Seneor07] (Fig.3.9.(c)). Further instrumentation of the DC bias enables to reached the second threshold and a second electron tunnels into and out of the dot given rise to two electrons current flowing trough the device (Fig.3.9.(c)). As the apply bias increases, a third and more thresholds can be reached leading to three and more electrons current flowing thought the device giving rise to the well known Coulomb staircases on the I-Vsd characteristics (Fig.3.9.(b)). A low dc-bias range in the CB regime, when no electron possesses enough energy to tunnel trough the device, the incrimination of Vg modulates the chemical potential of dot and displaces its discrete Coulomb levels. Each time a Coulomb level enters a dc-bias windows a single electron tunnel trough the device (Fig.3.9.(c)). This results to a gate dependent conductance oscillation (Fig.3.9.(e)). By incrementing both Vsd and Vg one realizes the electric spectroscopy of the current. A two dimensional representation of the current versus Vsd and Vg ($Isd(V_{sd}, V_g)$) presents regular Coulomb diamond patterns with periodicity $\Delta Vg = e/Cg$ and half size $\Delta Vsd = e/C_\Sigma$ where $C_\Sigma = C_D + C_S + Cg$ is the total capacitance experienced by the central island (Fig.3.9.(d)). The

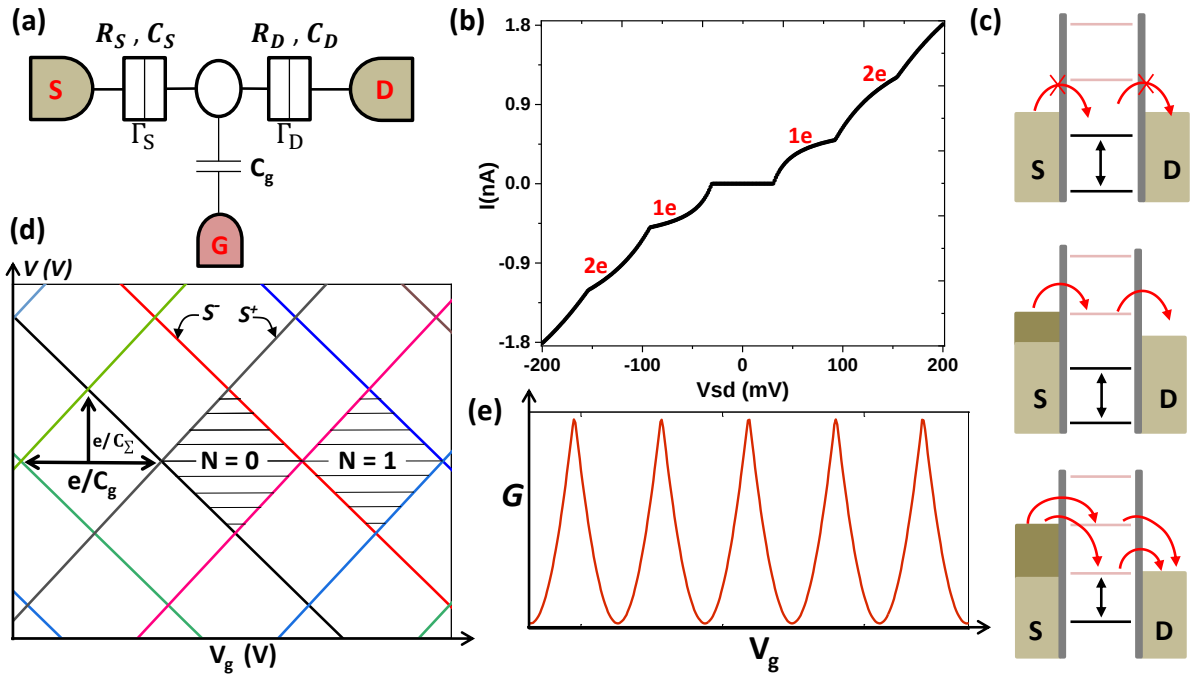

Figure 3.9 *– (a) Schematic of a typical 3 terminals SET. (b) A typical I(Vsd) characteristics of a SET demonstrating one and multi-electrons Coulomb staircases. (c) Band structure of a SET highlighting single electron tunneling mechanism. (d) Diagram of the positions of the thresholds dc-bias* v.s. *Vg defining regularly spaced Coulomb diamonds with a given size and periodicity. (e) Simulated conductance oscillation demonstrating V_g dependent oscillations.*

experimental observation of single electron transport processes required two essential con-

ditions. First, as already mentioned, the charging energy has to be larger than the thermal energy so at to prevent uncontrollable statistical thermal excitation of electron on (out of) the dot. The second essential condition is related to the wave functions of the electrons that have to remaind localized on the dot. Otherwise the number of electrons on the dot will fluctuate even in the Coulomb blockade regime driven by the uncertainty principle ($\Delta E \Delta t \geq \hbar/2$) preventing controllable single electron processes [Seneor07, Nazarov09]. Attributing ΔE to the minimum energy required to add an additional electron onto the dot (the charging energy $E_C = e^2/2C$) and Δt to the characteristic RC time constant for charging (or discharging) a capacitor C, the localization requirement imposes the resistance of the junction to be lager than quantum resistance $Rq = e^2/h \approx 26K\Omega$ [Seneor07, Nazarov09]. The orthodox theory which describes the single electron transport process is based on master equation. The current of the SED is proportional to the different between the two tunneling rate (the probability per unit time) which the calculation requires knowing the free energy of the system.

3.5.1 Energetic of single electron devices

The free energy of the system is defined as the total electrostatic energy subtracted the work done by each voltage source to add(receive) electrons to(from) the island. For the sake of generality, we consider that the central island is connected to M independent electrodes. The i^{th} electrode with a supplied bias V_i is coupled to the island through a junction characterized by a couple of capacitance-resistance (C_i, R_i). Assuming the central island to have a voltage V_0, the total charge induced on the island is given by : $Q = \Sigma_i^M C_i(V_0 - V_i) = -Ne - Q_0$, where Q_0 is the charge remaining on the dot when all the voltages are zero. It is called the environmental charge. Thus, $V_0 = \frac{1}{C_\Sigma}(\Sigma_i C_i V_i - Ne - Q_0)$. Therefore, the total electrostatic energy of the island is given by.

$$U = \frac{1}{2}\sum_i C_i(V_i - V)^2 = \frac{1}{2C_\Sigma}\sum_{i,j>i}^{N} C_i C_j (V_i - V_j)^2 + \frac{(Ne - Q_0)^2}{C_\Sigma} \tag{3.12}$$

The work done by the i^{th} electrode is given by the amount of charge δQ_i passing trough that electrode multiplied by its voltage V_i. As one electron tunnels from a junction let say j to the island, the potential of the island changes by $\delta V_0 = -e/C_\Sigma$. This charge is redistributed among all the capacitors and adds to each of them, the charge $C_i \delta V_0 = eC_i/C_\Sigma$. Hence, $\delta Q_i = -eC_i/C_\Sigma$ has flowed trough each capacitor including j which in addition has supplied the extra electron so that its total charge supplied is $\Delta Q_j = e - eC_i/C_\Sigma$. The total work done by the whole system at the end of the process of one electron tunneling to the island from the electrode j is given by.

$$W_j = \sum_i \Delta Q_i V_i = eV_j - e\sum_i V_i \frac{C_i}{C_\Sigma} = \frac{e}{C_\Sigma}\sum_i C_i(V_j + V_i) \tag{3.13}$$

The total work done when one electron has tunneled into(out of) the island from(to) all the junctions is obtained by integrating W_j to all the junctions. Given that n_j electrons may be

concerned by this process, the total free energy of the system is given by.

$$F = U - \sum_j n_j W_j = \frac{1}{2C_\Sigma} \sum_{i,j>i}^{N} C_i C_j (V_i - V_j)^2 + \frac{(Ne - Q_0)^2}{C_\Sigma} - \frac{e}{C_\Sigma} \sum_j n_j \sum_i C_i (V_j - V_i) \tag{3.14}$$

For a SET with three terminals (M=3), we adopt the notation 1, 2, 3 corresponding respectively to the drain (with the applied voltage $V_1 = V$), the source (grounded $V_2 = 0$) and the gate ($V_3 = Vg$). Under such consideration, one can write the free energy in the following form.

$$F = \frac{(Ne - Q_0)^2}{C_\Sigma} - n_D[\frac{C_g + C_S}{C_\Sigma} eV - \frac{C_g}{C_\Sigma} eV_g] + n_S[\frac{C_D}{C_\Sigma} eV + \frac{C_g}{C_\Sigma} eV_g] + constante \tag{3.15}$$

The constant includes all the terms not affected by tunneling involving the source, the drain and the island which are the only processes contributing to the current. The free energy change due to a tunneling to (from) the drain electrode is given by $\Delta F_D^{\pm}(N, n_D, n_S) = F_D^{\pm}(N \pm 1, n_D \pm 1, n_S) + F_D^{\pm}(N, n_D, n_S)$ and takes the form of Eq.3.16,

$$\Delta F_D^{\pm}(N, n_D, n_S) = \frac{e}{C_\Sigma}[\frac{e}{2} \pm (Ne - Q_0) \mp (C_g + C_D)V \pm C_g V_g]. \tag{3.16}$$

Similarly for the source,

$$\Delta F_S^{\pm}(N, n_D, n_S) = \frac{e}{C_\Sigma}[\frac{e}{2} \mp (Ne - Q_0) \mp C_D V \mp C_g V_g]. \tag{3.17}$$

Thus, the tunneling rate across the junction involving the source and drain can be obtained from the Golden-rule calculations.

$$\Gamma_S^{\pm} = \frac{1}{R_S e^2}[\frac{-\Delta F_S^{\pm}}{1 - \exp[\Delta F_S^{\pm}/K_B T]}]; \qquad \Gamma_S^{\pm} = \frac{1}{R_D e^2}[\frac{-\Delta F_S^{\pm}}{1 - \exp[\Delta F_D^{\pm}/K_B T]}] \tag{3.18}$$

One can therefore express the current as:

$$I(V) = e \sum_{-\infty}^{+\infty} P(n, V)[\Gamma_D^+(N, V) - \Gamma_D^-(N, V)] = e \sum_{-\infty}^{+\infty} P(n, V)[\Gamma_S^+(N, V) - \Gamma_S^-(N, V)] \tag{3.19}$$

Here $P(N, V)$ represents the probability of having N electrons on the island. Its times dependent variation is expressed by the master equation as follows.

$$\frac{dP(N)}{dt} = P(N+1)[\Gamma_D^+(N+1) + \Gamma_S^-(N+1)] - P(n)[\Gamma_D^-(N) + \Gamma_S^+(N)] \tag{3.20}$$

At the steady state, $\frac{dP(N)}{dt} = 0$ and the probability P(N) is given by:

$$P(N+1) = \frac{\Gamma_D^+(N+1) + \Gamma_S^-(N+1)}{\Gamma_D^-(N) + \Gamma_S^+(N)} \tag{3.21}$$

The current trough the device can thus be computed using an algorithm based on the equations 3.16, 3.17 3.18, 3.19 and 3.21 and well documented in the literature [Nuryadi11]. We have been using a similar algorithm during my thesis.

3.5.2 Threshold voltages and periodicity

In a SET, only the tunneling events minimizing the energy of the system are admitted. The condition for a tunneling event to happen is $\Delta F^{\pm}_{D,S}(N, n_D, n_S) < 0$. The upper limit of each of these inequations provide the thresholds voltages of tunneling events for different V_g.

$$\pm V_t = \frac{0.5e \mp (Ne - Q_0)}{C_D} \mp \frac{C_g}{C_D} V_g \qquad (3.22)$$
$$\pm V_t = \frac{0.5e \pm (Ne - Q_0)}{C_g + C_S} \pm \frac{C_g}{C_g + C_S} V_g$$

This system of equation represents two families of parallel straight lines with positive and negative slopes $S^- = \frac{C_g}{C_D}$ and $S^+ = \frac{C_g}{C_g + C_S}$. We plot in Fig.3.9.(d) the set of lines with slopes S^-; S^- for different number of charges N contained in the central island. One observes a network of diamonds each of which defines a particular state of the island with a given number of electrons contained. Experimentally, these lines represent the edges of the Coulomb diamonds and the capacitance of the SET can be determined from their slopes. Note that depending on the asymmetry of the capacitances the slopes can be different and the shape of the diamonds particularly distorted. The slopes of the edges of the diamonds permit to define the gate lever arm of the SET $\alpha_G = \frac{S^+|S^-|}{S^+ + |S^-|} = \frac{C_g}{C_\Sigma}$ which enables to have access to the change of the chemical potential of the island as the gate voltage is incremented $\Delta\mu = e\alpha_G \Delta V_g$. Inverting the Eq.3.22 enables to deduce the size of the diamonds in V_g direction $\Delta Vg = Vg(N+1) - Vg(N) = e/C_g$. Similarly, the size of the diamonds in the DC-bias direction is such that $e\Delta V_{sd} = 2Ec = e/C_\Sigma$ (Fig.3.9.(d)). In the case of two probe SED without gate electrode, C_g can be set to zero and the Eq.3.22 reduces to the first terms. The first three threshold voltages identified from the I(V) curves provide a system of three equations with three unknown variables representing the parameters of the SED (C_S, C_D, Q_0). This represents the accurate method to extract the experimental parameters of a SED [Hanna91, Bernand-Mantel08b, Bernand-Mantel09].

3.5.3 Interplay of Coulomb blockade and applied magnetic field

The extreme sensitivity of nanoparticle in coulomb blockade regime to their electrostatic environment makes the SED susceptible not only to the applied biases but also to any other external stimuli affecting the chemical potential of any of its complements either the leads or the central island. Indeed, the electrical response of a SED integrating ferromagnetic components can be modulated by a magnetic stimulus through the so called Magneto-Coulomb effect (MCE) [Seneor07, Shimada98] (Fig.3.9.(d)). This originates from the change of the electric charge on the island as the chemical potential of the ferromagnetic components of the devices are modified due to their magnetization rotation. Before addressing in detail the MCE,

it is convenient to remind the classical magnetoresistance (MR) of a 'simple' MTJs consisting two ferromagnetic electrodes sandwiching an insolating tunnel barrier (Fig.3.10.(a)).

3.5.4 TMR in spin valve devices

Under high applied magnetic field the two electrodes of such a junction are magnetized in the same direction. Thus, the DOS of both spin up and down are similar to each other in both electrodes and the tunneling of the spin polarized electron is facilitated. In low field range however, the difference of coercive field of the electrodes favors the antiparallel configuration of the magnetization of the electrodes (Fig.3.10.(a)). Therefore, the tunneling of the majority

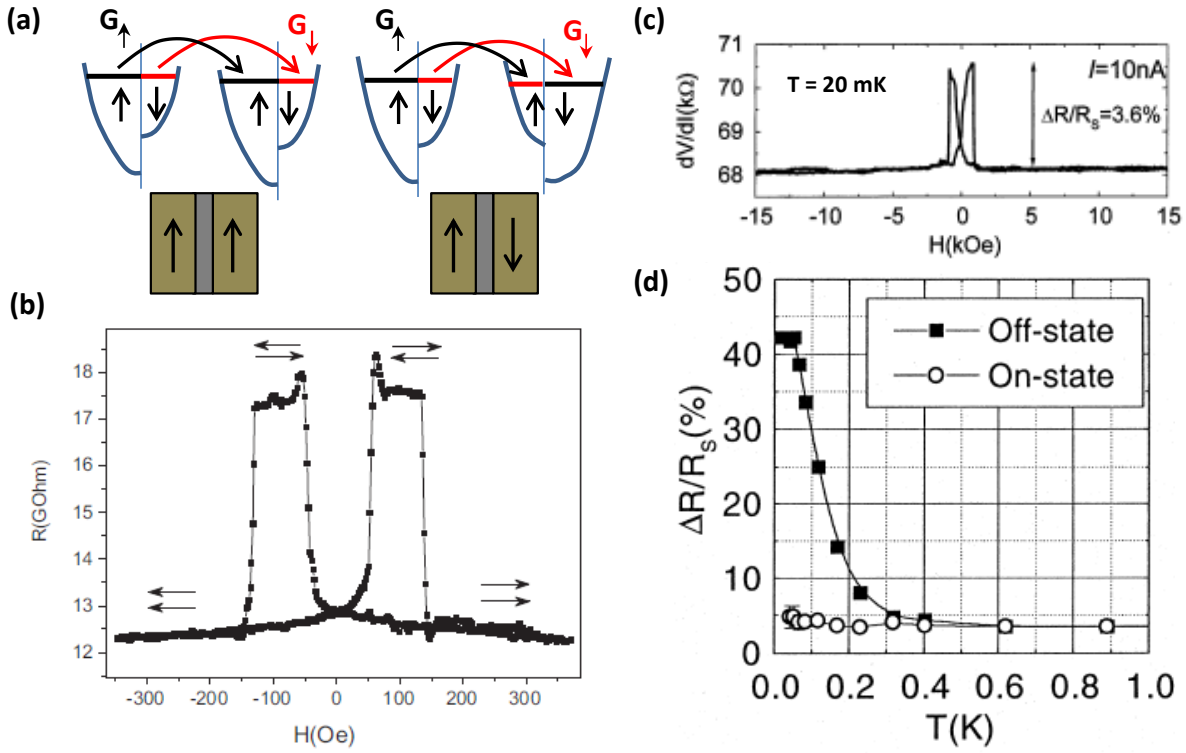

Figure 3.10 *– (a) Schematic representation of the DOS of the ferromagnetic electrodes of the tunnel junction in parallel and anti-parallel configurations. (b) The resistance of the junction as function of magnetic field. Adapted from [Bernand-Mantel08a]. (c) Low T magnetic dependence of the differential resistance of the small Ni/NiO/Co tunnel junction out of the CB regime (top panel). Temperature dependence MR in CB regime presenting an enhancement in lower T range (bottom panel). Measurement taken under V_{bias} = 0.8 mV. Adapted from[Ono98].*

spin electrons from the initial electrode is limited by the corresponding DOS not enough to accommodates them in the targeted electrode. It results a substantial increase of the resistance (Fig.3.10.(a,b)). The quantitative estimation of the resistance change of such a spin valve device has been proposed by Jullière [Julliere75] assuming that the spin of electrons is conserved during the tunneling process. It is based on Meservey and Tedrow's model [Tedrow71] giving the conductance of a tunnel junction as a quantity proportional to the DOS of the electrodes ($G \propto D_1(E_F)D_2(E_F)$). Considering the two parallel majority and minority spin conduc-

tion channels, the conductance of the junction is given by the Eq.3.23.

$$G_P \propto D_1^{\uparrow}(E_F)D_2^{\uparrow}(E_F) + D_1^{\downarrow}(E_F)D_2^{\downarrow}(E_F) \quad ; \quad G_{AP} \propto D_1^{\uparrow}(E_F)D_2^{\downarrow}(E_F) + D_1^{\downarrow}(E_F)D_2^{\uparrow}(E_F) \tag{3.23}$$

Where G_P and G_{AP} are respectively the conductance in parallel and antiparallel configuration and $D_{1,2}^{\uparrow,\downarrow}(E_F)$ the DOS at the Fermi energy of the electrodes for both spin orientations. Hence, the tunnel magnetoresistance (TMR) can be expressed as function of the spin polarization P of the electrode by Eq.3.25 [Julliere75].

$$TMR = \frac{R_{AP} - R_P}{R_P} = \frac{G_P - G_{AP}}{G_{AP}} = \frac{2P_1P_2}{1 - P_1P_2} \qquad with \quad P = \frac{D_\uparrow - D_\downarrow}{D_\uparrow + D_\downarrow} \tag{3.24}$$

This model developed in 1975 to describe the conductance change in Fe/Ge/Co [Julliere75] turned out being very successful in spintronics to describe magnetostransport experiment of spin-vale devices including those involving layered material presented in section.2.3. However, as the dimensions of the junctions becomes extremely small, the Jullière's fails to describe the observed MR.

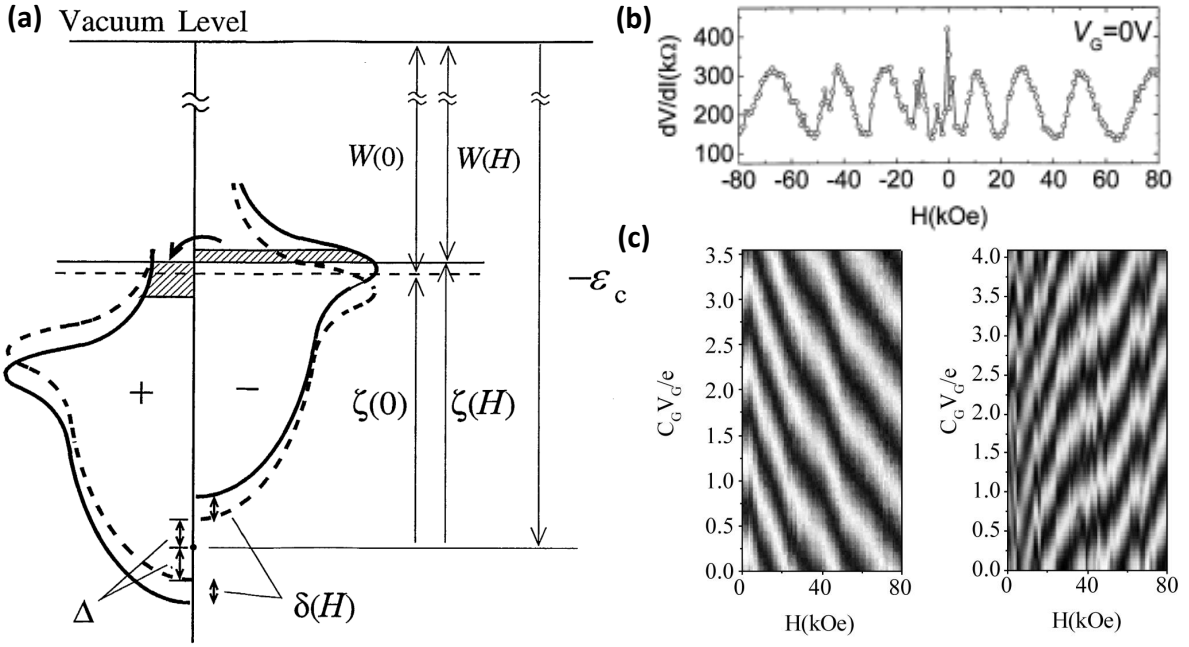

Figure 3.11 *– (a) Schematic of the DOS of a ferromagnetic material presenting the modification of the Fermi level $\xi(H)$ under applied magnetic field due to the Zeeman shifting $\delta(H)$ of the majority and minority spin bands in opposite direction. (b) Magnetic field induced Gate like oscillation of the device differential resistance $dV/dI(H)$ due to MCE. (c) Grey-scale representation of the differential resistance (dV/dI) versus Vg and the field (H) for Ni/Co/Ni and Co/Ni/Co SET (right and left figures respectively). The dark region are high resistance states. Measurement taken at 20 mK. Adapted from [Ono98, Shimada98, Ootuka01].*

3.5.5 TMR in spin valve devices

The first magnetotransport experiments on very small MTJs were reported by Ono et al on Ni/NiO/Co with junctions size $< 0.01\mu m^2$ [Ono98]. They observed that the MR follows the Jullière predictions exclusively at high T and high dc bias range (Fig.3.10.(c,d)).

In contrast, at extremely low temperature ($\sim 20mK$) and low dc bias, they observed 40% MR whereas the Julliére's model predicts a maximum TMR of only 17.5% considering the spin polarization of Nikel ($P = 23\%$) and Co ($P = 35\%$). They attributed this enhancement of MR to the Coulomb blockade induced change of the coupling of the ferromagnetic electrodes [Ono98]. Indeed, giving the small size of the junction, its capacitance was sufficiently small to induce a charging energy in the order of 50 to $100\mu eV$ that is much larger than the thermal energy in the mK temperature range. The enhancement of MR was also reported in tunnel junctions including a single island as well as in granular films in Coulomb blockade regime [Yakushiji05, Yakushiji02, Seneor07]. The reason for this enhancement was attributed to CB induces higher order tunneling processes known as cotunneling [Ono98, Shimada98, Ootuka01, Seneor07].

The cotunneling transport implies cooperative or simultaneous electrons tunneling on both side of the junction. Therefore, the tunneling probability across the structure is the product of the tunneling probabilities of each junction. Hence, the overall resistance of the structure is a power law R_t^j of resistance of a single junction resistance R_t (Fig.3.10.(d)). j being the number of the junctions involved in the cotunneling process all assumed hare to have the same resistances. The TMR in cotunneling regime (Fig.3.10.(d)) is given for two junctions by Eq.3.25 [Seneor07] :

$$TMR_{cot} = \frac{R_{AP}^2 - R_P^2}{R_P^2} = 2TMR + TMR^2 \tag{3.25}$$

it is worth noting that in a SED, this high order tunneling processes take place likely at very low voltage range i.e. when the supplied external energy is not enough to bring the system out of the central Coulomb gap [Ono98, Shimada98] (Fig.3.10.(d)). Above this range, the conductance is mediated by single electron tunneling processes expressed by Eq.3.18 and the MR (Fig.3.10.(c)) of the SED originates from MCE rather than Julière's spin coherent injection and detection [Bernand-Mantel09, Bernand-Mantel11]. In fact, under an applied magnetic filed, the magnetization of the magnetic components of the SET are modified either by Zeeman [Shimada98, Van Der Molen06] or magneto-crystalline effects [Bernand-Mantel09]. In the former case, the external field shifts the DOS of the majority spin and minority spin in opposite directions by the Zeeman energy $\Delta E_Z = \pm g_{FM}\mu_B B/2$ (Fig.3.11.(a)). Since the total electron density in the material is not affected by the Zeeman process, its chemical potential shifts by $\Delta\mu = \pm\frac{1}{2}Pg_{FM}\mu_B B$ [Shimada98, Van Der Molen06, Seneor07]. In the case of anisotropic magnetocrystalline effect, the shift of the chemical potential is mediated by the spin orbit interaction coupling the spin of electrons to the lattice through the crystal field [Bernand-Mantel09, Bernand-Mantel11] (Fig.3.12.(a)). Such a SOC is known to be prominent in 3d ferromagnetic such as Co. The modification of the magnetization orientation by the applied field displaces the bands with non-zero orbital moments inducing a redistribution of spin polarized electrons in the bands with the consequence of shifting the chemical potential of the magnetic electrodes. Because the ferromagnetic leads are always

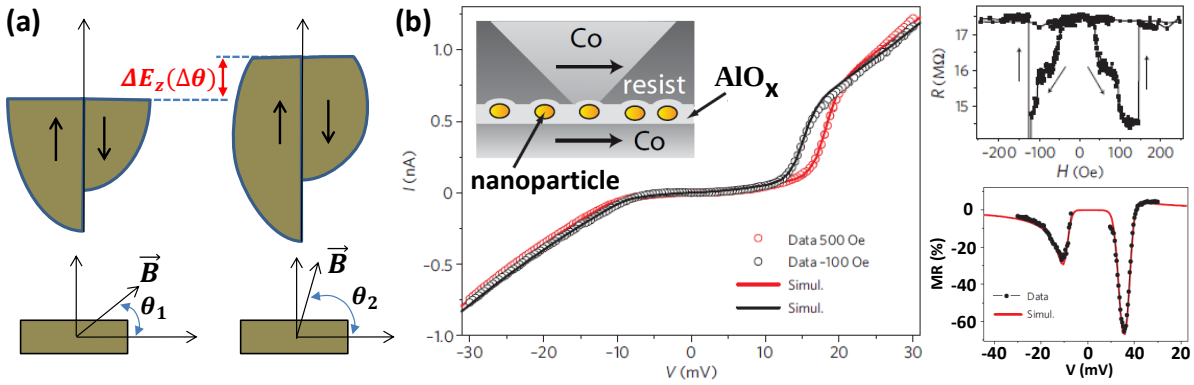

Figure 3.12 *– (a) Schematic representation of the anisotropy magnetocrystalline effect induced shift of the chemical potential of a ferromagnetic material. For the two applied magnetic field orientations θ_1 and θ_2, the modification of the DOS of the ferromagnet due to SOC mediated magnetocrystalline effect induced a shift $\Delta E_Z(\Delta\theta)$ of the chemical potential. (b) I(V) curves of a single nanoparticle SET at two different values of the field. The distinct magnetization orientations induce a shift $\Delta\mu$ of chemical potential affecting the tunneling threshold voltages and resulting to an oscillatory behavior of corresponding the MR(V) (bottom right). The MR(H) exhibits a spin-valve like behavior (top right, Vsd = 14 mV). The inset to the I-V curves presents the schematic of the sample. Experiment were carried out at 1.5 K. Adapted from [Bernand-Mantel09].*

connected to normal metal, independently to its origin, the chemical potential shift $\Delta\mu(\vec{M})$ induces an accumulation of charge at the FM/Metal interface creating an effective potential $\Delta\phi = \frac{1}{e}\Delta\mu(\vec{M})$ (Fig.3.12.(a)). This additional potential difference creates on the central island an additional charge $\Delta Q_{1,2} = C_{1,2}\Delta\phi$ (the digits refer to the contribution of electrode 1 and 2). Consequently, the total charge induces on the island by the MC process is given by the general Eq.3.26 assuming a magnetic central island with spin polarization P_{dot}.

$$\Delta Q = [C_\Sigma P_{dot} - C_1 P_1 - C_2 P_2]\frac{g_{FM}\mu_B}{2e}B \tag{3.26}$$

This magnetic field induced modulation of the charge held by the central island affects the charging energy and thus the threshold voltages (Fig.3.12.(b)) for tunneling events. This results to a gate like oscillation of the conductance (Fig.3.11.(b)) [Ono98, Shimada98, Ootuka01] or a spin-valve like TMR for a fixed DC bias (Fig.3.12.(b)) [Bernand-Mantel09, Bernand-Mantel11]. This MC TMR was demonstrated to oscillate with the applied bias (Fig.3.12.(b)) [Yakushiji02, Yakushiji05, Bernand-Mantel09, Bernand-Mantel11].

3.6 Conclusion

In this chapter I have presented the theoretical tools for analyzing the transport measurements that will be presented in the next chapters. I have reviewed the physics of FETs with particular emphasis on the layered materials based FETs. I have presented the intrinsic transport properties of graphene disordered systems characterized by a randomly distributed of localized states applied to the case of SC-TMDs. In graphene, we have observed that counter intuitively, phonon scattering do not affect much its mobility. The transport is instead controlled by Coulomb scattering sources at low doping regime while the transport at high dop-

ing regime is controlled by e-e interaction and neutral point defects. Thus, the intrinsic transport mechanism in graphene is either ballistic or diffusive depending on the dimension of the devices comparatively to the mean free path of carrier and the doping level. In SC-TMDs, the transport is mediatized by VRH at low T and doping and nearest neighbor thermally activated at higher T. We have observed that, from their semiconducting state and low doping density, SC-TMDs undergo a transition to a metallic state and higher doping with the transition debated to by either of Mott-Anderson or quantum type. As the doping increasing further, SC-TMDs undergo transition to a superconducting state. The last section of the chapter was dedicated to the orthodox theory describing the single electron transport processes in CB regime. We have also seen that in SED with magnetic electrodes an applied magnetic filed results to spin-valve like MR due either to ZMC or to AMC effect.

Chapter 4

Experimental method and Set-up

In this chapter, we present the fabrication method of 2D-0D MD-VdWh based SET and 2D materials based FET devices investigated in the thesis. We first present the exfoliation method of layered materials. Then we detail the fabrication of 2D-0D MD-VdWh consisting of Aluminum nanoclusters self-assembled onto the surface of the 2D materials. The 2D-0D MD-VdWh are obtained by Ebeam evaporation of thin Al film onto the surface of CVD or exfoliated 2D materials which play the essential role of a template for the growth of the self-organized assembly of Al nanoclusters. We show that after oxidation, the nanoparticles adopt a core-shell structure with metallic core embedded in an alumina shell. We present a comprehensive characterization of the 2D-0D MD-VdWh combining Raman spectroscopy to ascertain the quality of the 2D material prior and after Al deposition and a complementary physico-chemical characterization using X-ray Photoemission (XPS) and Scanning Transmission Electron Microscopy (STEM) and Energy Electron Loss Spectroscopy (EELS) which enable to confirm the core-shell structure of the deposited Al nanoparticles after oxidation. In the last section of the chapter, we describe our experimental set-up for transport measurements.

4.1 Sample fabrication

The sample fabrication is a multi-step process including respectively the production of single or multilayer (ML) graphene (Gr) or SC-TMDs (particularly MoS_2 and $MoSe_2$), the Al deposition and oxidation in the particular case of 2D-0D MD-VdWh based SET, the patterning of electrodes using Ebeam lithography followed by their macroscopic extension thanks to manual stencil mask alignment and finally the wire bonding of the sample on a chip holder.

4.1.1 Mechanical exfoliation

The production of single or multilayer (ML) Gr, MoS_2 and $MoSe_2$ used in this thesis relied mainly on a dry exfoliation method as first proposed by Novoselov et al. [Novoselov04] (see section.2.4). This method does not request particular means and facilities. Its consists of using a scotch tape to cleave from the corresponding pristine bulk material a single or ML Gr, MoS_2 or $MoSe_2$ flake. This exfoliation is possible thank to interlayer weak Van der Waals forces. The exfoliated flake is subsequently transfer on a Si/SiO_2 substrate. This exfoliation process can be resumed in four steps (Fig.4.1 for the particular case of Gr).

1. A piece of bulk crystal (graphite in the case of Gr) is placed on an adhesive tape (picture 1, Fig.4.1). A repeated process of folding and separating the adhesive tape enables to cleave the crystal on a large surface of the tape (picture 2).

2. Stick another adhesive tape to the one supporting the cleaved sample (picture 3). Press the two tapes on each other to improve their adhesion. Then, slowly peel off the two tapes in order to increase the chances of obtaining large flake on both tapes (picture 4). Repeat this step (picture 3 and 4) as many times as needed with clean tapes to obtain a sufficiently transparent films of crystals susceptible to be a single or ML Gr (or any other 2D material).

3. The next step consists to transfer the obtained transparent flake onto a Si/SiO_2 substrate. To do so, the adhesive tape supporting the transparent flakes is stuck on the substrate (picture 5). Massage the adhesive tape delicately on the Si/SiO_2 (with a finger for around a minute) by applying a moderate but sufficient pressure in a unique direction (parallel to the tape for practical reasons). This improves the adhesion of the flakes onto the substrate and increases the chances of obtaining large flakes. It is important to be carefully at this step, particularly if the sample is designated to measurements using p^+Si/SiO_2 substrate as a back gate electrode. I speculate that over pressure may induce microcracks in the only 280 nm thick oxide of the substrate resulting to gate leakage current. To avoid contamination and facilitate the adhesion of the flake, the substrate has to be very clean. In our case, it is cleaned using a triple successive bath of acetone, ethanol and isopropanol in order to dissolve eventual impurities sticking on the substrate. The first bath of acetone is always accompanied with ultrasonic agitation to improve such dissolution. After the cleaning we often submit the substrate to a plasma oxygen during 15-20 min to improve its cleaning and activate the surface so to favor the adhesion of the flakes. In this case it is recommended not to wait a long time before transferring the flake on the substrate.

4. The last step consists in peeling off slowly the adhesive tape from the substrate while maintaining the substrate immobile on the supporting table (picture 6). Any time that a pressure is applied to the substrate, it is important to keep in mind the problematic of leakage current.

An inconvenient using this exfoliation method are the residues of the tape left on the substrate and eventually on the surface flake during the transfer step. However, the latter possibility can be argued not to be systematic as the transferred flakes may result from an exfoliation of a ML sheet sticking on the tape. In any case this technics enables exfoliation of micrometer Gr with very good properties [Novoselov04] suitable for long distance spin injection [Tombros07] (see section.2.1 and section.3.1). By this exfoliation method, we routinely

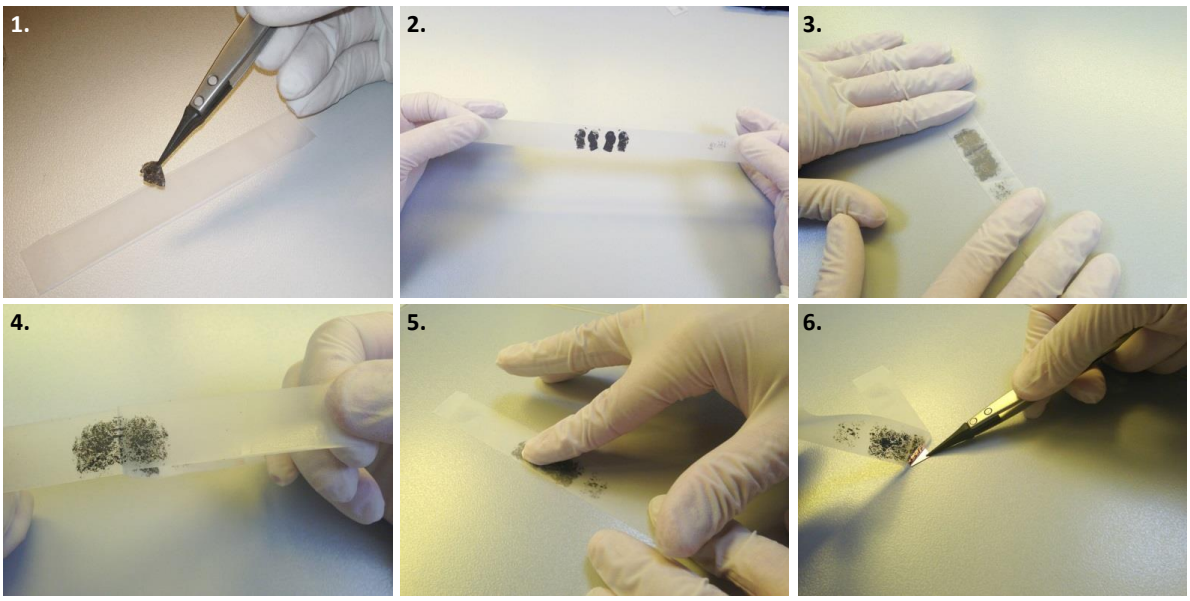

Figure 4.1 *– Exfoliation steps of Graphene. The illustration pictures have been taken by Guillaume Froehlicher from our group [Froehlicher16].*

obtained few tens micrometers of mono or multilayer Gr, MoS_2 and $MoSe_2$ (Fig.4.2). However, for the purpose of our usage for SET or FET, flakes of $10 \times 10 \mu m^2$ size are already quite sufficient. Often, the exfoliated flakes are surrounded by bulk residues complicating the patterning of electric leads while avoiding short-circuit. Transferring the flake from the tape onto the PDMS before to transfer it from PDMS to the Si/SiO_2 substrate helps to minimize this problem.

After exfoliation, the flakes are identified on the Si/SiO_2 using an optical microscope(Fig.4.2). For the purpose of the subsequent Ebeam lithography, an optical microscope equipped with micrometer precision screw enables to identify the coordinates of the position of the flakes on the surface of the substrate. During my thesis, I use $1x1cm^2$ and $0.5x0.5cm^2$ Si/SiO_2 square substrates. Thus, I always choose one of the corner as the origin of coordinates. The perpendicular sides joining the selected origin representing the x and y directions. The Fig.4.2 presents the optical micrograph illustration of the exfoliated single and multilayer Gr, MoS_2 and $MoSe_2$. The thickness of the flakes are primarily identified using optical contrast (Fig.4.2) which enables a first selection of the exfoliated the flakes with appropriate size and thickness. When required, a more accurate thickness characterization is carried out using Raman spectroscopy and/or Atomic Force microscopy (AFM). I would like to mentioned that, several devices was fabricate using commercial Gr synthesized on Ni substrate by CVD as

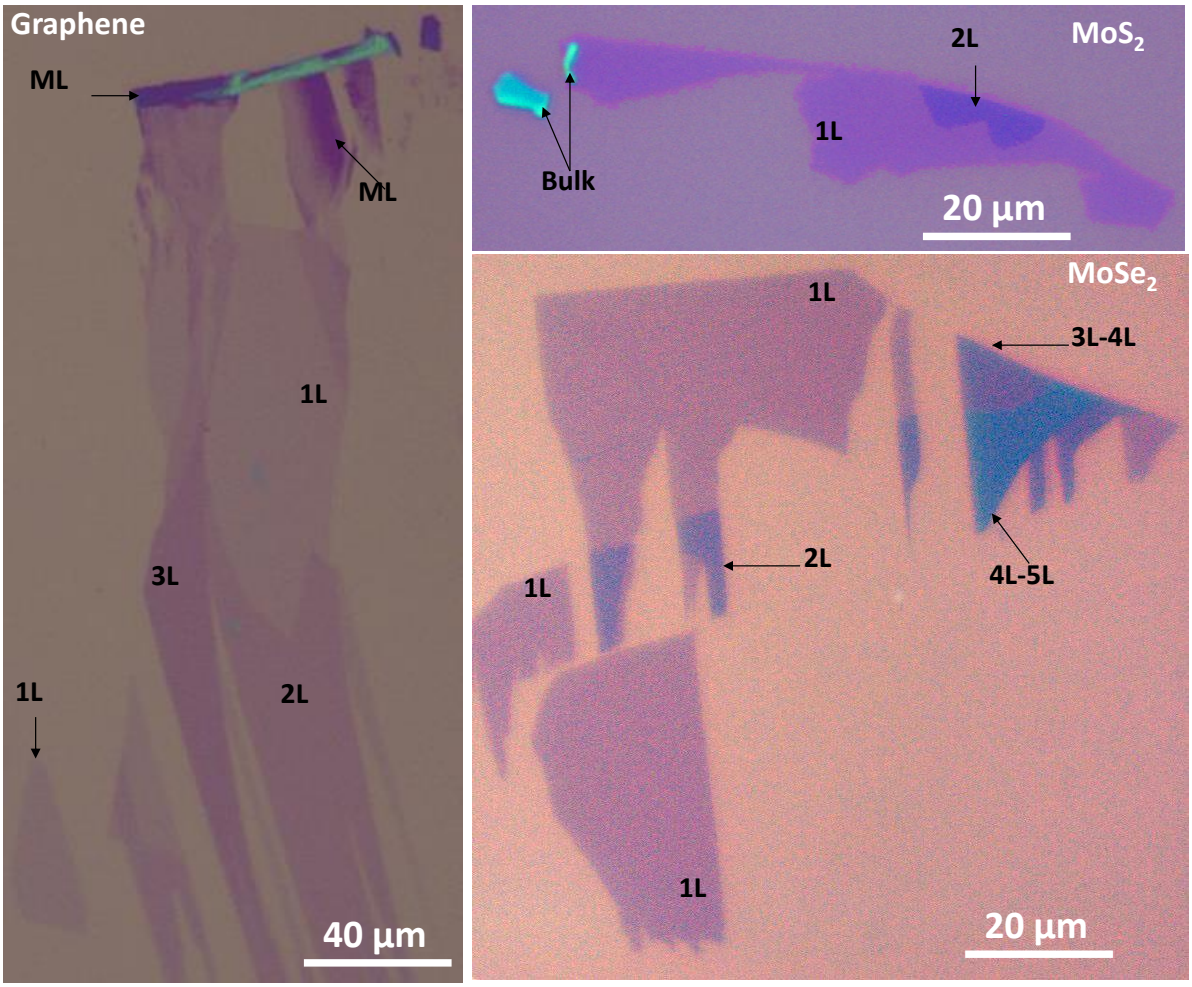

Figure 4.2 *– Optical images of the exfoliated single and multilayer Gr, MoS_2 and $MoSe_2$. The optical contrast depends on the thickness. The corresponding material and thickness are indicated on the corresponding image.*

described in section.2.4 using methane (CH_4) precursor in presence of hydrogen flux at temperature exceeding 1000 K. In this case, the flake covers all the surface of the substrate and no identification is required and the electrodes can be patterns anywhere on the substrate. This sample were used particularly for vertical SET. The next step after the identification of the flake is the patterning of electrodes using electron beam (Ebeam) lithography.

4.1.2 Electron beam (Ebeam) lithography of electrodes

To pattern the electrodes, we follow three Ebeam lithography steps using a Zeiss Supra 40 scanning electron microscope (SEM) equipped with a Raith lithography system allowing a precise control of the electron beam. For all the Ebeam steps, we use a bilayer PMMA (poly(methyl methacrylate)) resist consisting respectively of AR-PMMA 669.04 and AR-PMMA 600.02. Both resists are spincoated at 4000 revolution per minutes (rpm) during 1 min and annealed at 180°c during 1'30*s*. This results to a total (AR-PMMA 669.04)/(AR-PMMA 600.02) bilayer resist thickness of 290 nm corresponding to 220 nm for the first layer

and 70 nm for the second layer. It is worth mentioning that before to spincoat the second layer it is necessary to wait about 1'30*s* for the first layer to thermalize. The use of a bilayer resist is to facilitate the lift-off. The first lithography step consists of patterning a network of marks around the position of the selected flakes using the coordinated provided by the optical microscope. The marks are indispensable for the identification of the region of interest once the sample is introduced in the SEM. Indeed after spincoating the bilayer resist, a few layer thick flakes of a 2D material is not observable in the SEM microscope. Beside their role in the identification of the position of the flakes, these marks also serves for beam alignment during the second and third lithography steps which consist of patterning fine leads on the flake and the extension of this leads to enabled stencil mask alignment. The second and third lithography steps are separated mainly because they involve different materials (Co and Au respectively). When this is not the case, as for $MoSe_2$ based FET (see Chap.7), the two steps are not separated. It is very important to note that following the patterning of fines leads, before the Co leads deposition, we evaporate the thin aluminum layer into the fine leads patterned on Gr (or MoS_2) surface and oxidize to form the our Al-AlO_x/2D-crystal mixed dimensional VdWh (see section.4.2) of paramount importance for SET. For the fabrication of FET there is not such an Al deposition step. The lithography of electrodes is directly followed by Ti/Au deposition. We resume the lithography steps as followed :

Step 1 : Identification and alignment marks. After resist coating, since the flakes of a single or ML 2D material becomes indiscernible in the Scanning Electron Microscope, we use the coordinate obtained from optical imaging to displace the beam to the region of interest and exposed the predesign mark patterns. The sample is then taken out of the SEM and developed during 25 s in 1:3 MIBK-IPA (methyl isobutyl ketone-isopropyl) at 25°C. The evaporation of the Ti(3 nm)Au(47 nm) followed by lift off in acetone complete this step. The Fig.4.3.(a) presents an optical micrograph of Gr flake surrounded by a network of identification and alignment marks.

Step 2 : fine leads. After the lift-off of marks, the sample is again imaged with the optical microscope. An image with the marks is imported in the Ebeam lithography software for the design of the fine leads pattern. The design of the fine leads is done directly on the flakes with the desired shape, size and orientation. Subsequently, the same bilayer resist is spincoated on the sample which is then reintroduced in the SEM for insolation of the predesign fine leads pattern. Prior to the insolation, to ensure the proper alignment of the leads pattern to the flake, the beam is accurately aligned by affecting to three marks surrounding the flakes (out of four) their exact coordinates. This is known as three marks alignment technic (Fig.4.3.(b)). In the so defined coordinate system, the predesigned pattern automatically locates at the coordinates of the flake (given it is design there). Moreover, before insolation, we include an alignment step which enables to check that the marks are effectively located at their expected coordinates and thus to adjust if needed. After beam insulation, the sample is develop during 25 s in 1:3 MIBK-IPA as already mentioned. This procedure enables patterning fines leads with the best possible alignment. This step is particularly sensitive to the developing time

and it is important to regularly check the proper developing time by making a dose test. In such patterned electrodes on Gr or MoS_2 an ultra-thin Al film of 1.7 nm nominal thickness is deposited using Ebeam evaporation. The sample is then taken out of the vacuum chamber for oxidation in the air before to be reinserted into the evaporator for Ebeam evaporation of 40 nm Co and caped with 10 nm Au follow by lift-off in acetone. The Fig.4.3.(c) presents an optical micrograph of the patterned Co(40nm)/Au(10nm) electrodes on Gr flake.

Step 3 : fine leads extension. The last Ebeam lithography step concerns the extension of the small leads by patterning the 'recontacting' electrodes using a 1000 μm^2 write field following the same technical procedure described in step 2. This means the predesign of the pattern, the spincoating of the bilayer resist, and the insulation. The alignment of the beam is done similarly using three marks alinement method in order to ensure that the 'recontacting' extension electrodes get properly aligned with the fine ones intended to be extended. After development, Ebeam evaporation of Ti(3 nm)Au(47 nm) is followed by lift-off in acetone to end the process. The Fig.4.3.(c) shows the optical image of the fine electrodes (the white leads) together with their extensions (the yellow electrodes). For Al-AlOx/Gr based SET we always adopted a device configuration integrating two reference electrodes at the extremities of the flakes not containing the Al-AlOx layer Fig.4.3.(c). This makes possible the transport measurements with a device configuration including a single junction containing Al-AlOx the other electrode being one of the reference Ti/Au electrode.

4.1.3 Shadow stencil mask extension of the leads and wire bonding

Shadow stencil mask deposition. After lithography, the fabrication progresses with a manual alignment of the stencil mask on the Ti/Au microscopic extension of the fine Co leads patterned during the last lithography step. This enables a shadow deposition of Ti(3 nm)Au(47 nm) of macroscopic extension of the electrodes in order to make possible manual bonding of the sample onto a chip holder with Au wires permitting its adaptation onto the measurement set-up (Fig.4.3.(d)).

Wire bonding. This constitutes the last fabrication step. The substrate holding the fabricated sample is glued into a commercial metallic (non-magnetic) chip holder with a conductive silver paste. The conductive paste is indispensable for contacting the back p-doped Si of the substrate used as a back gate electrode. We then manually connect the macroscopic part of each leads (Fig.4.3.(d)) to the contact pads of the chip holder with Au wire using also conductive silver paste. The manual bonding although time consuming has the advantage that it does not require applying a force to ensure good adhesion of the wire to the electrodes contrarily to machine bonding (using a bonder) and thus circumvent the risk of creating cracks in the gate SiO_2 that may induce leakage of the gate electrode. The Fig.4.4 presents an example of so bonded sample on a chip holder.

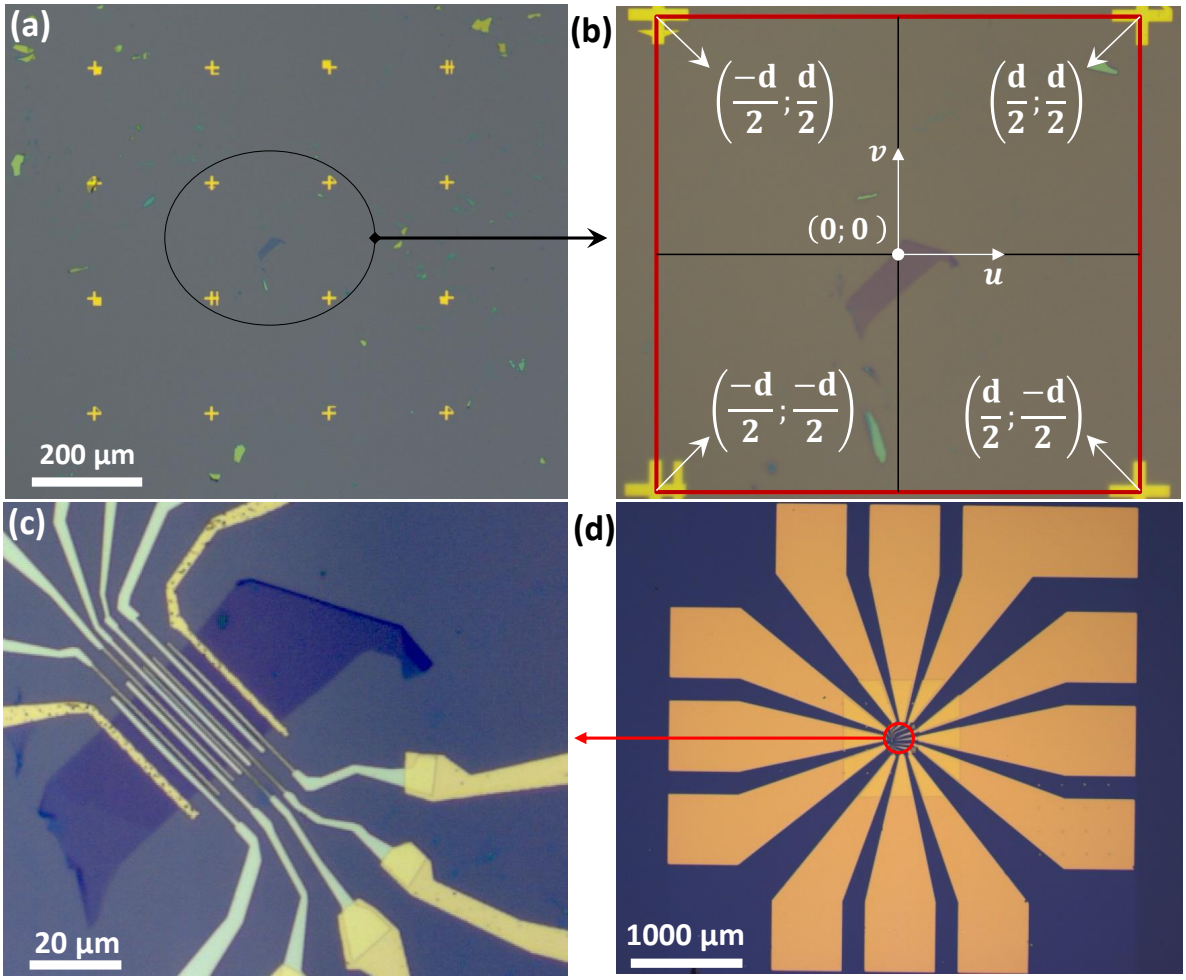

Figure 4.3 *– Sequence of the lithography steps (a) Optical image of the identification and alignment marks. (b) Coordinate used to align the beam before the exposure of the fines leads. (c) Optical image of the fines leads (white) and extension leads (Yellow). The two leads at extremity of the flakes are the reference electrodes. (d) The optical micrograph of the device after macroscopic extension of the leads using manual stencil mask alignment. One distinguishes the lithography extension limited within the smaller square at the centre of the device.*

4.2 Characterization of Al-AlOx/Graphene MD-VdWh

The 2D-0D MD-WdWh are dedicated essential for single electron transport processes. As already mentioned they are fabricated by simple Ebeam evaporation of a thin Al layer of 1.7 nm nominal thickness over Gr or MoS_2 surface. After the deposition, the sample is taken out of the evaporator for oxidation in ambient conditions during 1 to 3 hours. The morphology of the oxidized Al layer deposited either on Gr or MoS_2 characterized by TEM, SEM and AFM presents a granular structure with a self-assembled Al-AlOx nanoparticles covering the surface of the underneath 2D material (Fig.4.5.(a-e), 4.7.(a) and 4.8.(c)). The average lateral size of the nanoparticles (NPs) demonstrated a distribution well approximated by a Gaussian function with a peak at 6.9 nm and the full-width-at-half-maximum close to σ=2.8 nm (Fig.4.5.(e)) which corresponds to 20% size distribution. Such a morphology is reminiscent of a Stranski-Krastanov 3D growth process. Indeed, during Al evaporation over the surface

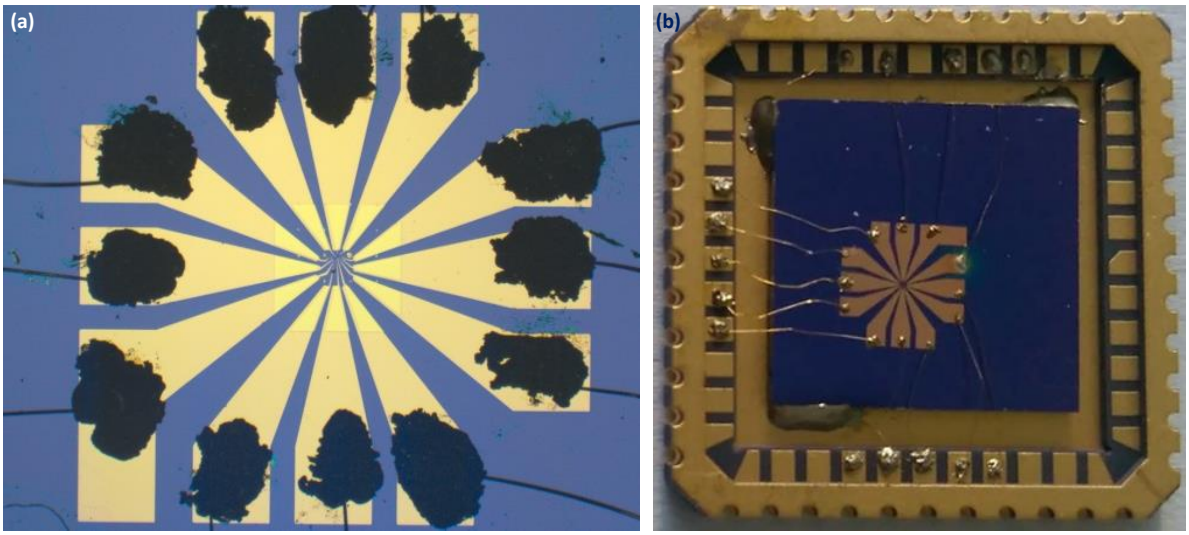

Figure 4.4 *– Bonding of the sample onto a chip holder. (a) Optical micrograph of a sample with silver paste drops sticking the Au wire on the electrodes. (b) A photograph a sample bonded onto a chip holder.*

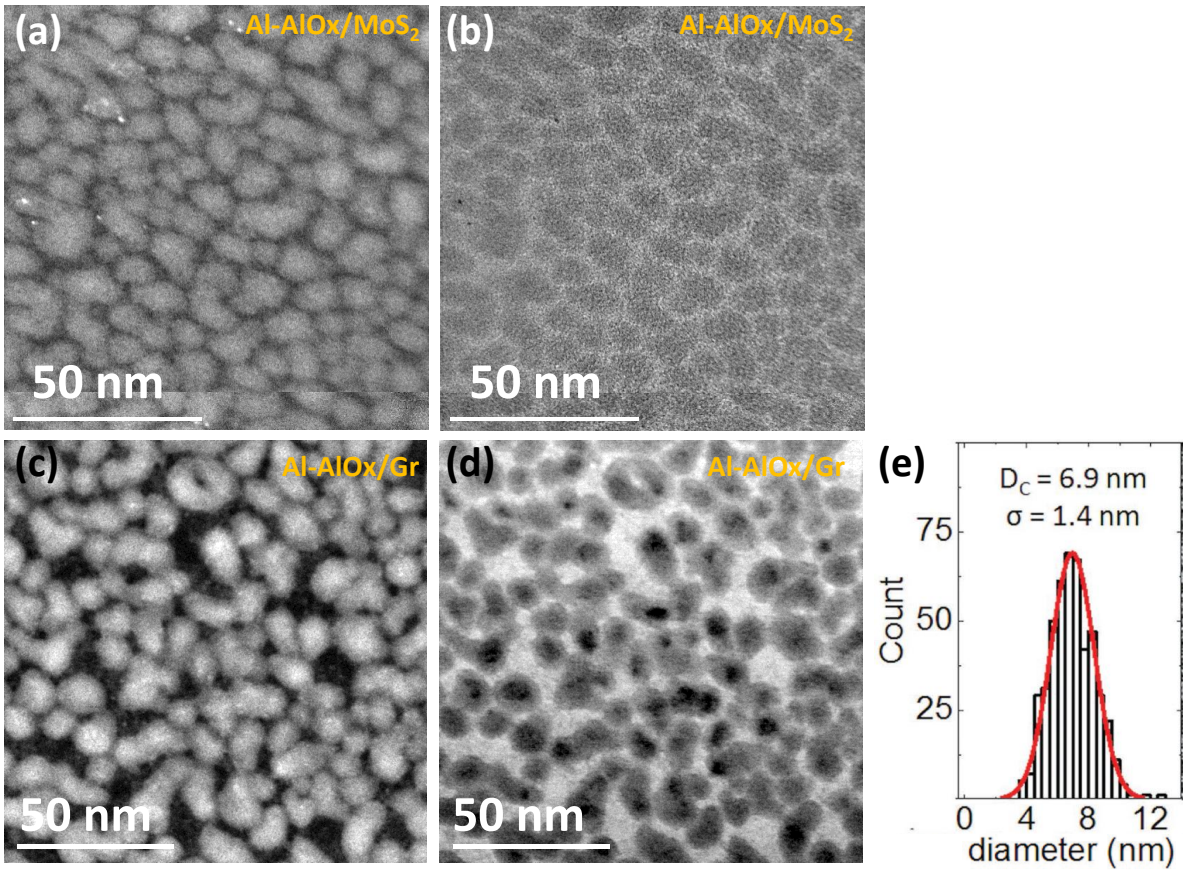

Figure 4.5 *– (a) STEM Bright Field image of the oxidized Al layer deposited on the surface of MoS_2. (b) The corresponding STEM dark field image. (c-d) Present similar images for oxidized Al layer deposited on the surface of Gr. (e) The corresponding histogram of the clusters diameter D fitted with a Gaussian function centered at $D_C = 6.9$ nm with a standard deviation $\sigma = 1.4$ nm (20%).*

of Gr or MoS_2 exfoliated on SiO_2, Al atoms, after adsorbed onto the 2D material surfaces, diffuse to the favorable nucleation sites probably conditioned both by surface tension and the

atom diffusion rate. The nucleated clusters increase in size thanks to a Stranski-Krastanov 3D growth process resulting to the observed cylindrical disk shape self-assembled Al NPs (Fig.4.7.(a)). This growth process is in agreement with a previous experiment demonstrating that for a nominal thickness below 1 nm, the growth of Al on Gr follows a Stranski-Krastanov 3D growth process [Shi14] (see also section.2.4 for other example of 3D growth of self-assembled NPs on Gr surface).

4.2.1 Raman characterization

We noticed in section.3.1.2 that atoms deposition on the Gr surface can dope the Gr sheet and substantially affect its transport properties. In addition, the granular Al layer may induce constrains on the Gr sheet, susceptible in principle to affect its transport properties. Our samples being intended to extremely sensitive single electron measurements, it is of paramount important to accurately addressed the effect of Al deposition on Gr so as to ascertain whether such Al deposition affects the physical properties of the underneath 2D materials and Gr in particular. Raman spectroscopy is a powerful tool to quantify doping and strain of layered materials. Fortunately, Raman spectroscopy is among other research directions of Prof Stéphane Berciaud who is one of the senior member of our team. We collaborated with him and Guillaume Froehlicher, his PhD student, for Raman characterization of our device. In order to ascertain the effects of extra doping and strain, we conducted a comparative study of spatial resolved micro-Raman spectroscopy acquired on pristine Gr exfoliated on Si/SiO_2 wafer before and after the Al deposition/oxidation. This analysis enable in addition an accurate measurement of the thickness of the 2D material (the number of monolayers).

The Fig.4.6.(a) presents the corresponding Raman spectra taken at a given position of an exfoliated bilayer Gr before and after aluminum deposition (see the black dot on the inserted optical image of the corresponding flake). The broader lineshape 2D-mode less intense than the G peak is characteristic of bilayer Gr [Ferrar07]. The absence of the D mode is a clear evidence of no defect in the exfoliated bilayer Gr. The frequency of the G-mode remains unchanged after Al deposition demonstrating that there is not additional doping induced [Ferrar07]. We repeated this Raman spectra to the whole flake. This enabled us to extract the frequency (ω_G and ω_{2D}) of the G and 2D modes at all the positions (or pixels) of the sample and report them on a two axis plot showing the pixel-to-pixel variation of ω_G correlated with ω_{2D} (Fig.4.6.(b)). Note that each pixel is a spectral averaging over $1\mu m^2$ which is the size of the laser spot. Such a plot enables a direct observation of the effect of extra doping and strain [Lee12a]. For pristine Gr, the reported data point are expected to fall on a single line with a slope $\Delta\omega_{2D}/\Delta\omega_G \approx 2.2$ as demonstrated by Lee et al. [Lee12a]. $\Delta\omega_{2D} = \omega_{2D} - \omega^0_{2D}$ and $\Delta\omega_G = \omega_G - \omega^0_G$ represents the frequency shift of the 2D and G mode relatively to that of a pristine freestanding Gr with no strain and doping and identified to be $(\omega^0_G = 1581.6 \pm 0.2; \omega^0_{2D} = 2676.9 \pm 0.7)$. Such a variation is a consequence of a tensile strain present in any pristine sample exfoliated on a substrate. The presence of doping induces a linear variation of the mode frequencies with a very different slope $\Delta\omega_{2D}/\Delta\omega_G \approx 0.70$. Thus,

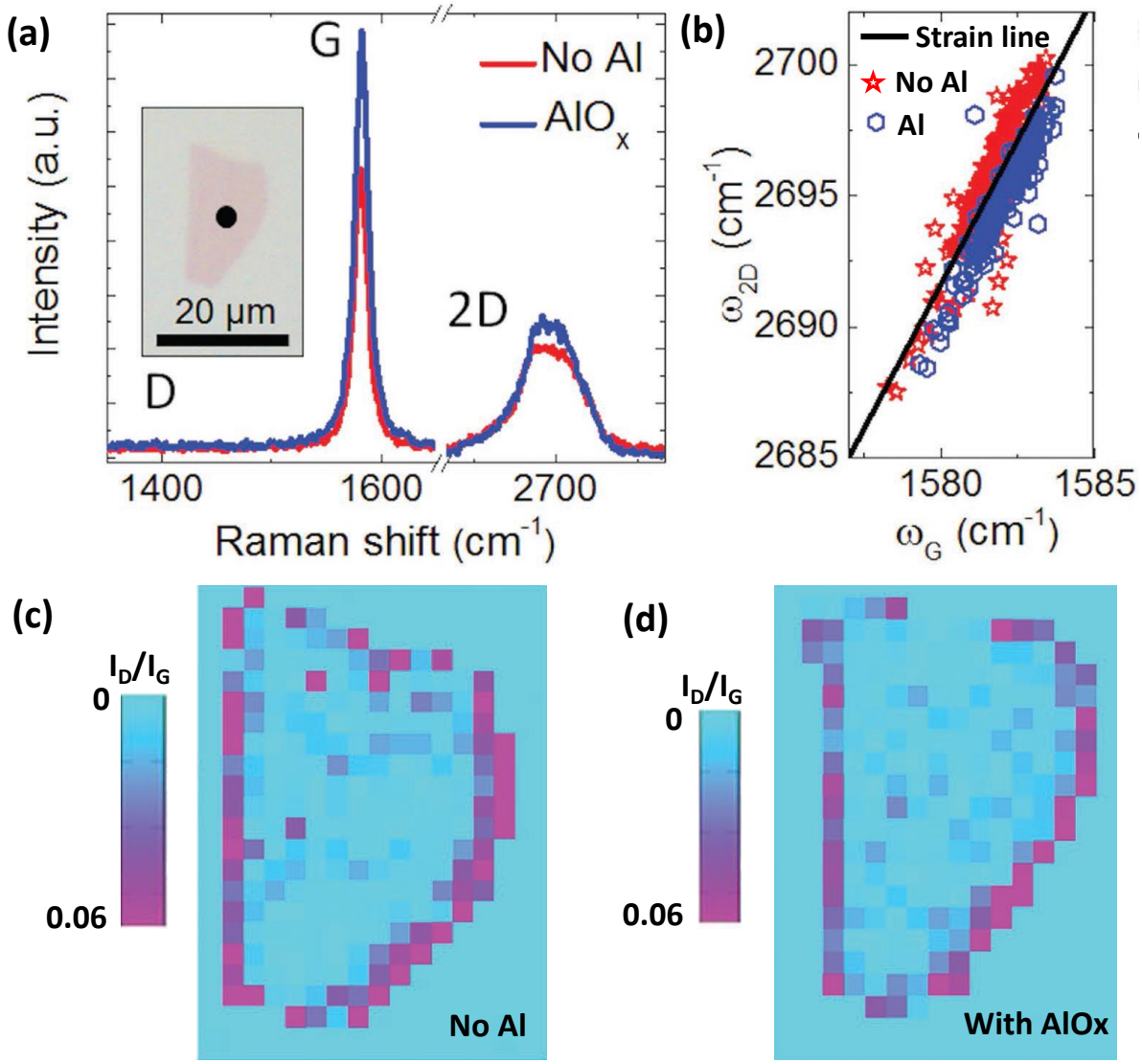

Figure 4.6 *– Micro-Raman spectroscopy on Gr before and after Al deposition and oxidation. (a) Raman spectra recorded with a 532 nm (2.33 eV) laser on bilayer Gr, before and after deposition of 2.2 nm of Al. The inset represents the optical micrograph of the corresponding bilayer Gr on SiO_2 (285 nm)/Si substrate. The black dot represents the position where Raman spectra have been taken. (b) Correlation between the 2D-mode and G-mode frequencies before (red stars) and after (blue hexagons) aluminum deposition/oxidation. The black line represents the strain line with a slope of 2.2. (c) and (d) are the maps of the I_D/I_G ratio recorded on the same sample before (left) and after (right) Al deposition.*

a combination of both doping and strain is expected to induce a slope comprises between this two extremes (2.2 and 0.70) [Lee12a, Godel15].

We observe in Fig.4.6.(b) that either before and after Al deposition and oxidation, all the data are very similar and all the (ω_{2D};ω_G) points fall on the straight line corresponding to tensile strain as existing in a pristine Gr exfoliate on a substrate. No contribution related to extra doping is reported. This demonstrates that Al deposition does not induce a detrimental effect the Gr quality. In addition, we observed no significant increase of the intensity of defects related D-mode features relative to that of the G-mode features as illustrated by I_D/I_G

ratio that remains very low (below 0.1) (Fig.4.6.(c))[1]. This illustrates that the good quality of the crystal structure of the exfoliated Gr is preserved after Al deposition and oxidation. The enhancement of this ratio at the edges of the bilayer flake is the indication of vacancies defect resulting from incomplete lattice. It should be noted that for Raman characterization Al is deposited to whole flake. Which is not the case for the sample concerned by transport measurement on which Al are deposited only within the leads. Therefore, the 2D-0D Gr based MD-VdWh can be considered made of pristine Gr flakes. This will be later demonstrated by the transport characterization of the Gr channel after device fabrication (see section.5.3.1).

4.2.2 Physico-chemical analysis of the Aluminium-Graphene heterostructure

Thanks to the collaboration with Dr. L. Simon's group at the Institute of Material Science of Mulhouse-France, X-ray Photoelectron Spectroscopy (XPS) was performed on the oxidized Al/Gr heterostructures. The XPS measurements were carried out in an hemispherical electron analyzer (Scienta R3000) equipped with a monochromatic Al-Ka X-ray source ($h\nu = 1468.6eV$). The measurements were performed at 60° incidence from the sample normal. The sample for XPS analysis consisted of CVD Gr on SiO_2/Si substrate with a 2 nm Al deposited at room temperature using a Knudsen cell under 1 to 2.10^{-10} mbar vacuum resulting to a similar granular film (Fig.4.7.(a)). Following Al deposition, the Al-Gr heterostructure was first analyzed. Then, the sample was transferred (without breaking the UHV) into a connected UHV steel chamber for oxidation. The oxidation was done by introducing O_2 gaseous through a leak valve from few Langmuir to atmospheric range of pressure in order to replicate the process of oxidation in the air. This was followed by another XPS characterization. Note that prior to Al deposition, an XPS spectra was taken serving as reference (Fig.4.7.(b)). The Fig.4.7.(c1,c2) represent the typical C1s and Al2p spectra of the Al-Gr heterostructure before and after oxidation. We observed after Al deposition, the appearance of a new component on the C1s spectra situated towards 285.4eV as indicated by the arrow in Fig.4.7.(c1). This component is associated to the covalent bonds between the Gr plane and a suboxide AlOx in the form of C-O-Al which creates an interfacial layer between the Al dots and the Gr plane. The surface of metallic Al is very reactive. Thus, even with very little oxygen content in the UHV chamber, just few minutes after Al deposition during the analysis (prior to oxidation), two oxide components Al_2O_3 (Al^{3+}) and AlOx could already be detected on the Al2p spectra (Fig.4.7.(c1)). This suggests that they may be a thin oxidized layer interfacing the Gr surface and points out an important argument to be considered when we will be discussing the transport measurements in Chap.5. After control oxidation under 600 mbar O_2 gaseous during 3 hours, the granular Al layer gets more deeply oxidized and we evidence in Al2p spectra a strong component of Al_2O_3, while the previously observed AlOx peak remains with little change (Fig.4.7.(d2)). Interestingly, although the component associated to metallic Al substantially decreases due to oxidation, a detectable quantity of metallic Al is clearly discernable as demonstrated by the small metallic Al component in Fig.4.7.(d2) (indicated

[1] French speaking readers can also refer to the ref.[Godel15] for more detailed discussions regarding the Raman characterization of graphene prior and after metal deposition/oxidation.

by the arrow). Typically we found after oxidation 78% of Al_2O_3, 20% of C-O-Al and 2% of metallic Al. This small percentage is fully consistent with STEM-EELS analysis. These XPS

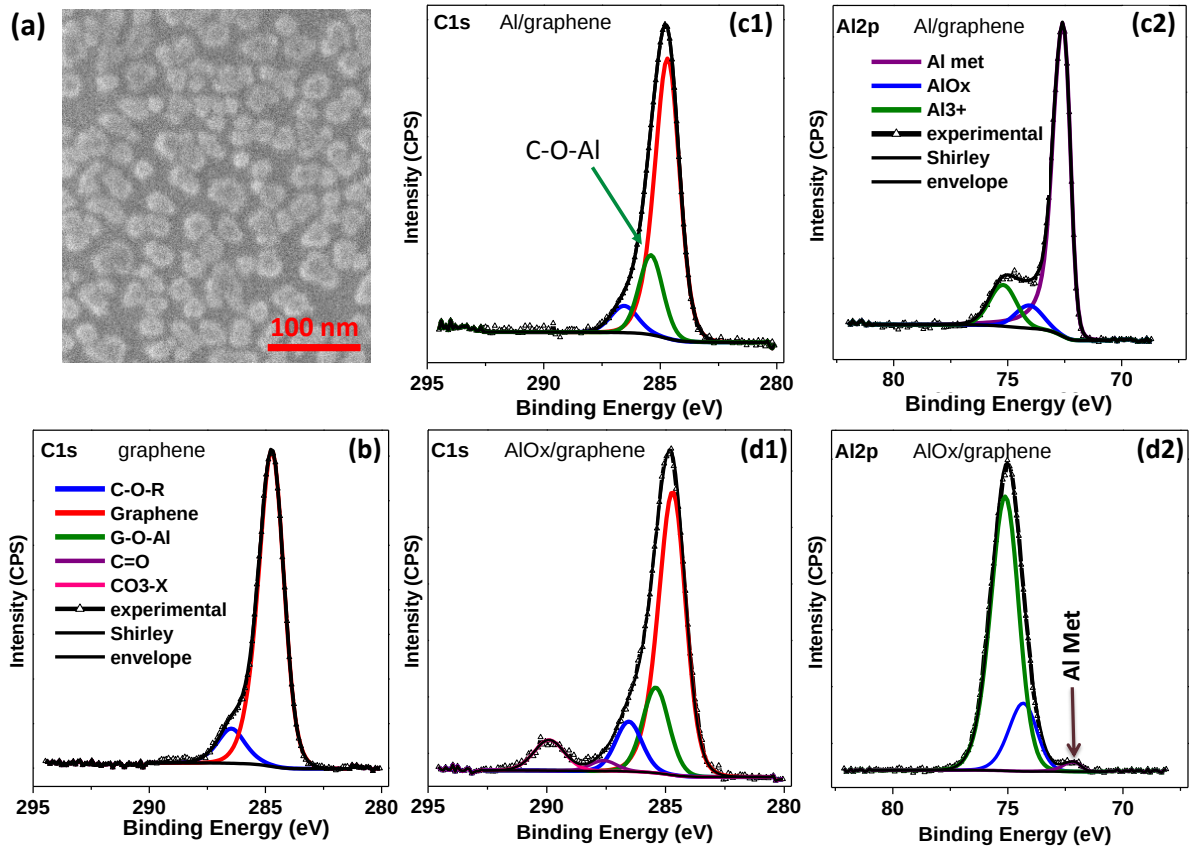

Figure 4.7 *– (a) SEM image of the sample used for XPS analysis consisting of 2 nm deposited on commercial CVD Gr on SiO_2/Si. (b) C1s core level peak of CVD Gr on SiO_2/Si (purchased by Graphenea) serving as reference. (c1) and (c2) C1s and Al2p core level spectra after deposition of 2nm of Al at room temperature prior to oxidation. (d1) and (d1) Present the C1s and Al2p core level spectra after subsequent oxidation from few Langmuir to 600 mbar during 3 hours. The main Al_2O_3 is surrounded by satellite structures attributed to sub-oxides labeled AlOx . The unoxidized metallic Al provides a weak shoulder in the peak indicated by the arrow (labeled 'Al-Met').*

analysis demonstrate without ambiguity a remaining unoxidized metallic Al in the granular film. There are however based on statistical averaging on an ensemble of nanoparticles of the whole granular film. Details of the spatial distribution of metallic Al and Al-oxide (either Al_2O_3 or AlOx) in a single nanoparticle requires scanning transmission electron microscopy (STEM) and electron energy loss spectroscopy (EELS) analysis.

4.2.3 STEM and EELS analysis of oxidized Al-Graphene heterostructure

The STEM and EELS analysis were conducted in collaboration of Pr Prof. O. Ersen's of the DMOS department of our institute (IPCMS), where I worked with Georgian Melinte. We characterized the structure of the oxidized Al layer by scanning transmission electron microscopy (STEM) and electron energy loss spectroscopy (EELS). For this purpose, we evaporated in similar conditions (in the same evaporator as used for device fabrication) a thin aluminium layer

of 1.7 nm nominal thickness over a CVD Gr transferred on a graphite or Cu TEM grids. We then oxidized the sample in the air at different duration before analysis (Fig.4.8). The analysis of the spatial distribution of Al and O elements within a single nanoparticle is presented in Fig.4.8.(a,b). They demonstrate a core-shell structure with a significant core part in a less oxidized state even after 1 day of ambient oxidation (Fig.4.8.(b)). These metallic Al and AlOx spacial distribution follow the schematic representation illustrated in Fig.4.8.(a). Recent detailed XPS analysis of a 2D arrays of oxidized Al NPs deposited over an insulating single crystal substrate also demonstrated similar core-shell structure [Maidecchi15]. From EELS

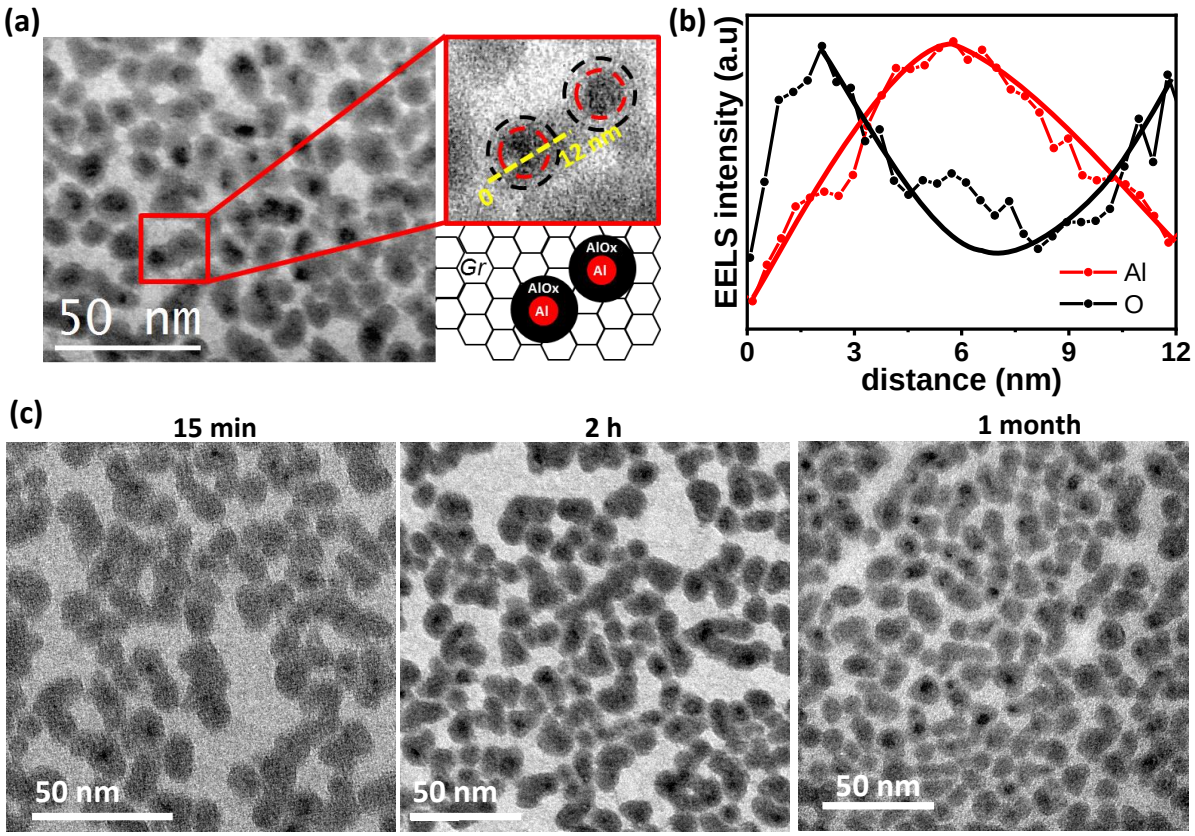

Figure 4.8 *– (a) TEM image of the 2D-0D heterostructure with 1.7 nm nominal thickness of aluminium deposited on CVD Gr transferred on a carbon TEM grid followed by 1 day oxidation in air. The red box shows STEM bright field image of nanoclusters presenting a core-shell structure as depicted in the bottom schematic. The yellow dot line indicates the line scan of the EELS analysis. (b) The corresponding EELS chemical composition profiles indicate the unoxidized Al core embedded in alumina shell. The Al profile (red curve) is more intense in the core contrary to the oxygen profile (black curve) which gets more intense in the shell. The solid lines are guide for the eyes. (c) The oxidation kinetics after 15 min, 2h and 1 month. The core-shell structure is complete after 15 min of oxidation.*

spectra (Fig.4.8.(b)), we can deduce an average metallic core diameter of approximately 5 nm for a core-shell cluster of 10 nm diameter, corresponding to a volume percentage of 12.5%. Moreover, STEM images indicate a ratio of about 20% of the nanoparticles demonstrating a core-shell structure. This corresponds to a proportion of 2.5% of the deposited aluminium being metallic, in agreement with the 2% of metallic signal of XPS spectra. Such a correspondence between STEM-EELS and the complementary XPS analysis demonstrates that the

XPS analysis also strongly support the core-shell structure observed by STEM and EELS. This argument indicate that the metallic core are indeed present exclusively on a fraction of the nanoparticles population.

4.3 Experimental SET-UP

Quantum phenomena involving energy scales in the order of few tens meV require low temperature to be resolved efficiently while reducing thermal noises. Furthermore, resolving a tens meV energy scale by electrical excitation (applying voltages) demands stable and sensitive low levels noise electrical measurement equipments with sub-mV bias precision and sub-pA current precision. This is all the most important when single electron processes are to be resolved in tunneling junction of nanoelectronic devices where the resistance can often reach TeraOhms [Yakushiji02, Yakushiji05, Seneor07]. For low-temperature electrical measurements, we dispose a closed cycle He-flow cryostat (Fig.4.9) consisting of two cryogenic liquid reservoirs with 1.5 K based temperature. The outer reservoir of liquid nitrogen maintains the temperature at 77 K and the inner liquid ^{4}He with 4.2 K basic temperature. Three vacuum insulations respectively decouple the cryostat first to the surrounding environment, then nitrogen vessel form the He reservoir and finally the He reservoir from the VTI so to avoid heat transfer by conduction. In addition, a shielding metallic film preventing the transmission of infrared radiation covers both cryogenic liquid reservoirs. The inner ^{4}He vessel is

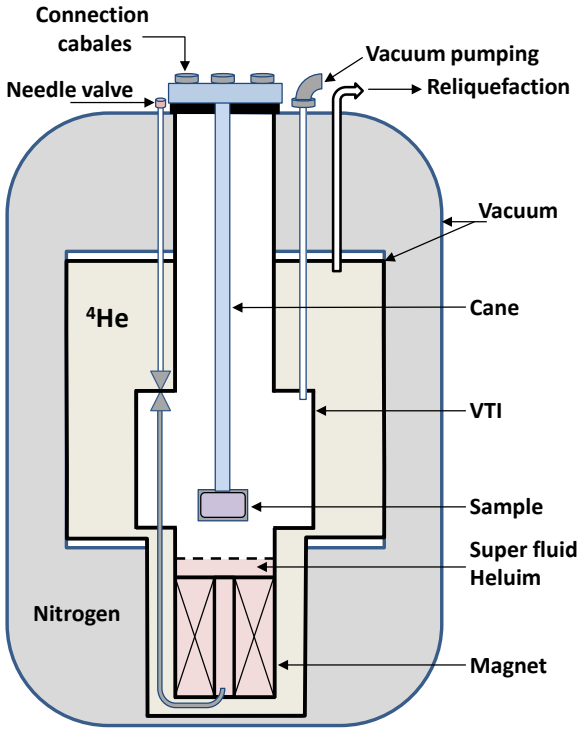

Figure 4.9 *– Schematic representation of our closed cycle He-flow cryostat. The needle valve enables to transfer the He from to the main bath to a smaller one situated within the VTI where a pumping system enables to achieve the 1.5 K base temperature. The superconductive coil enables accessing up to 7T vertical magnetic field.*

equipped with a variable temperature inserts (VTI) system transporting the ^{4}He liquid from the main inner bath to a small reservoir closer to the sample. Thank to pumping system, the normal liquid ^{4}He of the VTI reservoir undergoes a transition to super fluid ^{4}He phase accompanied by a further cooling close to 1.5 K which corresponds to the basic temperature of the cryostat. The Cryostat is equipped with a superconducting coil magnet located within the VTI super fluid ^{4}He container. This is to maintain the coil cooled even under 70 A (7 T) which is the maximum magnetic field of our system. The continuously pumped vacuum chamber included within the VTI system enables to accommodate within the cryostat the cane holding the sample and the electric cables connecting it to the electric equipments. For electric measurements we employ a high precision Keithley 2634b source meter with sub-pA precision and a K2182A nanovoltmeter coupled to Y7651 DC source. Many transport measurements were conducted during this thesis at Thales[2] in collaboration with Pr. Pierre Seneor, and in particular Dr. Florian Godel the former PhD of my group who have now joint Pr. Pierre Seneor's group. The measurement set-up there enables recording a dynamical conductance signal simultaneously with I-V characterization using a lock-in amplifier system. More importantly we could take benefit of low temperature rotative angle magnetic measurements of absolute importance for addressing anisotropic magnetic transport properties. It is to be notice that this possibility is now accessible in our group using a cane equipped with piezoelectric element enabling 180° sample rotation in both x and y direction.

4.4 Conclusion

In this chapter I have presented our experimental methods for sample fabrication and electrical characterization. I have detailed our simple and scalable approach for fabricating 2D-0D MD VdWh consisting of self-assembled Al-AlOx core-shell NPs deposited onto graphene or MoS_2. We have shown that the evaporation of a very thin Al film onto the surface of a 2D material results to self-assemble Al NPs which after oxidation adopt a core-shell structure with Al core embedded in AlOx shell. Interestingly, the deposited Al does not affect the physical properties of the underneath flakes. We have detailed the integration of these MD-VdWh into nanoelectronic devices using different nanofabrication steps including Ebeam lithography. We intentionally limited this chapter to the sample fabrication technic involving Ebeam lithography. Another aspect of this thesis have consisted to the study of magnetotransport properties of LSMO perovskite nanoparticles trapped into nanotranches. The fabrication methods of such nanotranches involves optical lithography together with shadow angle deposition technic. It will be presented in the last chapter addressing this aspect of the thesis.

[2]Unité Mixte de Physique, CNRS, Thales, Univ. Paris-Sud, Université Paris-Saclay, 91767 Palaiseau, France

Chapter 5

Graphene-Al 2D-0D heterostructures for single electron electronic

In the previous chapter we presented simple and scalable route for fabricating 2D-0D Al-AlOx/2D-material mixed dimensional VdWhs. We detailed the integration process of these heterostructures into Co/AlOx-Al-AlOx/2D-materials tunnel junctions. The 7 nm scale nanoparticles size with Al metallic embedded into insulating alumina shell provides a configuration suitable for single electron transport. In this chapter, we present the transport measurements of these devices limiting our investigations to those consisting of graphene. The transport properties of those consisting of MoS_2 will be presented in chap.8. We demonstrate that the conductance of our Al-AlOx/Graghene based 2D-0D MD-VdWh devices present unique and reproducible Coulomb oscillations which interestingly remain preserved on 100 μm^2 large scale junctions and at high T. The Coulomb levels of the supported nanoparticles are efficiently tunable by a back electric field gate trough the underneath graphene resulting to a gate dependent oscillation of the conductance. The conductance spectroscopy reveals discernable Coulomb diamond patterns characteristic of SETs

5.1 Low temperature single-electron transport

The electronic transport properties were investigated on two complementary geometries referred to as 'planar' and 'vertical' devices made respectively from Gr exfoliated on p^+-Si-SiO_2 substrate (Fig.5.1.(a)) or multilayer CVD Gr grown over Ni (Fig.5.1.(b)). We sketch on Fig.5.1(b,c) the carriers path in both device geometries. In the case of exfoliated Gr on p^+Si-SiO_2, the charge carriers are vertically injected from the Co top electrode to the Al metallic core of the NPs through alumina barrier. Then, from the Al metallic core to the underneath

Gr into which they laterally propagate to be collected by the Au reference electrodes patterned at the side of the Gr sheet (Fig.5.1.(a,c)). In vertical devices with CVD Gr grown over Ni, carriers are similarly transferred from the Co top electrode to the central Al core of NPs through the alumina barrier, then to the underneath CVD Gr before to be vertically collected into the Ni substrate (Fig.5.1.(d)). The vertical geometry allows large scale device processing

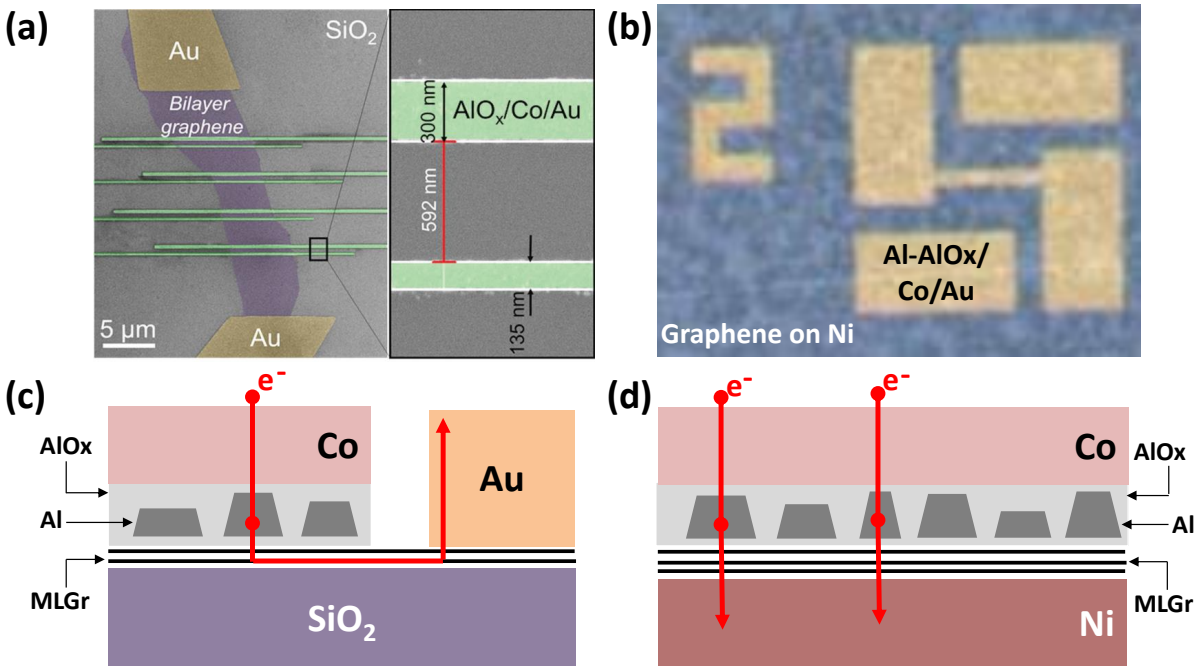

Figure 5.1 *– (a) Electron beam microscopy image of a planar device with exfoliated graphene on insulating substrate (left) with detailed zoom on the electrodes (right). (b) Optical micrograph of a typical vertical geometry of the device with CVD graphene on Ni. Schematics representation of the tunnel junctions in planar (c) and vertical (d) configurations together with the sketch of the carriers path.*

compatible with vertical integration scheme for low power memory applications whereas the planar architecture offers additional add values such as the possibility to modulate the electric state of the NPs trough the Gr layer with a vertical electric field applied to the p^+Si-SiO_2 back gate electrode substrate. It offers important prospect for single-electron logic devices (SET) (see section.5.3.

5.1.1 Experiential measurements of single electron devices

We present in Fig.5.2.(a,b) the typical Current ***v.s.*** source-drain voltage (I-Vsd) characteristics (black curve, left axis) together with the corresponding differential conductances (dI/dVsd-Vsd) (red curve, right axis) measured at low temperature (1.5 K) on both planar (Fig.5.2.(a)) and vertical(Fig.5.2.(b)) devices. We observe a central Coulomb-gap in the vicinity of zero DC bias where the source-drain current as well as the differential conductance drop almost to zero. This central conductance gap is consistent with the prevention of electron to tunnel through the central metallic core of the NPs by the charging energy E_C at low Vsd (Fig.5.2.(c)). Remarkably, as the DC bias is incremented, a first (Fig.5.2.(d)), second (Fig.5.2.(e)) and more tunneling threshold are reached and the I-Vsd characteristics of both devices present well-

defined Coulomb staircases. This is reminiscent of the single and few electrons current flowing through the devices and controlled by the charging energy of the central metallic core of the NPs in agrement with the orthodox theory of CB detailed in section.3.5. The corresponding differential conductance curves reveal well defined narrow Coulomb oscillations. Each peak represents a threshold from n to $n+1$ electrons currents flowing trough the device. Interestingly, the periodicity of the oscillations is found to be quite similar in both devices geometries and comprised between 65 – 70 mV.

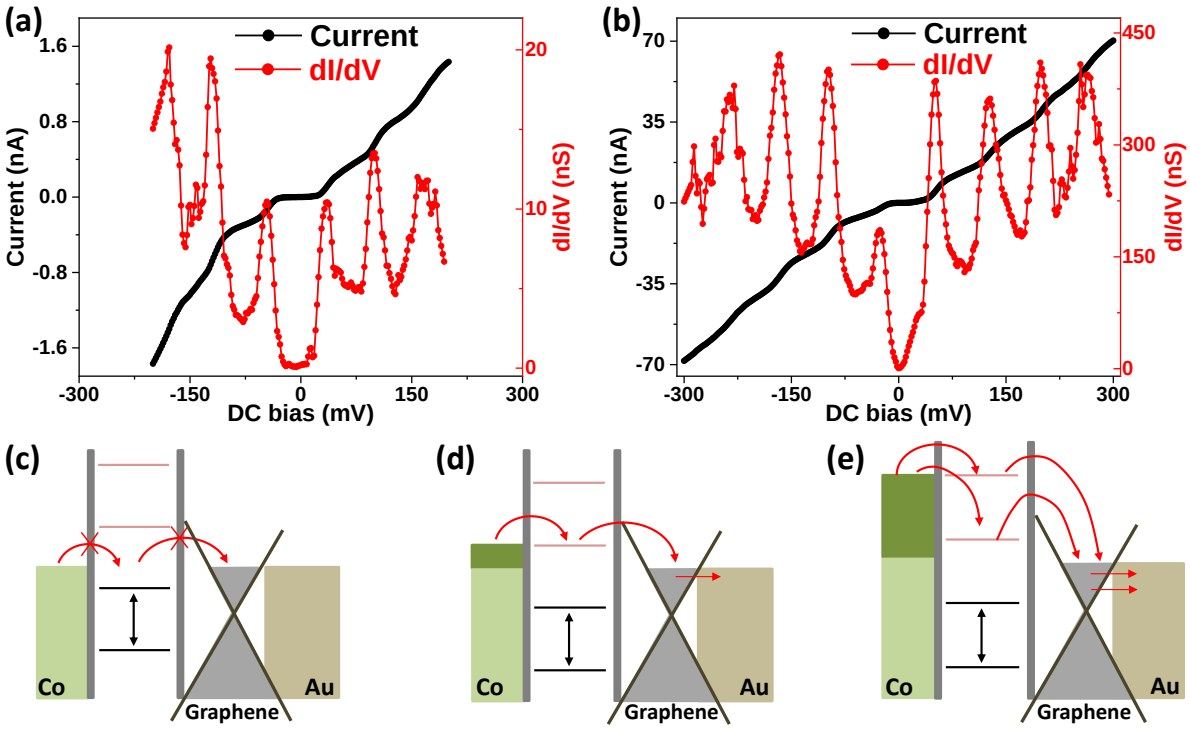

Figure 5.2 *– I-Vsd characteristics (black) and the corresponding dI/dV-Vsd curves (red) measured at 1.5 K on a 1 μm^2 tunnel junctions of the planar (a) and vertical device geometry (b). In both cases, clear Coulomb staircases and Coulomb oscillations are observed in I-Vsd characteristics and differential conductance respectively. Band structure of the device highlighting the blockade state (c) and the successive tunneling thresholds occurring any time the chemical potential of the source aligns with one Coulomb blockade level (d,e). The dark olive green region on the Co side shows the displacement of its Fermi energy by the dc bias (we refer to as the dc bias window).*

Similar low temperature Coulomb blockade induced single electron processes have been reported on devices consisting of a single metallic nanoparticles requiring advanced nanofabrication processes such as nanoindentation [Seneor07, Bernand-Mantel09, Bernand-Mantel11], electromigration break junction [Bolotin04] and alumina [Ralph95] and combined Ebeam lithography with reactive-ion etching [Ralph95]. The sharp and well defined Coulomb staircases and Conductance oscillations observed in such devices is inherent to the presence of a single NPs in the conduction channel. Our simple fabrication process results to junction sizes exceeding 1 μm^2 integrating thousand of Al NPs contacted by the underneath Gr template and all susceptible to participate to the transport due to the mixed dimensional configuration. Therefore, the sharp and well defined Coulomb staircases and Conductance oscillations (Fig.5.2) suggest a selection process of preferential conduction path

as will be discussed in section.5.1.3.

5.1.2 Simulation and devices parameters estimation

In order to access quantitative estimation of the electrical parameters governing the single electron transport processes, we carried out numerical simulations of the I-Vsd and dI/dVsd characteristics of our devices using the orthodox theory model (detailed in section3.5). The Fig.5.4.(a) presents the equivalent electrical circuit of the devices considered in the computation. The model contains five adjustable parameters : The resistances R_i and capacitances C_i of each tunnel junction (i=1, 2) and the background charge Q_0. As shown in Fig.5.3, this simple model reproduces fairly well the experimental data. In particular, the occurrence of the central Coulomb gap and the positions of the conductance peaks. The parameters extracted from the modeling are respectively R_1 = 130 MΩ, C_1 = 2.6 aF, R_2 = 74 MΩ, C_2 = 0.4 aF and Q_0 = -0.05e for the planar device and R_1 = 5.2 MΩ, C_1 = 2.35 aF, R_2 = 1.9 MΩ, C_2 = 0.4 aF and Q_0 = 0.2e for the vertical device. From the capacitances, the charging energy $E_c = \frac{e^2}{2(C_1+C_2)}$ of single Al core nanoparticle is deduced to be 26.7 meV and 29.2 meV for vertical and planar respectively.

Assuming a cylindrical disc shape for the NPs, the diameter of the contributing cluster can be deduced using a simple cylindrical capacitor model as $d = \sqrt{(4tC_1)/(\pi\epsilon_0\varepsilon_{AlOx})}$. t is the average Al-oxide shell thickness above the cluster and demonstrated by the STEM-EELS analysis to be 1-1.5 nm (section.4.2). ε_0 is the vacuum permittivity and ε_{AlOx} the dielectric constant of aluminum oxide taken equal to 9. We obtain a core diameter of the contributing cluster close to 5-6 nm for both vertical and planar devices, which is in agreement with the STEM-EELS analysis (see chap.4). The electric parameters extracted from the simulations (Fig.5.3) provide additional indications on the bottom tunnel barrier between Gr and the nanocluster (referred to as 2 in Fig.5.4.(a)). The values of the resistances R_2 although all smaller than that of R_1, remain non negligible relatively to it. This is consistent with the presence of a very thin alumina layer sandwiched by the metallic core cluster and the underneath Gr playing the role of a tunnel barrier. In good agrement which with XPS analysis (see section.4.2.2). The robust single-electron processes in our Gr based 2D-0D mixed dimensional SED and the rather good agrement with the simple orthodox theory model based on a single nanoparticle, can only be understood considering a transport processes relying on a selection of preferential conductive channels. It worths noticing that the junctions concerned by the experimental data presented in Fig.5.3 are $1\mu m^2$ large corresponding to approximately 10^4 NPs involved.

The robust single-electron transport with sharp staircases and conductance oscillations presented in Fig.5.2 and Fig.5.3 clearly point to the single electron tunneling processes through a single Al cluster. Indeed, assuming that all the clusters of the $1\mu m^2$ large junction contribute to the transport, given the 20% gaussian size distribution, it is expected to have as many possible set of threshold energies for singe electron tunneling as there are conductive channels. The positions of such single electron thresholds are likely randomly distributed, consequently of the NPs size distribution. The total current of the junction being the

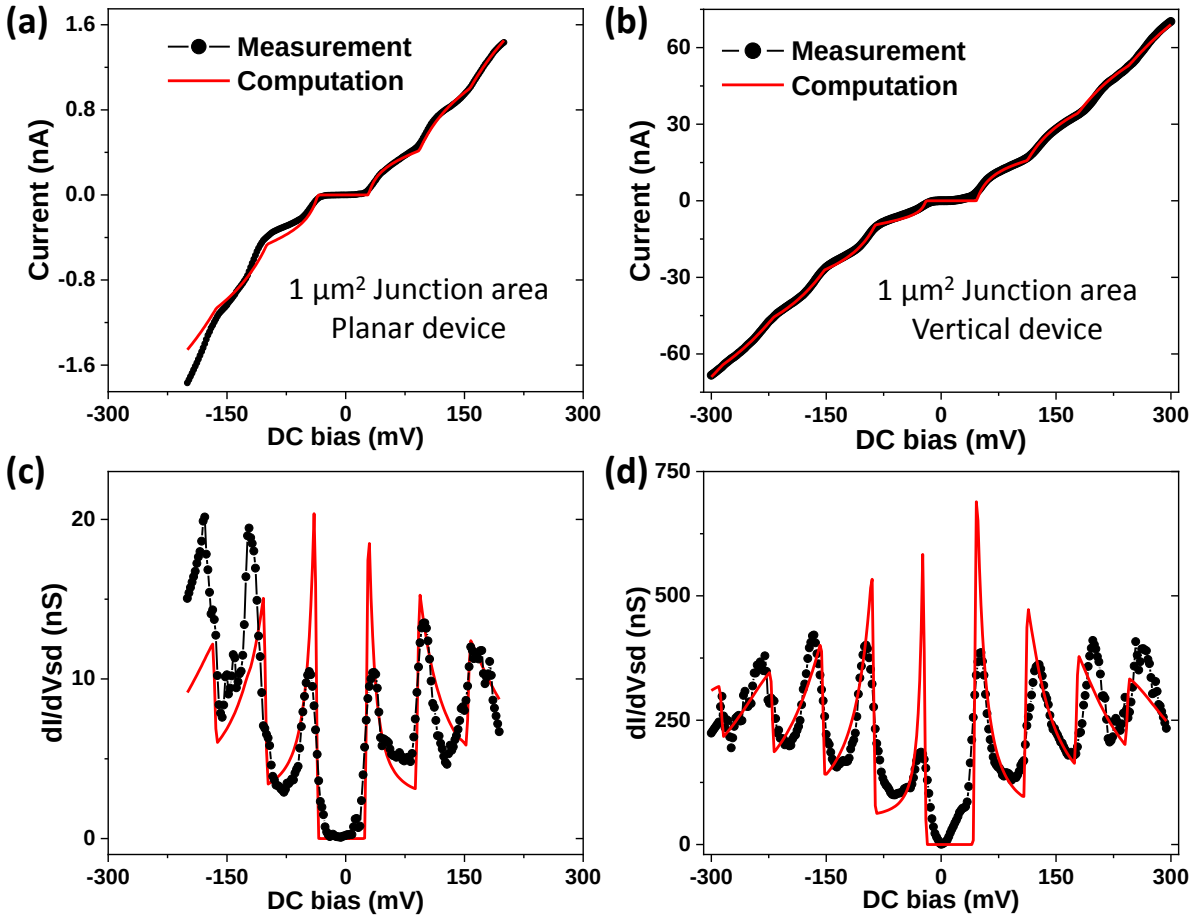

Figure 5.3 *– Comparison between experimental (black) and simulated (red) data. (a, b) Experimental and simulated I-Vsd curves of planar and vertical device geometries respectively. (c, d) Experimental and simulated differential conductances of planar and vertical devices respectively. Numerical simulations (red curves without symbols) based on the orthodox theory of CB considering the equivalent electrical circuit presented on Fig.5.4. The best modeling parameters are $R_1 = 130\ M\Omega$, $C_1 = 2.6\ aF$, $R_2 = 74\ M\Omega$, $C_2 = 0.4\ aF$ and $Q_0 = -0.05e$ for the planar device and $R_1 = 5.2\ M\Omega$, $C_1 = 2.35\ aF$, $R_2 = 1.9\ M\Omega$, $C_2 = 0.4\ aF$ and $Q_0 = 0.2e$ for the vertical device.*

integral of all contributing channels, the single electron features are expected not to be preserved. On the baseline of the electrical parameters extracted from the I-Vsd characteristics presented in Fig.5.3.(d), we have assumed many contributing clusters (100 clusters in total) to the transport and computed the conductance considering the size distribution (Fig.5.4.(c)). We observed that CB oscillations sharpness dramatically vanishes in the simulated conductance (Fig.5.4.(c)) and only the zero-bias gap remains. Importantly, even a smaller distribution of size of 5% is enough to considerably smear out the CB oscillations. This supports the conclusion that a single cluster does contribute to the conductance. Therefore the robust single-electron transport with sharp staircases and conductance oscillations are ineluctably the consequence of a statistical selection process of preferential conductive channels. This question the number of Al core clusters effectively contributing to the current in our devices.

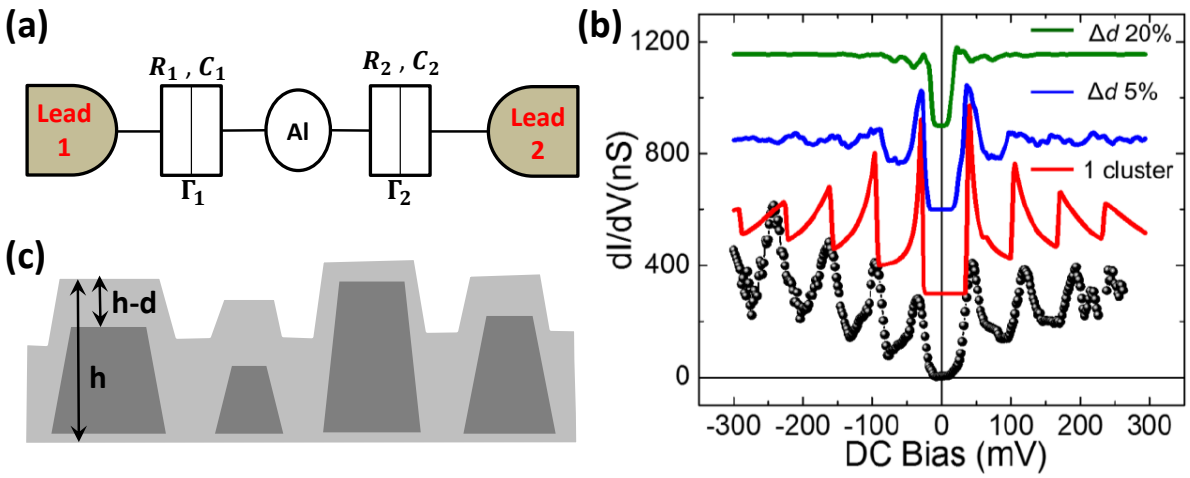

Figure 5.4 *– (a) Equivalent electrical circuit considered for the simulation. (b) Schematic representation of the granular aluminum layer. (c) dI/dV(V) recorded at 1.5 K on vertical junction (black dots) compared with different simulated data. The comparative curves suppose one contributing cluster with a diameter d = 5.6 nm (red curve) and a distribution of contributing clusters which diameters taken from a Gaussian distribution centered on 5.6 nm. The standard deviation considered are respectively Δd of 5% (blue curve), 20% (green curve). The simulated curves are shifted for the sake of clarity.*

5.1.3 Selection process of preferential conductive paths

A previous work [Costa00] provided experimental evidence that in metal-oxide-metal tunnel junction, a tiny fluctuation of the oxide tunnel barrier width (due for example to roughness) has a dramatic consequence on the statistical properties of the tunneling conductance. The total tunnel transmission current was demonstrated to be dominated by few highly transmitting channels. Furthermore, Yakimov et al [Yakimov94] reported a selection process of preferential conductance channels in single electron devices consisting of SiGe/Si heterostructures containing a sandwiched granular layer of doped Ge NPs. These selection processes based on statistical arguments detailed by Yakimov et al. reasonably applies to our devices [Yakimov94]. Indeed, because of volume conservation of the total Al deposited, the fluctuation of the lateral NPs size automatically implies a fluctuation of their height. Hence, similarly to their lateral size (section.4.2), we assume a gaussian dispersion of the height the Al-AlOx NPs (Fig.5.4.(c)). h denotes the height of a single NPs and H the average height of all the NPs. In this condition, the tunneling width w (the width of the top alumina barrier) is defined as $w = h - d$, with d representing the high of a metallic core of a given particle together with the bottom tunnel barrier (Fig.5.4.(c)). Therefore, since the tunnel current is proportional to $exp[-kw\sqrt{E_a}]$ (see section.3.2.2), its average over the NPs size distribution is given by Eq.5.1.

$$I \sim \int_0^\infty g(h)exp[-k(h-d)\sqrt{E_a}]dh \quad with \quad g(h) = \frac{1}{\sqrt{2\pi}\sigma H} exp[-\frac{(h-H)^2}{2(\sigma H)^2}] \tag{5.1}$$

Where $g(h)$ is the gaussian distribution function of the NPs high. The function $g(h)exp[-k(h-d)]\sqrt{E_a}$ involved in the integral 5.1 is a peak gaussian like function reaching its maximin at

$h_m = H - k(\sigma H)^2$, with a width $\delta = 2(\sigma H)$ at half maximin. The main contribution to the conductance originates thus from the channels containing NPs which the dimensions fulfil the condition of h_m. Hence, from the NPs size distribution $g(h)$ one deduces the optimal number N of the clusters contributing to the conductance, for a junction of area S and NPs density per unit area n the number of contributing NPs given Eq.10.1.

$$N = Sng(h_m)\delta = nS\sqrt{\frac{2}{\pi}}exp[-\frac{(\frac{\sqrt{8mV_0}\sigma H}{\hbar})^2}{2}] \tag{5.2}$$

$S = 1\mu m^2$ and the aluminum barrier height $V_0 = 1.6\ eV$ [Costina01]. The effective electron mass in alumina tunnel barrier is $m^* = 0.28m$ [Huang06] and σ =20% is the standard deviation of the distribution. The average NPs hight H can be deduced from volume conservation. Indeed, for a deposited Al layer with nominal thickness t, considering a cylindrical disk shape for the NPs, we obtain $H = 4t/(n\pi D^2)$, where $D = 7nm$ is the average lateral size of the NPs (section.4.2). The density of NPs is estimated from STEM images to be $n = 12300\mu m^{-2}$. It results an average height $H = 3.6\ nm$. Finally, we obtain an optimal number of Al clusters effectively contributing to the SED conductivity of $N \sim 0.05$. Considering the standard deviation σ =20%, the number of contributing clusters ranges from $N = 10^{-4}$ for $H = 4.3nm$ up to $N = 4$ for $H = 2.9nm$. We conclude from this calculation that only a single to few Al nanoparticles are expected to effectively contribute to the tunnel conductivity in our Gr based 2D-0D VdWh SED. This is consistent with the observation of single electron transport processes fitting a one particle orthodox theory model.

5.1.4 CB oscillations in large area junctions

We have also studied larger tunnel junction devices with surface area of 100 μm^2. Remarkably, we still observe well-defined Coulomb gap together with clear Coulomb staircases in the I-Vsd curves and conductance oscillations (Fig.5.5). The Coulomb staircases were although less pronounced in I-Vsd curves compared to that of the $1\mu m^2$ junctions, due to important contribution of direct tunneling (leakage) between the electrodes (Co and Gr) in this large area junctions. Coulomb staircases smoothed by direct tunneling is often observed in SED even with smaller junction area patterned by advanced nanofabrication technics as nanoindentation [Bernand-Mantel08a, Bernand-Mantel09]. The sharpness of the Coulomb staircases can be restored by simple substraction of such a direct tunneling contribution to the current [Bernand-Mantel08a, Bernand-Mantel09]. On the I-Vsd curves presented in Fig.5.5, we have subtracted such contributions.

Interestingly, for devices of the same composition (different junction on the same cheap), the resistance·area (RS) products of different junctions are observed to be comparable. For the four junctions reported in Fig.5.5.(a,b), the RS values are respectively 3.5, 4.1, 4.2, and 4.9 M$\Omega\mu m^2$ at 300 K under 100 mV applied bias. In this large area junctions, we expect several NPs to contribute in parallel to the observed current. Nevertheless, the periodicity of the conductance oscillation indicates that only selected ones with very similar characteris-

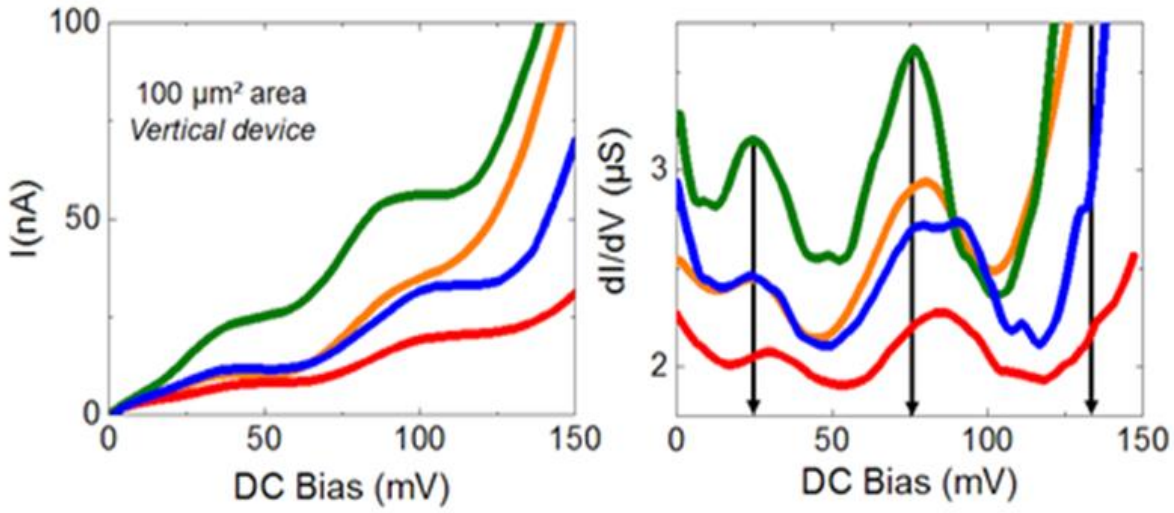

Figure 5.5 – *Large area junction transport behavior. I-Vsd and dI/dV curves obtained on four distinct vertical devices with* $100\mu m^2$ *junction area (left and right respectively). The black arrows underline the comparable periods of the conductance oscillations for the four distinct devices. A linear contribution to the current attributed to direct tunneling between the electrodes has been subtracted in to the IVsd curves.*

tics probably participate to the transport. Should this not be the case, Coulomb steps would be totally smeared out (as discussed in the previous section) and good reproducibility of the Coulomb oscillations observed on Fig.5.5.(b) could not be achieved. Such well-defined and reproducible single electron transport properties are often very difficult to obtain in so large area junctions. So far, sharp and clear single electron transport could only be observed in the case where transport occurred through a single nano-object as mentioned before either trapper between two electrodes [Bolotin04] or contained into tunnel junction with area reduced to 10^2-10^4nm^2 [Ralph95, Matsumoto96, Shimada98, Ootuka01, Bernand-Mantel09], that is up to six orders of magnitude smaller than our largest junctions.

5.1.5 Sharp CB oscillations : additional added value of graphene

The remarkable sharpness of the Coulomb staircases observed in our 2D-0D heterojunctions (Fig.5.5) are also exacerbated by the fact that the parameters (resistance, capacitance) of the each junction are both lager than their homologous of the other junction ($R_1 > R_2$ and $C_1 > C_2$, or, $R_1 < R_2$ and $C_1 < C_2$ respectively). Such an ideal configuration is usually difficult to realize in nanosdevices [Seneor07] as the capacitance and resistance of a tunnel junctions have opposite dependence with the tunnel barrier thickness. Hence the configuration $R_1 > R_2$ and $C_1 < C_2$, or, $R_1 < R_2$ and $C_1 > C_2$ is usually obtained. In our 2D-0D devices, assuming the bottom alumina layer (thinner than the top tunnel barrier) is responsible for the bottom tunnel barrier, we would have expected a less favorable condition with $R_1 > R_2$ but $C_1 < C_2$ contrarily to what we observed on the data in Fig.5.5. This points out an additional added value of the underneath Gr in theses devices. Probably, the mismatch of the wave vectors of the Fermi electrons of aluminum and Gr induces an additional resistance (tunnel barrier) at the bottom Al/graphene interface [Karpan07, Karpan08, Dlubak12]. This, together with

a second similar Graphene/Ni barrier in the case of vertical devices likely promote the ideal configuration with simultaneously $R_1 > R_2$ and $C_1 > C_2$.

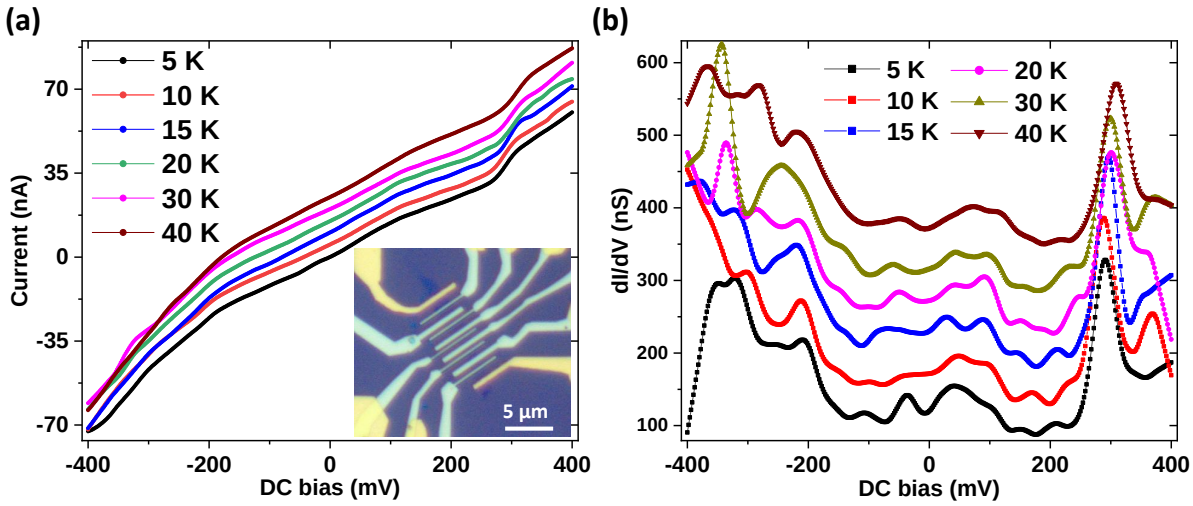

Figure 5.6 *– Temperature dependent transport measurements up to 40 K. (a) I-Vsd characteristics present Coulomb staircases in the whole temperature range. Consequently, the differential conductances with Coulomb oscillations up to 40 K. The data were vertical shifted to facilitate the reading. The inset in (a) is the optical micrograph of the device.*

5.2 Temperature dependent transport measurement

From the analysis of the low temperature data (1.5 K) we obtained the charging energy values of $E_C \gtrsim 26$ meV (Fig.5.3), all larger than the thermal energy at room temperature $K_BT = 25.8$ meV. This augurs the preservation of Coulomb oscillation at high temperature. In Fig.5.6, we present the I-Vsd and dI/dVsd curves measured on a different sample at different temperatures up to 40 K. Interestingly, Coulomb oscillations are preserved on the whole temperature range. The minimum gap between consecutive conductance oscillation peaks is about $\Delta V \approx 60$ meV. Assuming $\Delta V = e/C_\Sigma$, the corresponding minimum charging energy $E_c = e^2/2C_\Sigma = 30$ meV, a value $\sim 8.5 K_BT_{40K}$ (where K_BT_{40K} denotes the thermal energy at 40 K) and consistent with the preservation of Coulomb blockade at 40 K.

5.2.1 Toward room temperature CB in 2D-0D MD-WdVh based SED

In Fig.5.7 we present the temperature dependence of both I-Vsd characteristics and differential conductance up to room T on the same junction as in Fig.5.6.(a & b) and another (Fig.5.7.(c & d)) on the same chip. Remarkably, we observe the preservation of conductance oscillations up to room T. At 1.5 K, the gap $e\Delta V$ of two consecutive conductance peaks varies between 60-140 meV for both junctions indicating a charging energy comprised between $1.16K_BT_{300K} \precsim E_C \precsim 2.70K_BT_{300K}$. Bernand-Mantel et al. [Bernand-Mantel08a] observed a preservation of Coulomb oscillations in SED consisting on single metallic up to $E_C \approx 4K_BT$. We observed from Fig.5.7.(b,d) that the consecutive oscillations with smallest gap which are also the less sharp disappear faster with increasing T while the sharper oscillations with larger

gap persist up to high temperature. We can conclude therefore that the conductance channels integrating such pronounced peaks are the mains contributing to the transport while the minor peaks originate from parallel channels with probably smaller E_C.

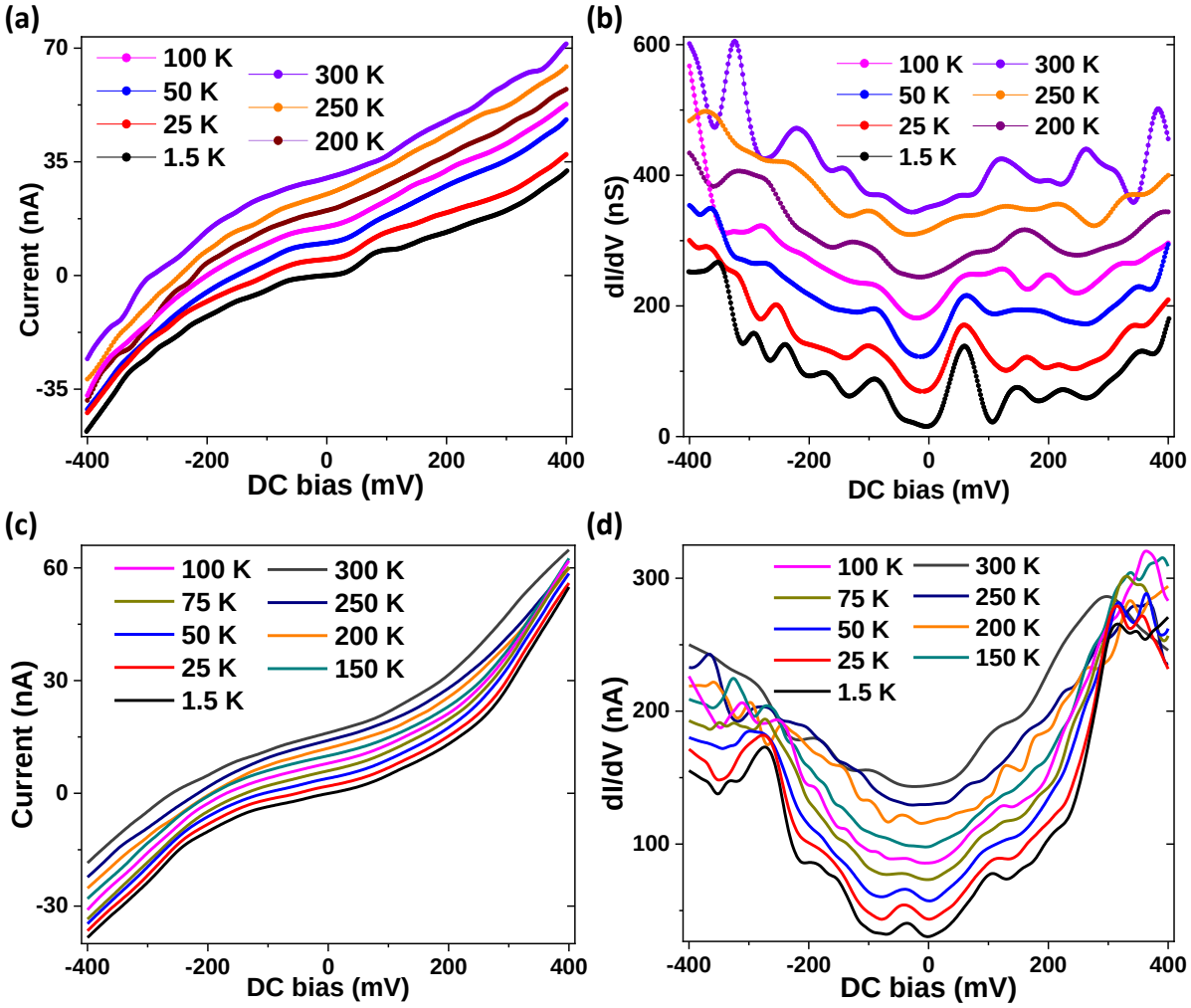

Figure 5.7 *– Temperature dependent measurements demonstrating room T Coulomb staircases in I-Vsd characteristics and Coulomb oscillation in the differential conductance. The data were recorded on two different junctions on the same chips (a,b) The same junction as in Fig.5.6. (c,d) A different junctions. The data were vertical shifted to facilitate the reading.*

Note that, the conductance in the Coulomb gap systematically increases with the temperature as seem from the slope of the I-Vsd curves (Fig.5.7). This corresponds to thermal excitation induced leakage quite common in quantum devices. Often, the peaks of conductances are not positioned at the same threshold voltages at different T. This might be related to the value of the environmental charge Q_0 being modified by the redistribution of the charges in trapped states located in the alumina tunnel barriers as the temperature is incremented between two consecutive values. Although such room T Coulomb oscillations was not reported in all the samples[1], their observations in more than three devices (on three deferent chips) demonstrates the prospect of Al-AlOx/Graphene 2D-0D MD-VdWh for high T SED

[1] It is relevant to precise that we did not systematically study high T CB oscillations in all the sample measured

applications.

5.2.2 Telegraphic noise as signature of CB at high Temperature ?

We recurrently observed at high temperature the appearance of random noise in I-Vsd characteristics. Although the specific study of such noise goes out of the scope of this thesis, their qualitative characteristics suggest a random telegraph noise also known as impulse noise. The Fig.5.8 presents two I-Vsd characteristics measured on two different samples at room temperature. Both curves present sudden step like transitions between two current levels. The difference between the two current levels increases with the applied voltage and the voltage values at which the noise steps jump occur are completely random. Telegraphic noise

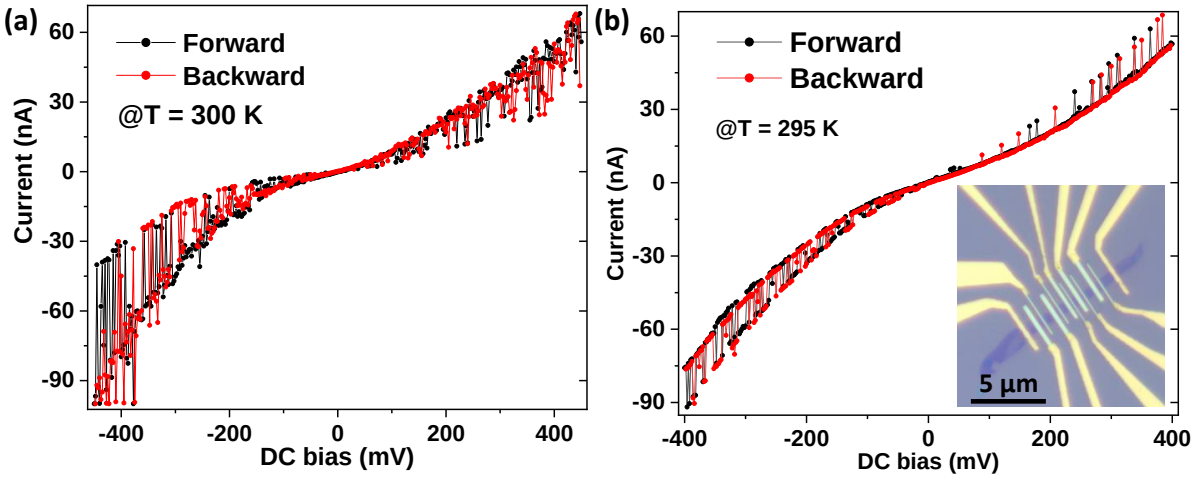

Figure 5.8 *– Room temperature measurement demonstrating random noise. (a) Data measured a different days (after many ramps in temperature) on the same junction as the data on Fig.5.6 and Fig.5.7.(a,b). (b) Data measured on a new sample presenting as well Coulomb oscillations including at high T. The insert is the optical micrograph of the sample.*

is often observed in CMOS with similar qualitative characteristics resulting from random trapping and release of single electron by specific trapping states in the semiconductor components [Kastner87]. In our SED it may be resulting from thermal energy which at high T is sufficiently important to compete with E_C. Indeed, the range of the charging energy values ($1.16K_BT_{300K} \precsim E_C \precsim 2.70K_BT_{300K}$) suggests that as high T, it is comparable to the thermal energy in the less favorable case ($E_C = 1.16K_BT_{300K}$). Thus, certain number of carriers may be thermally exited trough out the Co-AlOx-Al-AlOx-graphene junction resulting to the observed telegraphic noise in the room temperature I-Vsd characteristics (Fig.5.8). Therefore, the presence of room T telegraphic noise is a further demonstration of the preservation of Coulomb blockage at room T in our Al-AlOx/Graphene MD-VdWh based SED. Indeed, the noise reported here was observed to sometimes completely disappears. During this times, we could probe the transport characteristics of the sample.

5.3 Electric gate control of the single electron processes

Prior to analyze the back gate electric field modulation of single charge tunneling processes trough the NPs, it is relevant to first characterize the electric transport properties of the Gr template. The configuration of our devices always integrate Ti/Au electrodes in direct contact with the Gr flake which, in addition to serve as reference electrodes for realizing the electrical configuration including only one junction containing Al-AlOx NPs, also enables to probe the electric transport properties of Gr.

5.3.1 Electric characterization of the graphene channel

In Fig.5.9, we present the two terminals transconductance of a monolayer Gr for a typical sample together with the corresponding I-Vsd characteristics measured at 1.5 K using the Ti/Au electrodes patterned at the extremities of the flakes. The inset of Fig.5.9.(b) presents the optical micrograph of the concerned sample. The linear behavior of the I-Vsd curve is not

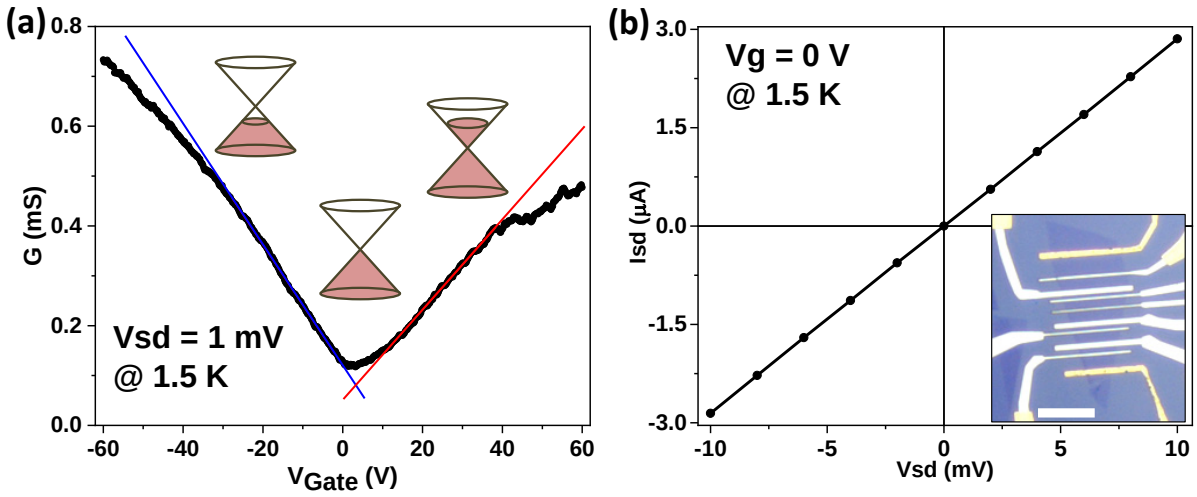

Figure 5.9 *– Low temperature transport properties of graphene. (a) The conductance dependence with the gate voltage. The red and blue lines are the linear fit demonstrating that at high gate voltage regime the conductance undergoes sublinear behavior. The inset schematics illustrate the occupation of the energy band diagram of the monolayer graphene by electrons ($Vg > 0$), holes ($Vg < 0$) and neutrality ($Vg = 0$). (b) I-Vsd characteristic of a Au/Ti-Graphene-Ti/Au FET demonstrating an Ohmic behavior. The insert in the optical micrograph of the sample.*

surprising and simply demonstrates the Ohmic character of the Ti-Au/Gr contacts reminiscent of the semimetallic nature of Gr. It represents a further indication that the CB induced single electron processes described in the previous section originated exclusively from the junctions containing the Al-AlOx core-shell NPs and not anywhere else in the device. Interestingly, the transconductance of the monolayer Gr presents all the properties described in section.3.1.2 for the state of the art samples. Indeed, we observe a linear behavior of the conductivity at lower carrier density. The red an blue lines in Fig.5.9.(a) are the linear fits to the data in the lower Vg ranges. Given the effective channel length of the sample superior to 10 μm, the linearity of the Gr transconductance in lower carrier density regime is

likely attributed to diffusive rather than ballistic transport. This is reminiscence of the presence of local gate potential fluctuations in SiO_2 dielectric of the substrate i.e. the randomly distributed Coulomb impurities identified as the main scattering source of carriers at low density (see details in section.3.1.2).

It is relevant to observe that this gate potential fluctuation in the substrate together with the presence of multiple leads containing granular Al layers bypassing the Gr channel (see optical image Fig.5.9.(b)) do not induce any fluctuation (aperiodic oscillations) of the Gr conductance at low temperature (Fig.5.9.(a)). The Gr conductance also presents more and more pronounced sublinear behavior [Das Sarma11] at high carrier density. This is due to charged impurities scatting sources being progressively screened making short range scattering becoming dominating and thus limiting the mobility of carriers (Fig.5.9.(a)) (section.3.1.2). The Dirac neutrality point is found to be very close to zero gate voltage, which is an indication of no substantial doping of Gr during the processing of the sample. These observations are in agreement with Raman characterizations which demonstrated that the deposition of the thin Al layer and its oxidation do not induce extra doping and more generally do not affect the physical properties of the underneath Gr (section.4.2.1).

5.3.2 Gate induced conductance oscillation in Al-AlOx/Gr based SET

The electric characteristics of the Gr channel presented above serve as a baseline to identify without ambiguity the electric gate response of an heterojunction containing the Al-AlOx NPs. In order to do so, we measured on the same device (see the inserted optical image in Fig.5.9.(b)) the dependence of the source-drain current with the back gate voltage using the same configuration as for the data presented in sections.(5.2 &5.1), that is including only one Co/AlOx-Al-AlOx/Graphene junction (Fig.5.10.(a)). In Fig.5.10, we present the Isd (Vg) curve observed at 1.5 K with Vsd = 5 mV applied dc bias. Obviously, it has no similarity with the transconductance of Gr (Fig.5.9.(a)), which is a clear evidence that the observed behavior is specific to the Co/AlOx-Al-AlOx/Graphene junction. More importantly, one observes an oscillating behavior of the curve in the whole range of Vg. The I-Vsd characteristics and the differential conductance (Fig.5.10.(b)) measured on the concerned junction respectively present Coulomb staircases an conductance oscillations. Therefore, we attribute the gate dependent oscillation of the current to the Coulomb blockade effect.

The Gate dependent current oscillation in our Al-AlOx/graphene 2D-0D VdWh devices can be understood by considering that the applied Vg does not only modulate the band occupation of Gr. In addition, it also tunes the electric state of the metallic core of the NPs standing on the Gr surface. Thus, incrementing the gate voltage linearly shifts the electrostatic potential of the NPs following the expression $\Delta\mu = e\alpha_G \Delta V_g$[2] and consequently their discrete Coulomb levels (Fig.5.10.(f)). Any time a discrete CB state enters the dc-bias window

[2]This assumes a constant gate capacitance contained in the definition of α_G. Logical since we showed in chap.3 that the quantum capacitance due to the modulation of the chemical potential of the underneath Gr is negligible compare to the Si-SiO_2 gate capacitance.

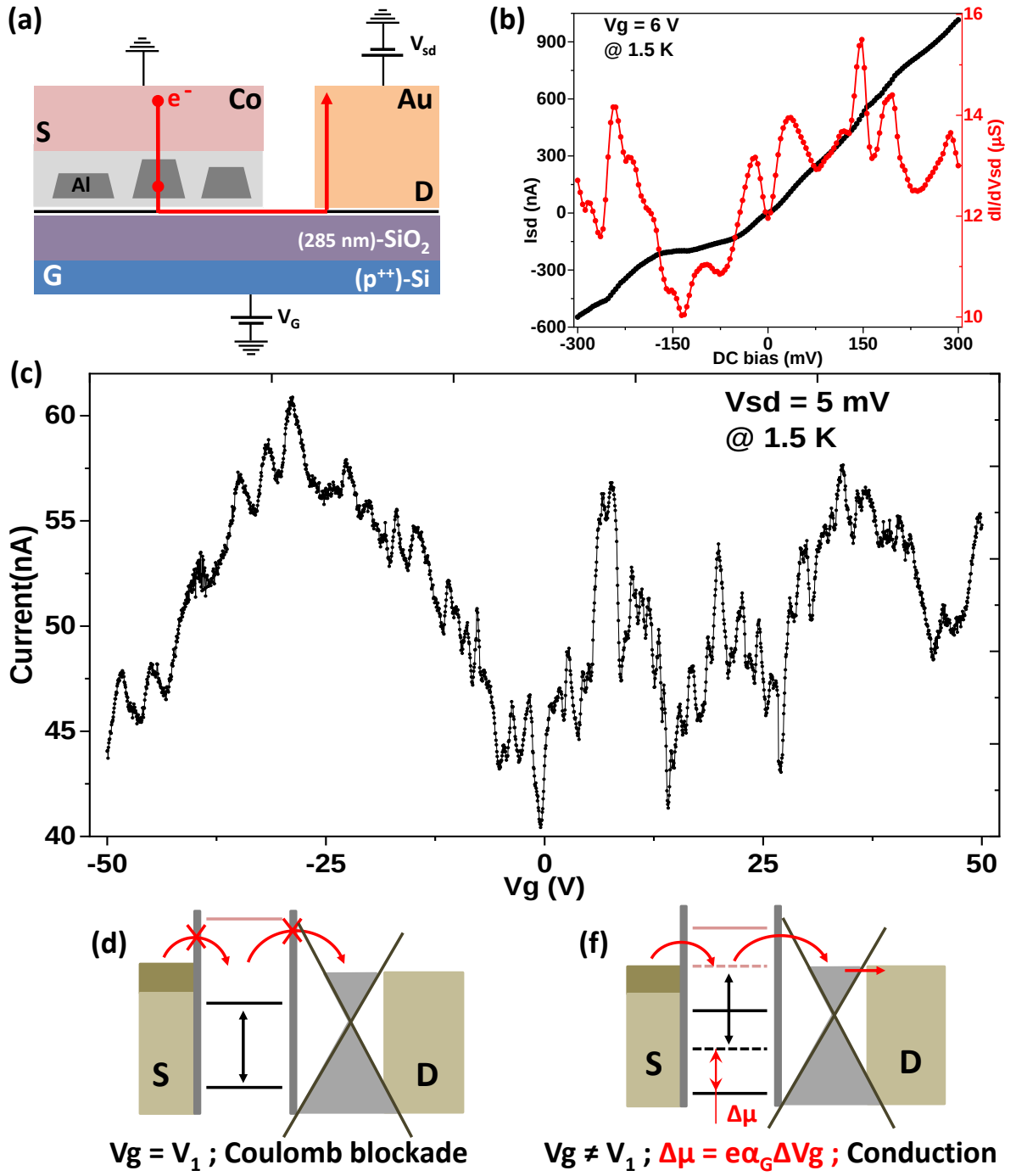

Figure 5.10 *– Low temperature (1.5 K) electric gate response of Al-AlOx/Gr based SET with schematic representation shown in (a). (b) Coulomb staircases of I-Vsd (subtracted direct tunneling contribution) and Coulomb oscillation of dI/dVsd (right curve). (c) I(Vg) curve demonstrating a logic Vg dependent oscillations. The schematic of the device band diagram of the device demonstrating alternative (d) miss-alignments and alignment (e) of the Coulomb levels with the Fermi levels of the leads. The oscillations are superimposed to global envelop resulting from direct tunneling contribution.*

$|eVs|$ defined by the source-drain potential difference, a single electron current flows trough the device resulting to an 'on state' ((Fig.5.10.(d)) right). In the contrary, when no CB state is located in such a window shifted out by Vg, no current flows. The device is in the 'off

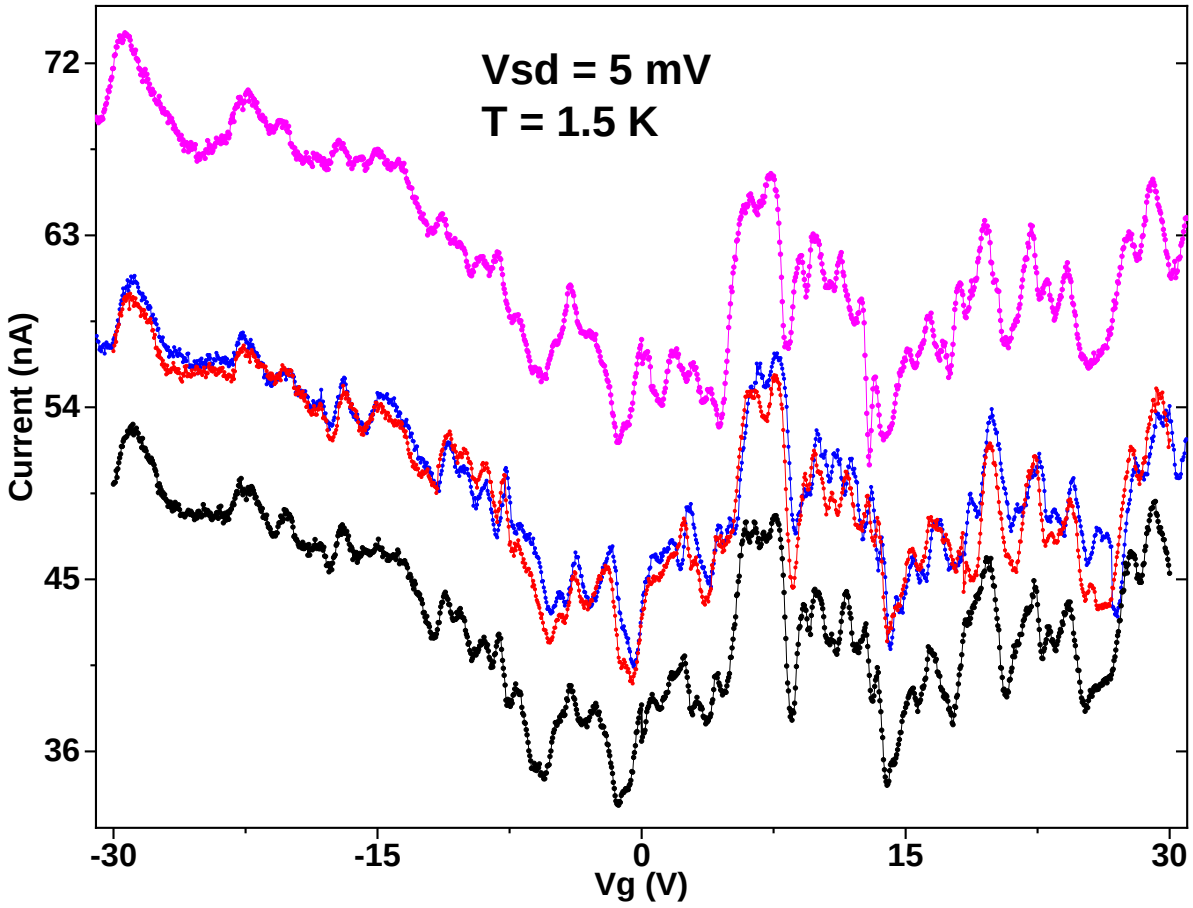

Figure 5.11 *– Reproducibility of the low temperature (1.5 K) electric gate response of Al-AlOx/graphene based SET. The black and the magenta curves have been respectively shifted downward and upward to facilitate the reading. All the oscillations are reproduced which demonstrate the robustness of the sample.*

state' (Fig.5.10.(d)). It results an oscillatory logic gate behavior of the current typical to single electron transistor (SET) [Nazarov09, Electronics07]. In the curve of Fig.5.10.(c) one can observe that the oscillations are not periodic in the whole range of Vg and are superimposed on a global envelope. In addition, not all the peaks have the similar I_{on}/I_{off} ratio and smaller peaks (smaller I_{on}/I_{off}) are superposed to the main peaks at certain Vg thresholds.

The curves presented in Fig.5.10.(c) has been repeated four times in the same conditions (Vsd = 5 mV and T = 1.5 K) and all the mentioned observations were reproduced including the less pronounced peaks (Fig.5.11). This illustrates the robustness and the stability of these 2D-0D vertical SET. The aperiodicity of the oscillations may be an illustration of multiple parallel contributing channels containing NPs with different E_c. In this case, the energy diagram of the SET exhibits disordered energy spacing due to the intermixing of different set of CB levels from all the contributing NPs (Fig.5.12.(b & c)). Small enough DC bias enables to resolved the discrete CB states individually[3] leading to a high frequency oscillation of the Isd (Vg) curves with a pronounced aperiodicity (Fig.5.11). It is worth noting that the number

[3] or only a few depending on the extension of the dc-bias window and the minimal energy spacing among consecutive states

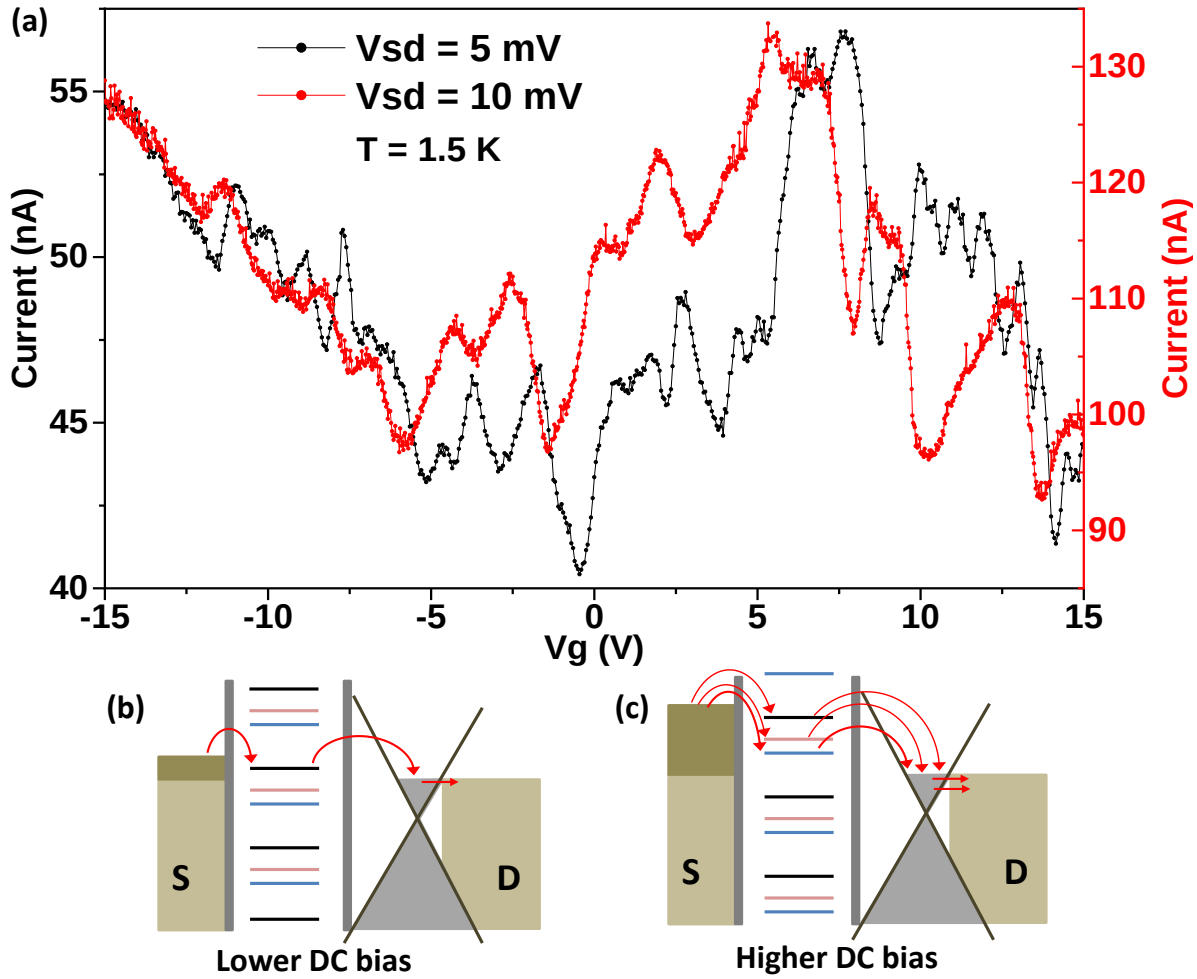

Figure 5.12 *– I(Vg) curves for two different values of Vsd. At low Vsd, the dc-bias window is small enough to resolve only a single (or few) Coulomb states at time (b) resulting to very oscillating I(Vg) curve (black curves). At higher Vsd, more states are resolved at time (c) and the fine structure of the curve disappears. The colors in (b) and (c) highlight the set of Coulomb states originating from distinct contributing conduction channels.*

individual states resolvable in 1 meV dc bias (Vsd = 1 mV) at time is limited to a few due to thermal broadening K_BT = 0.13 meV at 1.5 K. The intensity of the 'on state' current is expected to be proportional to the numbers of levels resolved at times. Therefore, the differences in the I_{on}/I_{off} of different peaks at different Vg values may be illustrating that not always the same number of CB levels enter the dc-bias window at time. In this context, higher source-drain potential difference (But not out of the energy range of CB) is likely expected to accommodate more discrete CB levels at time leading to broader peaks with higher I_{on}/I_{off} ratio.

In Fig.5.12.(a) we present a comparative study between one of the previous Isd (Vg) curve (Fig.5.10) and another curve measured on the same junction with an applied dc bias twice higher. Interestingly, we observe on the higher Vsd curve a substantial diminution of the frequency of the oscillations and a disappearance of smaller peaks as they have fused in the main peaks. The peaks are broader and have a higher Ion/Ioff ratio confirming that more

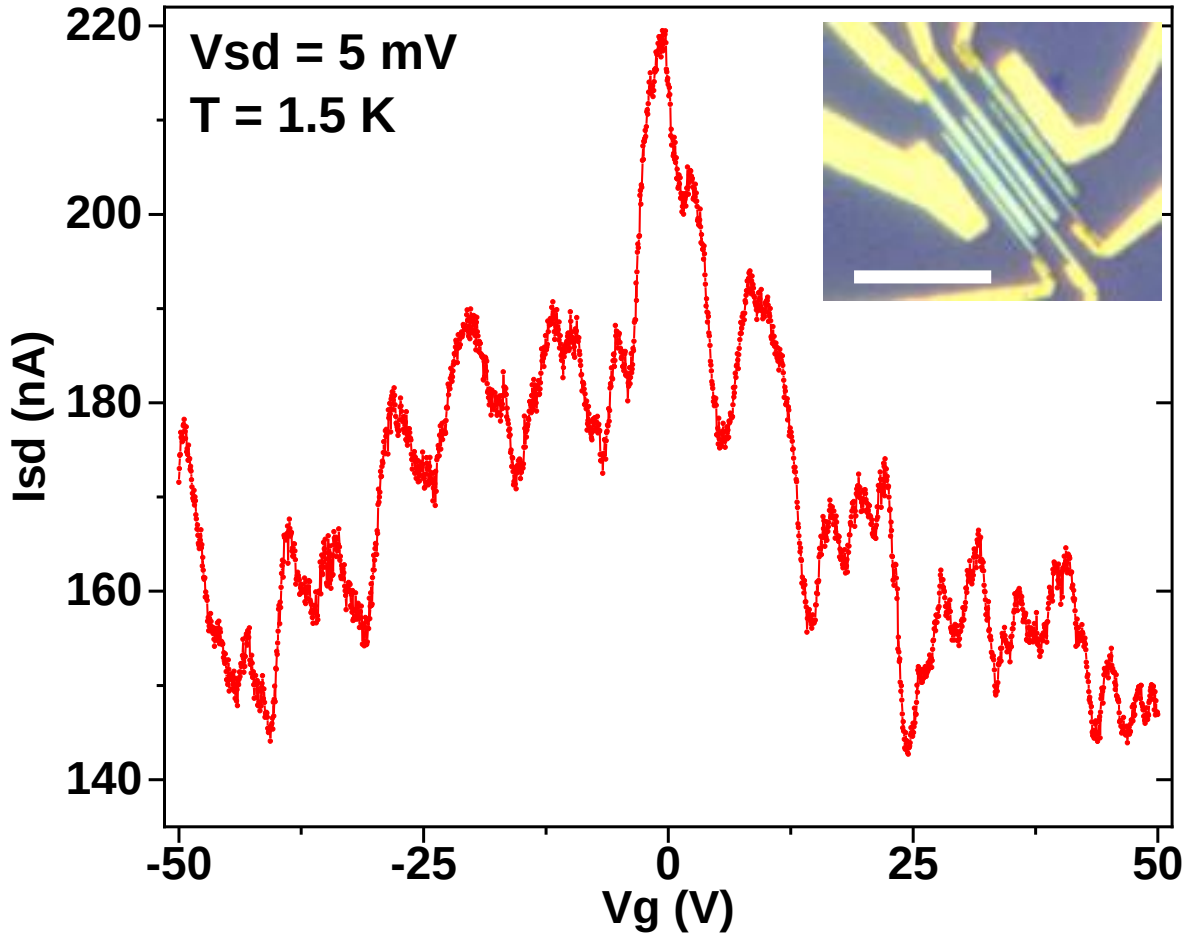

Figure 5.13 – *I(Vg) curves of a different sample consisting of bilayer graphene. The insert is the optical image of the sample, the scale bare is 20 µm. The global envelop due to direct tunneling is still present and have a different shape. The oscillations are regular and the broader that may be related to few contributing channels with similar characteristics.*

states are resolved at time consistently with the schematic of Fig.5.12.(b & c).

It is surprising that the global envelop onto which Coulomb oscillations are superimposed is not similar at least qualitatively to the transconductance of Gr. This envelop was found not to be noticeable in highly resistive sample unless a quite high applied dc bias (discussed in the next section). It results probably from direct tunneling (the leakage current) important in less resistive samples. Its shape differs from sample to sample and is probably determined by the alumina/Gr bottom interface coupling which can be affected as the Fermi energy of the Gr flake is being tuned by the gate voltage. In Fig.5.13 we present the Isd (Vg) curves measured on another low resistive sample with a different shape of the global envelope. The oscillations are regular and periodic which may be highlighting that either few channels contribute to the transport or the contributing channels share quite similar charging energies such that all their Coulomb levels merge into a single but broader state. It has to be notice that in any case, the magnitude of the gate modulation of the overall resistance in different samples due to direct tunneling is quite inferior to gate modulation of the sheet resistance (Fig.5.9).

5.3.3 Samples with negligible direct tunneling contribution

In Fig.5.14 we present the measurements reported on a more resistive sample with negligible direct tunneling contribution the current. A clear oscillatory behavior of the current expressing a successive opening and closing of the junction to the tunneling of one or few electrons controlled by Ec. The periodicity of the oscillations seems not to be regular consistently with multi-channel conduction processes. Not a global envelop is superimposed to the oscillations of I (Vg) curves unless at high Vsd = - 70 mV. The sharp peaks of the current demonstrate Ion/Ioff ratio exceeding 10 at Vsd = -5 mV.

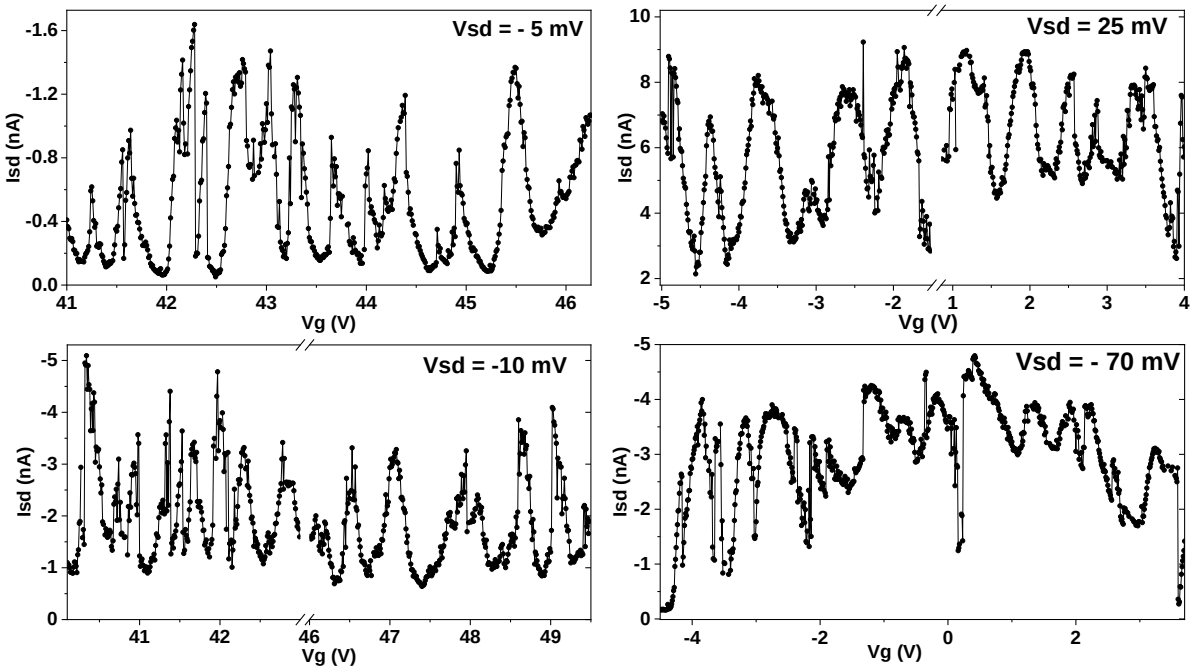

Figure 5.14 *– Low temperature I(Vg) curves of a more resistive sample at different dc biases. Sharp current peaks are distinguishable for all the Vsd values. The Ion/Ioff ratio exceeds 10 at Vsd = -5mV and clearly decreases with increasing dc bias.*

To gain deeper insight into the transport processes, we performed a charge transport spectroscopy of our Al-AlOx/Gr based SET. In Fig.5.15 we present in log scale a stability diagram of the differential conductance versus both dc bias and Vg. Interestingly, one can distinguishes a set of Coulomb diamonds with not regular shape characteristics of multi-channel SET [Danilov02]. An isolated diamond (highlighted by the dished lines in Fig.5.15) is clearly distinguishable and help to speculate the quantitative physical parameters of the SET. The vertical extension of the identified diamond $\Delta Vsd \approx 19$ mV results to a total capacitance of the clusters $C_\Sigma = e/\Delta Vsd \approx 8.43$ aF. From the lateral extension of this diamond $\Delta Vg \approx 0.6$ V, the gate capacitance is deduced to be approximately $Cg \sim 0.27$ aF[4]. The gate lever arm which expresses the modulation the chemical potential of the dot with the gate voltage is deduced form the capacitances to be $\alpha_G = C_g/C_\Sigma \sim 0.032$. This value is about 10

[4]To attempt a comparison with the well known 285 nm thick SiO_2 capacitance, Cox = $1.6x10^{-8}$ Fcm^{-2} the geometrical size have to be considered accordingly. Considering the μm^{-2} scale size of our junctions the obtained Cg value is quite reasonable.

time smaller that those reported on SETs consisting of single Au nanoparticle in direct contact with SiO_2 [Makarenko17] back gate and Al_2O_3 [Bolotin04]. May this suggest that the Gr affects the modulation of the electric state of the NPs by the back gate ? The answer may not be straightforward based on this comparison of the α_G factor as these experiments were done not in similar conditions (T, gate thickness, NPs nature).

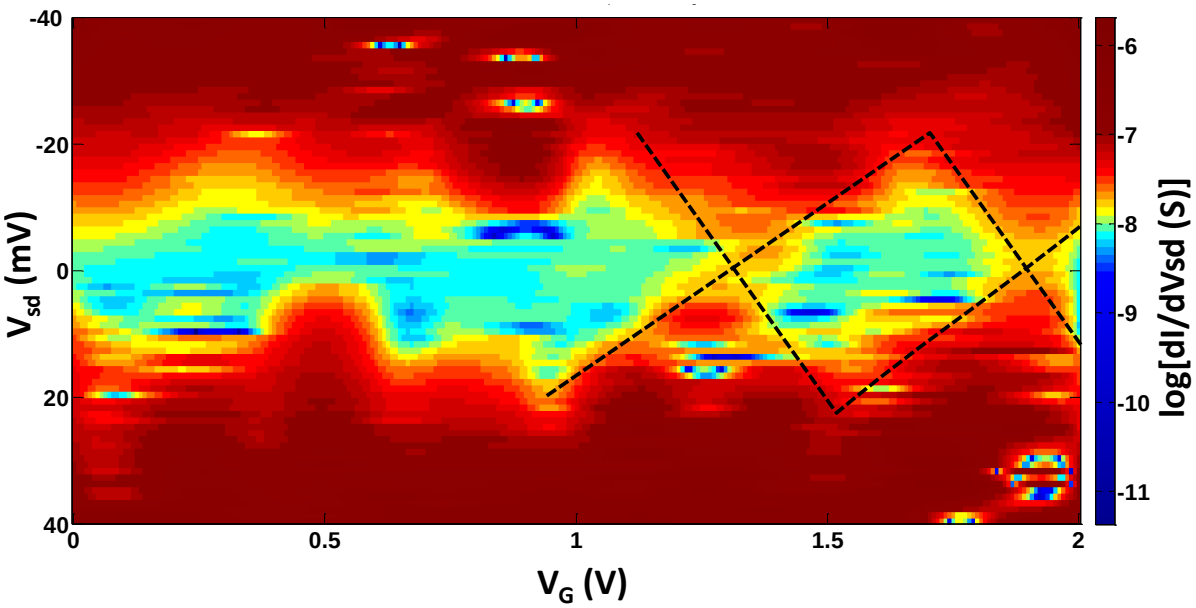

Figure 5.15 *– Charge transport spectroscopy of our Al-AlOx/Gr based SET. The stability diagram of the differential conductance dI/dVsd (Vsd, Vg) in decimal log scale. Coulomb diamond patterns with not regular shape are discernable characterizing a disordered SET. From the isolated diamond highlighted by the black dished lines one deduces* $Ec = e\Delta Vsd = 19\ meV$ *and a lateral extension* $\Delta Vg = 0.6V$.

5.3.4 Temperature dependent electric gate measurements

We have carried out the temperature dependence of the Coulomb oscillations on this specific low resistive sample. The gate dependent oscillations of the current are preserved even at 30 K corresponding to a thermal energy 7.3 times smaller than the Ec ($K_B T_{30K} = E_c/7.3$). In addition, the average maximum of the current peaks (I_{on}) are almost unaffected up to a temperature of $T = E_c/29.4K_B$ =7.5 K. This is in agreement with the orthodox theory of Coulomb blockade in classical regime which predicts the Coulomb peaks maxima to remain unaffected for $T \ll E_c/4.3K_B$ [Kou97, van Houten05]. Transport measurements on a single Au NPs on Si-SiO_2 wafer demonstrated gate induced conductance oscillations up to $T = E_c/3.15K_B$ and a preservation of conductance maximum up a $T = Ec/4.2K_B$T [Makarenko17]. This further point out the role of Gr in our samples and demonstrates that more experiments are still required to ascertain several observations reported here and address their fundamental meaning. This concerned in particular the role of Gr in the coupling of the back gate electric field to the supported NPs and on the temperature limit on gate Coulomb oscillations preservation.

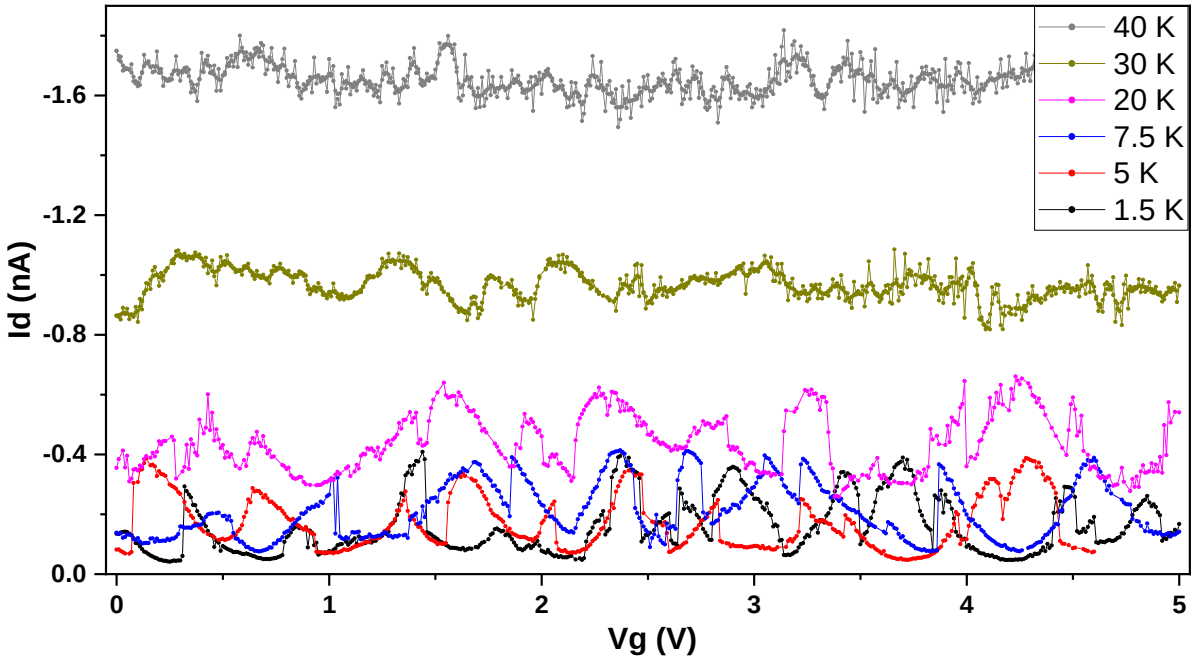

Figure 5.16 *– Temperature dependent Vg induced current oscillations in Al-AlOx/Gr based SET. The oscillations are distinguishable up to 30 K. The average maximin of the current peaks remains almost unaffected up to 7.5 K consistently with CB theory in classical regime.*

5.4 Conclusion

We have presented in this chapter the transport measurements of Al-AlOx/Graphene MD-VdWh based SET. We have observed robust and reproducible Coulomb staircases on the I-Vsd characteristics with the corresponding differential conductance oscillations on large area junction containing more than 10^4 NPs. We have demonstrated that the observed single electron features result from a statistical selection of preferential conductance paths leading to only one or few nanoparticles participating to the transport. Consequently, the transport characteristics are in good agreement with single particle orthodox theory of Coulomb blockage. We have shown that a vertical electric field applied at the back gate efficiently modulates the chemical potential of the supporting nanoparticles through the underneath monolayer graphene flake resulting to a logic gate oscillatory behavior of the current. The Coulomb staircases and the corresponding different conductance oscillations are preserved up to room T while gate dependent current oscillations are limited to temperature below 30 K. The stability diagram of the conductance presents Coulomb diamond patterns characteristic of single electron transistors.

Chapter 6

Anisotropic Magneto-Coulomb properties of 2D-0D heterostructures

We reported in the previous chapter, on the transport properties of Al-AlOx/Gr MD-VdWh integrated in Co/AlOx-Al-AlOx/Gr tunnel junction. We observed single electron processes originating from the CB effect of the metallic core of the NPs. This configuration with Co magnetic electrode set the conditions suitable for nanospintronic applications. In this chapter, we demonstrate the magnetic functionalities of such heterojunctions taking advantage of the top magnetic electrode. We show that the magnetization orientation of this single ferromagnetic electrode enables to modulate the electric charge experienced by the core Al nanoclusters thanks to the so called anisotropic magneto-Coulomb (AMC) effect resulting to a tunable spin valve-like magnetoresistance not requiring a spin coherent charge tunneling. This demonstration of magnetic functionalities in the CB regime on the scalable 2D-0D MD-VdWh paves the way towards novel device architectures at the crossroads of 2D material physics and spintronics.

6.1 Magnetotransport of 2D-0D MD-VdWh

6.1.1 Interest of 2D-0D MD-VdWh for nanospintronics

Effectively launched by the discovery of GMR in 1988 [Baibich88, Binasch89], the field of spintronic experienced an unprecedented rapid development ever reported in any scientific field [Hirohata14]. Indeed, only 10 years after the discovery of GMR, it was implementated into hard disk drives for information storage [Hirohata14]. In this dynamics of fast development, the research in spintronics is now moving into second-generation spin

dynamics and beyond [Hirohata14]. This includes exploring new nanomaterials and alternative technology to allow modulable charge-spin interactions, in the hope of future breakthroughs for information storage and data processing [Seneor07, Singamaneni11]. In this context, MD-VdWh made of a synergetic use of both Gr (or other 2D materials) and other n-dimensional materials (nD, with n = 0, 1, 2, and 3) [Liu16, Jariwala16] might be a possible direction towards new opportunities. Intense efforts at the interface between physics, chemistry, and engineering have already demonstrated promising potentialities of MD-VdWh for magnetic data storage [Baltic16], in addition to the nanoelectronic and optoelectronics applications [Jariwala16, Liu16, Gong18] already well discussed in the chap.1 & 2.

Nanospintronics building blocks require fabricating and addressing small nanostructures where single electron transport properties prevail as well as developing strategies to get their magnetic control. The fabrication strategies for (nano & opto)electronic devices based on MD-VdWh consisting of simple dropcasting onto a 2D materials template of chemically synthesized clusters passivated or not by organic molecules are well spread in literature (see section.2.4). However, these fabrication routes relying on wet chemistry synthesis approaches complicate the heterojunction's interfaces and makes it detrimental for spintronics applications. This illustrates the need for exploring alternative fabrication strategies such as vacuum-based growth processes, providing advantages in terms of scalability and compatibility with standard dry microelectronics technology. 2D-0D MD-VdWh fabricated using physical growth methods offer such advantages. The demonstration of robust single electron transport properties in Co/AlOx-Al-AlOx/Gr heterojunctions intergrating 2D-0D MD-VdWh with Al-AlOx core-shell NPs sets the prosper conditions for their nanospintronics applications.

6.1.2 The device

The configuration of the device used in this chapter is the same as in the previous chapter (Fig.6.1). It consists of mechanically exfoliated Gr flake (1-4 layers thick) onto a clean Si/SiO_2(285 nm) substrate. Following, a thin Al layer of 1.7 nm nominal thickness is deposited by electron beam evaporation into the leads patterned by electron-beam lithography onto the Gr flake. The deposited Al layer is then oxidized in ambient conditions during 1-3 h. Detailed on the device fabrication method are presented in the chap.4. All the previous discussions regarding the analysis of the physico-chemical composistion of the Al-AlOx/Gr heterostructures are to be consisder in this chapter. The average effective junction area ranged from 1 to 5 μm^2, consequently, the transport processes obviously admit as well the selection process of preferential conductance paths as detailed in section.5.1.3.

6.1.3 General zoology of the magnetoresistance

The electronic and magnetotransport characterizations were carried out at low temperature (1.5 K) in a He cryostats, using both AC lock-in amplifier and high precision dc sourcemeter

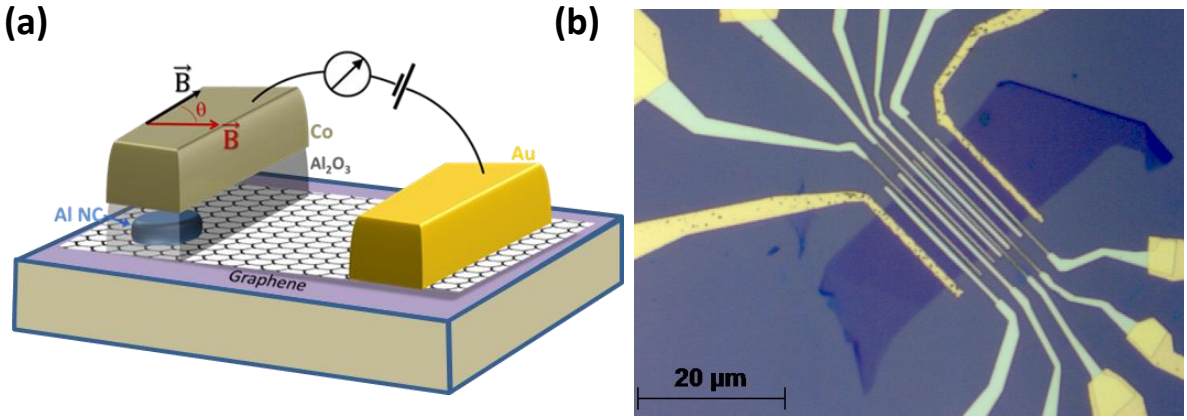

Figure 6.1 *– Device configuration for magnetotransport measurements. (a) Schematic representation the 2D-0D heterostructure based nanospintronics device. The metallic core of the Al nanoclusters grown over the Gr channel are connected to the ferromagnetic Co top electrode and to the mono or few layers Gr bottom electrode trough alumina tunnel barriers. The reference Au contacts patterned few micrometres away at the extremities of the Gr flake are used to extracted (or inject) the charges injected from (to) Co/AlOx-Al-AlOx/Graphene tunnel junction. (b) The optical image of a typical device with Gr flake exfoliated on Si/SiO_2(285 nm) substrate, contacted by multiple AlOx-Al-AlOx/Co tunnel junctions and two reference Au electrodes.*

providing simultaneous measurements of I-Vsd characteristics and of the dynamical conductance (dI/dV (V)) (see section.4.3). The device configuration for all the magnetotransport measurements always integrate a single Co/AlOx-Al-AlOx/Graphene tunnel junction together with Ti/Au electrode in direct contact with the Gr flake as illustrated in Fig.6.1.(a). The Fig.6.1.(b) presents the optical image of a typical sample. As detailed in the previous chapter, charges are injected from the Co electrode through the 2D-0D heterojunction into the Gr flake along which they diffuse and get extracted in the Au contact at the extremity of the flakes. We systematically investigated the magnetoresistance (MR) behavior of our devices while sweeping the applied magnetic field in plane as illustrated in Fig.6.1.(a) (black and red bold $\vec{B}$ vectors).

We observed from sample to sample, various MR signals that we could classify into three typical behaviors reported as the positive spin-valve like MR (Fig.6.2.(a)), negative spin-valve like MR (Fig.6.2.(b)), and hysteretic square like MR (Fig.6.2.(c)). The magnetoresistance amplitudes MR = $(R_{high} - R_{low})/R_{low}$ varies from less than 1% up to 20%. The respective I-Vsd and dI/dV-Vsd characteristics of the concerned sample measured before the magnetotransport measurements are represented in Fig.6.2.(d,e,f). They all present well-defined Coulomb staircases, the corresponding differential conductance also present Coulomb oscillations. The central Coulomb gap $\Delta Vsd = e/C_{\sum}$ of the I-Vsd and dI/dV-Vsd for all the samples concerned by the magnetotransport measurements is spread between 40 meV to 80 mV approximately. The resulting total capacitances $C_{\sum}$ range from 4.0 aF to 2.0 aF approximatly and the resulting charging energies $E_C = e^2/2C_{\sum}$ vary from 20 meV to 40 meV.
The diameter of the main contributing cluster(s) can be estimated following the already described method (section.5.1) by assuming a cylindrical plate capacitor model providing the diameter of the disc shape NPs by the simple expression $d = \sqrt{(2tC_S)/(\pi\epsilon_0\varepsilon_{AlOx})}$. Where t

represents the average Al-oxide shell thickness above the cluster and considered from STEM-EELS analysis to be 1-1.5 nm. Assuming $C_S = C_D = C_\Sigma/2$), we obtain a core diameter of the contributing cluster close to 5-6 nm that is in the same range with the value reported in the previous chapter and in agreement with the STEM-EELS analyses.

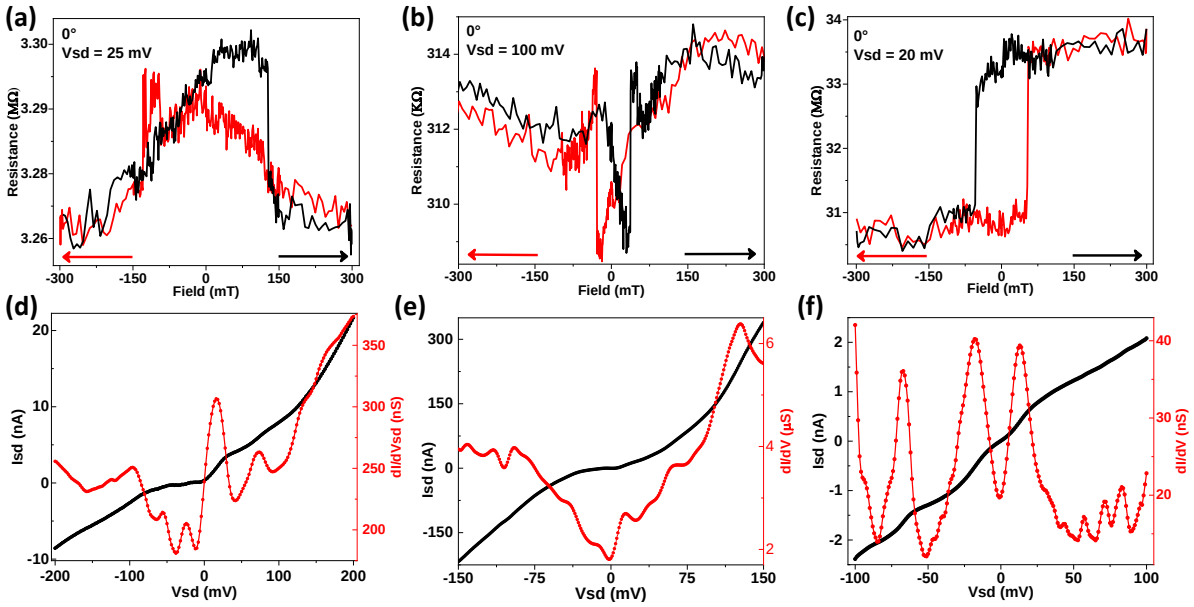

Figure 6.2 *– Complete zoology of MR signals. The data were measured at 1.5 K on three different devices. (a) positive spin valve-like, (b) negative spin valve-like, and (c) hysteretic square-like MR behaviors. The notation (0°) represents the magnetic field orientation along the electrode axis. The corresponding value of Vsd is reported on each MR curves. (d), (e) and (f) present the I-V characteristics (left axis, black curve) and dI/dV-V (right axis, red curve) characteristics of the samples (a), (b) and (c) respectively.*

6.2 Manifestation of AMC effect 2D-0D MD-VdWh

Majority of the devices studied (more than 10 different chips) exhibited a spin-valve like MR (Fig.6.2.(a and b)). However, our device architectures include only a single magnetic component (the Co top electrode). Therefore, the observed MR cannot be related to a coherent spin injection/detection as in standard spin-valve devices integrating two magnetic electrodes. Indeed, the Jullière model ($TMR = \frac{2P_1P_2}{1-P_1P_2}$) (section.9.4.2) predicts no MR signal as the spin polarization of the second electrodes either Gr or Au is systematically nil. The observed MR is instead explained by the modification of the electrostatic charge state of the central Coulomb island thanks to the interplay of CB and the applied magnetic field resulting to a mechanism referred to as Magneto-Coulomb effect (MCE) [Shimada98, Van Der Molen06, Bernand-Mantel09]. The MCE offers the possibility for controlling the operation of a SED with an applied magnetic field. In section.9.4.2 we presented the historical context and provided the general theoretical background of MCE. To summarize, in a SED with magnetic leads, an applied magnetic field induces a shift $\Delta\mu$ of the chemical potential of the ferromagnetic leads either by Zeeman effect or SOC, the later being mediated anisotropic magnetocrystalline effects [Shimada98, Van Der Molen06, Bernand-Mantel09]. This shift induces a

modification of the charge state of the Coulomb island and sets the device resistance resulting to the observed MR signal.

For our devices consisting of Al-AlOx/Gr 2D-0D MD-VdWh, the Zeeman effect can be ruled out since the observed MR signal do not exhibits the linear dependency with the applied magnetic field espected in this case [Van Der Molen06]. As the AMC effect is concerned, the spin-orbit interaction presents in 3d ferromagnet such as Co used here, couples the magnetic moments to the lattice through the crystal field. Hence, the energy band with non-zero orbital moments likely shifted as the magnetic moments are rotating. Its results a redistribution of electrons in the modified bands responsible for the anisotropic variation of the electrochemical potential $\Delta\mu = \mu(\theta_i) - \mu(\theta_f)$. $\mu(\theta_{i,f})$ denotes the chemical potential of the magnetic electrode at the initial and final magnetization orientations respectively [Bernand-Mantel09]. Because in spintronic devices the ferromagnetic leads are always connected to normal metals, the shifts of their chemical potential $\Delta\mu(\vec{M})$ induces an accumulation of charge at the FM/normal Metal interface creating an effective potential $\Delta\phi = \frac{1}{e}\Delta\mu(\vec{M})$. We illustrate this in Fig.6.3.(a). This potential induces on the central island an additional charge given by $\Delta Q = C_S\Delta\phi$ [Van Der Molen06, Bernand-Mantel09]. Where C_S is the capacitance coupling the central island to the FM leads (Fig.6.3.(b)). The magnetic field induced modification of the charge state of the central Coulomb island leads to a shift of the discrete Coulomb levels (Fig.6.3.(a)) resulting to a gate like modulation of the resistance of the sample and thus to the observed MR (Fig.6.2). To date, the AMC effect mediated spin valve-like MR signatures has been observed on (Ga,Mn)As semiconductor islands [Wunderlich06] and metallic nanoparticle [Bernand-Mantel09, Bernand-Mantel11].

6.2.1 Origin of sign variation of MR

The modification of the MR sign as the electric charge state of the nanoclusters is being modified by the applied magnetic filed can be understood by inspecting the charge a stability diagram of the SED as depicted in Fig.6.3.(c). Depending on the initial charge state Q_1 of the dot and the amplitude of change $\Delta\mu(\vec{M})$ of the chemical potential of the magnetic electrode, the device resistance may either increases or decreases (Fig.6.3.(c)). For an arbitrary applied bias V_i, one can report two possible situations higlited by the case 1 and case 2. In case 1, the change ΔQ_0 of the electric charge of the nanocluster brings the device from high to low resistive state consistently with Fig.6.2.(b). In case 2 instead, the situation is the opposite. The change ΔQ_0 increases the device resistance consistently with Fig.6.2.(a and c). The shape of the MR, either spin valve or square like is determined by the detailed roversal dynamics of the magnetization of the ferromagnetic electrode as will be discussed later.

6.2.2 Signature of the random nature of the initial value of Q_0

In single electron devices, the initial charge state Q_i of the metallic nanocluster is determined by the distribution of charges in the trapping states located in the tunnel barriers at the vivin-

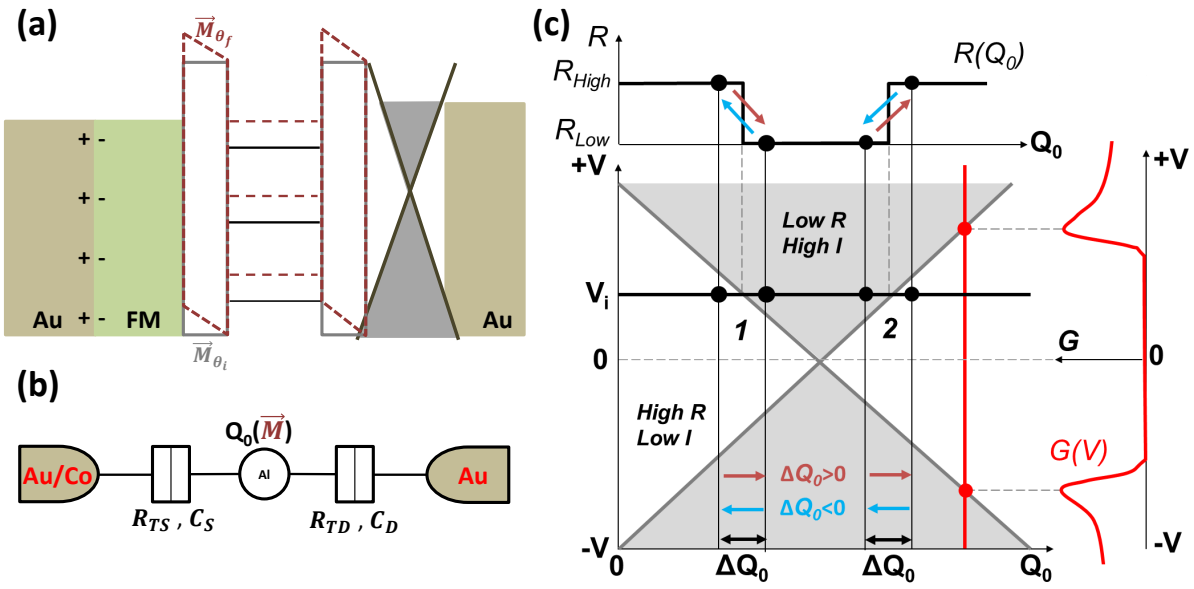

Figure 6.3 – *Energy band profile of the 2D-0D spintronics device illustrating the AMC effect. Our system is equivalent to a double-tunnel barrier coupling the central metallic nanocluster with quantified Coulomb levels to the Co top electrode and the Gr bottom electrode. FM denotes the Co electrode connected to Au pad. The energy profile of the Coulomb island is illustrated for two different magnetization directions referred to as $\vec{M}_{\theta_i}$ (black lines) and $\vec{M}_{\theta_f}$ (dashed red lines). The symbol ± denote the accumulation of charge accumulated at the FM/Au interface due to Co's chemical potential schift as its magnetization rotates from its initial θ_i orientation to the θ_f direction. (b) Equivalent electric circuit of the devices. The source (respectively drain) is characterized by a tunnel resistance R_{TS} (respectively, R_{TD}) and a capacitance C_S (respectively, C_D). (c) The schematic representation of the charge stability diagram of a typical SED as a function of the applied voltage and the environmental charge Q_0. The gray areas correspond to 'open' state of the device with a low resistive state while the white areas correspond to Coulomb blockade regime with high resistive state. These areas are delimited by the position of the first Coulomb peaks of the conductance G(V) of the junction (distributed along the gray bold gray lines) illustrated by the red curve on the righthand panel. The charge state of the dot can be modified from its initial state Q_i to a final state a Q_f ($\Delta Q_0 = Q_f - Q_i$), by the applied magnetic field. Consequently, for a given applied voltage V_i (horizontal black bold line), the device resistance is modulated as shown in the upper panel, and may either increase ($\Delta R > 0$) or decrease ($\Delta R < 0$) relatively, as shown in case 1 and case 2.*

ity of Coulomb island. Such traping processes are completly random and generally, the value of Q_i evolves with time. Particularly if during, this time the sample has experienced temperature variation. This is quite common in SEDs even with a single NPs. Bernand-Mental *et al.* have studied the time evolution of the evironemental charge of a single Au metallic NP based SED fabricated by nanoidentation [Bernand-Mantel08a]. They observed an environemental charge of $Q_0 = -0.07e$ the first day and $Q_0 = 0.32e$ the next day after thermal anealing of the sample.

In Fig.6.4 we present different MR curves measured at different days on the same sample with MR already in Fig.6.2.(c). We observe all the zoology of MR, highlighting the random character of Q_i. One also notices in Fig.6.4, a modification of the global resistance of the device. Although this be can a consequence of a change of Q_0 as we discuss in the next section in the light of the orthodox theory of Coulomb blockade, it may be as well be related to the redistribution of preferential contributing conduction paths. Note however that, the

change of MR shape with time was not systematic in all samples.

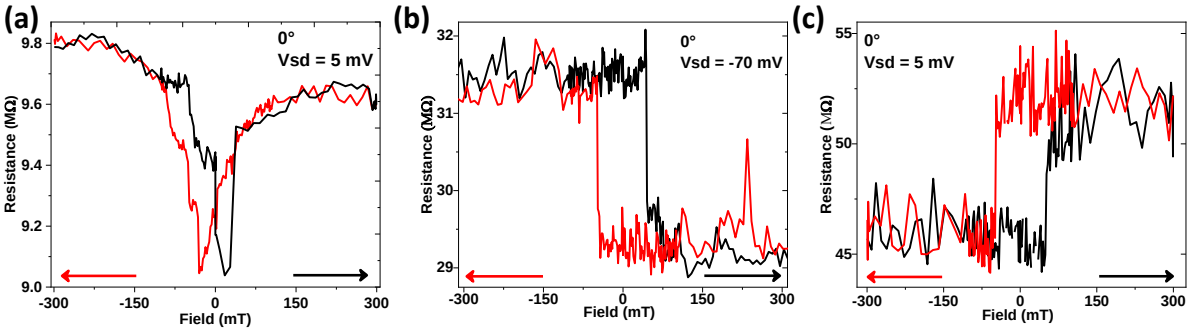

Figure 6.4 *– Modification of the MR sign and shape with time and thermal cycling. (a) Negative spin valve like MR. (b) Negative hysteretic square-like. (c) Positive hysteretic square-like. The sample were initily in state (a). The state (b) were obtained three day later and the sate (c) one day later after the state (c).*

6.3 Evidence of the magneto-crystalline anisotropy in the MR

To confirm the role of the anisotropy the magneto-crystalline on the observed MR, we carried out on a device exhibiting a spin-valve like MR, a comparative study of the I-Vsd characteristics at different values of the magnetic field corresponding the two states of the resistance observed in the MR curve (Fig.6.5.(a)). In Fig.6.5.(b,c), we illustrate the modification induced on the I-Vsd characteristics by the change of the magnetic state of the Co electrode. The Fig.6.5.(c) shows the I-Vsd traces measured under an in-plane magnetic field parallel to the leads (as depicted in the inset) for the amplitudes of -100 mT (in black) and +20 mT (in red) corresponding respectively to the high and low resistance states of the sample (Fig.6.5.(a)). Consistently, we observe two differents conduction behaviors. The high resistive state at -100 mT (Fig.6.5.(c), black curve) contrastes clearly the low resistive state at 20 mT ((Fig.6.5.(c), red curve)). The latter is characterized by the closing of the central Coulomb gap and a change of Coulomb staircases threshold voltages. These are clear indications of the modification of the environmental charge Q_0 of the nanocluster [Bernand-Mantel09, Seneor07].

To illustrate the anisotropic character of the MCE, we report in Fig.6.5.(b) the measured I-Vsd traces at high applied field (2 T) where the magnetization of the Co electrodes are completely saturated i.e. fully aligned along the directions of the applied field respectively at 0° and 90° orientations with respect to the Co electrodes. Similarly to Fig.6.5.(c), we observe two different conduction states for both orientations, characterized by the changes of Coulomb staircase threshold voltages and of the central Coulomb gap. In agreement with the MR measurement of Fig.6.5.(a). The 90° orientation of the magnetization I-Vsd curve corresponds to a higher conduction state as compared to the 0° oritation curve. This clearly supports the model of anisotropic magneto-Coulomb effect, with the top Co FM electrode acting as a magnetic 'knob' to modify the cluster environmental charge Q_0. To illustrate the role of the environmental charge on the I-Vsd characteristics as expected from the orthodox theory of Coulomb blockade, we show in Fig.6.5.(d) two I-Vsd curves computed for a single-dot

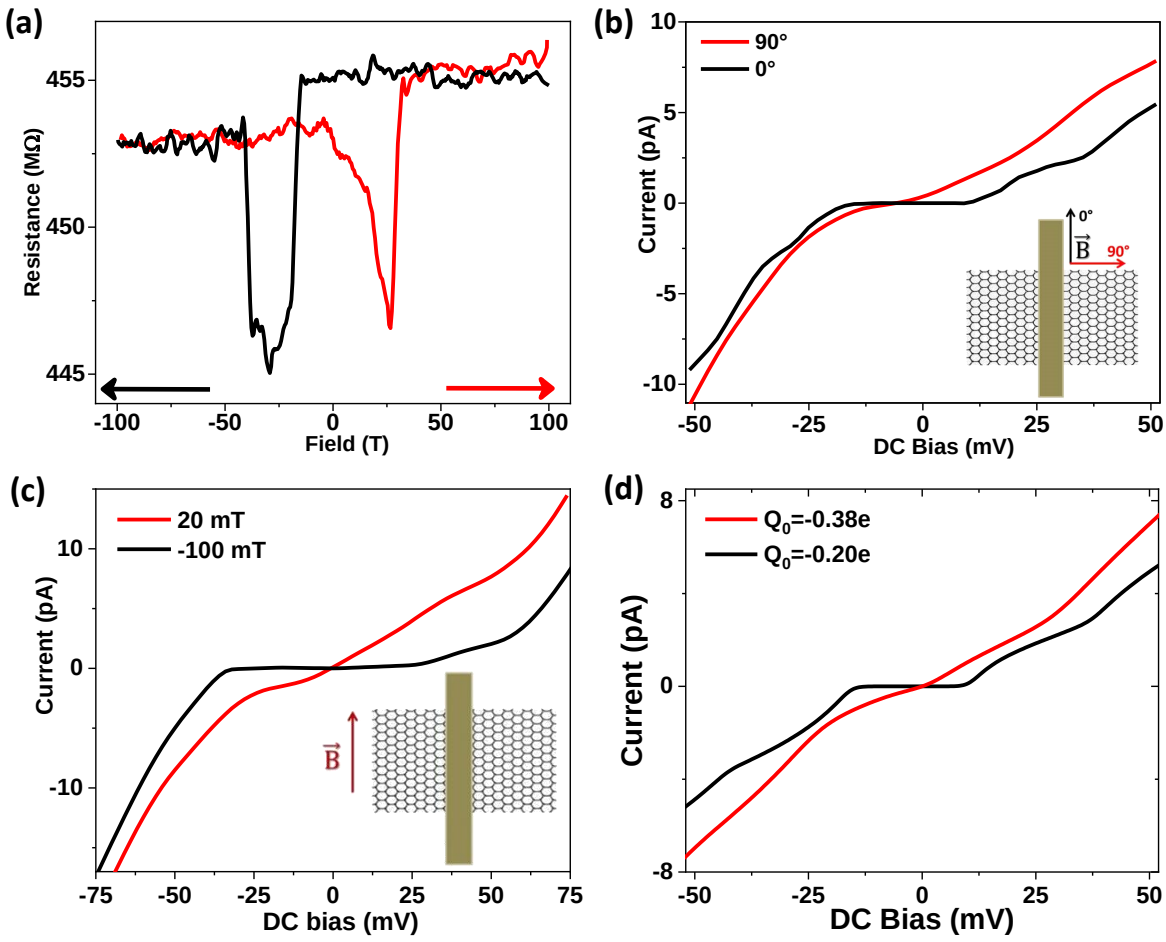

Figure 6.5 – *Evidence of the magneto-crystalline anisotropy in the MR. (a) The spin-valve like MR of the sample measured at Vsd = 125 mV. (b) I-V characteristics measured under saturated magnetic field of 2 T applied at 90° (red) and 0° (black) with respect to the electrode direction (inserted schematic). (c) I-V characteristics performed under magnetic field of 20 mT (red) and 100 mT (black) applied along the electrode direction (inserted schematic). (d) Best Coulomb blockade simulation of the 0° (respectively, 90°) applied field curves presented in (b). The respective modeling parameters are : C_S = 6 aF (same), C_D = 3 aF (same), R_{TD} = 2.2 GΩ (same), R_{TS} = 4.8 GΩ (2.6 GΩ), and Q_0 = -0.2e (-0.38e).*

model (Fig.6.3.(b)). Though the curves could not be perfectly modeled as in the section.5.1 due to their pronounced asymmetry, parameters were chosen to approach the best the curve of Fig.6.5.(b) and to reproduce the threshold voltages of the staircases. For both simulated curves, the source and drain capacitors (C_S, and C_D) and the bottom tunnel barrier (R_{TD}) are kept constant and the environemental charge changes from $Q_0 = -0.20e$ for the 0° applied field (red curve) to $Q_0 = -0.38e$ for the 90° curve (black curve). One notices in the red curve the Coulomb gap closing at low bias range and the change of staircase threshold voltages relatively to the black curve, in agreement with the experimental data of Fig.6.5.(b). This corresponds to the case 2 described in Fig.6.3.(c)) with $\Delta R > 0$. Hence, despite its simplicity, the model enables reproducing the main characteristics of our devices.

The modeling parameters extracted from the simulations enable an estimation of the chemical potential change of the ferromagnetic electrode : $\Delta\mu = e\Delta Q_0/C_S$ = 3.2 meV. This

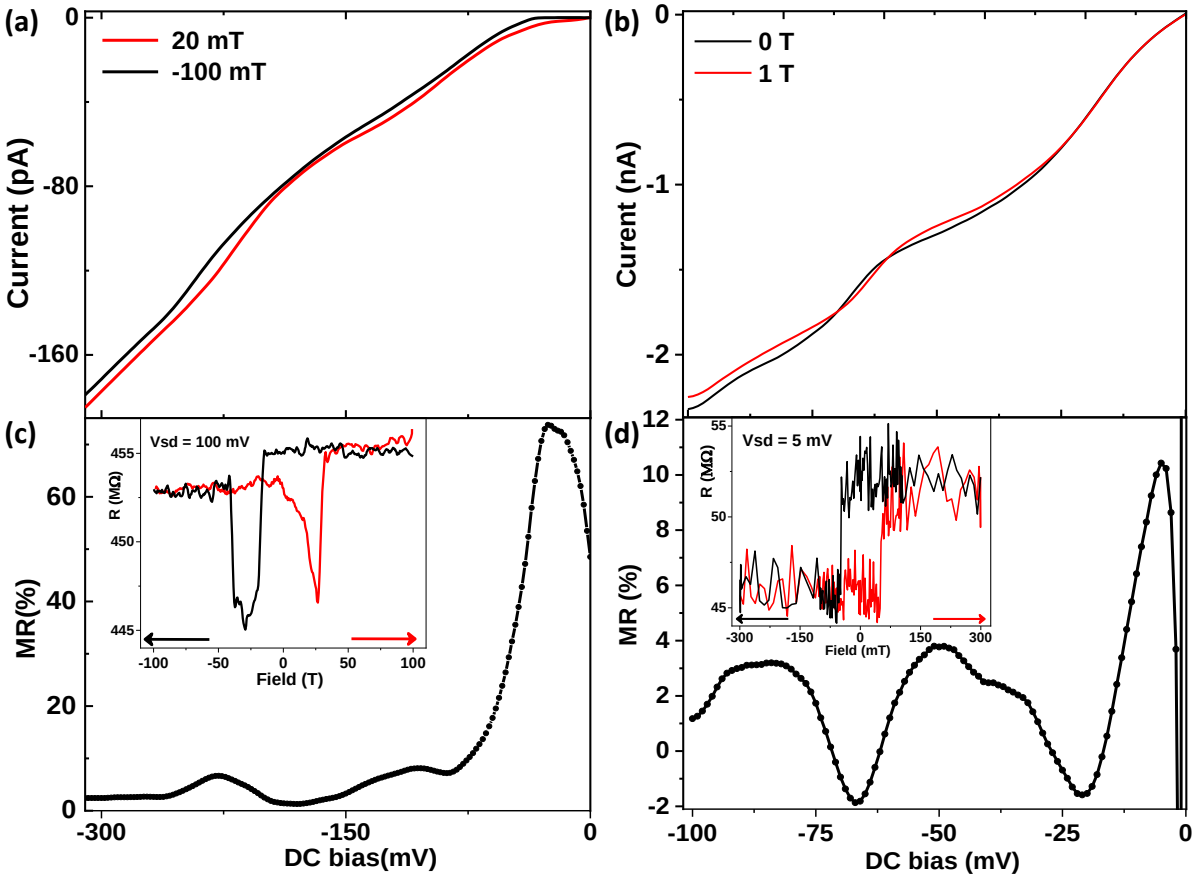

Figure 6.6 *– MR(V) oscillations of two different samples. (a) Sample presenting a spin valve like MR . (b) Sample presenting an hysteresis square MR (see the insert of the bottom panel in both cases). The MR(V) presented in the bottom panels are calculated from the I-V curves presented in the top panels. These I-V curves are measured following the magnetization history of the MR inserted in the bottom panel.*

value is in the same range with previous results on Au nanoclusters contacted by a Co electrode ($\Delta\mu$ = 1.15 meV) [Bernand-Mantel09]. However it is much lower than the values reported on InP nanowire with CoFe electrode ($\Delta\mu$ = 165 meV) [Zwanenburg09]. In any case all these experimentally reported $\Delta\mu$ values exceed what is usually expected for thin film. The reason for such enhancement in our case might be the spin-orbit interaction exacerbated at the nanocluster/Co interface where strong shape anisotropy is presente as primary discussed by Zwanenburg et al. in the case of nanowires [Zwanenburg09].

6.3.1 DC voltage dependent MR oscillations

The Fig.6.6 (bottom panel), presents the dc bias voltage dependency of the MR of two distinct samples. The Fig.6.6.(a) concerns the sample presenting a spin valve like MR and which the angle dependent magnetotransport characteristics are presented in Fig.6.5. The Fig.6.6.(b) concerns the sample presenting a hysteresis square MR as presented in Fig.6.2.(c) & Fig.6.4. The top panels of Fig.6.6 present the corresponding I-Vsd data from which both MR(V) where calculated extended to the concerned dc bias range. The I-Vsd characteristics of Fig.6.6.(a) (top pannel) are the same data as presented in Fig.6.5.(c). The I-Vsd curve of Fig.6.6.(b) (top

pannel) were measured under 0 T and 1 T (Fig.6.6.(b)) correspondingly to the magnetization history given rise to the MR presented in the insert of bottom panels.

The MR(V) curves present an oscillatory behavior in both cases with an average amplitude of the peaks decreasing with the Vsd. The positions of the peaks coincide with the Coulomb staircases threshold voltages (Fig.6.6.(a & b) top panels). This is an additional key feature of the MCE effectively originating from the change of the charge state of nanoisland which affect the positions of the threshold voltages of the staircases [Seneor07, Bernand-Mantel09, Bernand-Mantel11]. Their observation in the sample demonstrating both spin valve and hysteresis square like MR is a further argument sustaining the MCE. The same effect can be observed after a variation of the nanocluster environmental charge due to thermal cycling. This denote the importance of a particular care before to assign such an oscillations to the AMC effect.

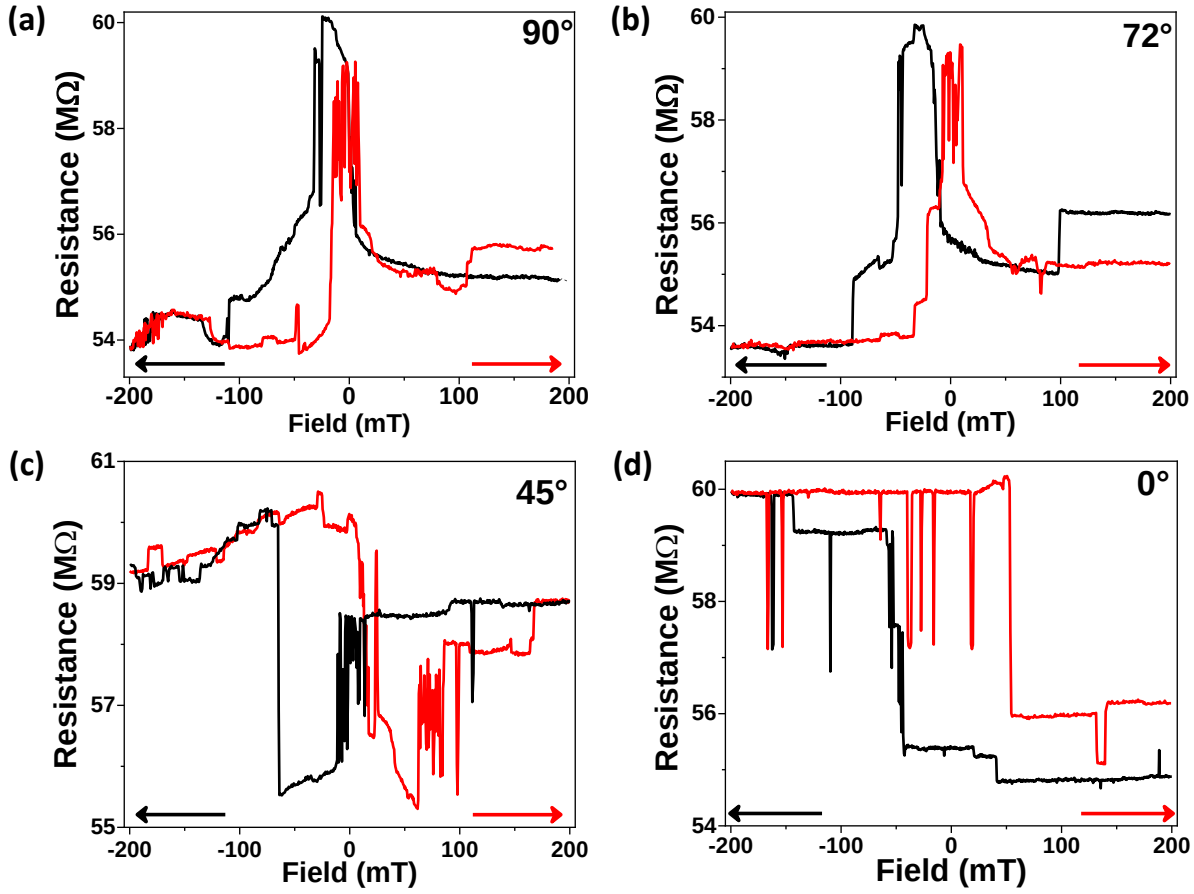

Figure 6.7 *– Angle dependent MR measured at Vsd = 20 mV for with magnetic field applied along 90°, 72°. 45° and 0° orientations with respect to the electrodes. All the MC features are reproduced on a single sample. (a,b) positive spin valve-like, (c) negative spin valve-like, and (d) hysteretic square-like behaviors.*

6.3.2 Angle dependent magnetotransport measurements

A complete study of the anisotropy effect on the magnetotransport properties requires angle dependent measurements. We report on Fig.6.7 several MR curves measured on a defferent

sample for magnetic field sweeps performed along different directions (0°, 45°, 72° and 90°). The corresponding I-V and dI/dV-V characteristics presented in Fig.6.8.(a) show well-defined Coulomb staircases and oscillations. In the framework of our collaboration with Pr. Pierre Seneor's group, these curves were measured at Thales[1]. For this purpose, I fabricated the samples and brought them a Thales where Florian and I conducted low temperature magnetotransport measurements on thier set-up enabling a low temperature rotative angle magnetic measurements. I acknowledge Florian and Pierre for their warmfull welcome and kind assistance during my week of stay.

Interestingly, for different magnetic field orientations, we recover on this unique sample all the MR signatures expected from AMC as reported in Fig.6.2 on several samples at a fixed field direction parallel to the Co electrode. This clearly confirmed that the resistance jumps observed in the MR signals originate from the modification of the magnetization configurations of the top Co electrodes. Indeed, as the applied magnetic field is sweeping, the magnetization of the Co electrode undergoes different orientations. Therefore, the angle dependent MR signal reported in Fig.6.7 is a direct fingerprints of the change of the electrochemical potential of the FM contact, associated to the successive pinned states experienced by its magnetization during the reversal dynamics. As the electrode width is much larger than the Co magnetic exchange length (≈2 nm), the evolution of the magnetization reversal of the Co electrode takes place via domain walls propagation through the structure as the applied field is being incremented. The multidomains configuration of the Co electrodes was confirmed by magnetic force microscopy (MFM) (Fig6.8.(b)).

Depending on the applied magnetic field direction with respect to the crystallographic

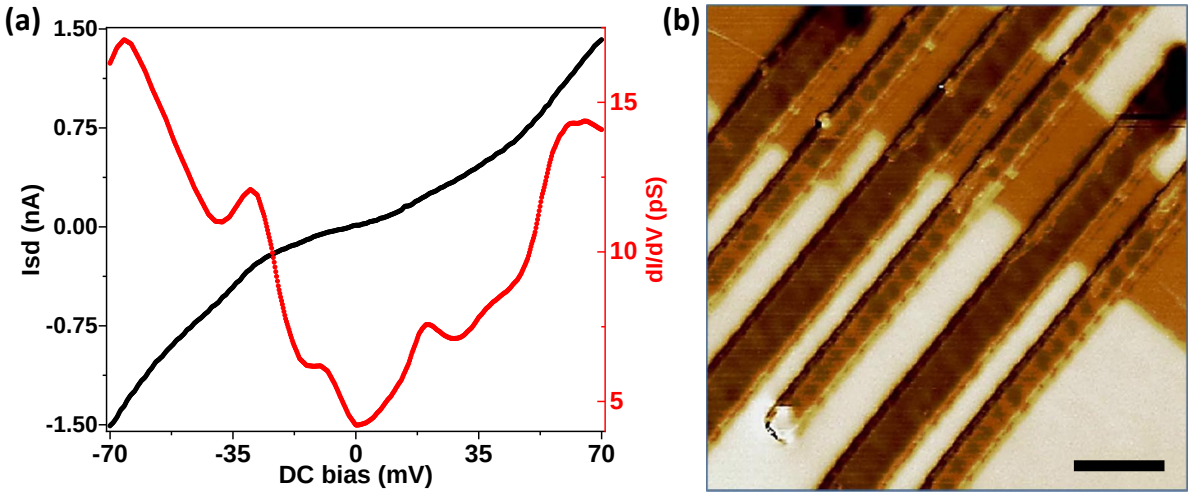

Figure 6.8 *– (a) I-V (black curve) and dI/dV(V)(red curve) characteristics of the sample used for the angular dependent MR study (Fig.6.7). Well defined Coulomb staircases and Coulomb oscillations are observed. (b) MFM image of the remanent magnetization showing multidomains magnetic configuration of Co electrodes grown by electron beam deposition onto Al-AlOx/Gr 2D-0D heterostructure. Before scanning the image, the electrodes have been magnetized perpendicular to the plane (scale bar = 1 µm).*

[1] Unité Mixte de Physique, CNRS, Thales, Univ. Paris-Sud, Université Paris-Saclay, 91767 Palaiseau, France in the team of Pr. Pierre Seneor

axes and the orientation of the contributing magnetic domain(s), different magnetic states may be involved at a specific field amplitudes. In addition, the micromagnetic structure of the contributing magnetic domain(s) and their respective orientations relatively to the applied magnetic field directly affect the dynamics of the magnetization. This explains why the magnetic field switching value(s) of the MR may be different for distinct samples and directions of the applied magnetic field. The observed spinvalve-like MR most likely results from an intermediate pinned state of the magnetization at low field along a thermodynamically stable orientation distinct from its direction at higher field amplitude [Cowburn95, Zwanenburg09]. In contrast, the hysteretic squarelike MR Fig.6.2.(c) stems from 180° direct reversal of the magnetization with no intermediate thermodynamically stable orientation [Cowburn95, Zwanenburg09]. This makes 20-0D SED a rich system opening up new opportunities for nanospintronics.

6.4 Conclusion

We presented in this chapter, the low temperature magnetoresistance properties of 2D-0D MD-VdWh heterostructures based SED consisting of a single magnetic electrode demonstrating a spin valve-like magnetoresistance signatures without requiring a spin coherent tunneling. The observed MR features originate from the AMC effect which enables to modulate the environemental charge state of the nanoclusters as the magnetization orientation of the single ferromagnetic electrode changes under the applied magnetic field resulting to a spin valve-like MR. This demonstration of the magnetic functionalities in the Coulomb blockade regime on scalable 2D-0D MD-VdWh based single electron devices paves the way towards novel device architectures at the crossroads of 2D material physics and nanospintronics.

Chapter 7

Interface transport mechanisms in bi-layer $MoSe_2$ Field Effect Transistors

In this chapter, we report on tunable Metal/$MoSe_2$ interface charge injection mechanism in bi-layer $MoSe_2$ field effect transistors with Ti/Au contacts demonstrating an on/off ratio up to 10^7 at room temperature. We demonstrate that the Ti/$MoSe_2$ interface energy band profiles modulation by the combined effects of temperature, gate and source-drain voltages enables to elucidate the complete map of the interface charge injection mechanisms. Thermal activation regime is identified at low carriers density while the transport at higher carrier density is mediated by filed assisted direct tunneling or thermionic emission and demonstrates a transition to high-field Fowler-Nordheim tunneling. The transition voltage V_{trans} to Fowler-Nordheim directly correlates to the Metal/$MoSe_2$ interface potential barrier highlighting the necessity for new investigations both theoretical and experimental for better understanding.

Contextual introduction

In the chap.(2 & 3), we presented the structural and electronic properties of 2D SC-TMDs and their prospect for nanoelectronic. Similar to other SC-TMDs, the band structure of $MoSe_2$ undergoes a transition from indirect bandgap of $\sim 1.41eV$ in few-layer, to a direct band gap close to 1.58 eV in the monolayer limit [Zhang14b]. Spin splitting at the valence bands maximum of SC-TMDs was found to be larger in $MoSe_2$ than in MoS_2, making $MoSe_2$ a better candidate for valley-spintronics [Kośmider13] and valleytronics applications [Zeng12, Zeng13, MacNeill15, Li14] (see section.2.2.2 for details). Initial demonstrations of few-layer $MoSe_2$ transistors [Larentis12, Chamlagain14] and ambipolar transistors [Pradhan14] together with low-frequency 1/f noise [Das15] and mobility improve-

ment [Chamlagain14] studies were already reported. However, detailed charge transport mechanisms at metal/SC-TMDs interfaces in general and $MoSe_2$ in particular is yet to be understood. Such and understanding is essential [Allain12, Yang17] for device engineering and performance improvement for the sake of achieving high 'on' state current [Das13a], large photoresponse [Lopez-Sanchez13] and high-frequency [Krasnozhon14] operations.

We present in this chapter detailed study of the interface charge injection mechanisms in bilayer $MoSe_2$ FET with Ti|Au source-drain electrodes. Bilayer $MoSe_2$ exhibits a direct bandgap similar to the monolayer under certain conditions [Tongay12] unlike Bilayer MoS_2. Indeed, in a bilayer $MoSe_2$, the direct energy band components are nearly degenerated with the indirect components. This means that the energy gap between the valence band maximum located at K points and the conduction band's second minimum situated also at K point, though larger compare to the normal indirect gap (involving the absolute conduction band minimum located else where in $\Gamma - K$ direction), the difference between both values is relatively low [Tongay12]. The relatively low difference between the two quantities makes possible a reversible tunability of bilayer $MoSe_2$ band from direct to indirect bandgap with external stimuli [Mak10, Tongay12]. This reversible band crossover also makes the bilayer unique.

7.1 Device fabrication and characterization

7.1.1 Device fabrication

The device was fabricated by exfoliating a bilayer $MoSe_2$ onto a commercial SiO_2/Si substrate. The electrodes were patterned in spin coated PMMA resist by Ebeam lithography followed by Ebeam evaporation of Ti(3nm)/Au(47nm). Details of the fabrication process are presented in section.4.1. Electric transport measurements were carried out in a closed cycle He flow cryostat with 1.5 K base temperature, using a low current source meter K2634B for low signal measurements (details in section.4.3). The Fig.7.1.(a) provides the schematic of geometry of the FET with the source (S) and drain (D) electrodes contacting the bilayer $MoSe_2$ channel and the capacitively coupled back gate (G) electrode for electrostatic doping of the $MoSe_2$ channel. The ultrathin bilayer crystal induces a minimal screening of the electric field resulting in an excellent gate control. The source-drain and gate voltages enable to modulate both the energy bands profile of the 2D crystal and the electrode chemical potential. This favors Metal/MoS_2 interface charges injection and their transport within the channel resulting to a good control of the 'on' and 'off' states of the transistor. The Fig.7.1.(b) presents the colored optical image of the fabricated devices with multi-electrodes. The width of each electrode is 500 nm and a the edge to edge electrode distance of about $1\mu m$.

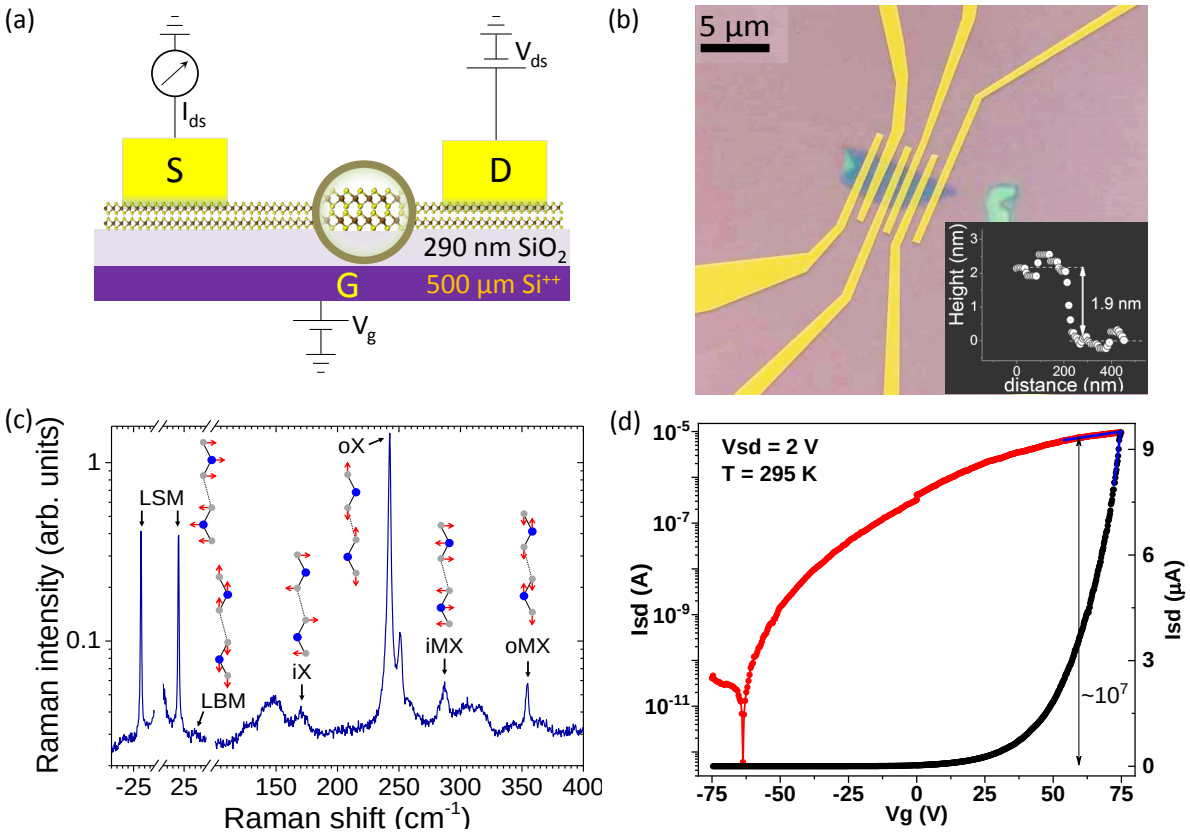

Figure 7.1 *– (a) Schematic of a bilayer $MoSe_2$ transistor with Source (S), Drain(D) and Gate (G) electrodes. (b) Optical image of the multi-electrodes device fabricated using e-beam lithography (colored image). (c) Micro-Raman spectrum taken on the bilayer $MoSe_2$ with schematic representations of the identified optical phonon modes. (d) Room T transfer curve at Vds = 2 V (black curve, right axis). The red curve (left axis) is the log scale representation. The blue lines indicate the linear fit used to extract the mobility.*

7.1.2 Device characterization

The thickness of the exfoliated $MoSe_2$ flake was characterized after electric measurements using both atomic force microscopy (AFM) and Raman spectroscopy. The AFM scan profile (inset of Fi.g7.1.(b)) shows a thickness of 1.9 nm which most likely corresponds to a bilayer [Lu14, Jung15, Pawbake16]. In Fig.7.1.(c) we present the Raman spectrum recorded using a laser photon energy of 2.33 eV. Raman spectroscopy is a powerful technique to study N-layer MX_2 TMDs [Zhang15b]. In particular, the low-frequency Raman modes present a quick and unambiguous way to determine the number of layers [Zhang15b]. Here, the sharp feature at 19.1 cm^{-1} is assigned to the in-plane interlayer shear mode (LSM) of bilayer $MoSe_2$ with E_g symmetry, while the very dim feature near 28 cm^{-1} is assigned to layer breathing mode (LBM) [Chen15a, Soubelet16]. Four other one-phonon features arising from intralayer displacements are also observed: (i) the in-plane, out-of-phase vibration of the Se planes, with Eg symmetry (iX mode at 171.7 cm^{-1}), (ii) the out-of-plane, out-of-phase vibration of the Se planes, with A_{1g} symmetry (oX mode at 242.4 cm^{-1}), (iii) the in-plane vibration of the Mo and Se planes against each other, with Eg symmetry (iMX mode at 287.1 cm^{-1}), and (iv) the out-of-plane vibration of the Mo and Se planes against each other, with A_{1g} symmetry (oMX mode at

354.3 cm^{-1}) [Chen15a]. The multiterminal device with similar electrode (Fig.8.1.(a)), enables performing the transistor characterization on several bilayer channels (Fig.8.1) to increase the level of confidence in measurements. After fabrication, the bonded devices were mounted on the dip-stick of a cryostat for temperature dependent electrical transport measurements as detailed in section.4.3.

7.2 Electric Characterization

In Fig.7.1.(d), we present the typical room T transfer characteristics of the bilayer $MoSe_2$ FET demonstrating an n-type unipolar behavior. The gate modulation of source-drain current could reached almost 7 order of magnitude (on/off ratio $\sim 10^7$) at room temperature, which is among the highest values so far reported on $MoSe_2$ based FET. The finite value of Ids at Vg = 0 V results from unintentional doping of the crystal leading to a displacement of the chemical potential from the middle of the gap to a position closer to the conduction band [Ovchinnikov14].

7.2.1 Field effect mobility

We computed the two terminal Field effect mobility using the expression $\mu = (\frac{dIsd}{dVg})\frac{L}{WC_{ox}V_{sd}}$ where W and L are respectively the length and the width of the channel and C_{ox} the gate capacitance, $\frac{dIsd}{dVg}$ is deduced from the linear fit of transfers curve (see the blue line at high Vg range in Fig.7.1.(d)). The room temperature $\mu = 10cm^2V^{-1}s^{-1}$ falls is the same range as the previously reported Field effect mobilities in 2D SC-TMDs based FET [Radisavljevic13] as well discussed in section.3.2.2. In Fig.7.2.(a) we plot the Isd(Vg) at different T. We clearly observe that the charge transport across the device is facilitate at high T. In Fig.7.2.(b) we plot the mobility (normalized with the room T value) calculated from the temperature dependent I(Vg) curve of Fig.7.2.(a). The field effect mobility decreases with decreasing T. A behavior in dark contrast with the intrinsic mobility of the SC-TMDs, which instead increases with decreasing T mediated by phonon scattering of carriers. This is well detailed in Section.3.3.

The contrasted behavior of the field effect mobility with respect to the intrinsic mobility is a clear proof that the transport of our device is mainly dictated by the interface mechanisms in this temperature range. It also demonstrates that phonon scattering is not the main limiting source of the FET mobility in SC-TMDs based devices. Similar behavior have also been observed in both CVD and exfoliated MoS_2 based transistors and were assigned to scattering from charged impurities [Radisavljevic13, He15] expected to become prominent with decreasing T. In addition, since the field effect mobility is evaluated from the two terminals conductance, a quantitative role of the contacts cannot be ruled out in the observed temperature dependence. We have seen in section.3.2.1 that as the temperature decreases, the current contribution from the thermionic emission at the Metal/SC-TMDs interface is considerably altered. This can likely altered the FET mobility as the temperature is decreasing.

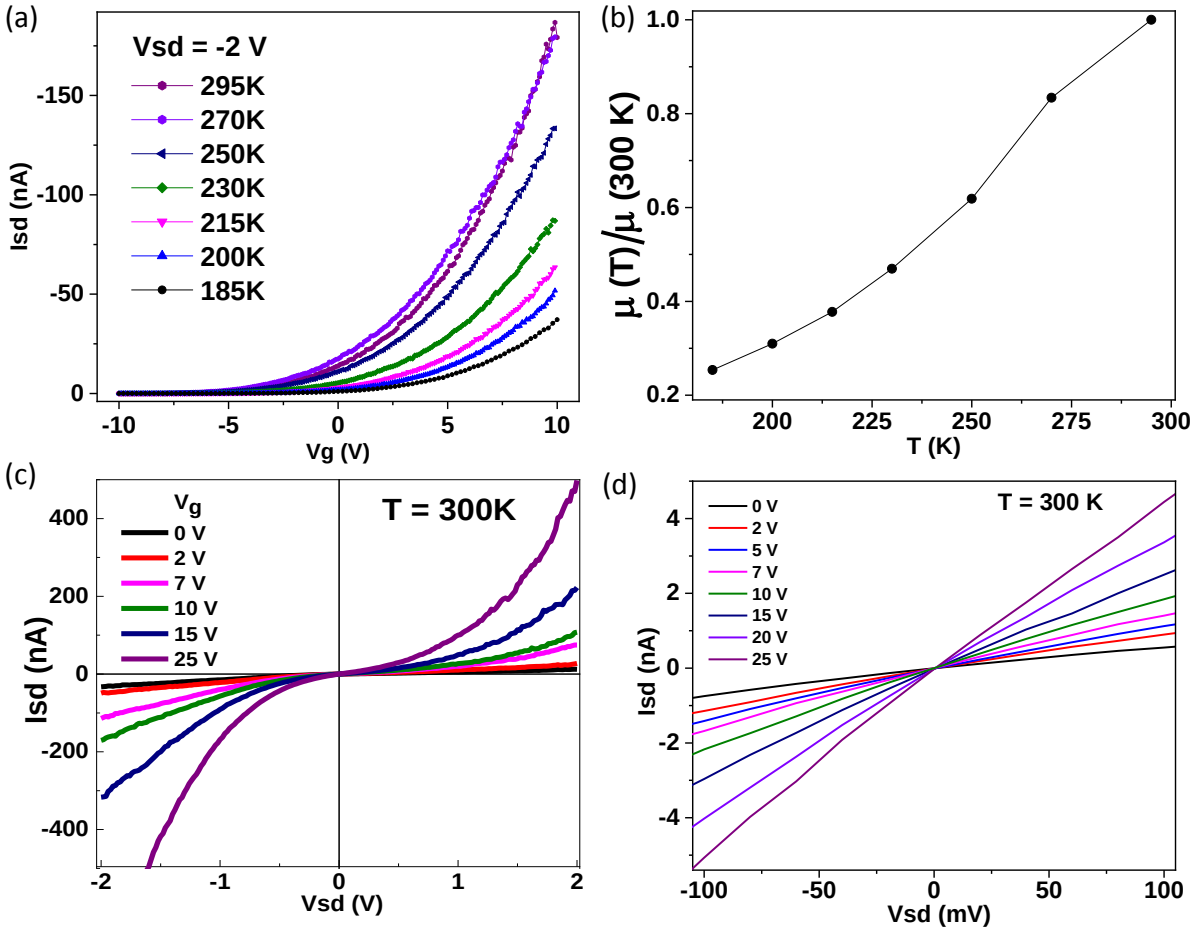

Figure 7.2 *– (a) Isd(Vg) curves measured at different T. (b) Mobility dependency with the temperature. The data were computed from the I(Vg) of (a) and normalized to the room T μ(300K). (c) Is-Vsd characteristics of a bilayer $MoSe_2$ FET at different back gate voltages. (d) Zoom of the of the I-Vsd characteristics of (c) in low Vsd range demonstrating a linear behavior characteristic of low energy direct tunneling/thermionic emission.*

7.2.2 Electric nature of Ti/$MoSe_2$ interface

The Fig.7.2.(c) shows the representative room temperature Ids-Vds curves for different Vg values. The quasi-symmetric non-linear behavior are typical for contacts with a Schottky barrier at the interfaces. It is worth noting that the work functions of $MoSe_2$ ~ 4.7 eV is slightly higher than that of Ti ϕ_{Ti}=4.3eV [Pan16]. Strictly speaking, with bulk material, Metal/semiconductor interface is expected to be Ohmic when the metal work function is smaller compare to the work function of an n-type semiconductor [H. Mathieu09]. The non-linear behavior of I-Vsd characteristics obviously show that it is not the case here. This might be due to the 2D confined nature of $MoSe_2$. Possibly, the VdW interface gap might alters the regime of charge accumulation mediated by electron diffusion from Ti to $MoSe_2$ that could have been responsible for Ohmic interface. Pan *et al.* argued that the Schottky barrier height (SBH) does not merely depend on the discrepancy between the intrinsic Fermi level of a metal and the intrinsic conduction band minimum or valence band maximum of the semiconductor

owing to the complex Fermi level pinning. Using both DFT and Quantum transport calculations, they demonstrated an n-type Schottky contact at $MoSe_2$/Ti interface with a Schottky barrier high (SBH) of 0.29 eV [Pan16].
Linear behavior of I-Vsd characteristics is recurrently observed in 2D SC-TMDs based FETs (most often at low dc bias range) and has been widely argued to originate from Ohmic contact formation at metal/SC-TMDs interface [Liu13, Radisavljevic13, He15]. However, Das et al. [Das13b] demonstrated that such a behavior is not necessarily an indication of an Ohmic contact and proposed that it may be originating from thermionic emission or thermal assisted tunneling through the interface energy barreir. They provided an unambiguous demonstration of the presence of Schottky barrier at the Metal/MoS_2 interface (see section.3.2.2). In Fig.7.2.(d) we plot the low Vsd range of I-Vsd presented in Fig.7.2.(c). They provide, in the low Vsd regime a linear behavior contrasting with their pronounced non linearity at high Vsd range. A Schottky type of interface between MoS_2 and different metal including Au and Ti was also confirmed by DFT and Quantum transport calculations calculation [Zhong16].

7.3 Metal/$MoSe_2$ interface transport processes

To uncover the charge injection mechanisms across Au-Ti/$MoSe_2$ interface, we performed thorough investigations of the Ids-Vds characteristics while varying the gate voltage in the temperature range of 200-300 K. Depending on the doping level, the barrier profile and the temperature, different transport mechanism regimes can be reached. From the quantitative dependency of the output characteristics, we could identify the dominant mechanism for given bias and temperature regime.

7.3.1 Interface band modulation and the injection mechanisms

To clarify the understanding of the tunable transport mechanisms, we show a schematic diagram of field effect induced band bending scenarios a Ti/$MoSe_2$ interface under different conditions in Fig.7.3.(c). At low gate voltages, the contact interface barrier is characterized by an activation energy E_a higher than the intrinsic SBH $q\phi_{B0} = q(\phi_m - \chi_{SC})$. The quantities $E_a = q\phi_{B0} + (E_c^{\infty} - E_c^0)$ and $q\phi_{B0}$ are the same as in section.3.2.1. We remind that $q\phi_m$ and $q\chi_{SC}$ denote the metal's work function and the 2D semiconductor's electron affinity. The activation energy description also takes into account the subthreshold regime (at very low gate voltages) of thermally activated transport $I \propto e^{(-E_a/kT)}$ in addition to the thermionic emission (TE) regime [Allain15].

Thermionic emission

Increasing the gate voltage V_G induces an increase of the doping level of the 2D SC-TMDs channel leading to downward bending of its conduction band until the flat-band (FB) condition for $V_G = V_{FB}$ where $E_a = q\phi_{B0}$ (see Fig.7.3.(d), middle schematics). Before the FB is reached, at high temperature and in low Vg & Vds regime, the width of the interface barrier is

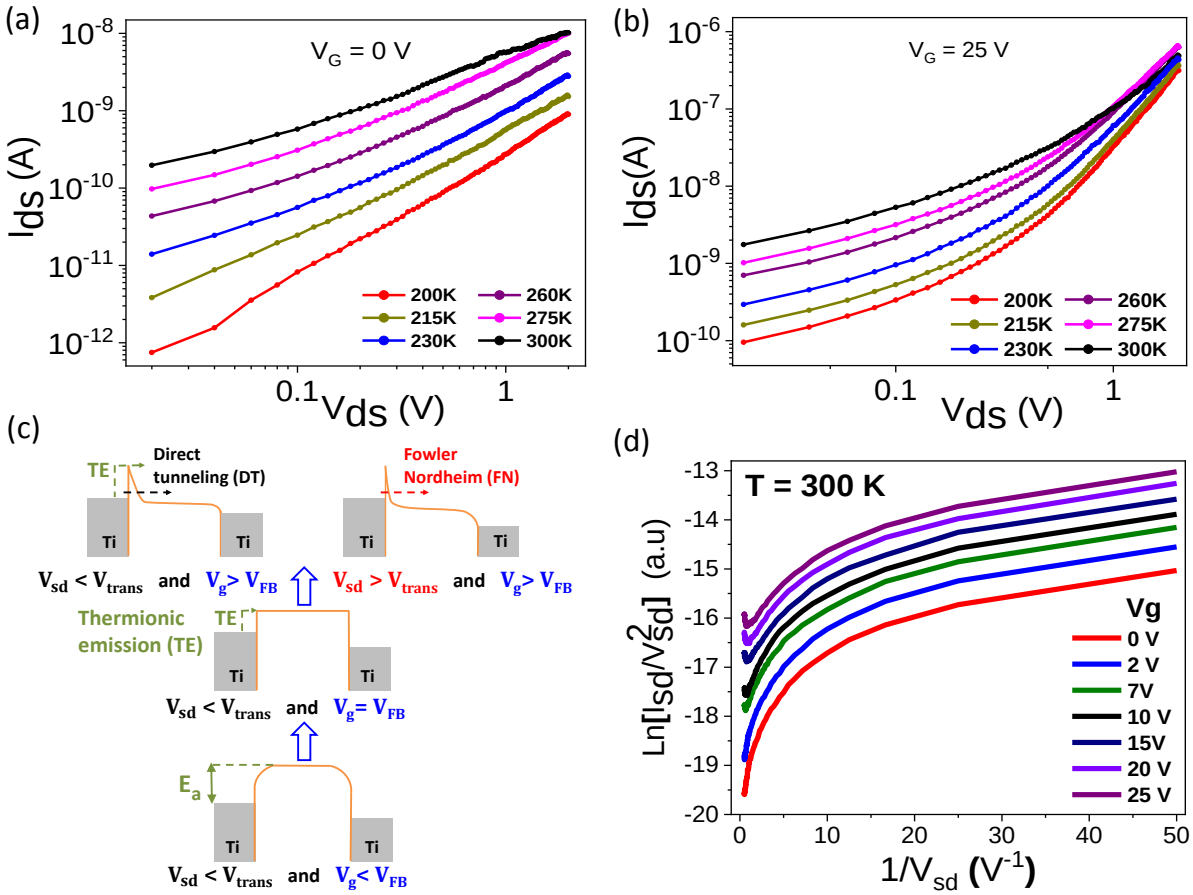

Figure 7.3 – *Temperature dependent I-Vsd characteristics of a bilayer $MoSe_2$ transistor at (a) Vg = 0 V, (b) Vg = 25 V. Both Isd and Vsd axis are in log scale to unveil linear behavior expected from direct tunneling. (c) $MoSe_2$/Ti interface band bending behavior with increasing Vg (from bottom to top) and dc bias Vsd after the flat band (top, from left to right). Flat band regime is reached for $Vg = V_{FB}$ (middle drawing). The injection becomes dominated by Fowler-Nordheim tunneling for $Vg > V_{FB}$ and $Vsd > V_{trans}$. (d) FN representation ($ln(I/V^2)v.s.1/V$) of the room T I-Vsd characteristics. No a contribution of FN tunelling is noticeable a low Vg.*

very large. The charge injection mechanism is primarily dominated by thermal emission over the contact energy barrier E_a from the metal Fermi level into the conduction band of $MoSe_2$. Then, the current trough the device is given by Eq7.1 as derived in the appendix.B (see also section.3.2.1).

$$Isd = AA^*_{2D}T^{3/2}\exp[-\frac{1}{k_BT}(E_a - \frac{qV}{n})] \tag{7.1}$$

Where A is the contact area, A^*_{2D} the effective 2D Richardson constant, q the charge of the electron and n the ideality factor. The Fig.7.3.(a) presents in log-log scale the I-Vsd characteristics measured at different T for Vg = 0. In low Vsd regime, one observes more than 2 orders of magnitude increase of the room T current relatively to the 200 K current. In contrasts only 1 order of magnitude enhancement is noticed at high Vsd regime. For Vg = 25 V (Fig.7.3.(b)), the enhancement of the room T Isd (Vsd) relatively to 200 K Isd (Vsd) is lower, but remains however higher in low Vsd range compare to high Vsd range. This clearly indicates thermionic emission or thermal activation as the dominant interface charge injection

mechanism at high T particularly in the low Vsd (up to 0.5 V approximately) and Vg regime. The distinction from low and high Vg and Vds regimes with the I-Vsd is particularly clear in Fig.7.3.(b) compare to Fig.7.3.(a). In the former, the characteristics measured at Vg = 25 V show less temperature dependency for Vds > 0.5 V compare to the later figure. This demonstrates a possible transition to a transport mechanisms different from thermionic emission.

Direct tunneling

Beyond the flatband condition where Schottky barrier is formed at the Au/Ti-$MoSe_2$ interface, higher gate voltages bend more deeply downward the bands of the semi-conductor channel. Then, due to the conjugate effects of both V_g and Vsd, the interface band structure of the device undergoes a triangular shape. The height ($E_a = q\phi_{B0}$) of the interface energy barrier becomes irrelevant as its width is getting progressively tinner driven by both Vsd and Vg (Fig.7.3.(c), top-left drawing). This band configuration is suitable for promoting direct tunneling transport mechanism most common in MIS or MOS devices as explained in section.3.2.2 [Sze81, Simmons63]. The current trough the device is thus given by Eq.7.2.

$$Isd \propto V_{sd} exp[-kd\sqrt{E_a}] \tag{7.2}$$

Where $k = 4\pi\sqrt{2m^*}/h$ and d represents the average barrier width, with m^* the electron effective mass and h the Planck constant. In the case of direct tunneling (DT) mechanism, a linear behavior of the VIsd curves is expected accordingly to Eq.7.2. Given that the I-Vsd curves of Fig.7.3.(a,b) are presented with log scale of both Isd and Vsd axis, the linear behavior of the current at low temperature for Vg = 0 (Fig.7.3.(a)) is a characteristic feature of low energy DT consistently with Eq.7.2 providing $log(Isd) \propto log(V_{sd})$. As the T increases, the Isd curves progressively deviated from the simple linear behavior and follows two sublinear behaviors at low and high Vsd with different slopes (smaller at low Vsd and higher at higher Vsd). Such a behavior is more pronounced at Vg = 25 V (Fig.7.3.(b)). We demonstrate in the next section that lower Vsd sublinear regime is still characteristic of DT while the higher Vsd regime is attributed to Fowler-Nordheim tunneling (Fig.7.2.(d)).

Fowler-Nordheim tunneling

Regardless of the temperature, as both Vsd and Vg increase further, the width of the interface barrier continues to decreasing and the system undergoes a transition at Vsd = V_{trans} above which the width of the interface barrier becomes extremely tiny (Fig.7.3.(c), top-right drawing). The current becomes essentially driven by Field assisted tunneling also known as Fowler-Nordheim tunneling given by Eq.7.3 (see section.3.2.2 for details).

$$Isd \propto V_{sd}^2 exp(-k^{'} d E_a \sqrt{E_a}/V_{sd}) \tag{7.3}$$

With $k' = 8\pi\sqrt{2m^*}/3qh$.
To unveil the Fowler-Nordheim mechanism, we plot the data in terms of $ln(I/V^2)$ ***v.s.*** $1/V$

expected to present a linear behavior (Fig.7.3.(d) and Fig.7.4). These FN plot enables to illustrate the transition from DT/TE regime at low Vsd range to FN at high Vsd regimes. Indeed, the low-bias regime with a positive slope originates from direct tunneling that varies as $ln(1/V)$ (Eq.7.2) and/or thermionic emission varying as $V + 2ln(1/V)$ (Eq.7.1). The negative slope regime is typical for Fowler-Nordheim tunneling or field emission through the tinny interface energy barrier width where the current evolves as $-1/V$ (Eq.7.3). At room temperature, we observed not an important contribution of FN tunneling (Fig.7.3.(d)) the same as at low gate voltage quite clear from Fig.7.4.(a) with no noticeable FN contribution in the whole T range. In higher Vg range however, when the temperature decreases, FN tunneling starts emerging first at high Vg and intermediate T before to propagate also at lower gate voltages as T decreases further (Fig.7.4.(b,c)). The frontier between the two regions lies at a particular

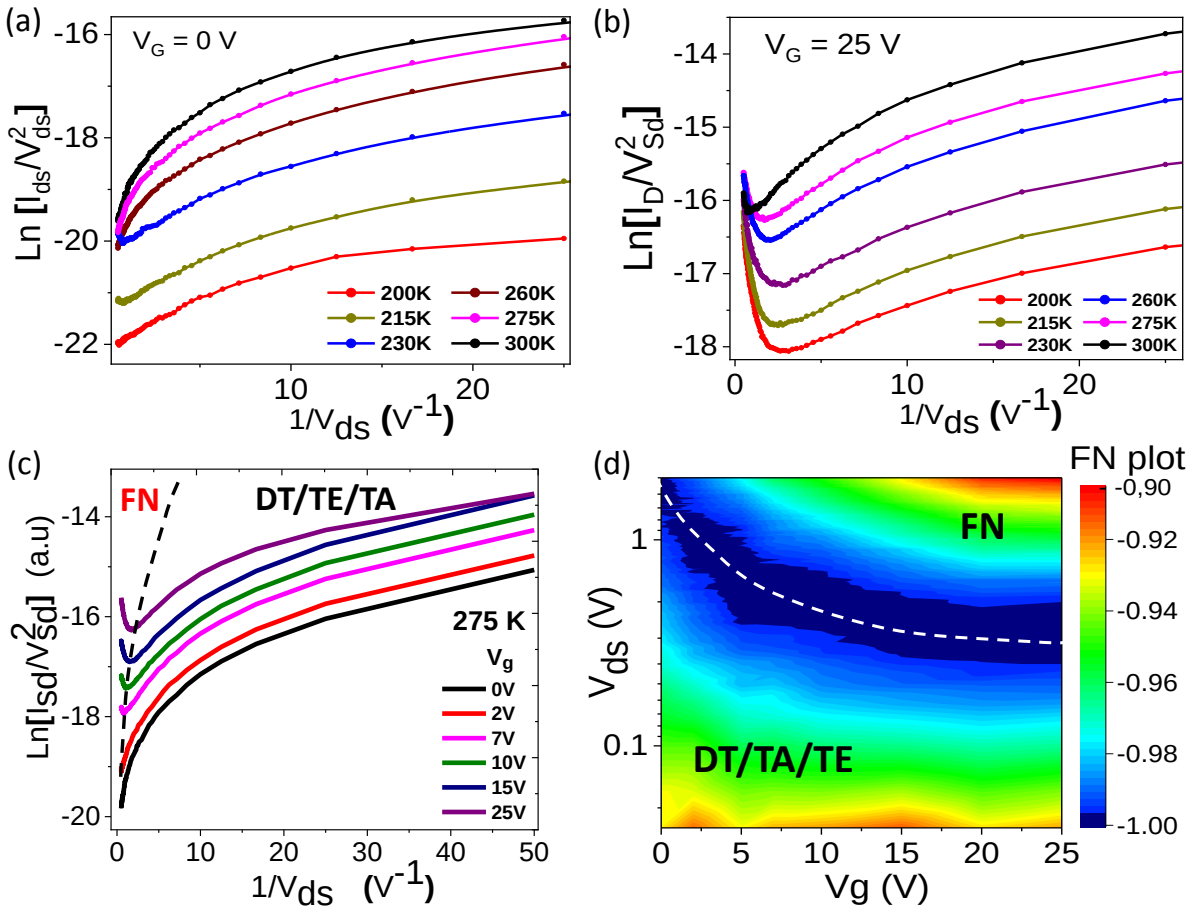

Figure 7.4 *– FN representation ($ln(I/V^2)$v.s.$1/V$) of the I-Vsd characteristics of at different temperatures and Vg. (a) Vg = 0 V. No noticeable FN tunneling contribution. (b) Vg = 25 V. FN tunneling dominate at high Vsd above V_{trans}. (c) FN representation of the IVsd curves for different Vg at 275 K. The black dished line shows the evolution of V_{trans} with Vg. (d) 2D color plot of normalized Fowler-Nordheim computation of the IVsd measured at 200 K versus Vg (linear scale) and Vds (log-scale) showing a transition at V_{trans}, corresponding to the minimum value of each FN trace for a given Vg (minima are at -1 in the normalized computed data). The white dashed line displays the variation of V_{trans} with Vg.*

dc transition bias voltage V_{trans}, which depends on the applied Vg and T (Fig.7.4.(c & d)). While at Vg = 0 we observe no transition to FN region in the whole T range (Fig.7.3.(d)), a clear transition to FN region is observed for Vg = 25 V, with a significant temperature depen-

dence of Vtrans (Fig.7.4.(c), black dished lines). A characteristic Vg dependency of V_{trans} can be evidenced in a contour plot presented in Fig.7.4.(d) (white dashed line), reporting the FN calculations of the data recorded at 200 K versus Vg. For the sake of clarity, the vertical axis of the contour plot is taken as Vds instead of 1/Vds, providing a direct reading of the value of V_{trans}. A correlation between V_{trans} and Vg reported on single molecule transistors [Song09] is uncovered here in 2D crystals based FETs. We will elaborate on this later.
To conclude, the FN tunneling dominates the transport at higher Vds (> V_{trans}) and Vg and lower temperature (T < 300 K) mediated by a tiny interface barrier width resulting from the electrostatic tuning of the band profile of $MoSe_2$ (as depicted in Fig.7.3.(c)). In contrast, the direct tunneling/thermionic emission across the interface energy barrier dominates the transport mechanisms in the temperature range 240-300 K and for $0.1 \gtrsim Vds \lesssim 0.5V$. It is supplanted by thermal activation out of this energy window. Such clear demarcation is essential to analyze the I-Vsd characteristics in the right Vds regime with the appropriate formalism.

7.3.2 Schottky barrier extraction

Having identified the main charge injection mechanisms and their corresponding bias ranges, we now analyze the back gate dependency of the interface activation energy within the optimum dc bias range ($0.1 \gtrsim Vds \lesssim 0.5V$) for a faithful evaluation of the intrinsic Schottky barrier height ϕ_{B0}. For this purpose we follow the methodology described in section.3.2.1 by reformulating the Eq.7.1 as follow :

$$ln(\frac{I_{sd}}{T^{3/2}}) = -\frac{1}{T}(\frac{E_a}{k_B} - \frac{qV_{sd}}{nk_B}) + ln(AA^*_{2D}) \tag{7.4}$$

In Fig.7.5.(a), we present the typical temperature dependency of the I-Vsd characteristics at a gate voltage of Vg = 15 V, plotted in the Arrhenius representation of $ln(\frac{I_{sd}}{T^{3/2}})$ ***v.s.*** $\frac{1000}{T}$ for different dc bias voltage values. The corresponding slope $S = (\frac{E_a}{k_B} - \frac{qVsd}{nk_B})$ obtained for each values of the dc bias voltages and plotted in Fig.7.5.(b) exhibits an expected linear behavior. The activation energy E_a is simply deduced from the value of the intercept (E_a/k_B) at $V_{ds} = 0$. The obtained values are presented in Fig.7.5.(c), for different gate voltages. One observes that before the interface energy band reaches the flat-band condition, the activation energy E_a decreases linearly with Vg as $E_a = q\phi_{B0} - q(Vg - V_{FB})/(1 + C_{int}/C_{ox})$, where C_{ox} and C_{int} are respectively the gate oxide and interface trap capacitances [Das13b, Allain15]. These values of E_a are similar to those found in other transition metal dichalcogenides [Das13b, Dankert14, Ovchinnikov14, Zhang15a] (see section.3.2.1). A change in the slope in Fig.7.5.(c) at Vg = 10 V indicates the flat-band condition where the activation energy is identical to the intrinsic SBH $E_a = q\phi_{B0}$. Above the FB ($Vg > V_{FB}$), we observed smaller modulation rate of E_a with Vg (smaller slope). This may be an indication of the change of the ideality factor n [Sze81]. It may as well be related to the fact that Ti/MoS_2 interface barrier height becomes less affected by Vg above the FB where its width takes over the control of the injection mechanism now arising from tunneling mechanisms rather than pure thermionic emission.

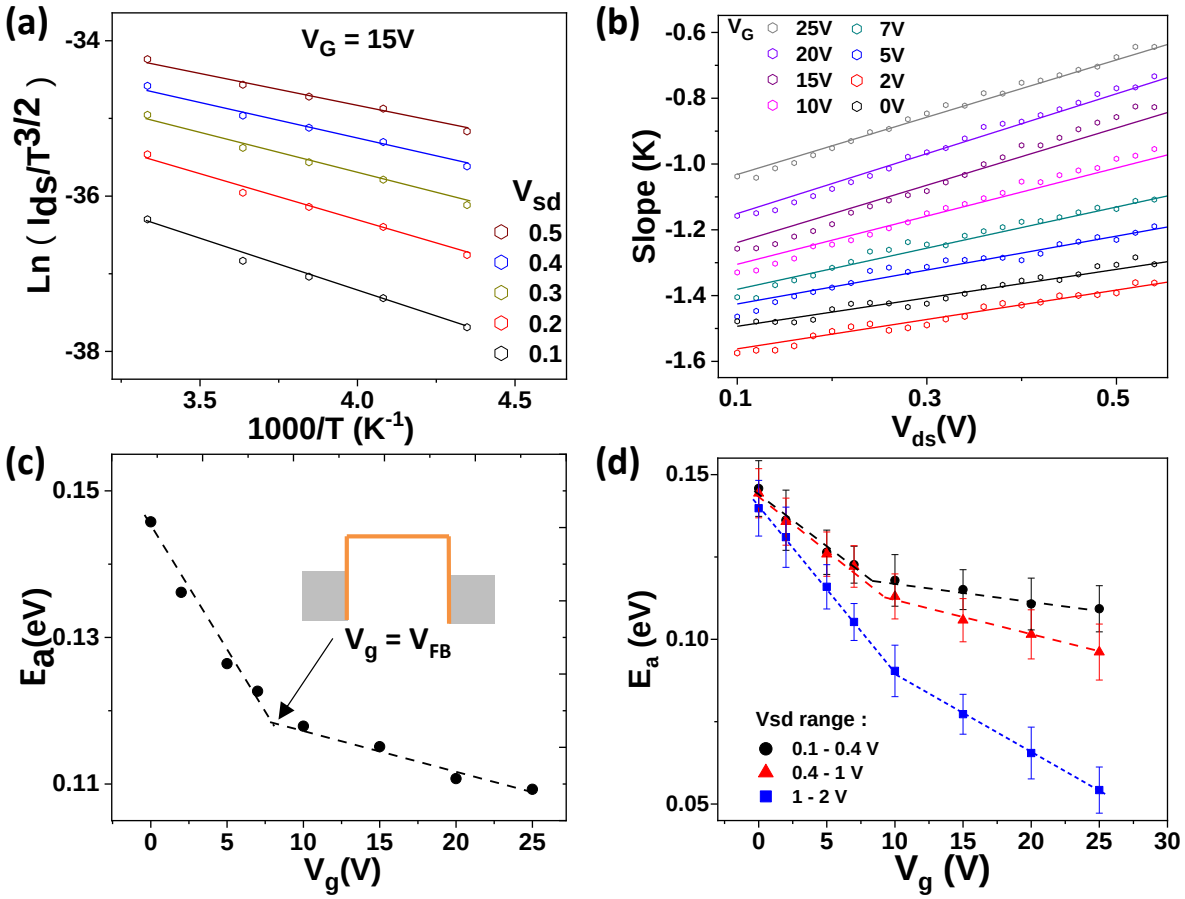

Figure 7.5 *– Evaluation of the Schottky barrier hight ($q\phi_{B0}$). (a) Arrhenius representation ($ln(\frac{I_{sd}}{T^{3/2}})$ v.s. $\frac{1000}{T}$) of the I(Vsd) curves for different temperatures for Vg = 15 V. A similar analysis were realized for all Vg values for the purpose of SBH evaluation. (b) Vds dependency of the slope obtained from the linear fit of the arrhenius representation (a) for all Vg. The intercept at Vds = 0 gives the activation energy E_a for the corresponding Vg. (c) E_a v.s. Vg plotted from the values extracted from (b). The flat band (FB) transition is achieved at Vg = 10 V. The corresponding value of E_a is equal to the SBH.*

The obtained Schottky barrier height at FB $q\phi_{B0} \sim 115$ meV is relatively lower compared to theoretical prediction for multilayer $MoSe_2$ [Pan16]. Nevertheless, it remains in the same range with previous reports on $MoSe_2$/Ti FET [Chamlagain14] and other SC-TMDs/metal FET [Dankert14, Allain15]. However, a caution is necessary when comparing the obtained value of the SBH with the available literature as the thicknesses of the 2D crystals used are often not the same. More importantly the SBH ϕ_{B0} is not always evaluated in the appropriate transport regime. Indeed, we observe a strong dependency of E_a with Vsd, particularly in high Vsd range (Vsd > 1 V) away from thermionic regime. In this regime, the SHB $q\phi_{B0}$ is significantly under estimated (Fig.7.5.(d)). For instance, although the extracted intrinsic SBH at the FB is about 115 meV in $[0.1V; 0.4V]$ Vsd range and a bit lower in $[0.4V; 1V]$ range, it is reduced to 80 meV $[1V; 2V]$ range (Fig.7.5.(d)).

7.4 Interplay between FN-tunneling and Thermionic emission

We now explore in detail the transition process from direct tunneling/thermionic emission regimes to FN tunneling regime. It is clear from the above analysis that the interface charge injection mechanisms at distinct transport regimes are directly related to the interface band profile characterized by its height E_a and width which are modulated by the voltages and temperature. A quantitative evolution of V_{trans} with increasing temperature for different Vg

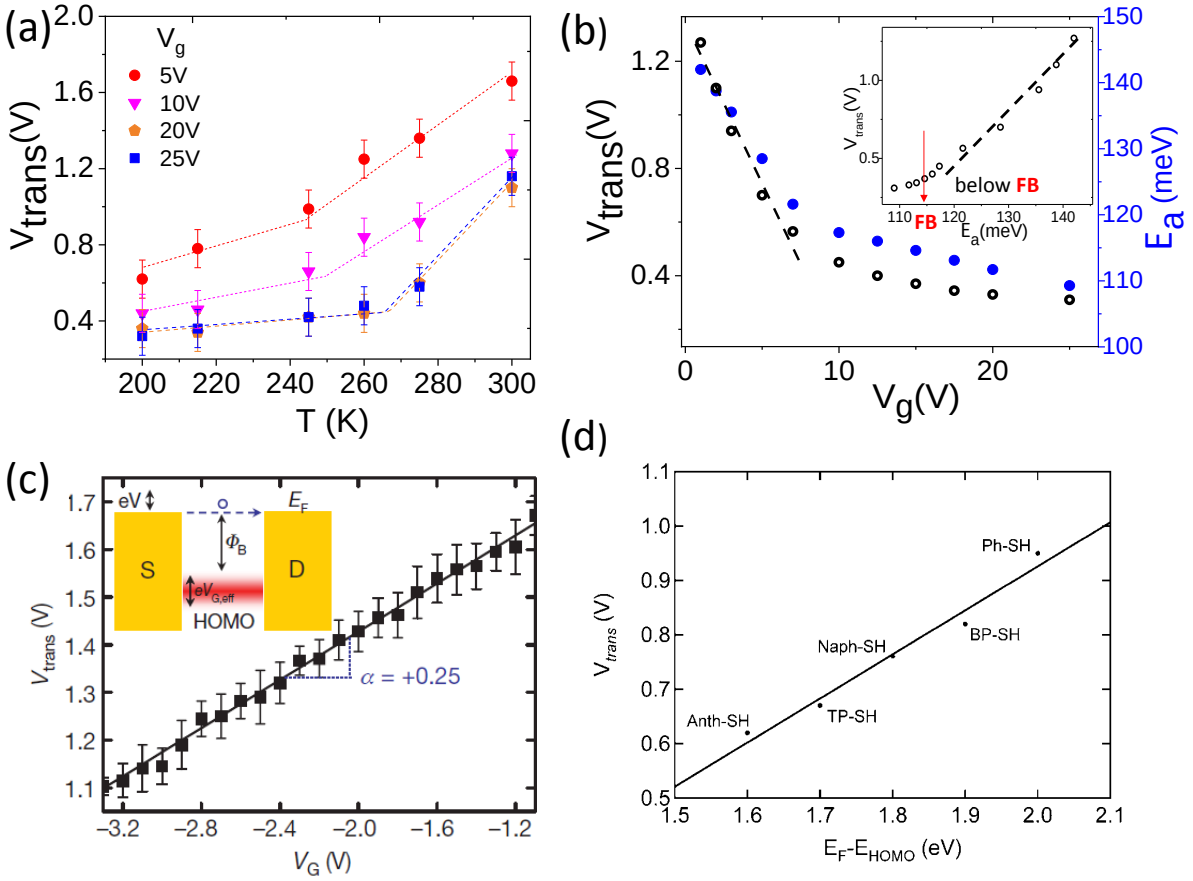

Figure 7.6 *– (a) Evolution of V_{trans} with temperature for different gate voltages. (b) Correlation between the transition voltage V_{trans} extracted from the Fowler-Nordheim computation at 200 K (black curve, left axis) and the activation energy E_a (blue curve, right axis) as function V_G. The inset is the correlation between E_a and V_{trans} with and almost linear scaling below flat band. (c) Dependency of V_{trans} with Vg in molecular junctions (see the inset). (d) V_{trans}* v.s. *ϕ_{mol} for different molecules.*

is presented in Fig.7.6.(a). At room T, one observes that the transition to FN tunneling regime takes place at relatively large dc transition voltages. This is consistent with the dominance of DT/TH at high T. The values of V_{trans} decreases with increasing Vg meaning that at room T, the high voltages distortion of the interface band profile however promote the contribution of FN tunneling (Fig.7.6.(a)). In addition, the decrease of V_{trans} with increasing Vg at other lower temperatures is consistence with the fact that the Vsd range of validity of FN tunneling is larger at lower T and can be extended by further Vg distortion of the 2D SC-TMDs band diagram (Fig.7.6.(a)). To better understand the correlation between V_{trans} and the E_a, we fo-

cus on the I-Vsd characteristics at 200 K where low voltages transport is solely dominated by DT since TH becomes negligible. In Fig.7.6.(b), we display the transition voltage V_{trans} extracted from the Fowler-Nordheim plots along with the activation energy E_a as a function of Vg. Remarkably, both curves demonstrate very similar Vg dependency. This reinforces an expected correlation between Vg and E_a. An analogy can be done between the V_{trans}-E_a correlation observed here for Metal/2D SC-TMDs interfaces and the correlations previously explored in single molecule tunnel junction transistors [Beebe06, Song09, Huisman09] in which the transition from DT to FN is common (see section.3.2.2). These reports observed a simple linear dependency of V_{trans} with with the gate voltage [Beebe06] (Fig.7.6.(c)). In addition, they observed that V_{trans} scales linearly with ϕ_{mol} for the transport measurements done on different molecules (Fig.7.6.(d)) [Huisman09, Song09]. Note that ϕ_{mol} denotes the energy difference between the electrode's chemical potentials and the lowest unoccupied molecular orbital (LUMO).
In our case, before the flat band condition (Vg<V_{FB}), the activation energy is the energy difference between the electrodes chemical potentials and the interface conduction band minima of the 2D SC-TMDs. Hence, in the overall activation energy description of the 2D SC-TMDs/metal interface, E_a can be argued to play a role similar to ϕ_{mol} in the molecular junctions. Its modulation with Vg enables a direct correlation of both quantities for a unique device. Before the FB condition, we observe a reasonably linear behavior of the V_{trans} with both Vg (Fig.7.6.(b)) and also with the activation energy E_a (the insert of Fig.7.6.(b)). However, we do acknowledge that the 2D material systems have distinct interface band landscape compared to molecular systems. Specifically, the larger barrier width, and its modification with Vg, can significantly alter the simpler dependency observed in molecular systems. We believe that further theoretical studies in different transport regimes, together with fine modeling of the electrostatics interaction at contact interfaces explicitly including charge image induced reduction of the barrier (as involving 2D SC-TMDs) are desired for a better understanding of the of the V_{trans} (E_a) dependency.

7.5 Conclusion

We have presented in this chapter the detail investigation of the interface charge injection mechanisms in bilayer $MoSe_2$ FETs with high on/off ratio. A comprehensive study based on Ti/$MoSe_2$ Schottky interface energy band profile modulation using both Vsd, Vg and the temperature enables to elucidate a complete picture of the charge injection mechanism. At higher temperature, thermal activation is identified at very low Vsd and Vg while thermionic emission or direct tunneling mediates the injection mechanism at intermediate Vsd and Vg independently of the temperature range. We have observed a transition to Fowler-Nordheim tunneling at high voltages particularly in the lower T range. Such a clear demarcation of different transport regime enables a faithful evaluation of the intrinsic Schottky barrier ϕ_{B0} = 115 meV in the appropriate thermionic emission regime. Furthermore, the analysis of the transition voltage form TE/DT to FN tunneling unveils a direct correlation with the activation

energy providing thus an opportunities for further theoretical and experimental investigations. Such an understanding of the transport mechanism(s) across Metal/2D SC-TMDs interfaces is crucial for appropriate contact engineering targeting 2D materials based spin-FETs devices [Allain15]. Our approach being generic, it can be extended to the interfaces between metal and other 2D semiconducting crystals.

Chapter 8

MoS_2-Al 2D-0D heterostructures for vertical Single Electron Transistor

In this chapter, we report on the transport properties of Al-AlOx/MoS_2 based 2D-0D SET. We demonstrate that an evaporation of an ultra thin Al layer (1.7 nm) onto the surface of a MoS_2 flake exfoliated on Si-SiO_2 substrate results to a granular layer of Al nanoparticles which after oxidation provides a core-shell configuration suitable for single electron transport processes. Low temperature measurements demonstrate a back gate voltage dependent conductance oscillations with a superimposed field effect characteristics of the MoS_2 channel. The stability diagram of conductance exhibits remarkable Coulomb diamonds patterns characteristic of SET. This work opens doors to alternative SET architectures using 2D-0D MD-VdWh circumventing the usual fabrication challenges and provides the important prospect of 2D-0D MD-VdWh for nanoelectronics.

8.1 Device and characterization

The devices studied in this chapter consist of a monolayer MoS_2 mechanically exfoliated on a clean p^{++}-Si/SiO_2 substrate. Electrodes are subsequently patterned onto the exfoliated flake using electron beam lithography. A thin aluminum layer of 1.7 nm nominal thickness is then deposited into to the prepatterned electrodes. The resulting granular Al layer is after oxidized in ambient atmosphere during one hour to form the 2D-0D heterostructure composed of 2D MoS_2 and Al based nanoclusters with average diameter close to 7 nm. E-beam evaporation of 40 nm thick Co top electrode capped by 10 nm Au completes the stack. The details of the sample fabrication methods are described in chap.4 were we presented our fabrication method for both Gr and MoS_2 based 2D-0D heterostructures and their integration into

heterojunctions suitable for SED. The Fig.8.1.(a) shows the schematic representation of the device with a 'planar' architecture of the 2D-0D SET. Each SET cell consists of a stack of a Au/Co top electrode contacting the granular oxidized Al layer grown on the surface of the underneath MoS_2. The capacitively coupled doped Si (p^{++}-Si) serves as a back gate (G) electrode for electrostatic doping of the MoS_2 and for the modulation of the electric state of the supported Al NPs while exploiting the transparency of the 2D material to the vertical gate electric field (see also Chap.5 for graphene based 2D-0D SET). It is worth emphasizing that the Physico-chemical analysis of the oxidized granular Al layer on MoS_2 are ongoing in collaboration with Dr. L. Simon's group at the Institute of Material Science of Mulhouse-France, for X-ray Photoelectron Spectroscopy (XPS) and Pr Prof. O. Ersen (IPCMS) for STEM and EELS analysis. However, given that these heterostructures are fabricated in the same environment and conditions and present similar morphology as the Al-AlOx/Gr 2D-0D heterostructures for which the NPs demonstrated a core-shell structure with a metallic core embedded in an alumina shell matrix (section.4.2), we also admit such a core-shell structure for the NPs of the Al-AlOx/MoS_2 heterostructures at this stage of our study.

On the optical image of the device presented in Fig.8.1.(b), one distinguishes multiple ter-

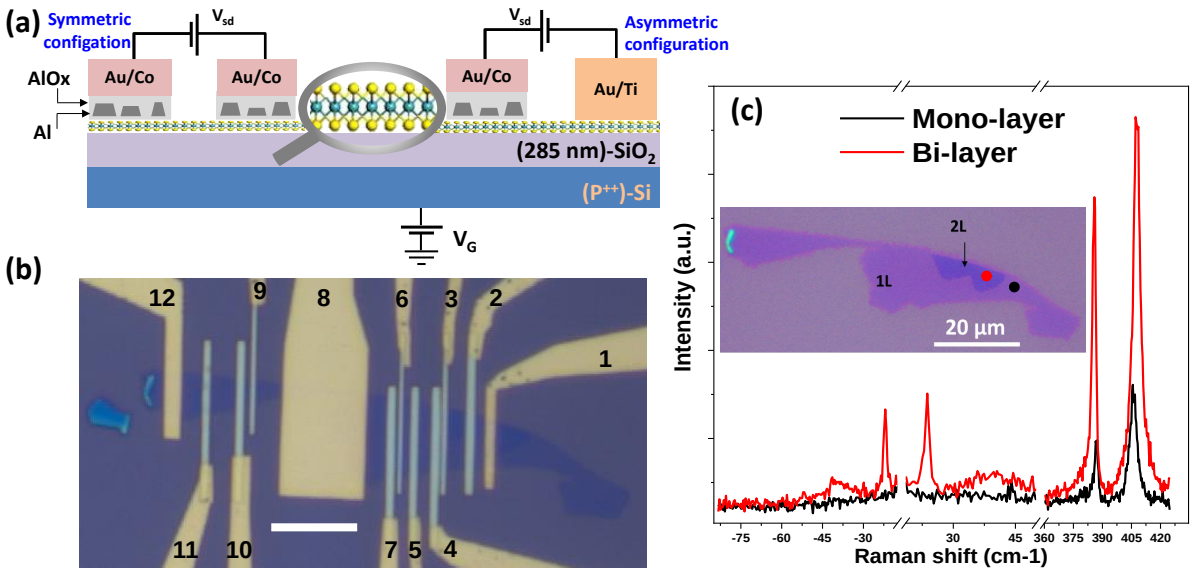

Figure 8.1 *– (a) Schematic representation of the devices highlighting the symmetric and asymmetric electric polarization configurations. (b) The optical micrograph of the device. The scale bar is 10 µm. The digits serve for electrodes identification as refereed to in the text. (c) Raman spectrum recorded respectively at the mono and bilayer regions indicated by the black and red dot on the inserted optical micrograph of the flake.*

minals 2D-0D SET cells over the MoS_2 flake (the white smaller electrodes : 2 to 7 and 9 to 11) in addition to the Ti(3nm)/Au(47 nm metallic electrodes (the electrodes 1, 8 and 12) in direct contact with the MoS_2 flake forming thus Schottky junctions. Hence, a typical three terminals 2D-0D SET can either be composed of two distinct SET cells as illustrated in the schematic representation, or one 2D-0D cell and one MoS_2/Ti-Au Schottky contact. We refer to as "symmetric" and "asymmetric" configurations respectively (Fig.8.1.(a)).

The thickness of the exfoliated MoS_2 flake was characterized by optical contrast and Raman

spectroscopy. In Fig.8.1.(c) we present the Raman spectrum recorded using a laser photon source with energy of 2.33 eV. The red and black dot on the inserted optical image of the flake indicate the location of the Raman spots corresponding to the red and black curves respectively (Fig.8.1.(c)). One denotes on the black curve the absence of low-frequency in-plane interlayer shear modes and layer breathing modes near 19.1 cm^{-1} and 28 cm^{-1} respectively. These particular characteristics of monolayer TMDs present on black Raman spectrum contrast with the red spectrum taken on the bilayer region. Indeed, two other one-phonon intralayer Raman modes also generally present in bulk MoS_2 are observed in both curves at high frequency close to 387 cm^{-1} (E_{2g}) and 408 cm^{-1} (A_{1g}). The (E_{2g}) peak arises from out of phase vibration of the two S atoms with respect to Mo atom while the A_{1g} mode arises from out of plane vibration of the S atoms in the opposite directions.

8.2 Low temperature transport measurements

8.2.1 Asymmetric configuration

In Fig.8.2.(a) we show the typical low temperature I-Vsd (black curve, left axis) and the corresponding differential conductance (dI/dVsd-Vsd, red curve and right axis) characteristics of the device measured at Vg = 40 V in asymmetric configuration with a single SET cell involving the electrodes 1 and 3. The channel length between the electrodes is 3.5 μm and its width is 5 μm. We observe a pronounced asymmetry of the current (respectively the conductance) for positive and negative Vsd. This is related to the asymmetric configuration of the device. In usual SC-TMDs FET with both the source and drain electrodes in direct contact with the channel forming two Schottky diodes connected to back-to-back in series [Allain15], when the dc bias is positive, the Schottky diode at the source (respectively the drain) is forward polarized (respectively reverse polarized) and the current of the device mainly originates from charge injection from the source. For negative dc bias, the situation is reversed and the drain diode takes over the functioning of the FET. This often results to transport characteristics presenting a less pronounced asymmetry originating from the unavoidable slight inequality of the interface activation energy of the Schottky contact. In Chap.7, where we presented our experiment results of the detailed study of interface charge injection mechanisms, the asymmetric of the I-Vsd characteristics where not sufficiently pronounced to be mentioned. In the asymmetric configuration discussed here, the junction with alumina tunnel barrier is expected to be more conducting since oxide tunnel barriers have proven to reduce Schottky barrier height and the contact resistance between MoS_2 and metallic electrodes (see section.3.2.1).

Superimposed to this asymmetric non-linearity, we observed Coulomb staircase like behavior of the I-Vsd characteristics. Although hidden by the rapid exponential increase of the current (Fig.8.2.(a), black curve, left axis), these single electron features appear much better in the log scale of dI/dVsd which presents regular and well defined peaks in both polarities of the dc bias as highlighted by the black arrows in Fig.8.2.(a). The Fig.8.2.(b) presents the corresponding transfer characteristics (Isd-Vg) of the SET measured in the same asymmetric

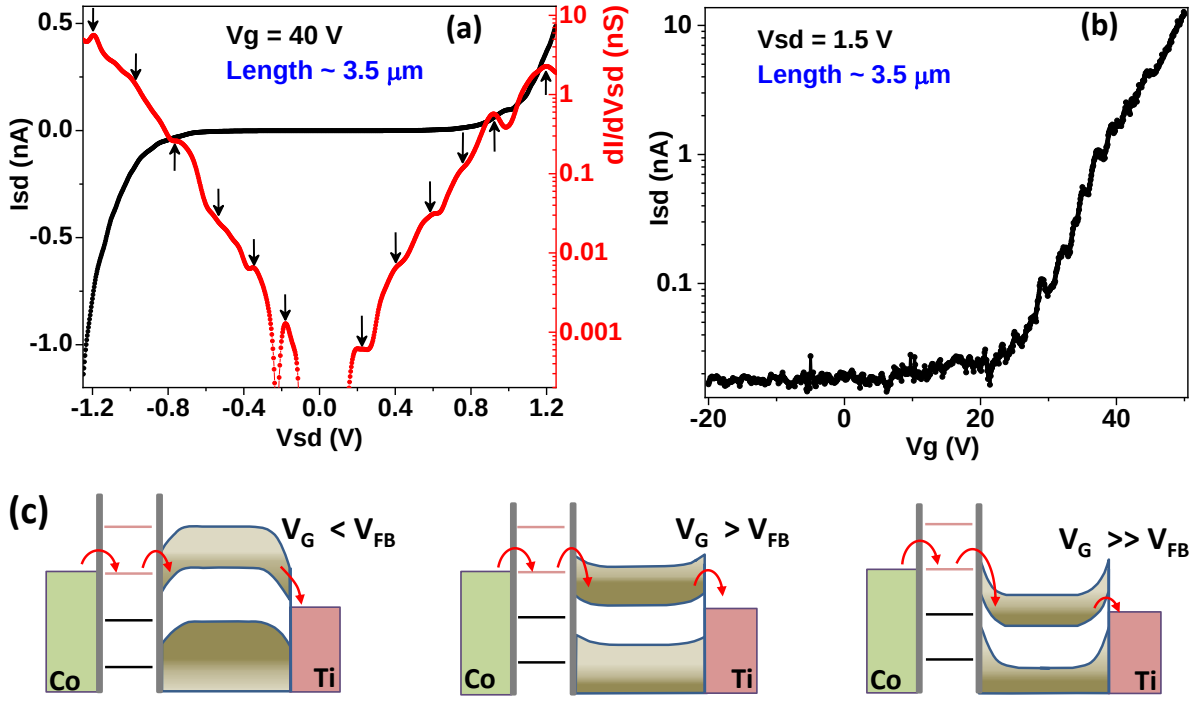

Figure 8.2 *– Transport measurement at 1.5 K in the asymmetric configuration involving the electrodes 1-3. The channel length is 3.5µm (a) I-Vsd characteristic (black curves, left axis) and the corresponding differential conductance (red curve, right axis) measured for V_G = 29 V. The black arrows highlight the positions of the conductance peaks. (b) I(Vg) curve measured for Vsd = 1.5 V. (c) The energy band diagram illustrating the tunneling process within the devices. V_{FB} stands for Flat band gate voltage value where bands of MoS_2 undergoes a rectangular shape. The representation at $V_G \leq V_{FG}$, $V_G \geq V_{FG}$ and $V_G \gg V_{FG}$ represent the energy band profiles below, close to and fare above the Flat band condition.*

configuration with an applied dc voltage of 1.5 V. We observe a negligible current up to high positive Vg ~ 19 V. This indicates that for Vg < 19 V, the Fermi energy E_F of the MoS_2 is situated deep within the bandgap where no carriers are available for transport resulting to a high resistance of the channel. This contrasts with the behavior of the bilayer $MoSe_2$ FET presented in the previous chapter were we observed a finite non-zero current due to unintentional doping of the 2D crystal displacing its chemical potential from the middle of the gap to a position closer to the conduction band [Ovchinnikov14]. We attribute this low Vg range of negligible current to the semiconducting gap of MoS_2. A minimum threshold gate voltage of approximately V_{TH} = 19 V is required to drag the Fermi level of MoS_2 close to the vicinity of minimum conduction band edges where a percolating conductive path likely appears within the MoS_2 channel and trigger the conduction through the device. Beyond V_{TH}, Isd (Vg) exponentially increases as highlighted by the linear behavior of the log scale current, in agreement with the percolation type of transport as presented in section.3.4 (Fig.8.2.(b)). The slope discontinuity at high Vg might be related to the change of the transport regime within the channel. Interestingly, we find superposed to this typical n-type field effect transconductance of the channel remarkable aperiodic coulomb oscillations (Fig.8.2.(b)). We attribute these oscillations to single electron processes origination from the CB effect of the oxidized Al NPs integrated in Co/AlOx-Al-AlOx/MoS_2 heterojunction. It appears thus that, the transport

our devices is governed by two distinct phenomenons. On one hand the field effect modulation of the semiconducting MoS_2 channel resistance leading to the exponential increase of the conductance of the device and on the other hand, the Coulomb blockade (CB) controlled of charge tunneling at Co/AlOx-Al-AlOx/MoS_2 heterojunction.
In chap.7 we abundantly discussed the 2D SC-TMDs band curvature by the applied voltages. We take benefice of such understanding here. In Fig.8.2.(c) we present the evolution of the band diagram of the device with the gate voltage taking reference at the flat band where the band of the semiconductor have a rectangular shape. Both the Coulomb levels of the supported NPs and the semiconducting band of the underneath MoS_2 channel are modulated. It results the dual behavior of the device with electrostatic channel doping induced exponential increase of the current and interface heterojunction NPs induced coulomb oscillations of the current. Such dual behavior were systematically present on asymmetric SET with channel lengths up to 7 μm involving the electrodes 4 and 8. This makes the transport characteristics of our devices qualitatively comparable to that of classical Si based CMOS quantum devices and n-GaAs based SET [Poole83, Staring92, Yakimov94, Kouwenhoven97, Zwanenburg13]. We will return to this point later in the section.8.3.

8.2.2 Symmetric configuration

The Fig.8.3.(a, b) present the transport properties of the device polarized in the symmetric configuration involving the electrodes 3 and 4 both contacting the MoS_2 channel trough the granular oxidized Al layer. This geometry with a shorter MoS_2 channel length of 350 nm and the contacts integrating tunnel barrier which lower interface energy barriers likely results to a lower resistance of the device. The Fig.8.3.(a) presents the I-Vsd and the corresponding dI/dVsd-Vsd characteristics measured at 1.5 K with an applied gate voltage of Vg = 25 V. They also present an asymmetry common in tunnel junction devices due unavoidable differences in tunnel barriers and different resistance·area products. Similarly to the asymmetric configuration, we observed the dual behavior characteristics. This includes the very large central gap of I-Vsd and dI/dVsd-Vsd characteristics. The dc threshold voltages for the elevation of the conductance is approximately $\pm 120mV$ in Fig.8.3.(a) (red curve), which is too large to be attributed exclusively to the Coulomb blockade effect. In addition, as the Fermi level of the channel remains deep in the band gap where no carriers are available for the transport, the transcconductance curve measured at Vsd = 230 mV (Fig.8.3.(b)) presents a zero current Vg range preserved up to a threshold of V_{TH} = 19 V (see the inset of Fig.8.3). Beyond (Vg > V_{TH}), the current undergoes an exponential increase with Vg driven by the electrostatic doping of the channel. Superposed to these field effect characteristics of the channel, we observed clear Coulomb staircases in the I-Vsd curves better highlighted by Coulomb aperiodic oscillations of the corresponding differential conductance with a minimum peak to peak interval of about ΔVsd = 60 meV. More importantly, these single electron features are characterized in the transconductance curve by remarkable aperiodic Coulomb oscillations with well defined sharp current peaks highlighted by the back arrows in Fig.8.3.(b). The insert presents the lower Vg oscillations hidden by the

exponential increase of the current in lower Vg regime. The Fig.8.2.(c) we present the evolution of the band diagram of the device in this symmetric also taking the reference at the flat band. As before, both the Coulomb levels of the supported NPs and the semiconducting band profile of the underneath MoS_2 channel are modulated leading to the dual behavior of the device comparable to previous semiconductors based quantum device experiments [Poole83, Staring92, Yakimov94, Kouwenhoven97, Zwanenburg13].

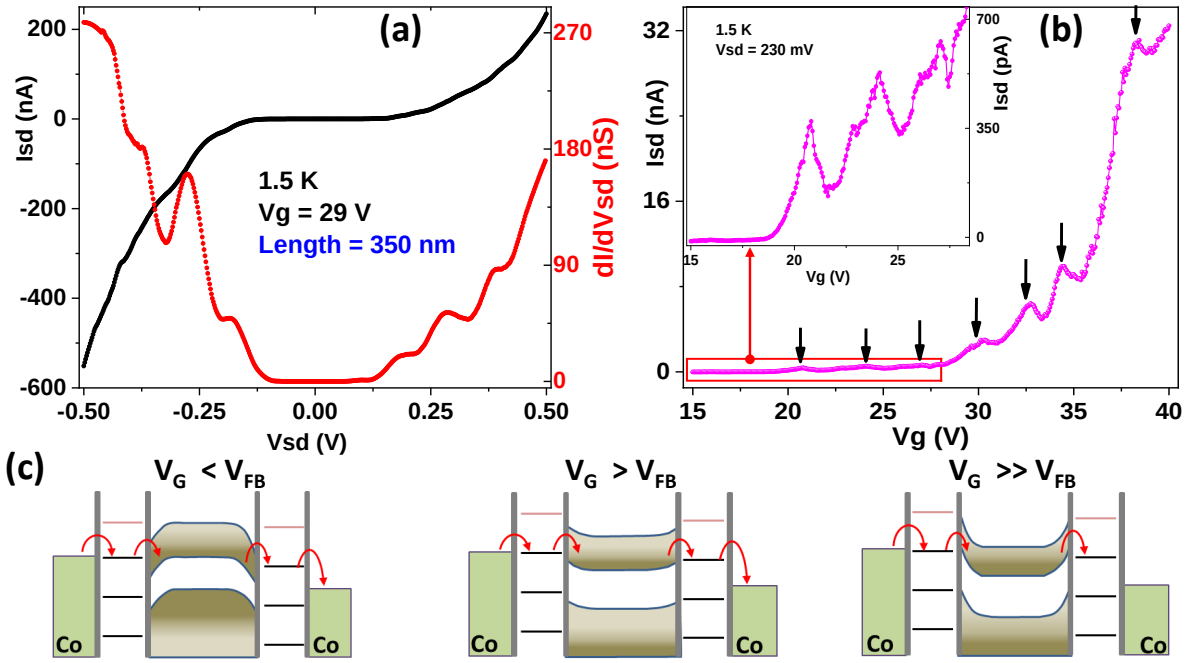

Figure 8.3 *– Transport measurement at 1.5 K in symmetric configuration involving the electrodes 3-4. The channel length is 350 nm. (a) I-Vsd characteristic (black curve, left axis) and the corresponding differential conductance (red curve, right axis) measured at Vg = 29 V. (b) I(Vg) curve measured for Vsd = 230 mV. The black arrows highlight the positions of the conductance peaks. The inset highlights the low Vg region of the main curve. (c) The energy band diagram illustrating the tunneling process within the device. V_{FG} stands for Flat band gate voltage value where bands of MoS_2 undergos a rectangular shape. The representation at $Vg \leq V_{FG}$, $Vg \geq V_{FG}$ and $Vg \gg V_{FG}$ represent the energy band configurations below, close to and fare above the Flat band condition.*

Attributing the conductance oscillations observed here for Al-AlOx/MoS_2 2D-0D MD-VdWh to the Coulomb blockade effect of the NPs present into the interface heterojunction as in the case of Al-AlOx/Gr 2D-0D MD-VdWh presented in the chap.5 and the chap.6 is absolutely not straightforward. Indeed, contrary to Al-AlOx/Gr heterostructures, the semiconducting character of the channel in the Al-AlOx/MoS_2 heterostructures sets the conditions in 'principle' adequate for the emergence of other quantum transport processes with qualitative characteristics similar to the curves presented in Fig.8.2 and Fig.8.3 [Poole83, Staring92, Yakimov94, Kouwenhoven97, Zwanenburg13]. In Fig.8.4.(a), we present an example of a low T characteristic of a GaAs based FET with a dual characteristic similar to our case. It is therefore of paramount importance to review the quantum effects susceptible to induce similar conductance oscillations behavior and discuss the reason for their discrimination in our devices, so to avoid mis-interpretation of the data which may be

guided by our experiments on Al-AlOx/Gr based SED presented in the chap.5 and chap.6.

8.3 Conductance oscillation in semiconductor quantum devices

Low temperature transport properties of quantum devices consisting respectively of 1D narrow channel defined by split-gate technique in the inversion layer 2D electron gas of $GaAs/Al_xGa_{1-x}As$ epitaxial heterostructures [Kouwenhoven97, Poole83, Staring92], narrow channel Si-MOSFET [Kastner87], semiconductor nanowires [Kastner92, Zota16, Li17] and carbon nanotubes up to some extent [McEuen99, Kamimura10] share several qualitative similarities with the properties of our devices.

8.3.1 Narrow channel devices

Narrow channel Si-MOSFET [Kastner87] demonstrated Vg dependent dual behavior of the conductance with aperiodic oscillations superposed to an exponential increase attributed to the field effect doping of the 1D channel similar to our low T transport measurements. Such a dual behavior was reported for the first time by Poole et al. [Poole83] in large junction of GaAs FET (Fig.8.4.(a)). The origins of conductance oscillations are multiple and depend on channel length, the purity of the materials, the geometric regularity of the wire on one hand and fluctuation of the splitting gate potential on the other hand. Kastner et al. [Kastner87] reviewed the earlier experiments on disordered narrow Si wire based MOSFET segmented into small islands by disorder. At Low T, these devices present Vg dependent conductance fluctuation often qualified as chaotic [Zwanenburg13]. This was attributed to phonon assisted hoping of carriers on the localized states within the wire consistently with numerical simulation prediction based on VRH theory [Lee84]. In 1D electron gas obtained by splitting-gate in $GaAs/Al_xGa_{1-x}As$ epitaxial heterostructures, low T conductance dependency with Vg presents aperiodic oscillations attributed to CB effect of the small segment of islands. The islanding of the 1D channel being induced by the unscreened electric field of either the ionized randomly distributed impurities donors unintentionally incorporated in $Al_xGa_{1-x}As$ or acceptors intentionally introduced in the GaAs buffer layer [Kouwenhoven97, Poole83, Staring92].

Many other experiments on semiconductor Si wires or CNT devices demonstrated CB oscillations of the conductance for similar reasons related to the partitioning of the channel into small Coulomb islands due to disorder [Kastner92, Zota16, Li17]. In general, the regularity of the oscillations is strongly related to the number of contributing Coulomb islands present in the channel as well as their charging energy distribution. It has to be notice that perfect CNT [Liang01] and semiconductor nanowires [Mann03] often exhibit metallic behavior with ballistic charge transport (see section.3.1.2). In these conditions Vg dependent conductance revealed Fabry-pérot oscillations with almost no Field effect contribution. The oscillations are nearly perfect approaching a sinusoidal behavior and result from repeated reflections of carriers at the electrodes/wire contacts [Liang01].

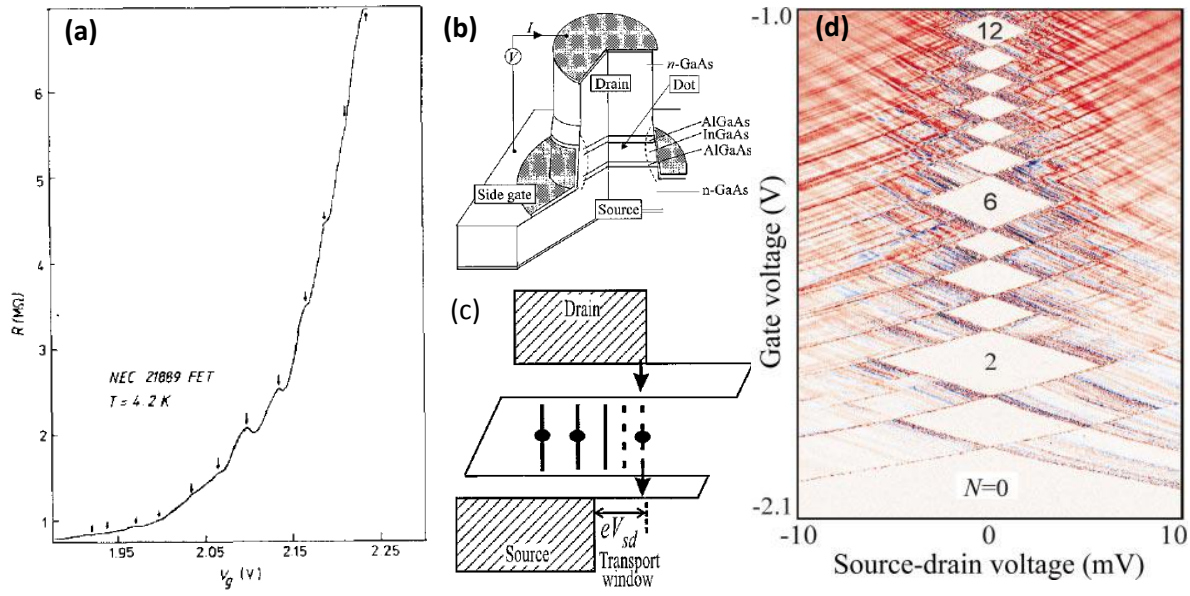

Figure 8.4 *– (a) Low temperature resistance measured in 1983 on large large area 2D GaAs FET by Poole* et al. *[Poole83]. The oscillations of the resistance were qualified as anomalous.(b-c) SET experiment on small area AlGaAs/GaAs based circular junction of 0.5 µm diameter. (b) Schematic of the junction illustrating the heterostructure pilar. (c) Energy diagram along the vertical axis of the device. (c) Differential conductance dI/dVsd(Vg,Vsd) color plot. The white diamond regions, dI/dVsd = 0 due to Coulomb blockade.*

8.3.2 Classical semiconductors based SETs

Vertical Si/p^+-Ge/Si epitaxial heterostructure sandwiching a granular layer of p^+-Ge consisting on dispersed islands of about 10 nm average size also demonstrated conductance oscillations with qualitative features similar those observed here [Yakimov94]. The oscillations where associated to classical CB tunneling into isolated p^+-Ge quantum dots. At low enough temperature, additional conductance peaks were observed superposed to CB peaks and were attributed to resonant tunneling through the discrete states of the islands. Similarly, aperiodic CB conductance oscillations were observed in ultra small vertical junctions (point contacts) consisting of n-GaAs/AlGaAs/InGaAs/AlGaAs/n-GaAs epitaxial heterostructure (Fig.8.4).(b) [Kouwenhoven97]. The n-GaAs layer served as source and drain electrodes and AlGaAs as tunnel barrier to the isolate InGaAs quantum dot. This experiment demonstrated one of the historical charge stability diagram with clear CB region of the dot (Coulomb diamonds) with a defined number of electrons (Fig.8.4.(d)). This stability diagram also presents a set of lines parallel to the diamond edges resulting from resonant tunneling of charges trough the exited quantized states of the quantum dots. The charging energy was reported to be comparable to the discrete energy level spacing ΔE, the later being subject to important variation as the dot was successively filled by tunneling electrons it results a pronounced aperiodicity of the diamonds.

8.3.3 Discrimination of tunneling processes in Al-AlOx/MoS_2 heterostructures

In our devices, the situation may seem apparently complex since our geometries combine both the lateral transport within the channel and the vertical tunneling trough the granular oxidized Al layer. Nonetheless, most of the causes of conductance oscillations reported above are to be excluded. First, VRH transport does exist in the channel at the subthreshold regime (close to V_{TH}) when the E_F lies in the vicinity of the minimum conduction band edges inducing percolating conduction paths in channel. However, it is not expected to leads to conductance fluctuation in 2D geometry. More importantly, the experiments that have reported VRH induced conductance fluctuation in 1D devices require ultra low T to resolve the activation energy difference between the random localized states [Fowler88, Kastner92]. In our case, the oscillations are not chaotic and are preserved above 50 K (see section.8.5 below).

The oscillations are systematically present in long channel devices, excluding the possibility of resonant tunneling on the eventual impurities states located within the channel. Such a process requires two ingredients : First, the alinement of the chemical potentials of the electrodes with a discrete state of an impurity. Second, the tunneling distance between the electrodes and the discrete state must be smaller enough to enable partial overlapping the wave functions. In our case, this is not guaranteed even for the shortest channel length of 350 nm, more as AlOx tunnel barrier are used. Resonant tunneling trough the interface due to Al-AlOx/MoS_2 interface defects states are much less probable as well. It is well established by both first principle simulations and transport experiments that 2D SC-TMDs/Metal interface defect states induce localized states within the gap of SC-TMDs [Gong14, Kim17]. In pure vertical geometry, such interface defect states (given that they are quantized) may induced resonant tunneling resulting to a conductance oscillation. In the planar geometry however, such resonant tunneling can only be consider if E_F is still located within the gap of MoS_2[1]. However, in such a doping regime, the channel is insulating and no transport trough the devices is possible. Moreover, the interface states are in general sufficiently abundant to induce a partial Fermi level pinning [Gong14, Kim17]. In Fig.(8.2& 8.3) we have seen that a minimum threshold gap voltages are needed to induce the conduction in the channel as the E_F moves close enough to minimum conduction band edges. Which means that the E_F pinning if it exists, it does not affect much the transport beyond V_{FT} .

Moreover, a previous report has demonstrated conductance oscillations in a confined FET geometry MoS_2 device with restricted channel lengths up to 300 nm (and a width up to 1.2 μm) using Zinc metal electrodes. The oscillations were attributed to the Coulomb blockade effect of the electrons so confined into the restricted MoS_2 channel. In our case, the minimum channel length measured is 350 nm with a width of 5μm. A very naive estimation of the confinement energy based on a simple 2D square quantum well using the formula $E = \hbar^2\pi^2/mL^2$ provides a value of 13.6 μeV, considering the more favorable case for confinement with L =

[1] Otherwise, in the degenerated regime when E_F is in the conduction band, the states are not quantized and no resonant tunneling is to be expected.

350 nm and $m = 0.45m_0$. This value doubles when considering the double valley degeneracies of SC-TMDs but remains infinitesimal to induce CB effect in our devices at 1.5 K. Other recent reports on electrostatic gate-controlled electrons quantum dot of about 250 nm radius in a high quality single layer MoS_2 using high-k hBN dielectric (section.2.3) demonstrated a charging energy of only 2 meV [Pisoni18, Wang18a]. Therefore, we exclude any hypothesis of confinement in our devices, especially as we observe the oscillations up to 7×8 μm^2 channel area with the electrodes 4 and 8.

It appears therefore that, the only reason for the observed conductance oscillations in our devices is related to CB from the NPs of the Al-AlOx/MoS_2 heterostructure. Eventually, resonant tunneling from the quantized states of defect situated within oxidized Al layer may in principle be envisaged. However, the physico-chemical analysis of the granular layer did not point out any suspicion of the presence of defects susceptible to induced such tunneling contributions. Note that the signature of such tunneling contribution was not reported in the case of Al-AlOx/Gr based SET (Chap.5). More importantly, the hypothesis of CB is sustained by the regularities of oscillations leading to well defined Coulomb diamond patterns in the conductance stability diagram as well be discussed in the next section. It is also supported by the preservation of the oscillations even at high temperature and voltages were resonant tunneling on defect states localized within the tunnel barrier is expected not to be preserved (see section.8.5). Hence, in our 2D-0D Al-AlOx/MoS_2 based devices, charges tunnel from Co electrodes to the MoS_2 trough the discrete Coulomb levels of the Al-AlOx NPs and extracted either similarly at the other Co electrode (for symmetric configuration) or trough a Schottky barrier at Ti/Au contact consistently with the schematic representations in Fig.(8.2.(c)& 8.3.(c)).

8.4 Low temperature charge transport spectroscopy

To gain deeper insight into the transport processes of our devices, we performed the charge transport spectroscopy at 1.5 K within a wide range of Vsd and Vg from 40 V to 70 V. We observed two different gate coupling regimes depending on the MoS_2 doping state. We refers to them as low and high doping regimes corresponding respectively to the highly resistive and low resistive states of the MoS_2 channel.

8.4.1 Low doping coupling regime

The Fig.8.5.(b) displays the differential conductance (dI/dVsd (S)) color map of the SET in the low doping regime where the MoS_2 channel is highly semiconducting inducing an important conductance gap ΔEg incorporated in the regions of constant charge state (the Coulomb diamonds). The curves presented in Fig.8.5.(a) is an illustration of a typical dI/dVsd-Vg characteristics used for the color map. The semiconducting gap ΔEg highlighted with the white dashed lines and arrow decreases as the MoS_2 channel's doping density linearly increases with Vg $n = C_{SiO_2}(V_G - V_{TH})/e$. Where the C_{SiO_2} corresponds to the Si-SiO_2 gate capaci-

tance. As mentioned before, increasing Vg and Vsd also bend downward the conduction band at the source and drain interface reducing the energy barrier heights resulting to the average reduction of the resistance of the device. This combination of factors leads to a modification of the coupling parameters of SET (C_G; C_Σ) which explains the reduction of the Coulomb diamond size (Fig.8.5.(b)). Considering the diamond centered at Vg = 42.4 V

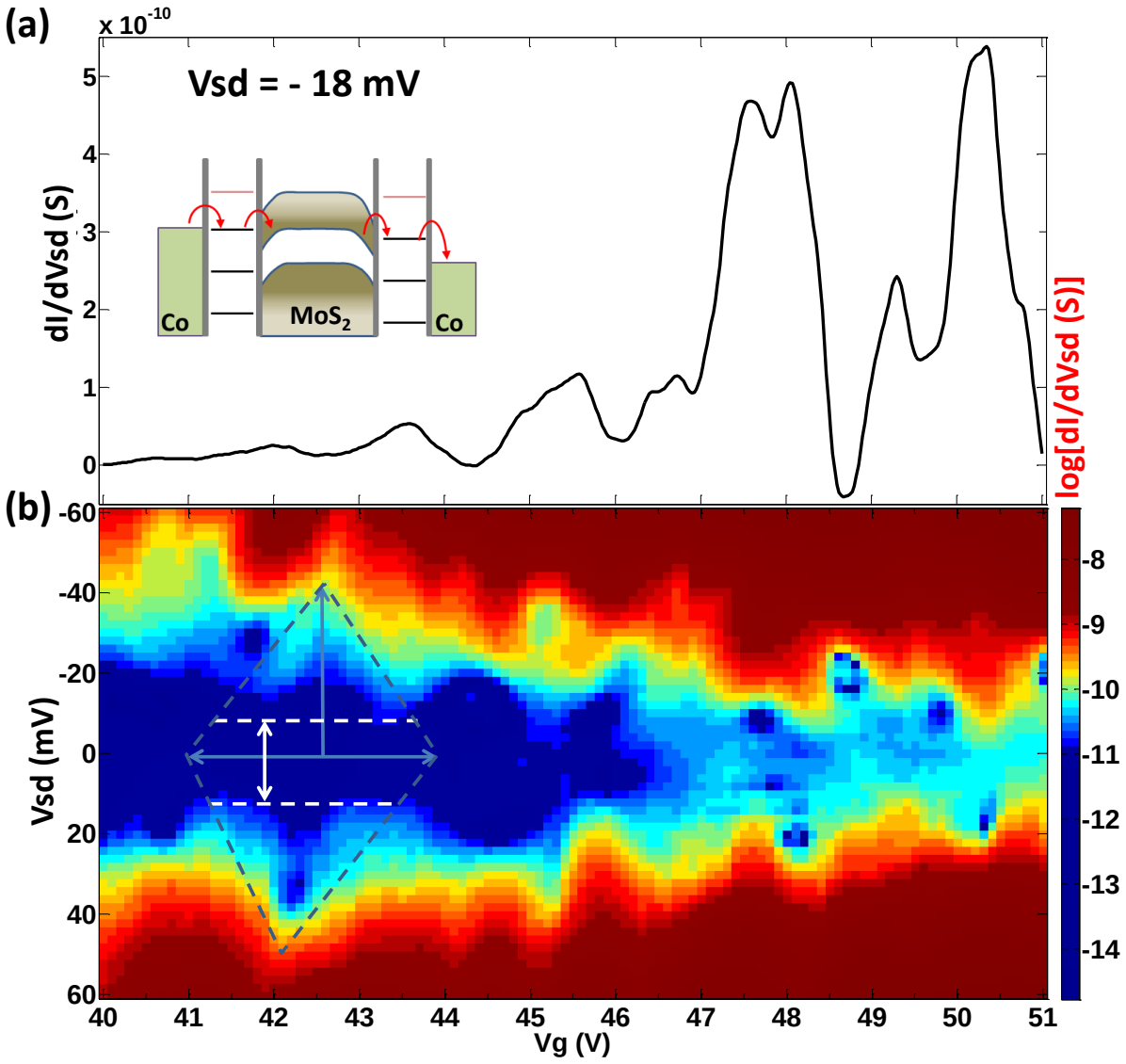

Figure 8.5 *– Conductance spectroscopy in the low doping regime. (a) Illustration a typical dI/dVsd (Vg) curve extracted from stability (b). The inset reminds the energy diagram of the device. (b) Color map of the stability diagram of dI/dVsd (Vsd, Vg). The blue dashed diamond indicates the Coulomb blockade region centered at 42.4 V. The blue dashed arrows illustrate the extension ΔVsd and ΔV_G of the diamond. The white dashed lines illustrate the semiconducting gap ΔEg. Notice that the data where smoothed to remove artificial noise originating from mathematical derivation.*

(dashed blue line diamond in Fig.8.5.(b)), the total capacitance C_Σ of the SET is approximated to be $C_\Sigma = e/\Delta V_{sd} = 5.72$ aF, where $\Delta V_{sd} = 39.5mV$ is the half width of the diamond along the Vsd axis (see the vertical blue arrow). This corresponds to a charging energy of $E_C = e^2/2C_\Sigma = 18.25$ meV. From the lateral spreading $\Delta V_g = 2.4 \pm 0.2V$ of the selected dia-

mond, we deduced the back gate capacitance C_g of the SET for the corresponding channel doping range to be $C_g = e/\Delta V_g$ = 0.067 aF. This results to a gate coupling coefficient of the SET (the lever arm) of $\alpha = C_g/C_\Sigma$ =0.012. These electrical parameters of the 2D-0D Al-AlOx/MoS_2 based SET highly contrast with those recently reported on electrostatically confined quantum dot in layered materials found to exhibit E_C in the range of 100 μeV up to 2 meV [Pisoni18, Eich18, Hamer18, Wang18a]. However, they are in a comparable range with that of metallic NPs based SET [Bolotin04, Makarenko17].

The observation of diamond patterns in the conductance stability diagram is an unambiguous confirmation of the CB origin of the oscillations. Strictly speaking, as the core-shell structure of the NPs of the granular Al layer is yet to be confirmed, the origin of CB can be questioned. From the discussion of section.8.3, it is difficult to admit other source of CB effect in this devices. Therefore, motivated by the core-shell structure demonstrated in Al-AlOx/Gr heterostructures resulting to CB SET and by the fact that the Al-AlOx/MoS_2 heterostructures are fabricated in the same condition following the same method, we admit at this stage that Al-AlOx are responsible for observed CB conductance oscillations. In this context, Coulomb diamond patterns are not surprising even for the symmetric configuration of sample which can be approximated as set of parallel conduction channels each of which contains two NPs in series. Indeed the orthodox theory calculation in classical regime provides the understanding that, in a multiple grain systems, even though each tunneling junction defines a particular set of staircases (i.e. of lines in conductance stability diagram) with distinct slopes, only the set of staircases corresponding to the most conductive junction per grain dominate [Danilov02]. The Coulomb diamond features in Fig.8.5.(b) are clear evidence that despite the thousand of double dots channels potentially available, only few conduction paths are responsible of the Coulomb oscillations in our devices. The intermixing of different set of stairs of these few channels also participate to the aperiodicity of the oscillations. The contributing conductance path participating results from the selection processes already abundantly discussed (section.5.1.3).

8.4.2 High doping coupling regime

The Fig.8.6 displays the transport properties of the devices in the high doping regime (Vg > 58 V). The semiconducting gap ΔEg is almost absent. This may be an indication that the semiconducting channel has undergone a degenerated state with its E_F located within the conduction band driven by the electrostatic doping. It has to be noticed that, with four probes measurements, we observed a metal to insulator transition in this gate voltage range at higher T (see section.8.6). Isolated Coulomb diamonds are well discernible in Fig.8.6.(b). The aperiodicity of the Coulomb oscillations is illustrated in Fig.8.6.(a) presenting the dI/dVsd *v.s.* Vg extracted from the map for Vsd = -18 mV. The insert in Fig.8.6.(b) shows the dI/dVsd *v.s.* Vsd curves extracted from the color map respectively at Vg = 59.8V, 61.3V, 62.7 V when the 2D-0D SET is in the 'on' state (black curve) and in the 'off' state (red and blue curves respectively). We observe more than 3 decades of conductance modulation between the 'on' and

'off' states when the conductance completely vanished due to CB (see the inset of Fig.8.6.(a)). This is an additional indication of CB control of charges tunneling trough the SET despite the high conductivity of the MoS_2, it further confirms that carriers necessarily tunnel through the CB path leading to a negligible contribution from direct tunneling.

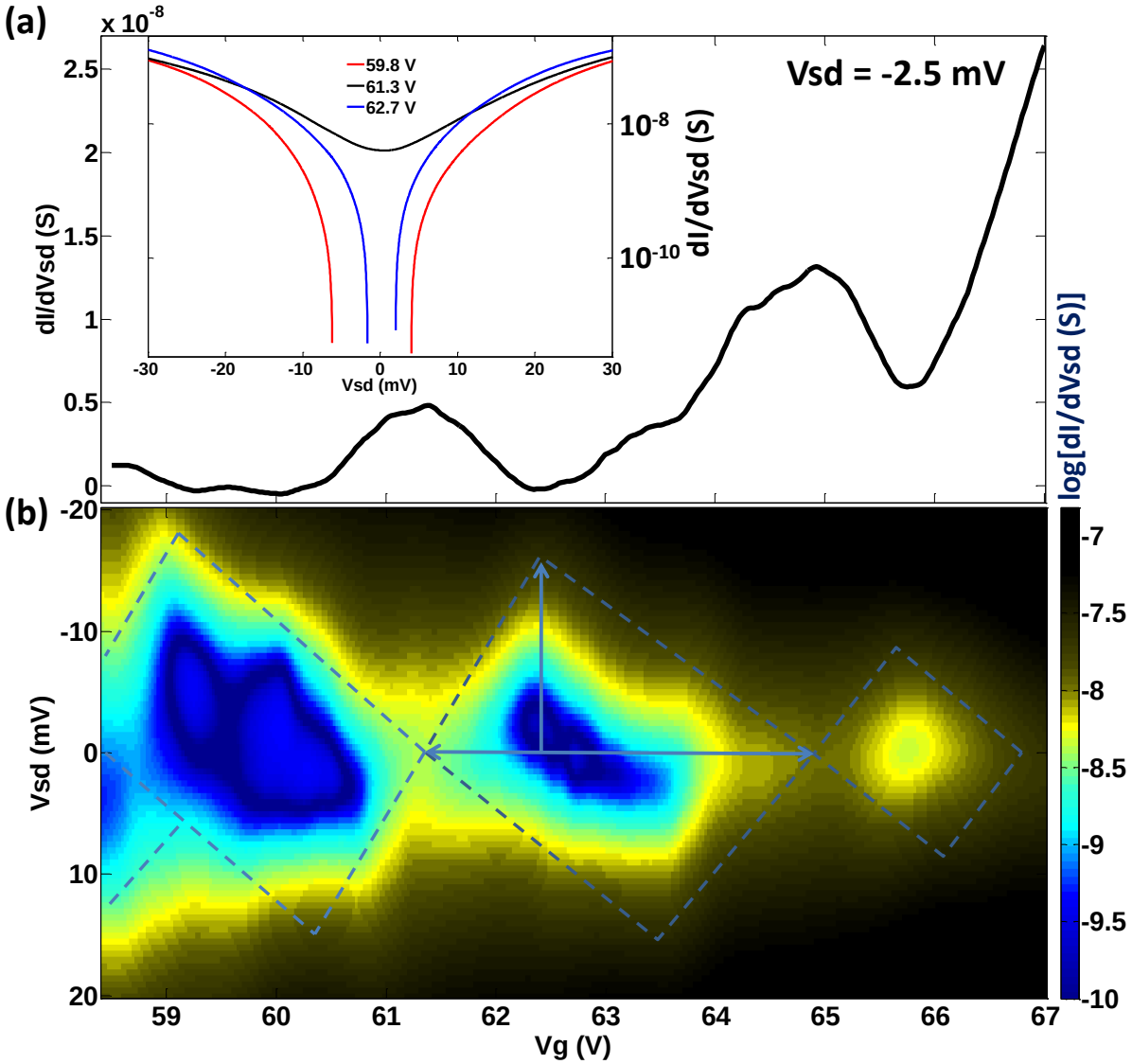

Figure 8.6 *– Electric spectroscopy in the high doping regime. (a) Illustration a typical dI/dVsd (Vg) curve extracted from stability (b). The inset presents the dI/dVsd (Vsd) when the SET is opened (black curve) and closed (red and blue curves). (b) Stability diagram of dI/dVsd (Vsd, Vg). The dashed line indicate the Coulomb blockade diamonds. The blue dashed arrows illustrate extensions ΔVsd and ΔV_G of the diamond. Notice that the data where smoothed to remove artificial noise originating from mathematical derivation.*

The total capacitance of the SET in this doping regime is deduced from the half height ($\Delta Vsd = 16.5 \pm 0.5$mV) of the diamond centered at Vg = 63 V to be C_Σ = 9.71 aF. A value 1.7 times higher than the corresponding value reported at Vg = 42.4 V in the low doping regime. In the meanwhile, the resulting Ec is reduced by a factor of 0.59 (= 1/1.7) to $E_C = e^2/2C_\Sigma$ = 8.2 ±0.3 meV. It is noticeable how effective the gate modulation is affecting the coupling parameters of the SET. Notably, the periodicity of the diamond has increased from ΔV_g = 2.4

V at lower doping regime to about ΔV_g ~3.04 V in higher doping regime leading to a higher voltage gate coupling capacitance of C_g = 0.053 aF an resulting gate coupling coefficient α_G = 0.00543 that is about 20 times smaller than its lower voltage counterpart. This is a clear evidence that the doping of the channel modulates as well the electric parameter of the SET. Note that at very low doping regime (15 < Vg < 40V) the semiconducting gap was very large requiring high Vsd to access a detectable signal. In this low Vg and high Vsd and regimes we observed quantum transport processes that are not fully understood yet.

8.4.3 Charge transport spectroscopy in asymmetric configuration

The Fig.8.7 presents the charge transport spectroscopy recorded at 1.5 K in asymmetric configuration involving the electrode 1 and 2 with a channel length of 820 nm. A strong asymmetry of I-Vsd characteristics (Fig.8.2.(a)) is confirmed, reminiscing the presence of high Ti/MoS_2 Schottky barrier at one of the junction in contrast to a tunnel barrier at the other. The conduction gap exponentially decreases with increasing Vg. The devices was polarized

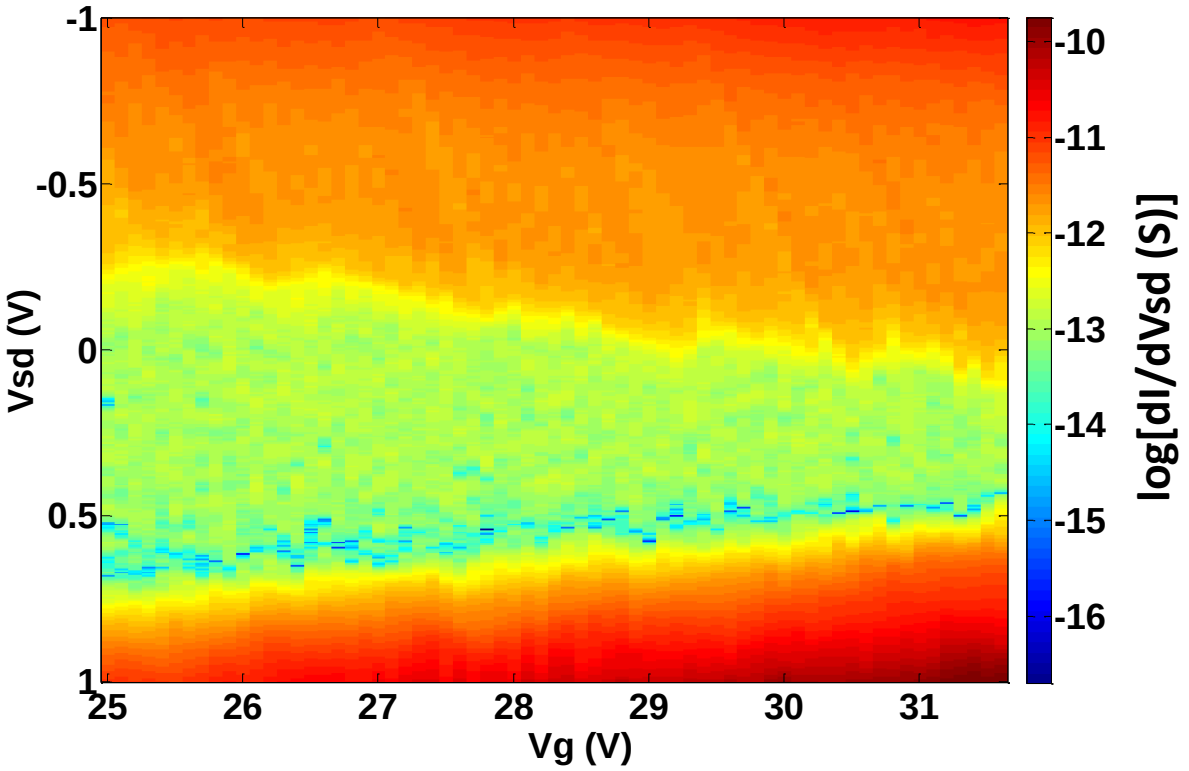

Figure 8.7 *– Stability diagram of dI/dVsd (Vsd, Vg) measured in the asymmetric configuration with a channel length of 820 nm. Single electron features are better distinguishable in negative Vsd when charges tunnel form the Co/Al-AlOx heterojunction.*

such that the Au-Ti/MoS_2 Schottky barrier contact was grounded. Thus, for $Vsd > 0$, charges tunnel from Ti/MoS_2 electrode to Co/AlOx-Al/MoS_2 heterojunction. A very high dc threshold bias is required to inject charges trough the high Ti/MoS_2 Schottky barrier. The situation is reversed in negative dc bias, with charges tunneling from the Co/AlOx-Al/MoS_2 heterojunction containing the NPs. As a matter of fact, coherent single electron features are better

distinguishable in negative Vsd when charges tunnel from Co/AlOx-Al/MoS_2 side of the heterojunction. A periodicity of such coherent features is observed to be $\Delta V_G = 1.5V$ below 30 V and $\Delta V_G = 1.2V$ above.

8.5 Temperature and dc bias dependent transport properties

The Fig.8.8 presents the Isd *v.s.* Vg characteristics of the device in the symmetric configuration for different temperatures (Fig.8.8.(a)) and dc biases (Fig.8.8.(b)). The logarithmic scale representation enables scaling all the Isd (Vg) curves on the same graph. Characteristic features intrinsic to the semiconducting MoS_2 channel are observed in both measurements. This includes the diminution of threshold gate voltage V_{TH} and the increase of the conductance with increasing T and Vsd. At high T, the thermal excitation facilitates the mobility of carriers. At

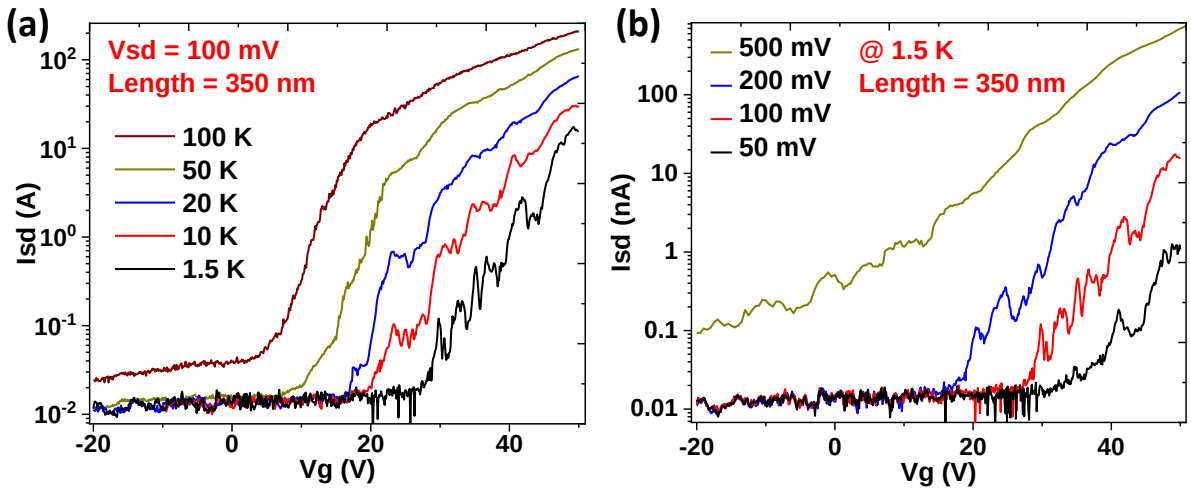

Figure 8.8 *– (a) Temperature dependent transfer characteristics of the 2D-0D SET in symmetric configuration. (b) Transfer characteristics at different applied dc bias.*

higher Vsd, it is the downward conduction band bending combined with the displacement of E_F toward the conduction which reduce the tunneling barrier and consequently conductance gap favoring thus the increase of conductance. Beyond the V_{TH}, the oscillations of conductance remain preserved for all Vsd values at 1.5 K (Fig.8.8.(b)). The 1.5 K curves (the same for both figures) is characterized by a fine structure of the oscillations certainly resulting from the intermixing of the set of CB levels of the few distinct contributing conduction paths. As the temperature increases, the fine structure progressively vanishes due to thermal broadening which artificially merges the Coulomb levels with energy spacing included within $\pm K_B T$ into a single level. This results to a subsequent broadening of conductance peaks. In addition, the conductance minima of different peaks increase much faster than the corresponding maxima. It results a plateau like oscillations when both quantities become equal in agrement with other observation of CB is semiconductor device [Staring92, Yakimov94]. This is noticeable at the temperature range of 20 to 40 K. Above, the minima become progressively larger than the maxima resulting to a vanishing of oscillations around 50 K. This corresponds to a thermal energy of $k_B T_{50K}$ = 4.3 meV = $Ec/4.24$. Where Ec = 18.25 meV is charging energy

reported at low doping regime for a comparable value of gate voltage.
The behavior of the oscillations is up to some extent similar with increasing Vsd. At lower Vsd, the dc-bias windows $|eVsd|$ only resolves few Coulomb levels at time resulting to Isd(Vg) curves with large numbers peaks (Fig.8.8.(a), red curves). The number of peaks certainly competes with the resistance of the channel a very low Vsd ((Fig.8.8.(a), black curves). As Vsd increases, the dc-bias windows $|eVsd|$ increases as well followed by the number of Coulomb levels resolved at time. The result is the observed broadening of current peaks. The oscillations are preserved even at 500 mV in this case.

8.6 Metal to insulator transition in MoS_2

To clarify the role of the channel in the observed transport characteristics of the Al-AlOx/MoS_2 heterostructures, we probe the intrinsic properties of the MoS_2 channel using four terminal geometry as depicted in Fig.8.9.(a). We observed a remarkable and reproducible metal-to-insulator transition with all the qualitative characteristics described in section.3.4.1. For 1 nA dc current, the transition takes place around 175 K (Fig.8.9.(b & c)) while for a dc current of 10 nA its takes place a bit higher T close to 200 K (Fig.8.9.(d & e)). At lower T and Vg, the four terminals conductance (G_{4T}) increases with increasing T consistently with the typical semiconductor behavior. At high T and Vg instead, G_{4T} decreases with increasing T following a typical metallic behavior. As sustained by Schmit et al. [Schmidt15] MIT is a manifestation of a transition from a transport regime via localized states when E_F is in the vicinity of the minimum conduction band edges to a band transport when E_F moves deep into the conduction band driven by doping.
Hence, the observation of MIT in our 2D-0D Al-AlOx/MoS_2 based device clearly justified the exponential vanishing of the semiconductor gap in the stability diagram of conductance as described above.

8.7 Conclusion

We have reported in this chapter the transport measurements of 2D-0D Al-AlOx/MoS_2 based SET MD-VdWh consisting of granular Al layer decorating the MoS_2 surface. We observed at low temperature CB conductance oscillations superposed to the intrinsic field effect characteristic of the MoS_2 channel. Our comprehensive analysis attribute the conductance oscillation to the CB effect of the nanaparticules composing the 2D-0D heterostructures. Charge transport spectroscopy reveals well defined Coulomb diamond patterns in conductance stability diagram. The electric parameters of the SET are intrinsically related to the doping level of MoS_2 the channel. The Coulomb oscillations are preserved up 50 K. Four terminal transport measurements reveal a metal-to-insulator transition of the MoS_2 channel. This work opens doors to alternative SET architectures using 2D-0D MD-VdWh circumventing the usual fabrication challenges and demonstrate the important prospect of 2D-0D MD-VdWh for nanoelectronics.

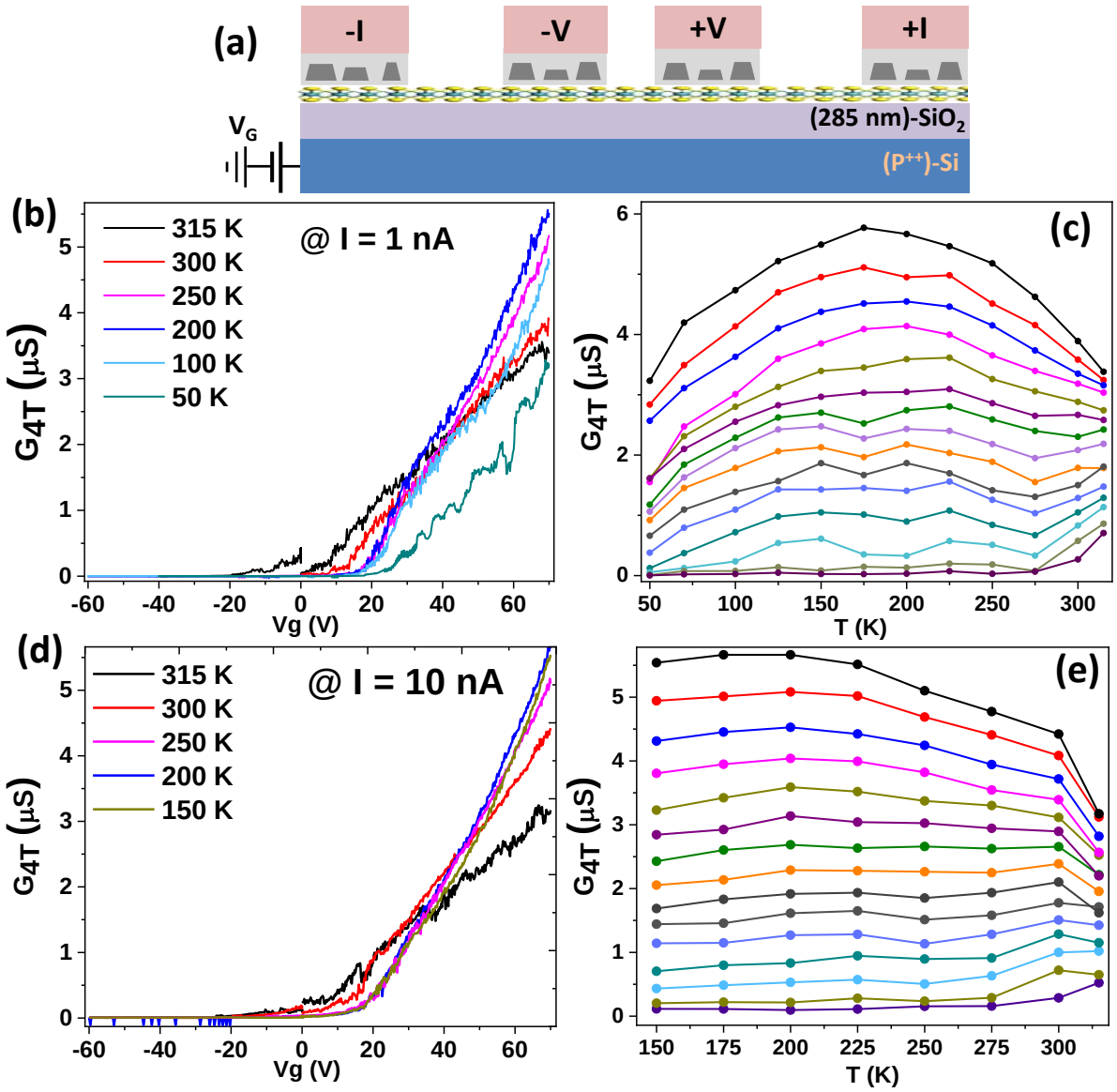

Figure 8.9 *– Metal-to-insulator transition in 20-0D Al-AlOx/MoS_2 based devices. (a) Electric geometry of the measurement. (b) Four terminals conductance (G_{4T}) versus Vg for an applied dc current of 1 nA. (c) Corresponding temperature dependency of G_{4T} for Vg range of 14 V to 70 V from to bottom to top with and increment of 4 V. (d) G_{4T}(Vg) for an applied dc current of 10 nA. (e) Corresponding temperature dependency of G_{4T} for Vg range of 14 V to 70 V from to bottom to top with and increment of 4 V.*

Chapter 9

Magnetotransport properties of perovskite Nanocrystals

In this chapter we report on the magnetotransport properties of 20 nm ligand-free $La_{0.67}Sr_{0.33}MnO_3$ perovskite nanocrystals of nearly perfect crystalline quality. We observe an exceptionally large magnetoresistance at low temperature essentially triggered by a chemically altered 0.8 nm thick surface layer of the nanocrystals independently of the spin polarization of their ferromagnetic core. This work reveals the way the nanoscale impacts the magnetotransport in this material widely used as electrode in hybrid spintronic devices. This work was conducted in the framework of a large consortium including three main poles. The pole of Paris at Pierre and Marie Curie University (the Sorbonne University) and particularly the 'Laboratoire de Chimie de la Matière Condensée de Paris (LCMCP)' for the synthesis of the synthesis of $La_{0.67}Sr_{0.33}MnO_3$ nanoparticles (NPs). The pole of the Complutense University of Madrid, department of inorganic chemistry for Physico-chemical analysis and our team for magnetometery characterization and magnetotransport study.

9.1 Introduction

The manganite perovskite of composition $La_{0.67}Sr_{0.33}MnO_3$ (LSMO) has been of prime importance for spin electronics [Coey99]. Ferromagnetic and metallic up to room temperature, it has been claimed to possess a fully spin-polarized density of states (DOS) at its Fermi level. Hence, it should be ideally suited as spin injector or detector for spintronic devices taking advantage of the spin degree of freedom of current carriers. While experiments unambiguously show that the diffusive current is highly spin polarized in the bulk

material [Nadgorny01], the degree of spin polarization of the tunneling current remains controversial [Nadgorny07]. This surface sensitive quantity, expected to reflect the spin-split DOS, usually exhibits values in the 40-60% range, with exceptionally larger values (between 80 and 90%) found only at low temperature on samples grown under very specific conditions [Tsymbal11]. The chemical stability makes LSMO the 'gold standard' for spin transport through molecular moieties. Hybrid organic-inorganic spintronics studies have relied on it extensively, with the vast majority of successful devices making use of LSMO as one of the electrodes [Dediu09]. Within these devices, interfaces between LSMO and the organic medium dominate the transport. The properties of these open surface electrodes exposed to atmosphere and solvents are however hard to reconcile with those of epitaxial (buried) interfaces in thin films grown under stringent high vacuum or controlled oxygen pressure conditions. Especially, quantitative measurements from surface studies [Li11a, Galbiati15] require measurements over large areas due to the limited sensitivity of experimental tools, so that nanoscale variations of electrical transport properties are not reported [Gambardella14], thus leaving an open question: how does spin transport occur at the surfaces and interfaces of LSMO nanostructures and how does it impact hybrid spintronics? Due to the increased surface-to-volume ratio, LSMO nano-particles should be ideal systems to unravel the physical properties that are highly surface-sensitive, in particular magnetism and electrical transport. They also enable long-term stability of surfaces exposed to air and solvents to be addressed. Nanoscale size reduction or patterning of perovskite manganites also opens the door to magnetic property tuning [Rajapitamahuni16] or electronic phase separation (EPS) control [Shao16, Zhu16]. These recent examples demonstrate the key relevance of manganite nanoparticles for the fundamental understanding and insight into the applicability of these materials in the field of spin electronics. However, such studies require well-defined and well-crystallized nano-objects, attaining the structural quality of epitaxial thin films. Reported synthesis processes do not meet such stringent requirements. Indeed, LSMO nanoparticles obtained mainly through ball milling [Balcells98] or the combination of the sol-gel process and combustion reactions exhibit significant amounts of defects and unknown surface composition and properties [Pradhan08, Epherre11, Thorat12]. We highlight herein remarkable low temperatures spin transport behavior of LSMO nanomaterials by using an original combination of a dedicated colloidal synthesis of high crystalline quality nanocrystals, and a device geometry ideally suited for robust magnetotransport studies through a small number of nanoparticles [Tian07, Pradhan08, Epherre11, Thorat12, Tian16].

9.2 Sample fabrication and characterization

Our work was motivated by recent progress made by our collaborators of the team led by Professor Clément Sanchez at CMCP. They developed a dedicated colloidal approach to synthesize a high crystalline quality nanocrystals cubic-shape LSMO nanocrystals of about 20 nm in size. This synthesis approach consists of metal nitrates in molten potassium nitrate at 600°C during 1 h. The heating profile was adjusted to optimize the particle size distribution.

High temperature ionic molten salt enables relatively large-scale synthesis of black powder nanocrystal which after exposed to water during the purification step are stored under ambient atmosphere. This enables gram-scale synthesis of inorganic molten salt that provides well defined ligand-free surfaces with very low amounts of defects in contrast to previous reports. More Details of the synthesis method are provided in our related contribution [Thi N'Goc17]. Fig.9.1.(a,b) provide the SEM and TEM images of the resulting nanocrystals.

9.2.1 Physico-chemical properties of the nanocrystals

The physico-chemical properties of the nanocrystals were analysed by our collaborators, here I report the mains conclusions. The structural properties of the nanocrystals were analyzed by X-ray powder diffraction (XRD). The nanocrystals revealed a typical unstrained rhombohedral perovskite structure expected from bulk LSMO with $a = 5.50387(15)$Å, $c = 13.3451(5)$Å cell parameters from Rietveld refinement, in agreement with tabulated values [Radaelli97]. Hence, the particles can be considered strain-free. The unit cell volume is evaluated to be 350 $Å^3$, also in very good accordance with the expected structure and composition [Radaelli97]. Elemental analysis by inductively coupled plasma optical emission spectrometry (ICP-OES) yields Sr:La ratio of 0.51, close to the ideal $La_{0.67}Sr_{0.33}MnO_3$ composition and agrees with the value expected from the initial ratio of La and Sr precursors. State-of-the-art analytical scanning transmission electron microscopy (STEM) and magnetometry studies provide a clear picture of particles having core-shell properties. The remarkable structural quality of the nanocrystals makes possible atomic-resolved electron microscopy imaging of the core and the surface and enables to provide the first quantitative insight into chemical deviations from a perfect LSMO material and show that they are limited to a surface shell of less than 1 nm thickness.

High resolution scanning electron microscopy (SEM) (Fig.9.1.(a)) shows that the powder is predominantly made of 15-30 nm nanocubes, as confirmed by TEM and the corresponding size distribution (Fig.9.1.(b)). The maximum of the statistics is measured at 21 nm. In order to get deeper insight into the structure of individual nanoparticle, atomic resolution STEM images (Fig.9.1.(C-K) have been recorded on an aberration-corrected transmission electron microscope operating at 120 kV, in order to limit the beam damage to these potentially fragile nanostructures. Z-contrast images were acquired in the high angle annular dark field (HAADF) mode to highlight heavy elements La, Sr, and Mn (Fig.9.1.(C-E)), and in annular bright field (ABF) to image the lighter element oxygen (Fig.9.1.(F-H)). Both detection modes confirm the perovskite structure. The few crystalline defects observed in the core (Fig.9.1.(E,H) are identified as inclusions of cubic La_2O_3 that do not disturb the high crystalline quality of the perovskite. According to the crystallographic orientation (Fig.9.1.(C,D,F,G)), the nanocubes exhibit 001_{cubic} facets of the ideal cubic perovskite structure, corresponding to the {012} faces of the rhombohedral LSMO structure.

The mean oxidation state of manganese was measured by high energy resolution electron energy loss spectroscopy (EELS), along line scans in the particles cores (Fig.9.1.I). The in-

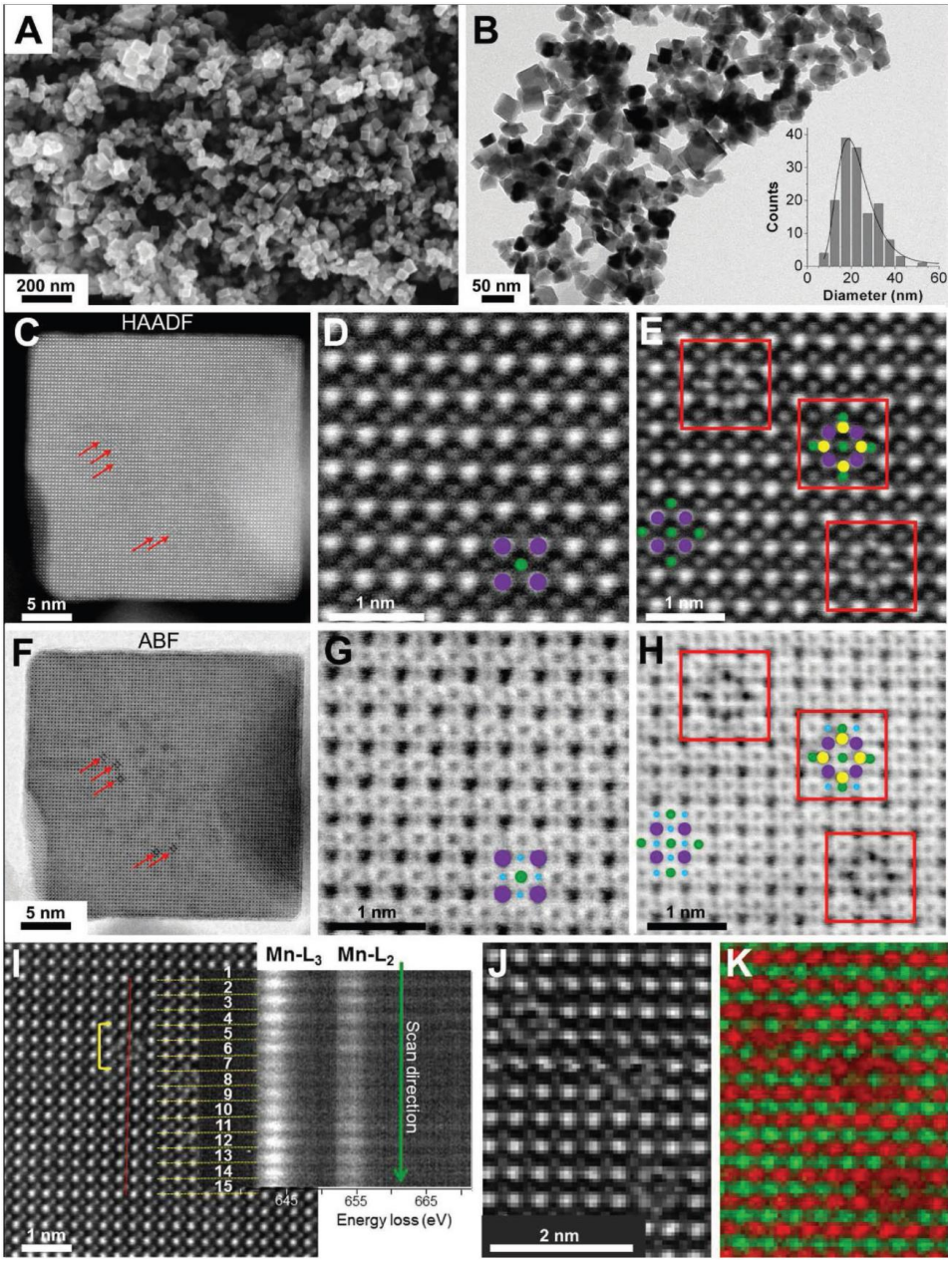

Figure 9.1 *– Electron microscopy study of LSMO nanocrystals. Analysis of the shape and the particles core. (A) SEM and (B) low magnification TEM images of LSMO particles showing the homogeneous nanocube morphology. The inset of (B) shows the TEM size distribution of the nanocubes with log normal distribution. (C) STEM-HAADF images of a whole nanocube. (D) The perovskite crystalline structure of the core with a few defects observed (E). (F-H) STEM-ABF images were recorded simultaneously with the STEM-HAADF pictures (C-E). Purple, green, blue, and yellow disks highlight La/Sr, Mn, O, and La atomic columns, respectively. (I) STEM-HAADF image of a part of the core where high energy resolution EELS spectra was recorded along a scan line (red line). Mn-$L_{2,3}$ EELS spectra for each unit cell are shown in two dimensions. They were obtained by averaging the 5 spectra recorded over each unit cell. The yellow bracket highlights a defect on the 5th, 6th, and 7th unit cells. (J) STEM-HAADF image and (K) corresponding atomic resolution mapping obtained by summing the Mn-$L_{2,3}$ (green) and La-$M_{4,5}$ (red) EELS maps.*

tensity ratio of the Mn-L_3 and Mn-L_2 lines was used to quantify the average oxidation state versus a calibration curve from references of known oxidation states of Mn^{2+}, Mn^{3+}, and

Mn^{4+} [Thi N'Goc17]. Measurements over different scan lines show that the core is very homogeneous, with an average Mn oxidation state of +3.3±0.1, in good agreement with the value of +3.34 expected from the La/Sr ratio measured by elemental analysis on the whole batch of particles. In summary, all data demonstrate that the nanoparticles cores exhibit the expected structure and composition of unstrained LSMO. These nanocubes can then be considered as nanoscaled pieces of bulk crystalline LSMO. Unprecedented high magnetoresistance (MR) is observed at low temperatures. We demonstrate that such large effects cannot rely on the half-metallic character historically used to explain MR properties in bulk polycrystalline LSMO [Hwang96] and magnetic tunnel junctions [Martin96]. These findings bring therefore new perspective on the problem of spin transport in LSMO, especially on its properties that are robust upon exposure to air and solvents.

9.3 Magnetometery characterization of LSMO nanocubes

We conducted temperature dependent magnetization measurements using a Superconducting QUantum Interference Device (SQUID). The engineer responsible for the SQUID acquired the data. The magnetization curves (Fig.9.2.a) confirm that the particles are ferromagnetic. The non perfect saturation at high magnetic field > 3 T including at low temperature suggest a two-phases magnetic behavior with the superposition of a ferromagnetic-like component and a paramagnetic-like phase resulting from spins disorder. Such systems in sub-100 nm nanoparticles are often interpreted in terms of a 'core'-'shell' model of the magnetization of nanoparticles [Zhang14a]. We conducted a quantitative analysis based on the molecular field theory (Eq.10.2) illustrated in Fig.9.2.b, using the low-temperature magnetization curve as baseline for an approximation [Coey10].

$$m(B) = \Theta(B)m_F + L(\alpha B)m_P \tag{9.1}$$

In this equation, the magnetization $m(B)$ is the superposition of a ferromagnetic curve $\Theta(B)$ for the expected 'core' of the particles with a saturation magnetization m_F and a paramagnetic-like contribution described by a Langevin function with a saturation value (at infinite field value) of m_P. The prefactor $\alpha = \frac{\mu}{k(T+T_0)}$ includes an effective temperature correction T_0 that describes interactions between the moments μ, expected from the antiferromagnetic coupling in manganites resulting to the overall paramagnetic like behavior [Coey10]. We performed experimental curves fittings between 1.8 and 50 K in high-field regime enabling to estimate the values of $T_0 \approx 100$ K and $\mu \approx 10\mu_B$, which corresponds to the magnetic moment of ~ 3 Mn ions, reflecting interactions between the Mn nearest neighbors. The ferromagnetic component $\Theta(B)$ is calculated as the difference between the total measured magnetic moment and the fitted Langevin function (Fig.9.2.b). It dominates the 'low field' magnetization response while the paramagnetic-like contribution dominates the 'high-field' magnetization response and illustrates a resulting sample magnetization difficult to saturate. The ferromagnetic component shows a magnetization of roughly 25% of the expected saturation of bulk LSMO at low temperatures ($3.6\mu_B$/f.u.). The symmetry breaking at the

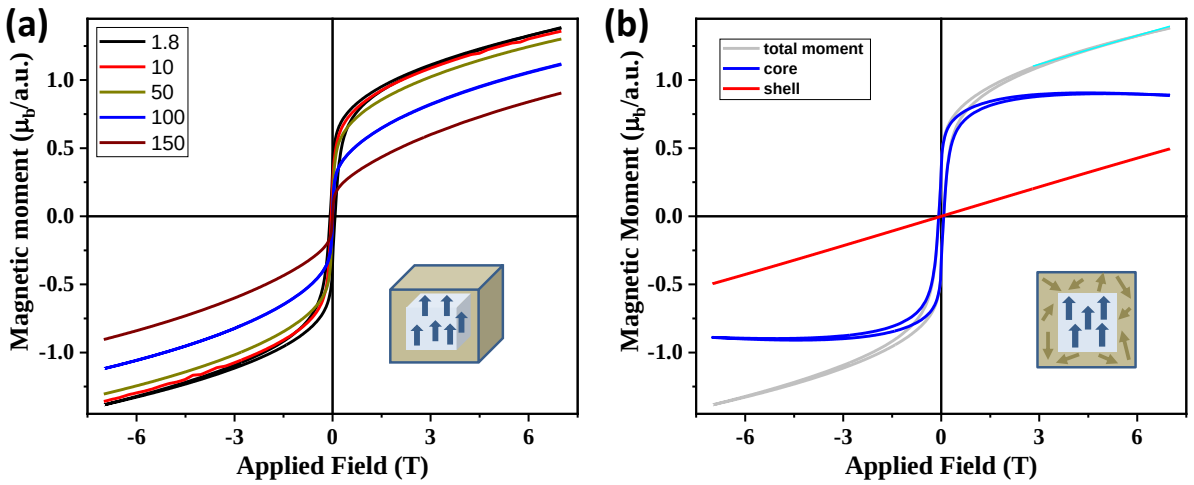

Figure 9.2 *– Magnetic properties of LSMO nanocubes. (a) Magnetization curves at several temperatures. (b) Decomposition of the magnetic signal at 1.8 K into a ferromagnetic core component (blue curve) dominant at low field and a paramagnetic-like shell (red curve) dominant at high field. The experimental data (grey curve) was fitted for the applied $\mu_0 H$ between 3 and 7 T, (light blue curve). Inset in (a) and (b) are the schemes of a core-shell nanocube with aligned core magnetic moments.*

surface of the material, as well as possible changes in the Mn oxidation states near the surface related to oxygen vacancies, may disturb the ferromagnetic double exchange Mn^{3+}-Mn^{4+} mechanism toward antiferromagnetic interactions. This results to the so-called 'dead magnetic layer' [Boschker11] or surface antiferromagnetic/spin glass-like phases [Valencia14] reported for thin films of LSMO, in agreement with the magnetic 'core'-'shell' model usually considered to describe the magnetic properties of sub-100 nm nanoparticles [Zhang14a]. In this approximation, for particles of ~20 nm size, a shell thickness would extend up to 4.0±0.5 nm. Thin films typically exhibit 2 nm thick dead layers [Verna10], with larger thicknesses when grown on nonepitaxial substrates [Borges01] while smaller values, down to 1 nm, have been reached on optimized strain-controlled epitaxial thin films [Valencia07].

The two components description of the data captures the key idea of nanoparticles made of two magnetic phases. Coexistence of electronic phases is recognized as a general phenomenon under the term EPS. Generally, EPS stems from the peculiar interplay between several orderings intrinsic to complex systems, like manganite perovskites, and can persist far from the bulk transition temperature [Dagotto01]. For compounds prone to phase segregation, the EPS length scale can reach the 500-800 nm range [Shao16]. We are not aware of unambiguous experimental insight into the EPS length scale in LSMO, except that it should be much smaller, not exceeding the 10 nm range [Wu06, Liang14]. Hence, the two-phase model extracted from magnetic measurements is coherent with the EPS model. In our specific nanoparticle configuration, we expect the paramagnetic-like phase to dominate at the surface of the particles (as in thin films), while the ferromagnetic component is likely located in the core, thus pinning the EPS in a core-shell structure [Zhang14a]. The larger volume fraction of the shell compared to films illustrates how freestanding nanoparticles amplify the proportion of surface atoms relative to bulk ones. This suggests that LSMO presenting open

surfaces should exhibit significant surface-sensitive transport properties.

9.4 Charge and spin transport in LSMO nanocrystals

For the magnetotransport measurements, we fabricated a dedicate device geometry consisting of reliable high aspect ratio nanotranches [Dayen10] ($w/l > 100$) with a width comprised between 20μm to 100μm and gate of about l=80±10 nm (Fig.9.3).

9.4.1 Nanotrenches fabrication

The nanotrenches are fabricated by standard optical lithography in two steps making used of angle deposition during the second step which enables obtaining the nanogaps from the shadow of the edges of first electrodes [Dayen10]. The first layer of micrometer wide electrodes is patterned on Si/SiO_2 substrate using LOR + AZ5214 bilayer photoresist in order to have straight and well-defined edges. The exposition to UV light (Suss microtec MJB4) last 3.6 s through a positive mask followed by 35 s flood exposure for image reversal. AZ726 MIF is used as a developer. This step is completed by Ebeam evaporation of a Ti(3 nm)/Au(47 nm) bilayer and lift-off in AZ remover. The second layer of electrodes is patterned using a single exposition step in AZ5214 negative resist. The optical mask is designed such that the alignment ensures sufficient overlapping of the extremities of first layer electrodes with that of the second layer pattern to guaranty a shadow deposition from the edges of the first electrodes. After the development in AZ726 MIF, 60° tilted angle deposition technic is used for ebeam evaporation of Ti(6 nm)/Au(54 nm) bilayer (Fig.9.3.(a)). The second layer is lifted off similarly as the first layer in AZ remover. The nanotrenches gap is given by $w = h\tan(\theta)$ where h is the thickness layer. For 60° angle and h = 50 nm, the expected gap is 86 nm. The optical microscopy and SEM images of the nanotrenches are presented in Fig.9.3.(b-d). After the nanofabrication, a drop of $La_{0.67}Sr_{0.33}MnO_3$ nanoparticles solution conserved in ethanol solvent is deposited onto the nanotrenches using an eppendorf micropipette. I optimized the concentration of the solution to ensure efficient filling of the nanotrenches and no to have bulk filling which may complicate the analysis of the transport measurements. The Fig.9.3.(e) presents the SEM images of a typical device presenting chains of 3 to 4 nanoparticles bridging the electrodes providing thus a straightforward experimental access to their average resistance.

9.4.2 Transport measurements

The I-Vsd characteristics of the devices are provides in Fig.9.4 for zero and applied magnetic field. A strong nonlinearity dominates the low temperature properties. The current present a simple power-law dependency at low dc bias voltage while an exponential increase is notably at high voltage regime (Fig9.4.(c)). The exponents of the power-law decreases with temperature in high Vsd regime. This is reminiscent of multi-step tunneling transport through localized states [Glazman88]. Such a model has been invoked to explain the properties of

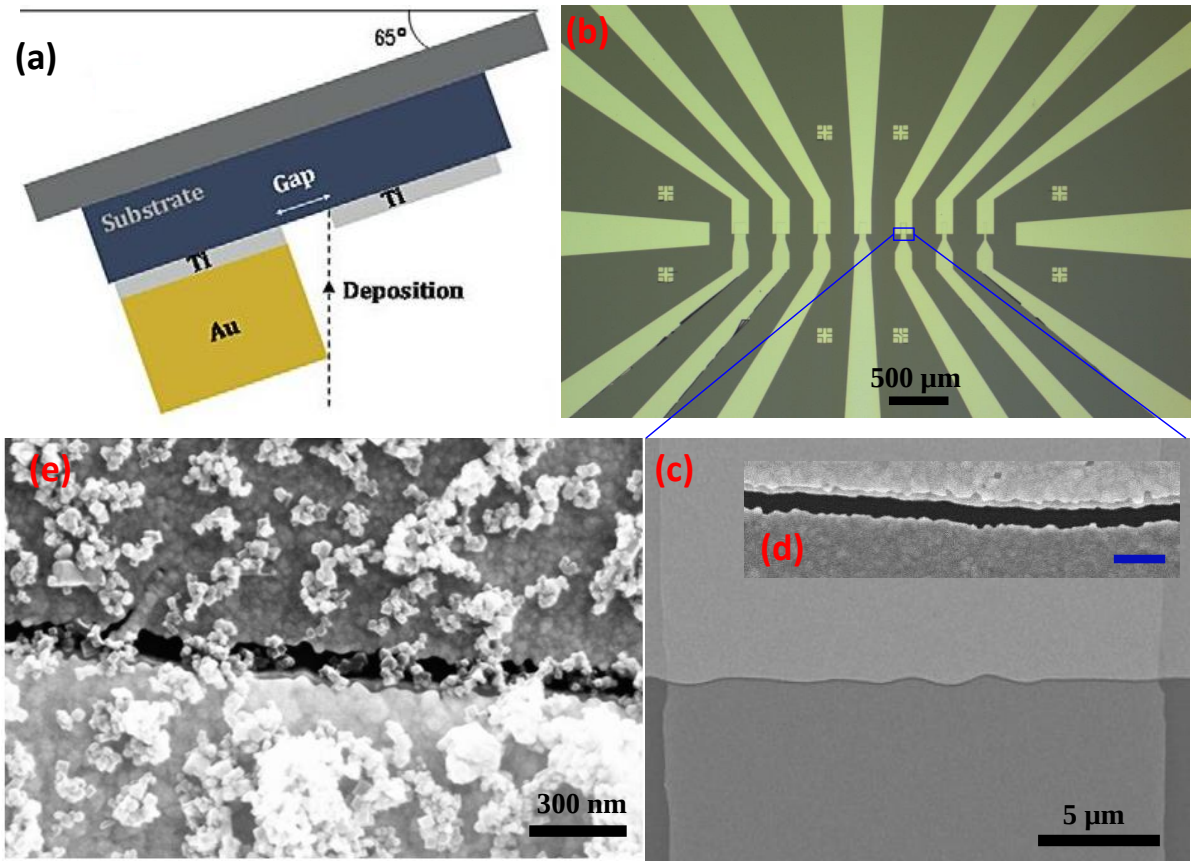

Figure 9.3 *– Fabrication procedures of the device for magnetotransport measurements. (a) Tilted angle deposition of the second layer. The nanotranches result from the shadow of the edges of the first layer. (b) Large scale optical image of the nanotrenches after optical lithography. (c) SEM image of a single nanotrench and a partial large magnification image (d). (e) SEM image of a device with dropcasted* $La_{0.67}Sr_{0.33}MnO_3$ *NPs briging the nanotrench.*

perovskite thin films with artificial grain boundaries [Gross00]. The I-Vsd curves recorded at zero and maximum applied magnetic field provide a straightforward method to determine the effect of the magnetic field on the resistance of the device and evolution of the resulting MR with the applied bias (Fig.9.4.(b)). A significant decrease with bias is observed, with MR ratios exceeding one order of magnitude in the low bias range (Fig.9.4.(c)). Even at 6 V bias, the MR exceeds predictions of a factor 2 from the tunneling model in a randomly magnetized ensemble of particles. The measurements are confirmed by magnetic field dependent resistance of the devices. The samples exhibit a remarkably high change of resistance as the applied magnetic field is sweeping, reaching one order of magnitude. Note that the MR data (Fig.9.5.(b,c)) are recorded under a rather large voltage bias of 2 V, essentially to improve data precision recording for these samples of high resistance. Larger MR values are found at smaller bias. The measurements are reproducible within 10% from sample to sample. Devices are stable over months when left under ambient conditions. We only observed a significant decrease of MR properties, typically by 20%, (and increase of typical device resistance values) when nanoparticles were left for more than one month in ethanol prior to drop-casting on devices. The large change of resistance reaching factor 8 under large applied

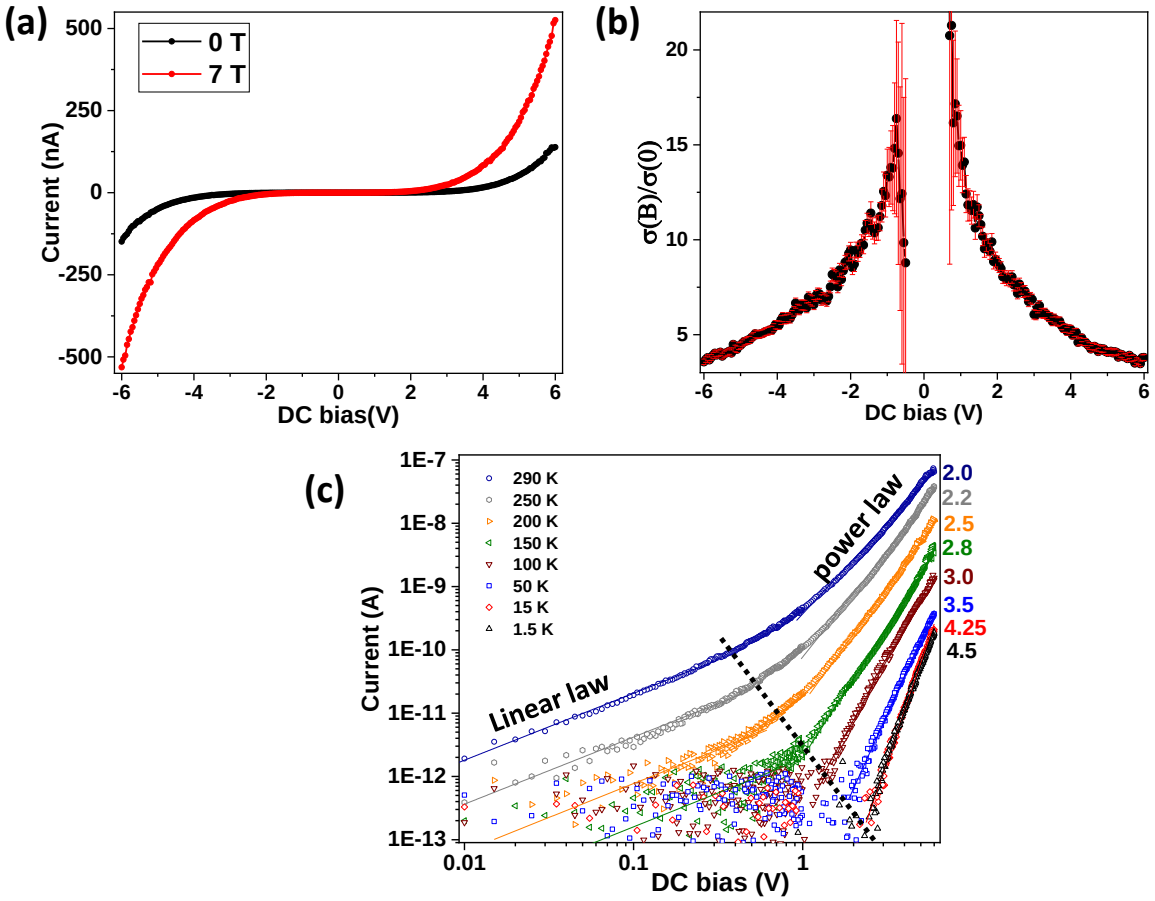

Figure 9.4 *– Electrical properties of LSMO NPs and voltage dependence of the MR. (a) Current measurements at 1.6 K under 0 T (black curve) and 7 T field (red curve). (b) The related normalized Magnetoconductance amplitude as a function of the applied voltage bias. (c) I-V curves recorded at several temperatures. The values on the right are the corresponding exponents of the power law.*

field and even 20 under smaller voltage bias values (Fig.9.4.(b)), cannot be explained by a simple model of spin-polarized tunneling between neighboring particles. Indeed, under the hypothesis that we are probing an ensemble of particles with expected random magnetic orientations at a coercive field, the MR resulting from spin-dependent interparticles tunneling should follow the Eq.10.3.

$$MR = \frac{R(B) - R(0)}{R(0)} = \frac{1}{1 + m^2 P^2} \tag{9.2}$$

Where m denotes the normalized magnetization value and P, the tunneling spin polarization. Under the hypothesis of tunneling between perfectly spin-polarized half-metals, the Eq.10.3 limits the MR to 50% (or double of the magnetoconductance). Interactions between adjacent particles can lead to deviations from random neighbor magnetic alignment. But this model remains hard to reconcile with our data showing a magnetoconductance more than four times larger than the maximum expectation of Eq.10.3. Coulomb blockade effects, and in particular cotunneling enhancement of the MR (see section.) cannot explain the high MR values as well, especially as they persist up to large voltage bias (higher than 1 V/junction, see Fig.9.4.(b)), largely exceeding all estimates of Coulomb blockade energy values.

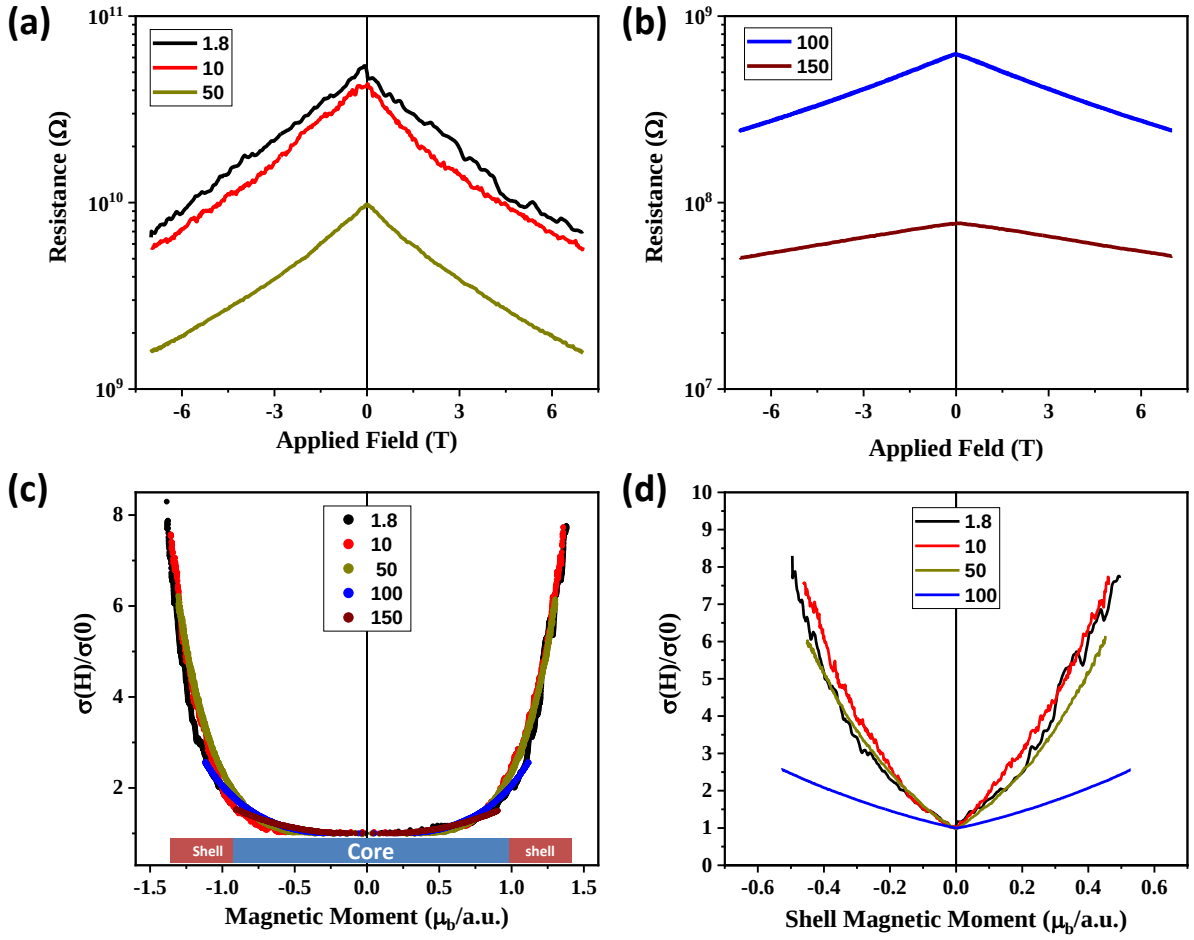

Figure 9.5 *– Magneto-transport properties of LSMO nanoparticles. (a,b) Magnetoresistance curves at several temperatures for an applied bias of 2 V. (c) Normalized magnetoconductance (from a and b) as function of the sample magnetic moment (Fig.9.2). The bottom colored areas reminder of the dominant magnetic component contributing to the moment (blue: ferromagnetic core, red: paramagnetic-like shell). (d) Normalized magnetoconductance as function of the fitted paramagnetic-like $L(\alpha B)m_p$ shell magnetic moment (see Eq.10.2 and Fig.9.1.(b)).*

The key experimental results indicating that the (half)-metal ferromagnetic component of the nanoparticles do not contribute to the MR are shown in Fig.9.5.(e) illustrating how resistance evolves with the sample magnetization. Only negligible variation is noticeable when the magnetization change relates to the core particles while the resistance varies approximately like m^2P at higher fields (Fig.9.5.(d)). Remarkably, all measurements between 1.5 and 150 K merge onto a single master curve (Fig.9.5.(d)), even though the sample resistance changes by three orders of magnitude, and the MR ratio by a factor 8 (Fig.9.5.(a,b)). This key result shows that our low temperatures MR behavior is strikingly different from what is documented for bulk LSMO samples ranging from bulk single-crystals down to nanocrystalline materials. Hwang et al. [Hwang96] reported a significant low-field change of the resistance (LFMR) that was attributed to the alignment of LSMO domains in the bulk and to the tunneling between highly spin polarized domains or grains. On the contrary for the high-field magnetoresistance (HFMR) their report was of limited magnitude and related to the intrinsic properties of LSMO single crystal domains. The LSMO nanocubes exhibit a completely

different behavior with negligible LFMR. Hence, the magnetization process that aligns the core magnetic moments of our nanoparticles resulting to more than half the magnetization scale in our applied field window, does not affect the sample resistance. In our case, the large field necessary to align the paramagnetic-like component changes the sample resistance value drastically and results in a huge HFMR. The master curve in Fig.9.5.(d) illustrates how the amplitude of the MR simply reflects the degree of paramagnetic alignment reached at a maximum applied field. The MR therefore does not rely on tunneling from/to the half metallic core of LSMO.

To explain such peculiar behavior, we propose that the observed magnetoresistance in assemblies of nanocubes originates from a mechanism similar to the colossal magneto-resistance (CMR), well-documented for manganites close to their Curie temperature [Coey99]. CMR is the very large change of resistance that occurs under modifications of the magnetic alignment of neighbor Mn cations coupled ferromagnetically through the double exchange mechanism in Mn^{3+}O-Mn^{4+} units. The charge transfer probability is enhanced in the magnetically aligned state. CMR therefore relates to the huge change of resistance near the magnetic transition between disordered (usually paramagnetic) and ordered (usually ferromagnetic) phases. The corresponding change of the conductivity stems from the insulator-to-metal transition as the material goes through magnetic ordering, at around 360 K for LSMO [Coey99] where a typical one order of magnitude change of conductivity is observed under high magnetic fields (typically 10 T). In our case, magnetic alignment, especially at the nanoparticles surfaces, is forced under high magnetic fields applied at low temperatures, even though the material is far from its bulk transition to a paramagnetic state. Such behavior can be related to the magnetization configuration in the LSMO nanocubes described as a two-phase material. Electrical measurements provide therefore further support to a phase-separation model, with the magnetic field driving the paramagnetic insulating phase toward metallicity. Our well-defined single-crystal nanoparticles with small grain size therefore provide insight into electrical properties dominated by charge transfer between conductive metallic islands through insulating barriers. The core of the particles, expected to exhibit magnetic ordering, should therefore be metallic-like, while the spin disordered nanoparticles surfaces should play the role of insulating shells. A more precise analysis of the magnetic and magneto-transport characterization as well as the structural properties of the LSMO nanocubes outer surfaces has been conducted to confirm this hypothesis.

9.4.3 Exchange bias coupling

In the magnetic core-shell systems such as our LSMO nanocubes, an exchange bias coupling is expected originating from the Ferromagnetic/Anti-ferromagnetic (FM/AFM) interfacial exchange anisotropy. Exchange bias coupling is therefore a characteristic feature of FM/AFM biphasic systems [Coey99]. It has been systematically investigated in chemically synthesis $Fe_3-\delta O_4$/CoO core-shell NPs [Lee12b]. To evidence the exchange bias coupling in our LSMO NPs, Field Cooled (FC) and zero-field cooled (ZFC) magnetometery and transport measure-

ments were conducted. For FC measurements, the sample was heated at 400 K above the curie temperature (found to be close 365 K) and cooled down to 1.5 K under a saturating field of 7 T. The FC hysteresis loop was measured by applying the same field sweep as the ZFC curves. Similarly, -7 T FC magnetization and magnetoresistance were recorded. In Fig.9.6.(a,b) the ZFC and FC magnetization curves are presented. The first remarkable feature is that the saturation magnetization are quite similar for both FC hysteresis loop while being larger compare to ZFC saturation magnetization (Fig.9.6.(a)). More importantly, the 7 T (-7 T) FC magnetization curves shows a negative (positive) horizontal shift comparatively to the ZFC curves (Fig.9.6.(b)). These observations are characteristic of exchange bias coupling resulting from the pinning of the FM core spins with the AFM shell spins at the FM/AFM interface due to the applied magnetic field during the cooling. It arises from the anisotropy energy of nanocrystal shell which is higher than the coupling energy between FM core and AFM shell phases [Lee12b, Skoropata14]. Hence, the interface spins of the FM core experienced during the reversal dynamic a strong unidirectional anisotropic barrier created by the exchange coupling at the FM/AFM interface. This exchange bias coupling is often quantified by calculating the exchange field $B_{ex} = (B_{c1} + B_{c2})/2$ [Skoropata14], B_{c1} and B_{c2} denote the coercive field in positif and negative field [Skoropata14]. In our case, it is estimated to be $\sim$ 25mT which is relatively larger compare to Fe_3O_4/CoO particles [Skoropata14] reaching and order of magnitude deference in some cases [Lee12b]. The magnetotransport properties are affected by this FM/AFM interface exchange bias. In Fig.9.6.(c) we present the FC MR(H) curves presenting an hysteretic behavior characterized respectively by a negative (red curve) and positif shift of the coercive field for magnetization reversal (black curve) switching field directions. This behavior less pronounced in ZFC magneto-transport measurements is exacerbated by field cooling. In Fig.9.6.(d) we compare ZFC magneto-conductance curves and FC curves. On observes that although the FC curves are shifted toward positif and negative fields correspondingly to the instrumentation direction, the ZCF remains almost symmetric. This clear signature of the exchange bias coupling in the magnetization characterization correlated with magneto-transport further confirms the hypothesis of core-shell structure of our LSMO NPs and question the role of the surface properties.

9.4.4 Structural properties of the nanoparticles shells

A more precise analysis of the structural properties of the LSMO nanocubes outer surfaces is performed below by using state-of-the-art STEM. To address the core-shell picture suggested by magnetic and electric measurements, the surface structure has been assessed by high-resolution STEM techniques. First, STEM-HAADF (Fig.9.7) shows that contrary to many other oxide nanoparticles, the crystal structure is retained right up to the outer surface layer. Hence, the 2-phase magnetic structure does not originate from surface amorphization contrary to Fe_3O_4/CoO particles [Lee12b, Skoropata14]. Chemical information was then retrieved from state-of-the-art analytical STEM. The Mn oxidation state is the key parameter governing the charge and magnetic ordering and can be accurately measured by EELS (Fig.9.7). The mean value is measured along line scans from the exterior of the particle to its

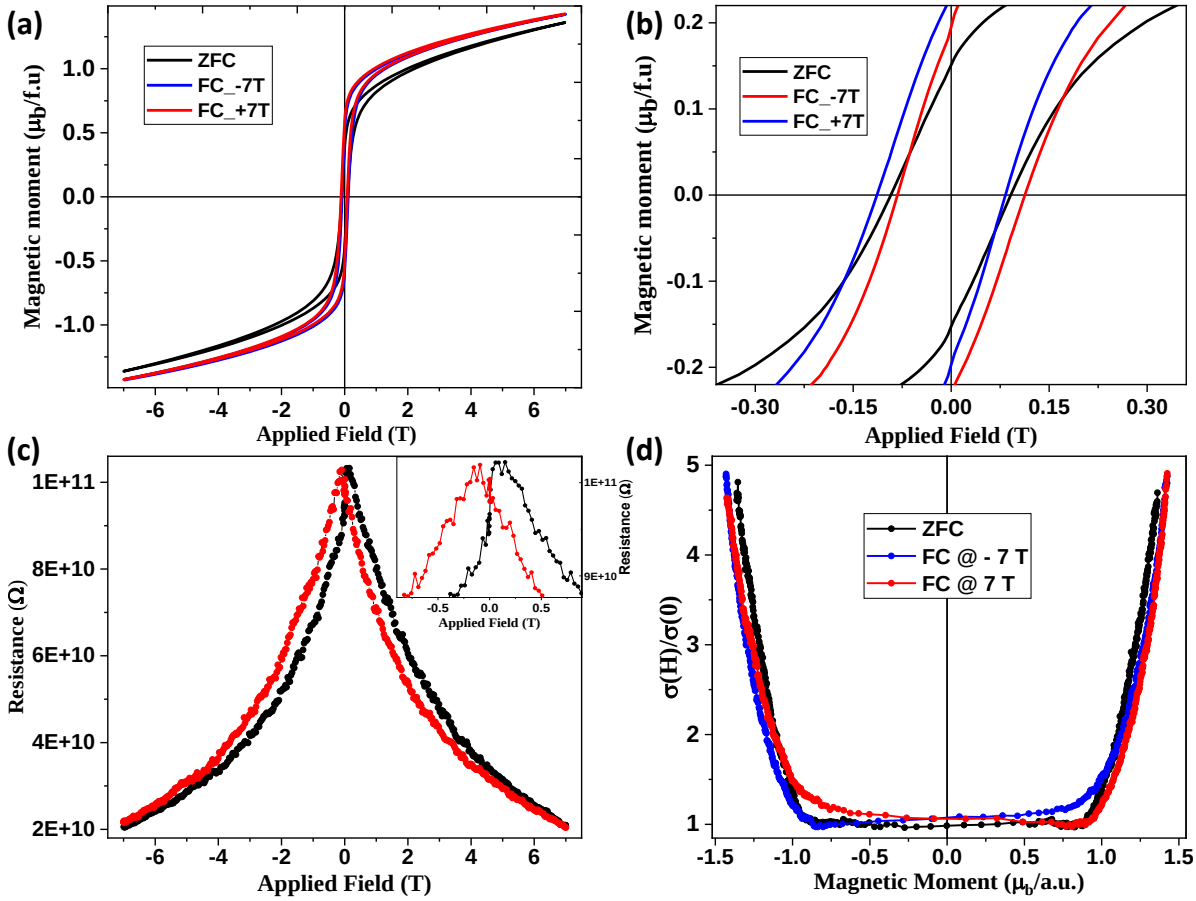

Figure 9.6 *– Exchange bias coupling characterization. (a) FC and ZFC hysteresis loops of the magnetization recorded at 1.6 K. (b) Details zoom of the FC and ZFC hysteresis loops of the magnetization around the coercive field to highlight the negative field shift (blue curve) and positive field shift (red curve) of the data recorded after cooling the sample under negative and positif applied magnetic field respectively. (d) FC MR(H) presenting an hysteretic behavior close to zero magnetic field as highlighted by the inset. (d) Normalized FC and ZFC magnetoconductance (from c) as a function of the sample magnetic moment (from a). The ZFC is presented for comparison.*

core (Fig.9.7). As described above, the Mn average charge of +3.3 ±0.1 is homogeneous over the whole particle, except for the outer two pseudocubic unit cells that correspond to a thickness of 0.8 nm. These two surface layers with three manganese-containing planes exhibit a significant decrease of the Mn oxidation state to $Mn^{+2.8\pm0.1}$. To understand the charge compensation in the strongly reduced perovskite shell, we then address the exact composition of the nanocube outer atomic layers. The La, Sr, and Mn atomic distribution across the edges of the nanocrystals is monitored by EELS and energy-dispersive spectrometry (EDS) spectra simultaneously since the low signal-to-noise ratio of the Sr-$M_{4,5}$ line (at 1940 eV) prevents its analysis by EELS [Thi N'Goc17]. The zero-energy-loss EELS signal (Fig.9.7) intensity is homogeneous over the entire nanocube and shows that the thickness is constant, so that any change in the relative intensities can be ascribed to chemical features and not morphological causes. The EDS/EELS-derived overall atomic composition of the nanocrystals is in agreement with the nominal one and the ICP-OES values [Thi N'Goc17]. No difference in the Sr:La ratio is detected across the surface of the nanocrystals (Fig.9.7.(f)), so that any change in the

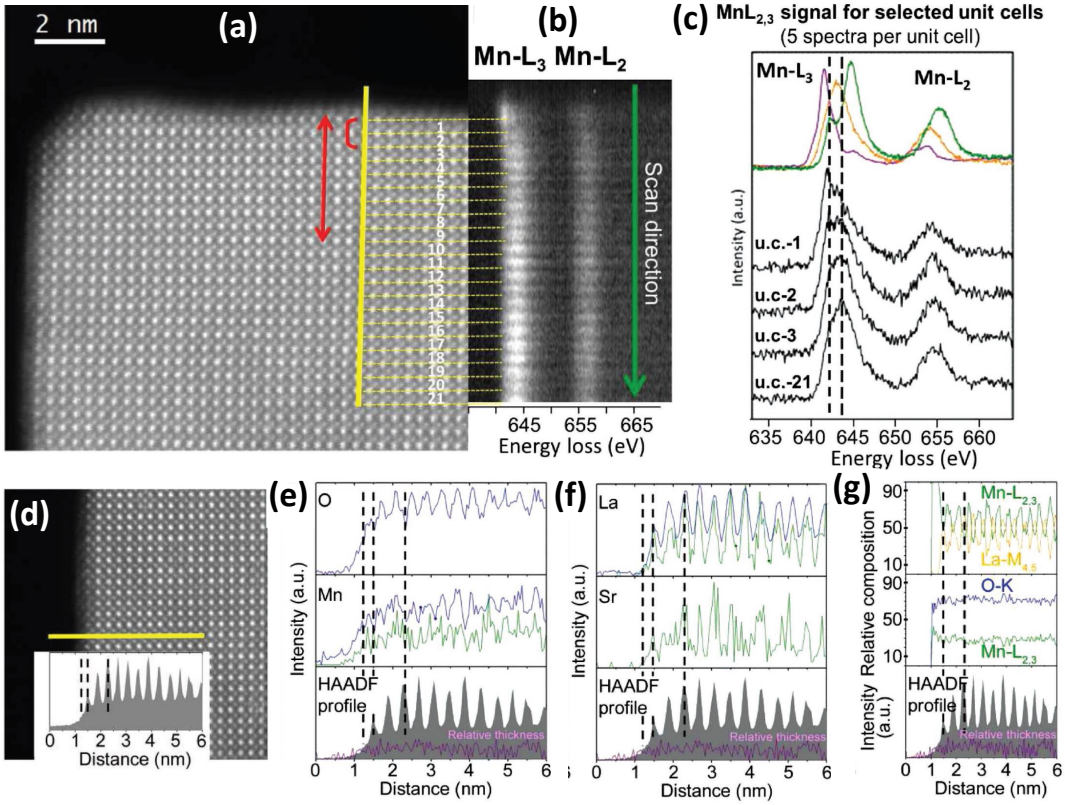

Figure 9.7 *– STEM analysis of the particles edges. (a) STEM-HAADF image of a nanocube edge where high energy resolution EELS spectra have been recorded along the scan yellow line. (b) Mn-$L_{2,3}$ EELS spectra for each unit cell in two dimensions. The red bracket in panel (a) highlights the two outer unit cells where the Mn oxidation state is decreased according to the energy loss value and the intensity ratio of the Mn-L_3 and Mn-L_2 lines in panel (b). The red arrow in panel (a) highlights the thickness of the shell where magnetization is disturbed. (c) EELS spectra of selected unit cells (black) and references of Mn^{2+} (purple), Mn^{3+} (orange), and Mn^{4+} (green) oxidation states. (d) STEM-HAADF image of a nanocube edge where high energy resolution EELS spectra have been recorded along a scan yellow line. Inset shows the HAADF signal recorded during the simultaneous acquisition of EELS and EDS line spectra. (e,f) Signal profiles of the different elements obtained from EDS (green) and EELS (blue) signals. (g) La:Mn and Mn:O relative compositions (%) obtained from EELS signals. The HAADF signal and the black dashed lines are included to better identify the first Mn-O and La/Sr-O planes, as well as the two first unit cells in the STEM-HAADF image. The relative thickness computed from the simultaneously acquired zero loss signal is also shown (purple line).*

Sr:La stoichiometry can be discarded, even at the outer surface layer. This contrasts with previous surface studies on LSMO films suggests that Sr can possibly segregate to the surface, making its first atomic layers transform in another possibly insulating phase [Dulli00]. Next, the oxygen content is questioned. The atomic resolution analysis of the Mn:O relative concentration (%) of the core (Fig.9.7.(g)) is in good agreement with the 25:75 (±5) ratio expected for the LSMO perovskite structure. However, a slight increase in the Mn:O relative content is evidenced within the two pseudocubic unit cells close to the edge of the LSMO nanocubes (Fig.9.7.(g)). These features point to a decrease in the oxygen concentration within a ~1 nm thick shell. As the La:Sr and La:Mn stoichiometries are constant over the nanocrystal (Fig.9.7.(f,g)), the depletion of the Mn oxidation state at the 0.8 nm thick-shell is then due to oxygen vacancies. According to the Mn mean oxidation state of $Mn^{+2.8\pm0.1}$ in the shell, the oxygen vacancy content is about 8 in percentage. Further discussion of this analysis are

provided in Ref.[Thi N'Goc17] and it related supplementary information.

In summary in relation to magnetic and transport properties, the nanocubes can be described as core-shell nanocrystals on the basis of the atom-scale composition. The core is made of highly crystalline LSMO with ideal stoichiometry, and ∼1 nm thick shell contains strongly reduced manganese cations and a significant amount of oxygen vacancies with no alteration of the perovskite structure. The thickness of the layer containing the reduced Mn ions is remarkably small, revealing the sample of quality similar to epitaxial thin films grown in ultra-high vacuum or oxygen-controlled environments. Such a core-shell compositional relates with the magnetic properties. Indeed, the low Mn oxidation state in the shell suggests insulating properties of the nanoparticle surface, in agreement with the paramagnetic-like component of the two phases magnetic configuration at low applied magnetic field. Clearly, the changes in surface composition affects the magnetic properties over a depth exceeding the expectations inferred from composition and structural considerations. This difference may arise from (i) the above-mentioned detection threshold of EELS-STEM suggesting nonstoichiometry gradient extending deeper than 0.8 nm; (ii) the competition between the different spin configurations in a 0.8 nm thick paramagnetic-like layer and the ferromagnetic core, causing misalignment of spins at the core-shell interface over a larger depth than ∼1 nm; (iii) occurrence of EPS. This latter model describes mixed-phase nanocrystals and is actually in agreement with a core-shell picture where the paramagnetic-like phase would be 'pinned' by the surface compositional deviations from ideal LSMO. The EPS model does also agree with the large volume fraction of spin disordered phase.

9.5 Conclusion

We presented in this chapter the magneto-transport properties of $La_{0.67}Sr_{0.33}MnO_3$ perovskite nanocrystals with unprecedented structural quality. The nanocrystals synthesized from metal nitrates in molten potassium nitrate at high T yield a single crystal structure of LSMO with oxygen deficiencies and related manganese reduction confined to just the two outer surface perovskite layers. The composition and structural order are on par with epitaxial thin films, yet the magnetically disordered volume fraction of these freestanding nanoparticles reaches 75%, extending over a depth significantly larger than the thickness of detected chemical disorder, and suggesting the occurrence of EPS in LSMO nanocubes ∼20 nm in diameter. Magnetoresistance data highlight that the transport is controlled by the paramagnetic-like phase component, expected at the particle interfaces. The large magnetoresistance values relate to the drastic change of conductivity under magnetic alignment of the spins in the paramagnetic-like phase analogous to normal CMR, although the experiments are performed very far from the bulk LSMO magnetic transition and the CMR temperature range. This finding is in strong contrast with models invoking very high spin polarization of current or density of states when extracting charges from LSMO. In view of the structural quality of the nanocrystals reported herein, the results indicate that the magnetoresistance properties intrinsic to LSMO and its interfaces should not be neglected when

investigating heterogeneous devices using LSMO electrodes, especially when exposed to air, solvents, and organic moieties. The outer surface properties we unveil highlight unexpected physical and chemical phenomena associated to charge and spin transport in LSMO-based devices. These new behaviors thus shed a new light on the well-established use of such materials in hybrid and organic spintronics. They also provide a unique test bench material for gaining fundamentals insight into electronic phase separation in magnetic perovskites.

Chapter 10

General conclusion and perspectives

We have investigated in this thesis the transport and magnetotransport properties of novel nanolectronic devices consisting of low dimensional nanocrystals. Three geometries of devices have been studied including SETs consisting of Al-AlOx/graphene and Al-AlOx/MoS_2 2D-0D mixed dimensional heterostructures, $MoSe_2$ based FET making used of Ti/Au contacts and LSMO NPs trapped into nanotranches.

10.1 General conclusion

10.1.1 2D-0D MD-VdWh based SETs

Device fabrication

We have developed a relatively simple process to fabricate 2D-0D MD-VdWh composed of Al-AlOx core-shell NPs self-assembled onto Graphene or MoS_2 templates. This fabrication process consisted of single step Ebeam evaporation of a thin Al of 1.7 nm nominal thickness onto the surface of either exfoliated Gr or MoS_2 on Si-SiO_2 wafer or Gr grown by CVD on Ni. It results to a granular Al layer with a self-assembled Al NPs decorating the 2D material surface. After oxidation in ambient atmosphere, a certain number of Al NPs adopt a core-shell structure with a metallic Al core surrounded by alumina (AlOx) shell providing thus a configuration suitable for single electron transport processes. Comprehensive the physico-chemical analysis of the Al-AlOx/2D material heterostructures combining XPS in collaboration with Laurent Simon, STEM and EELS in collaboration with Prof Ovidiu Ersen confirmed the core-shell configuration of the NPs. We integrated these heterostructures into tunnel junctions devices for transport and magneto-transport measurements.

The case of Al-AlOx/Gr heterostructures

Transport measurements: Low temperature transport measurements have revealed remarkable single electron processes originating from Coulomb blockade effect of Al metallic core of the NPs and manifested by robust and reproducible Coulomb staircases in the I-Vsd characteristics and Coulomb oscillations of the differential conductance (dI/dV-Vsd) in agreement with classical CB theory. In addition, remarkable gate dependent conductance oscillations were interestingly reported. Charge transport spectroscopy revealed discernable Coulomb diamond patterns in the conductance stability diagram. Gate dependent conductance oscillation was observed to be preserved up to 30 K. In other samples, two probes conductance measurements demonstrated characteristics attributed to CB up to room T.

Magneto-transport measurements: Low temperature Magneto-transport measurements of the 2D-0D Al-AlOx/Gr MD-VdWh heterostructures based SED consisting of a single magnetic electrode demonstrated reproducible MR not requiring a coherent spin injection and detection. The magnetroresistance reaching 20% results from the AMC effect which enables to tune the electric charge experienced by the core Al of the NPs and thus modulates the resistance of the device. This observation of magnetic functionalities in the CB regime on our scalable 2D-0D MD-VdWh based nanodevices paves the way toward novel device architectures at the crossroads of 2D material physics and spintronics.

The case of Al-AlOx/MoS_2 heterostructures

In the case of SET integrating Al-AlOx/MoS_2 heterostructures, low temperature transport measurements demonstrate a back gate dependent conductance oscillations with a superimposed field effect increase of the conductance characteristic to the gating of the MoS_2 channel. A behavior typical to semiconductor based SET [Yakimov94, Staring92, Wang17]. Similar to Al-AlOx/Gr based devices, the oscillations conductance are attributed to CB effect from the Al-AlOx NPs. The stability diagrams of conductance exhibits remarkable Coulomb diamonds patterns characteristic of SETs in classical regime. The parameters of the SET are observed to depend on the doping level of the MoS_2. The Coulomb oscillation of conductance are preserved above 50K. Four terminals measurements demonstrated a clear metal-to-insulator transition of the MoS_2, a characteristic common in MoS_2 FETs.

The add values of 2D-0D MD VdWh

2D-0D MD-VdWh are essential for our devices both from sample engineering point of view as well as from the fundamental processes governing the transport in the devices. First, the used of 2D materials favors the self-organization of NPs at their surfaces during the 3D growth process. Secondly, they enable a relatively simple lithography process circumventing the technological challenges required for contacting a single particle. Finally, the intrinsic low density of states (DOS) of the 2D materials make them transparent to the electric field of

the back gate which enables the gate modulation of the supported NPs. An indispensable condition enabling our novel vertical SET architecture. The role of 2D material template is also quite important in the selection processes of preferential conductive path as discussed in the manuscript. Clearly, our results extend the capability of Gr and SC-TMDs to act both as electrode and as a platform for the growth of 2D-0D mixed-dimensional van der Waals heterostructures and more importantly as atomically thin dielectric providing multifunctionalities in the Coulomb blockade regime on scalable spintronic devices and SETs.

10.1.2 $MoSe_2$ Field Effect Transistors

Prior to our study of Al-AlOx/MoS_2 heterostructure based SET, we investigated the carrier injection mechanisms across the metal/2D-TMDs interface in bilayer $MoSe_2$ FET with Au/Ti contact. We demonstrated that the modulation of the energy band profile at the Ti/$MoSe_2$ Schottky interface by the combined effects of temperature, gate and source-drain voltages enables to elucidate a complete map of interface charge injection mechanisms. Thermal activation regime is identified at low doping regime while in high doping regime, interface injection mechanism is mediated by filed assisted direct tunneling/thermionic emission. A transition to high-field Fowler-Nordheim tunneling is observed at high dc bias. The corresponding transition voltage V_{trans} to Fowler-Nordheim directly correlates with the Metal/$MoSe_2$ interface potential barrier. These comprehensive approach is quite generic and can be extended to the interfaces between metal and other 2D semiconducting crystals.

10.1.3 Magnetotransport in Perovskite Nanocrystals

We investigated the magneto-transport properties of 20 nm ligand-free $La_{0.67}Sr_{0.33}MnO_3$ perovskite nanocrystals chemically synthesized by our collaborators with unprecedented structural quality. We observed an exceptionally large magnetoresistance at low temperature triggered by a spin disordered magnetic surface of the nanocrystals independently of the spin polarization of their ferromagnetic core. This work reveals the way the nanoscale impacts magnetotransport in this material widely used as electrode in hybrid spintronic devices.

10.2 Perspectives

Numerous of perspectives emerge from my thesis work. In this section, I point out those I consider to be the most promising.

10.2.1 Oxidation dynamic of Al nanoparticles on MoS_2 surface

In chap.4 we discussed the fabrication processes of our devices. We presented the physiochemical analysis of the our 2D-0D heterostructures, particulary in the case of Al-AlOx/Gr, we observed that a certain number of Al NPs adopts after full oxidation in the air a core-shell configuration with a metallic Al core surrounded by AlOx alumina shell. A structure

favoring the observation of Single electron processes presented in chap.5 and the AMC effect presented in chap.6 thanks to the CB effect of the Al core decoupled from its environment by the insulating alumina shell. In the case of Al-AlOx/MoS_2 such a core-shell configuration is yet to be confirmed. This constitutes an important point to further sustained the understanding of the transport properties of our 2D-0D Al-AlOx/MoS_2 based SET in terms of CB effect originating from Al-AlOx NPs as presented in chap.8. In this regard, the observation of a metallic Al signals in XPS spectrum after Al deposition and oxidation is quite promising.

In the same frame, the data presented in chap.8 demonstrated that a relatively large threshold gate voltage (V_{TH} ~19 V) is required to trigger the transport within the channel and results to an important conductance gap attributed to the MoS_2 channel. We related this to the necessity for Fermi energy of the channel to be displaced by doping sufficiently close to conduction band minimum edges where percolating conduction channels start to emerge. Such an interpretation neglect the role of interface states if they exist, whereas they may play an important role in setting the V_{TH} value. First principle calculation demonstrated that not only covalent bonds are required to induce localized interface states in band gap of a SC-TMDs in metal/SC-TMDs heterojunctions. They can as well can originate from Mo d-orbitals character by the weakened intralayer S-Mo bonding due to the interface metal-S interaction [Gong14]. Meaning that the pinning of E_F may be systematic at Metal/MoS_2 interface. This opened several important questions regarding the energy band profile through our Al-AlOx/MoS_2 heterostructure. First, how pronounced is the pinning shifted E_F in MoS_2 after Al deposition ? Second, is the pinning preserved with oxidation ? If not, how does it evolves ? These information can be accessed by angle resolved photoemission spectroscopy (ARPS). Particularly, if the set-up is equipped with a metal deposition column and a steel chamber for controlled oxidation by O_2 gaseous through a leak valve. In this case, a comparative analysis of the ARPES spectrum of pristine MoS_2 relatively to Al-AlOx/MoS_2 with different Al thickness and different oxidation times is possible. This study, already initiated by our collaborators in the group of Laurent Simon, will provide sufficient ingredient to have a complete picture of the energy band in our Al-AlOx/MoS_2 heterostructure as well as their evolution with Al thickness and oxidation.

10.2.2 Sub-threshold transport regime of Al-AlOx/MoS_2 heterostructures

Although in chap.8 we limited our analysis of the conductance spectroscopy to the regime far beyond the conductance threshold of the MoS_2 channel reported to be close to $V_{TH} \simeq 19$ V, the regime around the threshold remains interesting to explore. Indeed, we conducted preliminary transport measurements in this regime and we reported peculiar properties that have yet to be fully understood. In such regime, because of the highly insulating state of the channel, very large dc voltages are required to trigger the transport trough the device. In Fig.10.1, one observes a set of parallel conductance thresholds (better highlighted in the second derivative of the conductance (Fig.10.1.(b))) in the dc-bias regime where the CB effect is, in principle, expected not to be preserved. Although these observations are not fully understood, one

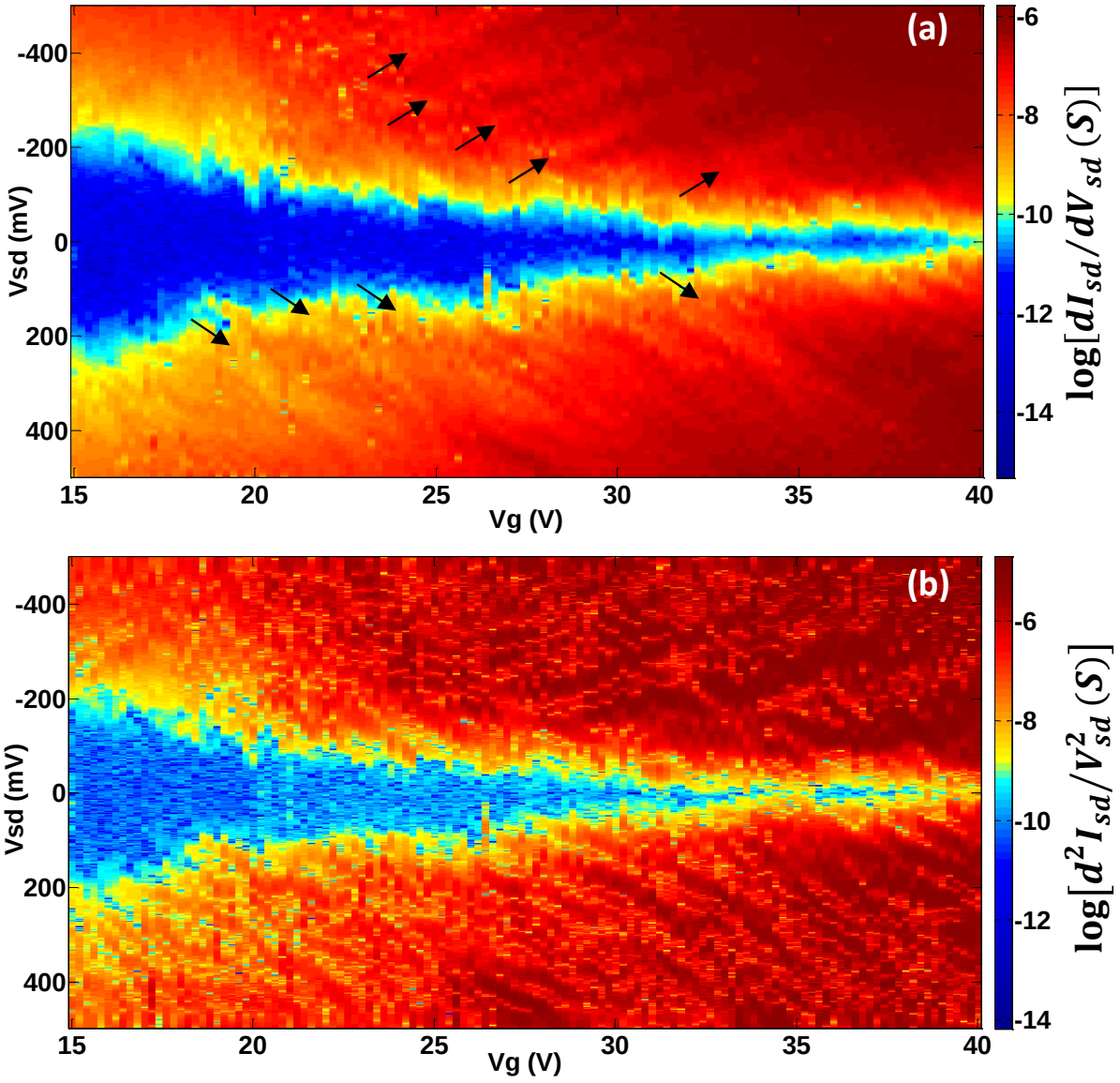

Figure 10.1 – *(a) Differential conductance measured in symmetric configuration at 1.5 K. The arrows highlight few of the lines probably indicating the positions of dc threshold voltages for tunneling electrons. (b) The corresponding second derivative of the source-drain current better highlighting the set of lines that some are indicated by the arrows in (a).*

can speculate about their origin. It is well known that in SETs with pronounced asymmetric source and drain resistances ($R_S \gg R_D$ for example), the slopes of one side of the diamonds are completely smeared out and one observes a single set of parallel lines originating from a single tunnel barrier [Carlsson99, Danilov02]. The feature reported in Fig.10.1 may be of similar origin. This assumes that under such large dc-bias, the AlOx/MoS_2 interfaces energy barriers are sufficiently distorted to drive the device toward a strong asymmetric regime. The understanding of those features in terms of CB assumes that most of the potential drop takes place within the highly resistive channel such that at least one SETs cell remains in a dc-bias regime suitable for CB. In this context the symmetry of the lines with respect to the Vsd = 0 line may be related to symmetric configuration the device where each contact diode probably

takes over the functioning of the device as the sign of the dc-bias changes. A better understanding of the transport processes in this regime requires more accurate measurements together with a deeper fundamental analysis.

10.2.3 AMC in Al-AlOx/MoS_2 heterostructures

An additional important perspective of this work is the demonstration of AMC in Al-AlOx/MoS_2 heterostructures. In section.2.3 we discussed the difficulties faced by the community to realize lateral spin-valve devices with SC-TMDs material channels due to high contact resistance and large SOC preventing long distance coherence spin propagation [Dankert17a, Liang17]. AMC is an interesting alternative to implement magnetic functionality in lateral devices since it does not require coherent spin and detection. This carries the hope of developing multifunctional spintronic-SETs devices.

10.2.4 Small size junction

A next step toward sample processing is the nano-indentation lithography process which enables patterning nano-sized vertical tunnel junctions to address the transport through a much smaller Metal/AlOx-Al-AlOx/2D-material junctions targeting a single NPs. Nano-indentation consists in pressing an AFM tip into hard baked resist to form a nanohole after the withdrawal of the tip [Bernand-Mantel09]. The hole depth is directly related to a calibrated value of the cantilever deflection. Then, the hole is then enlarged with a solvent in order to remove the excess of resist and to take an electric contact on the bottom electrode. Our collaborators in the team of Pr. Pierre Seneor at Thales, have expertise of such nano-indentation method. We provided them with a commercial CVD Gr on Ni substrate after I deposited a 1.7 nm thin Al layer. Florian Godel processed the sample and conducted initial low T the transport measurements which were quite promising. Fig.10.2.(a) shows the schematic summary of the nano-indentation process (from step 1 to step 4) and the device structure (step 5), with nanocluster(s) contacted through alumina tunnel barriers to a top Co nanocontact and a bottom CVD graphene/Nickel. Fig.10.2.(b) shows the dynamical conductances dIdV(V) measured at 1.5K. Very well defined and sharp Coulomb oscillations with periodicity of 30 mV are measured, indicating that only a single cluster has been successfully contacted.

10.2.5 Ultra low temperature transport measurements

In the perspective of a better understanding of the fundamental processes governing the sample in these 2D-0D MD-VdWh heterostructures, ultra low temperature measurements are of great interest. Indeed, if the sample is cooled down to a dilution refrigerator temperature range, the energy spacing of the intermixing Coulomb levels of different conduction paths could becomes smaller than the thermal broadening and the fine structure of the multi-grain system is likely expected to be resolved. Precisely, under theses conditions, it has been

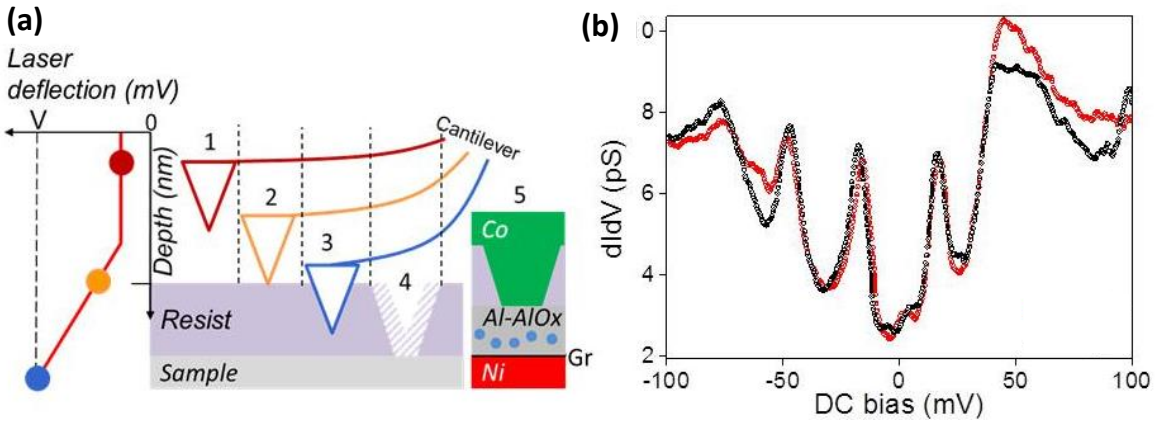

Figure 10.2 *– (a) Schematic representation of the nano indentation lithography technique. 1. The AFM tip is positioned on top of the resist. 2. The tip is engaged at the resist surface, the laser deflection increases to press the tip on the resist. 3. Tip is hammered into the resist until laser deflection reaches a calibrated value V corresponding to an optimal depth. 4. Tip is removed and nano-hole size is increased through chemical attack of the resist. 5. The indentation is finalized by the filling of nano hole with top electrode deposition. The schematic representation of the resulting Co/Al-AlOx/Gr/Ni nanojunction. (b) Dynamical conductance measured at 1.5 K.*

demonstrated that the conductance spectroscopy of disordered multi-grains SETs presents multiple sets of parallel lines, each of which originates from a given contributing tunnel barrier in the device, such the total number of the set of parallel lines provides a direct reading of the detail sample topology i.e. the exact number of contributing grains [Danilov02]. At low enough T, the stability diagram of conductance of our devices may likely provide sufficient details to access the the exact topology of the devices. More importantly, Al is known to be superconductor below 1.2 K. Therefore, at ultra low T, provided that the superconductive state of the core Al is stable and robust enough, our 2D-0D VdWh heterostructures may demonstrate fancy phenomena resulting from the interplay between CB and single Cooper-pair type of transistors.

Résumé détaillé

Introduction

Dans les années 60, en dépit des progrès effectués en mécanique quantique permettant la compréhension du comportement de la matière à l'échelle microscopique, rien de ce qui concerne la nanoscience tel que connu aujourd'hui n'existait. En 1959 lors de sa présentation visionnaire intitulé "Il y a pleines de portes en dessous" (traduit du titre original en anglais "There's Plenty of Room at the Bottom") au congrès annuel de la société américaine de physique, le prix noble de physique Richard Feynman déclare "Lorsque les générations des années 2000 jetteront un regard rétrospectif sur le passé, ils se demanderont pourquoi jusque dans les années 60 personne n'avait sérieusement commencé à s'orienter vers cette direction" [Feynman60]. Bien qu'il soit difficile d'estimer à quel point il avait ainsi pu motiver la communauté à regarder dans la direction des nanosciences, il est évident que dans les années 2000 les progrès majeurs réalisés laissaient peut de place à de telles questionnements. Cela s'illustre entre autre par l'invention des circuits intégrés et partant, le passage du premier ordinateur 'Eniac' tenant sur deux étages à des ordinateurs portatifs et mieux des téléphones intelligents. Les premiers développements de la nanoscience ont permis l'émergence de différents types nanostructures. En fonction du nombre de dimension(s) supérieur(s) à 100 nm, ils sont classifiés en nanoparticules (0D), nanofile (1D), film mince (2D), en nanocomposites et les matériaux massifs nanostructurés (3D). A l'échelle nanométrique, la prépondérance des effets quantiques a ouvert de nombreuses directions de recherche dont la nanoelectronique et la spintronique avec de forts potentiels applicatifs. En occurence, ces deux directions ont permis des découvertes majeures notamment la magnéto-résistance géante (GMR de l'ainglais 'Giant Magneto-Resistance') [Baibich88, Binasch89] et tunnel (TMR de l'ainglais 'Tunneling Magneto-Resistance') [Julliere75] observées dans les multicouches magnétiques ayant en sandwich une couche métallique non magnétique (GMR) et une couche isolante (TMR). Bien plus, les avancées techniques en nanofabrication permettent la conception des dispositifs avec les tailles de composants en constante diminution. En dessous d'un certain seuil, la prépondérance des effets quantiques devient systématique. A cela s'ajoute l'émergence des matériaux lamellaires ou 2D constitués d'un empilement de plans liés entre

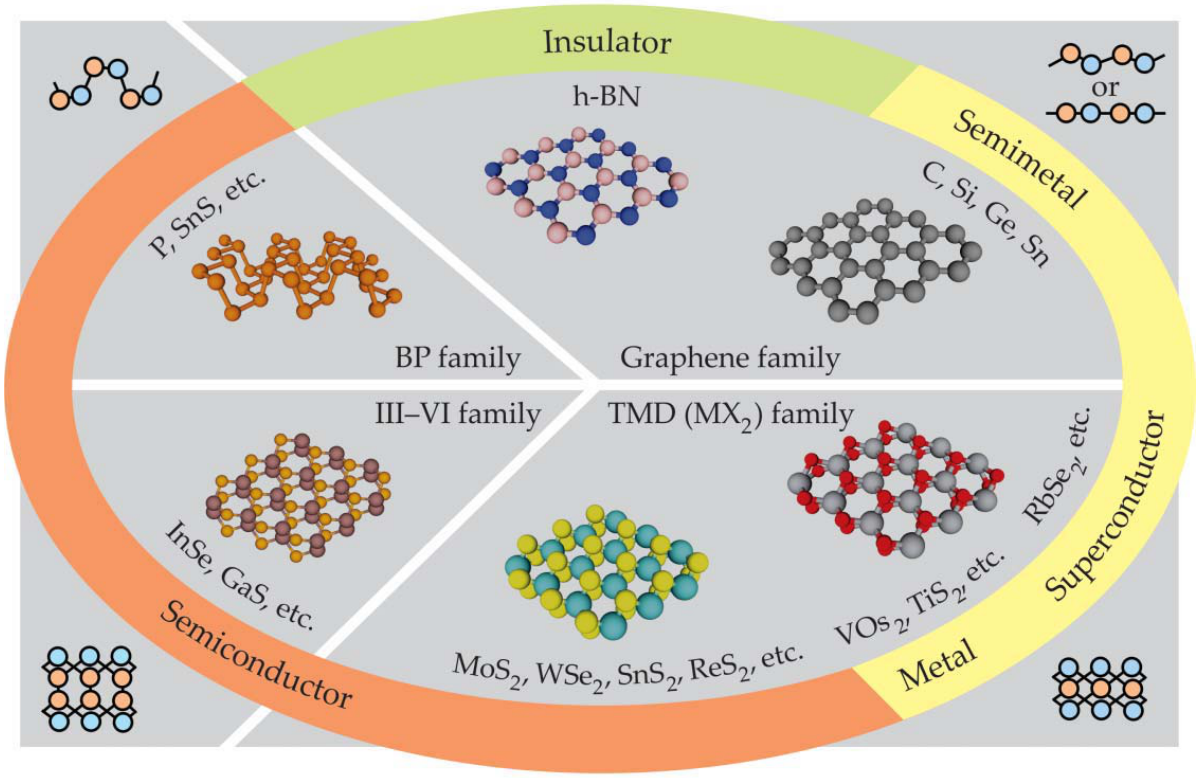

Figure 10.3 *– La grande famille des materiaux 2D couvre quasiment toutes les propriétes electriques connues : Les isolants, les semiconducteurs, les métaux et semimetaux et les supraconducteurs. Elle a été enrichie en 2018 par la decouverte des materiaux 2D magnetiques [Gong17, Huang17]. Figure extraite de [Ajayan16].*

eux par des liaisons faibles de type van der Waals offrant la possibilité les séparer (cliver) les uns des autres et ainsi produire des matériaux ultimement minces [Novoselov04]. La Fig10.3 illustre cette grande de famille de matériaux 2D [Ajayan16].

Selon le matériaux, chaque plan constitutif de l'empilement peut être composé d'un unique plan atomique (cas du graphite composé d'un empilement de plan de carbone appelé graphene) ou de plusieurs plans atomiques comme c'est le cas des dichalcogenures des métaux de transition MX_2 (M désigne l'atome de métal de transition et X l'atome de chalcogenure) constitué de trois plans atomiques dont un plan de métal de transition pris en sandwich par deux plans de chalcogenures. Reduites à quelques monocouches, ces matériaux sont très sensibles à diverse stimuli externes dont le champ électrique faisant d'eux des candidats idéaux pour les applications en électroniques. De nombreux travaux ont montré que l'intégration des matériaux 2D dans des dispositifs nanoélectroniques et optoélectroniques avec la fabrication des transistors à effet de champ (noté FET pour Field Effect Transistor) ou des phototransistors [Novoselov04, Radisavljevic11]. Ils offrent également d'énormes possibilités en spintronique avec la réalisation par exemple des dispositifs TMR à base de graphene permettant une communication de spin à longue distance[Tombros07].

La surface des matériaux bidimensionnelle étant passivée de liaisons pendantes, il est possible de les empiler les uns sur les autres pour en faire des hétérostructures 2D-2D de

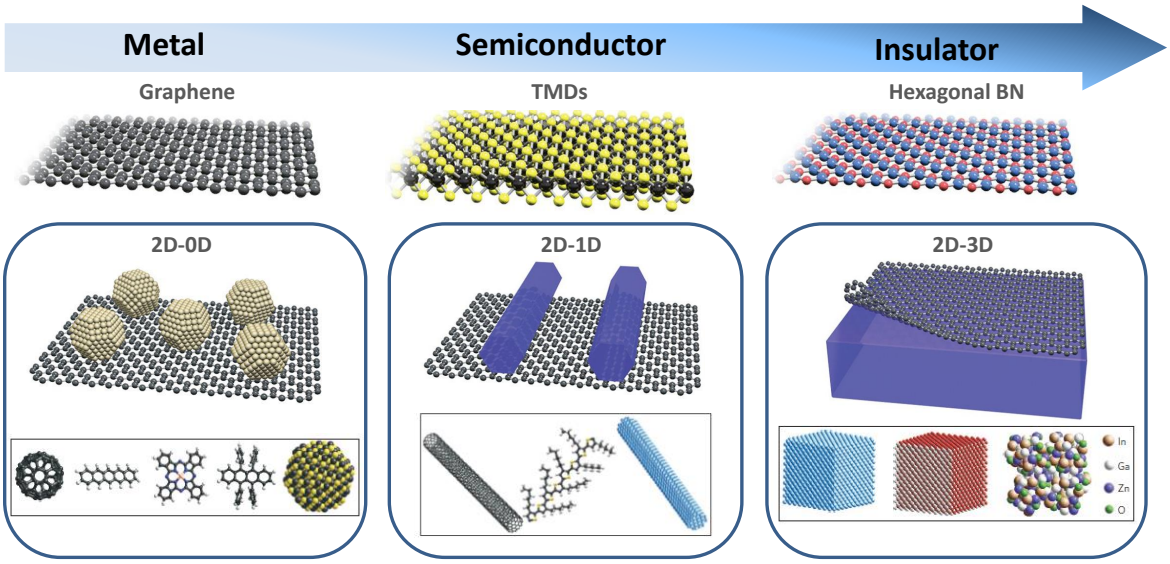

Figure 10.4 *– Hétérostructures de dimensionnalité mixte de van der Waals : Interaction entre les matériaux 2D et les nanostructures 0D (Nanoparticles, molecules dispersées, fluorine C_{60}), 1D (Nanofils et nanotubes), 3D (substrat massif ou tout autre matériau massif nanostructuré) [Liu16, Jariwala16].*

Van der Waals (h-VdW) sans la contrainte d'équivalence des paramètres de mailles comme c'est le cas pour les hétérostructures multicouches épitaxiées traditionnelles. Cela donne lieux à des nouvelles propriétés et ouvre la porte à de nouvelles applications. Cependant, Les h-VdW ne se limitent pas qu'aux systèmes 2D-2D. En effet, tout matériau donc la surface est passivée de liaisons pendantes, interagit avec d'autres par les liaisons de types VdW [Jariwala16]. Ainsi, les développements récents consistent à faire interagir les matériaux 2D avec des nanostructures de dimensionnalité déférente (n=0, 1,3) conduisant aux heterostructures dit de dimensionnalité mixte [Jariwala16] (Fig10.4). Ces derniers sont susceptible de donner lieu egalement à de nouvelles propriétés très prometteuses pour diverses applications. Les résultats très intéressants en électroniques et en optoelectroniques ont déjà été démontré [Jariwala16, Liu16].

Dans les matériaux 2D, la longueur d'écrantage de Thomas-Fermi λ_{TF} qui exprime la profondeur de pénétration du champ électrique dans un matériaux est susceptible de dépasser plusieurs monocouches. Cela offre la possibilité dans les hétérostructures de Van Der Waals à dimensionnalité mixte (h-VdW-DM) de moduler à la fois les propriétés électriques du matériaux 2D, mais aussi et surtout celles des nanobjets qu'ils supportent. Ceci fixe les conditions idéales pour le développement de nouvelles géométries de dispositifs à base d'h-VdW-DM.

Dans ce contexte général, mon projet de thèse consiste à développer les approches alternatives pour la fabrication des nouveaux nanodispositifs pour la nanoélectroniques et la nanospitroniques à base de nanoparticules et les matériaux 2D d'une part, d'heterostructures de dimensionnalité mixte 2D-0D de van der Waals d'autre part. Ensuite d'étudier les mécanismes de transport de charge et de spin ayant lieu des ces nanodispositifs. Nous nous sommes spécifiquement intéressés aux nanoparticules de $La_{0.67}Sr_{0.33}MO_3$ piégés dans les

nanotranchées à fort rapport d'aspect, puis aux FETs à base bicouche de $MoSe_2$ et par suite, nous avons développé une approche alternative pour fabriquer les h-VdW-DM 2D-0D à base de nanoparticule d'Al oxydées en interaction avec le soit le Graphene soit les TMDs. Nous avons intégré ces heterostructures dans les nanodispositifs et avons étudié les processus de transport à électron unique qui régissent leur fonctionnement électrique. Nous avons démontré leur fonctionnalisation spintronique basée sur les effets magneto-coulomb anisotropique.

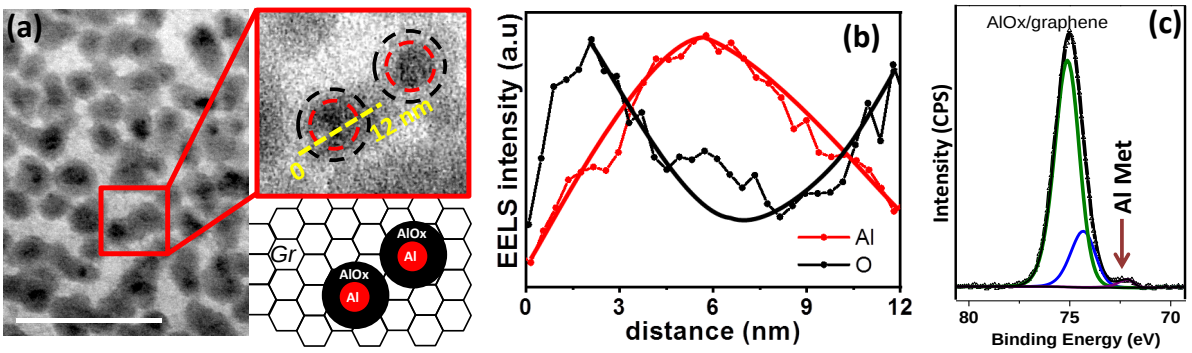

Figure 10.5 *– (a) Image MET de l'hétérostructure 2D-0D après un dépôt d'une couche d'Al de 1,7 nm d'épaisseur nominal sur du Gr CVD transféré sur une grille MET en carbone suivie d'une oxydation à l'air. Le carré rouge montre une image METB présentant une structure cœur-coquille telle que schématisée la partie inférieure. La ligne en interrompue jaune indique la direction de balayage. (b) Les profils de composition chimique selon la direction de balayage indiquée sur la figure (a). Ils indiquent une forte accumulation d'Al (courbe rouge) au centre de la NP et une accumulation de l'O en surface (courbe noire). Les courbes rouge et noire servent de guide pour les yeux. (c) Spectres de photoémission des rayons X montrant qu'après oxydation complète, le signal de l'Al métallique reste clairement discernable.*

Nanodispositifs à un électron à base d'hétérostructures de graphene/Al-AlOx

Les dispositifs à un électron à base des hétérostructures de dimensionnalité mixte 2D-0D reposent sur la combinaison par ces derniers des propriétés propres d'une part au nanoparticules et d'autre part aux matériaux 2D. Les nanoparticules offrent les propriétés de blocage de Coulomb à la base des processus à électron unique. Les matériaux 2D quant à eux offrent la possibilité d'auto-assembler les nanoparticules en leur surface avec des propriétés suffisamment proches pour permettre la préservation des propriétés de blocage de coulomb dans un grand ensemble de nanoparticules. Ce faisant, les matériaux 2D servent aussi d'électrodes et de diélectrique atomiquement fin à travers lequel les propriétés électrique des nanoparticules peuvent être modulées par une grille arrière permettant d'implementer la fonctionalité de logique characteristique des transistors à un electron (SET pour le terme anglais Single Electron Transistor). Plusieurs travaux antérieurs ont montré que le graphene est une plateforme adéquate pour la croissance auto-assemblée des nanoparticules [Pan09, Allain12]. Ainsi, pour réaliser nos dispositifs à un électron, nous avons de développé une approche intuitive de fabrication des h-VdW-DM 2D-0D à base de Al-AlOx/graphene. Nous avons montré que le

dépôt d'une fine couche d'Al sur du graphene exfolié sur un substrat de Si ou du graphene CVD sur Ni conduit par un mode de croissance 3D, à un ensemble auto-organisé de nanoparticules d'Al. Après oxydation à l'air, certains grains présentent une structure cœur-coquille constituée d'un cœur métallique et d'une coquille alumine (Fig10.5). Cette structure a été démontrée par des analyses de spectroscopie de photoémission des rayons X et confirmée par les études combinées de microscopie électronique à transmission et à balayage (METB) et spectroscopie à perte d'énergie (EELS pour Energy Electron Loss Spectroscopy) comme l'illustre la Fig10.5. Nous avons intégré ces hereterostructures d'Al-AlOx/Gr dans les jonc-

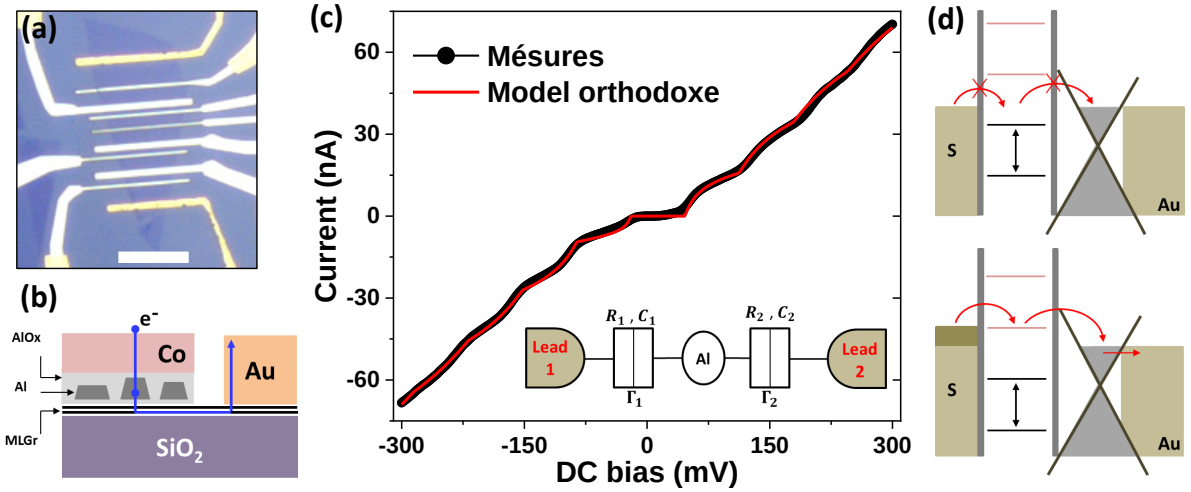

Figure 10.6 *– (a) Image optique d'un échantillon type. (b) Représentation schématique de l'échantillon avec une indication de la trajectoire des électrons. (c) Caractéristique Isd(Vsd) mesurée à 1.5 K. La courbe rouge représente l'ajustement par la théorie orthodoxe du blocage de Coulomb basé sur le schéma électrique équivalent représenté en encart. Le paramètres obtenus de cette ajustement sont : R_1 = 130 MΩ, C_1 = 2.6 aF, R_2 = 74 MΩ, C_2 = 0.4 aF et Q_0 = -0.05e. (d) Structure de bande d'énergie du dispositif présentant l'état bloqué (schéma du dessus) et l'état passant (schéma de dessous).*

tions tunnels réalisées par lithographie électronique (Fig10.7.(a & b)). Les mesures de transport à base température ont révélé la présence des escaliers ce Coulomb qui traduisent le processus de quantification de la charge tunnel due au blocage de Coulomb (Fig10.7.(c)). Les simulations réalisées dans le cadre de la théorie orthodoxe du blocage de Coulomb en adoptant un modèle simple intégrant une seule particules avec juste 5 paramètres d'ajustement à savoir l'environnement de charge Q_0, les couples de résistances, capacités tunnels (R_1, C_1) et (R_2, C_2) caractéristique respectives des deux jonctions tunnels qui couplent la nanoparticules aux électrodes source et drain (voir encart de la Fig10.7.c). De manière surprenante, ce modèle simpliste reproduit parfaitement les données expérimentales (Fig10.7.c). En réalité le nombre de nanoparticules contactées dans ces jonctions qui fait en environ 1 μm^2 de surface avoisine 10^4. De plus, ces processus à un électrons ont été observés sur des jonctions de 100 μm^2 intégrant plus de 10^6 nanoparticules. La raisons du parfait accord des données expérimentales avec un modèle simple s'explique par un processus de sélection statistique des canaux préférentielles de conduction. Un tel processus de sélection avait été introduite par Yakimov et al. [Yakimov94] pour expliquer la préservation des oscillations de coulomb dans les dispositifs à base d'hétérostructure SiGe/Si contenant en sandwich une couche granulaire

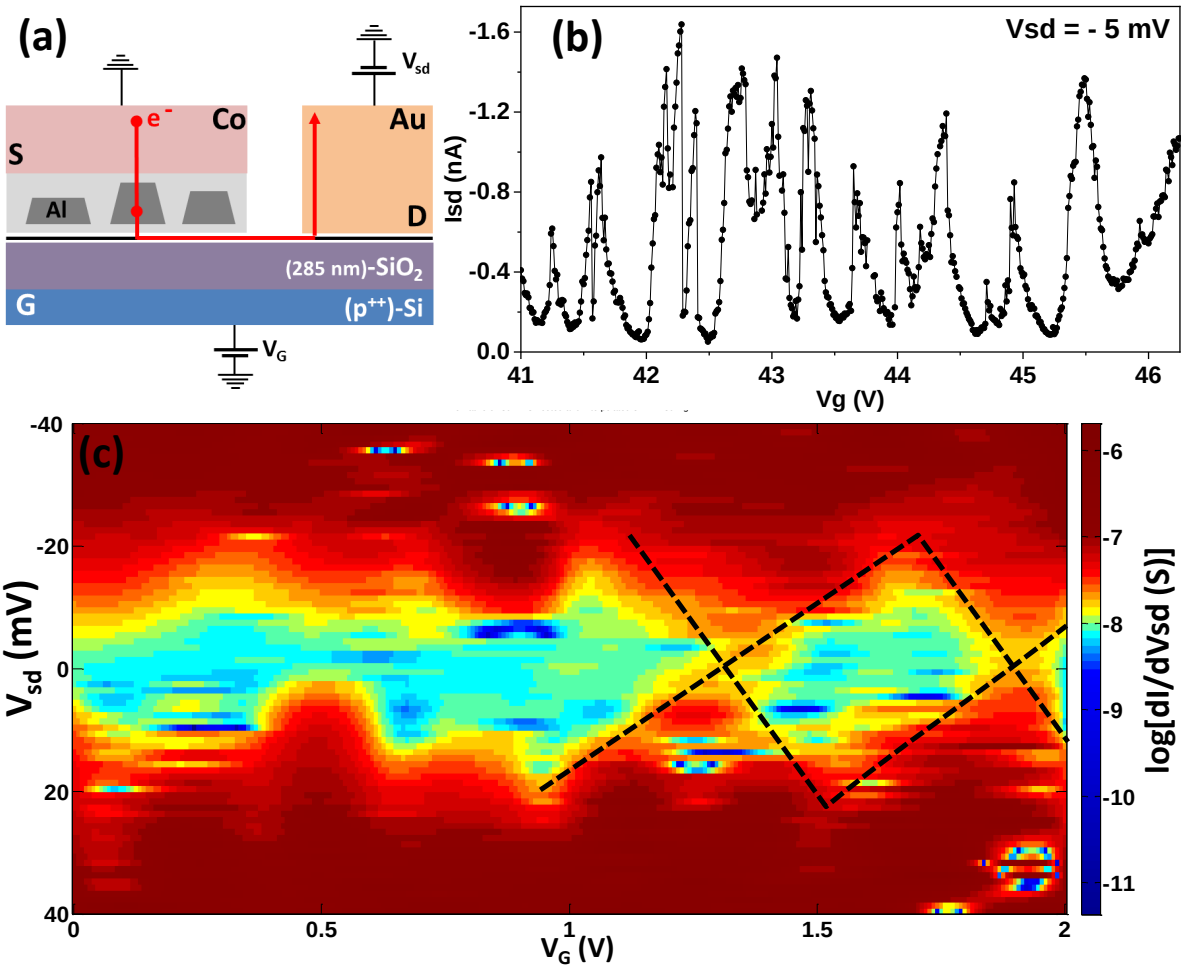

Figure 10.7 – *(a) Représentation schématique du dispositif S, D et G indiquent respectivement les électrodes Source, Drain et Grille. (b) Comportement oscillatoire du Courant en fonction de la tension de grille. (c) Le diagramme de stabilité de la conductance différentielle dI/dVsd (Vsd, Vg) en échelle logarithmique. On discerne les diamants de Coulomb caractéristiques du SET. L'énergie de charge déduite du diamant mis en exergue par les traits interrompus noires est* $E_c = eVsd = 19\ meV$.

de Ge dopé. En adaptant cette démarche à notre échantillons, nous obtenons un nombre de canaux préférentiels donné par l'équation10.1.

$$N = nS\sqrt{\frac{2}{\pi}}exp[-\frac{(\sqrt{8mV_0}\sigma H)^2}{2}] \tag{10.1}$$

Où $S = 1\mu m^2$ est la surface de la jonction, $V_0 = 1.6eV$ la hauteur de barrier tunnel pour l'alumine [Costina01] avec pour masse effective des electrons $m^* = 0.28m$ [Huang06]. σ =20% est la distribution de taille des nanoparticules donnée par les imageries MET. $H = 3.6nm$ et $n = 12300\mu m^{-2}$ sont respectivement la hauteur moyenne des nanoparticules et leur densité par unité de surface. Ainsi, nous aboutissons à un nombre de canaux préférentielles variant entre 0 et 4 en prenant en compte la dispersion de taille. Ceci démontre que seulement un à quelques nanoparticules contribuent effectivement au transport et justifie d'une par la préservation de la quantification de la conductance dans nos dispositifs mais surtout l'accord entre les données expérimentale et le modèle orthodoxe simple. Les paramètres extraits de

l'ajustement et notamment les capacités nous ont permis de déduire l'énergie de charge d'une particule d'Al $E_c = \frac{e^2}{2(C_1+C_2)}$ de 26.7 meV. En approximant les nanoparticules à des disques cylindriques, les tailles obtenues à partir des capacités déduites reproduisent bien les valeurs observées en imagerie. De manière générale les énergies de charges obtenues pour plus d'une vingtaines d'échantillons étudiés restent supérieurs à K_BT à 300 K présageant une préservation des processus de quantification de conductance à haute température. En effet nous avons observé que les processus à un électrons sont préservés à des températures proches de l'ambiante.

Effet de grille

Dans la suite, nous avons implémenté sur ces dispositifs la fonctionnalité de logique en nous servant du substrat de (p^+)Si-SiO_2) comme une électrode de grille (Fig10.7.(a)). Ainsi, nous avons observé que le champ électrique vertical de grille module efficacement le potentiel chimique des nanoparticules à travers la couche de graphene et déplace les niveaux discrets de Coulomb. Ces derniers sont alors alternativement conduits de manière plus ou moins périodique à l'intérieur et en dehors de la fenêtre de tension source-drain appliqué. Ceci donne lieu à un comportement oscillatoire du courant source-drain en fonction de la tension de grille ($I_{sd}(V_g)$) (Fig10.7.(b)). Cette observation produit la première démonstration claire et sans ambiguïté de la possibilité de moduler grâce à la grille les propriétés électriques aussi bien du graphene que des nanoparticules décorant sa surface et ouvre sans doutes des perceptives importantes en nanoélectronique. J'ai effectué la spectroscopie de conductance et la dépendance $Isd/dVsd(V_g, V_{sd})$ représenté en diagramme de couleur sur la Fig10.7.(c). On observe une série de diamants de Coulomb caractéristique des transistors à électron unique. Les oscillations de courant en function de V_g sont préservées jusqu'à 30 K. Le maximum de courant reste quasi inchangé avec la température jusqu'à 7.5 K en accord avec la théorie orthodoxe [Kou97, van Houten05].

Propriétés magnéto-coulomb anisotropique : Spintronique à un électron

L'étape suivante de notre étude a consisté à sonder l'effet du champ magnétique sur ces dispositifs à un electrons. Nous avons observé à basse température des magnétorésistances atteignant parfois 20% (Fig10.8.(a)). Le fait que nos echantillions intégrant une seule électrode magnétique elime toute possibilité d'interpretater les MR observées en terme de l'injection et de détection cohérente de spin comme pour les TMR standarts. Notre étude détaillée et systématique a permis d'établir que les MR observées proviennent de l'effet Magnéto-Coulomb anisotropique [Seneor07, Bernand-Mantel09, Bernand-Mantel11].

Nous montrons que l'orientation de l'aimantation de l'unique électrode ferromagnétique de Co permet de moduler la charge d'environnement subie par les nanoparticules grâce à l'effet magnéto-coulomb anisotrope (AMC) conduisant à des MR de type de vanne de spin.

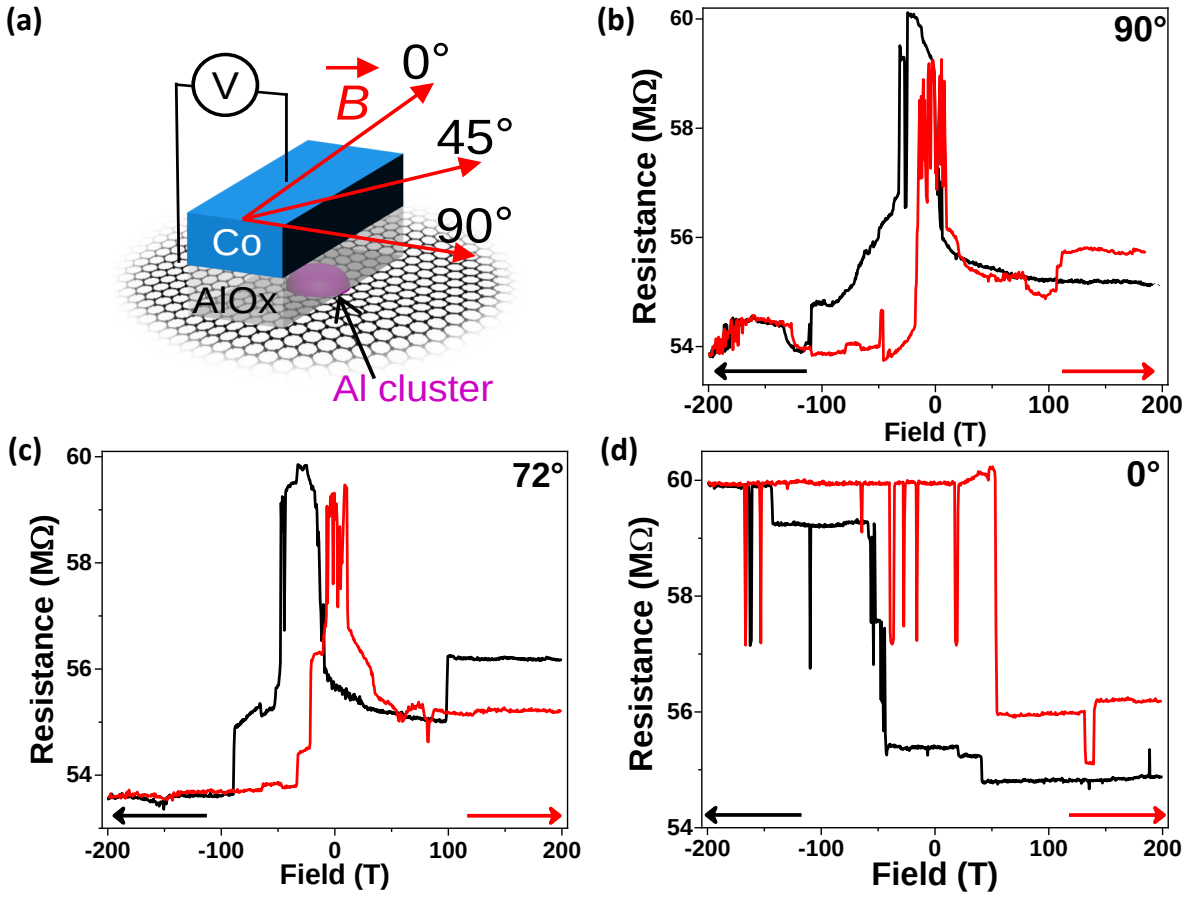

Figure 10.8 *– Mesure de magnétorésistance anisotropique. (a) Représentation schématique du dispositif avec les différentes orientations du champ magnétique appliqué. (b) et (c) MR type vanne de spin positif et négatif respectivement. (d) MR de 'forme hystérésis carrée'. Ces différentes formes du signal de MR traduisent la modification de la charge d'environnement Q_0 lors du retournement de l'alimentation de l'électrode.*

Nous avons établie que les comportement vanne de spin provient d'une dynamique de retournement en plusieurs étape tant dis que le comportement hystérésis carrée proviendrait d'une dynamique de retournement direct sans état intermédiaire. Cette démonstration des MR en régime de blocage de Coulomb sur des échantillons à base d'h-VdW-DM 2D-0D ouvre la voie à de nouvelles architectures de dispositifs à l'intersection de la physique des matériaux 2D et de la spintronique.

Études des dispositifs à base de TMDs et Al-AlOx/TMDs

Un volet important de la thèse a été de réaliser cette étude de transistor à électron unique sur des dispositifs intégrant les heterostructures de dimensionnalité mixte 2D-0D à base de Al-AlOx/TMDs en substituant le Gr semimétal par le TMD semiconducteur. Une étape intermédiaire importante a consisté l'étude des transistors à effet de champs à base de TMDs enfin de comprendre dans le détail les mécanismes d'injection de charge à l'interface entre le métal et le TMD avant par la suite, de complexifier le problème en incorporant entre le métal et le TMD la couche granulaire d'aluminium oxydé.

Mécanisme de transport dans les FET à base de TMDs

J'ai fabriqué par lithographie électronique des FETs à base de MoS_2 exfolié sur un substrat de (p^+)Si-SiO_2 utilisé comme électrode de grille arrière (encart de la Fig10.9.(a)). Les électrodes de Ti/Au utilisées ont permis d'observer des rapports courant d'ouverture/fermeture (On/off ratio) important soit autour de 10^7. Nous avons réalisé une étude systématique des mécan-

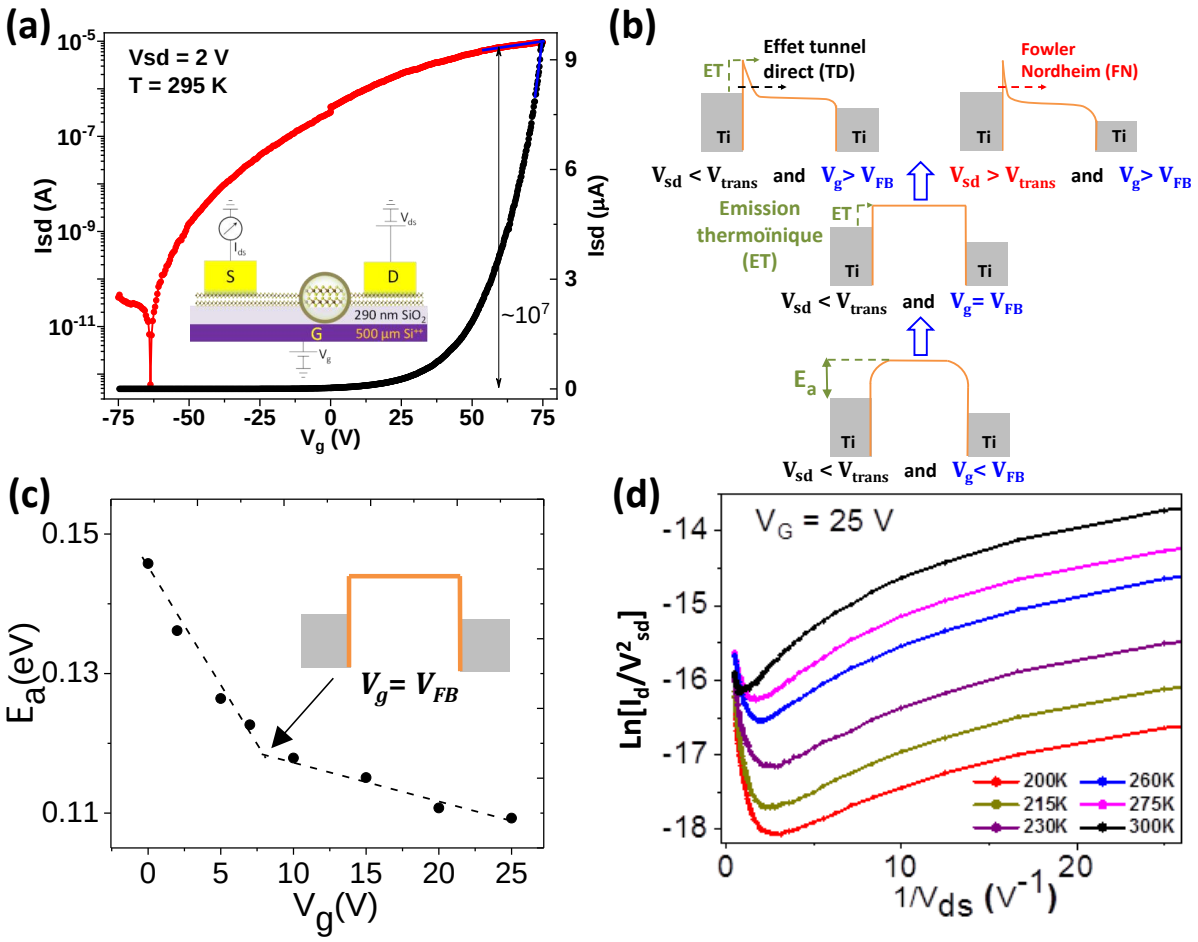

Figure 10.9 *– (a) Courbe de transfert Ids(Vg) de FET mesurée à température ambiante avec Vds = 2 V (courbe noire, axe de droite). En rouge (axe de gauche) nous représentons la même courbe en échelle logarithmique. On y constate un rapport On/Off de* 10^7*. En encart : schéma du dispositif. (b) Évolution de la structure de bande du dispositif en fonction des tension Vsd et Vg. Les différents régimes d'injection de charge sont identifiés. (c) Évolution de l'énergie d'activation avec la tension grille. La valeur en régime de bande plate (voir encart) correspond à la barrière Schottky* $\phi_B 0 = 115$ *meV. (d) Caractéristiques Isd (Vsd) à mesurées différentes T pour Vg = 25 V. Les courbes sont tracées sous la forme* $ln(I/V^2)$ *v.s.* $1/V$ *afin de ressortir la transition vers le régime Fowler-Nordheim à haute tension Vsd.*

ismes d'injection de charge à travers la barrière Schottky d'interface MoS_2/Ti en modulant le profile de bande énergie par les effets combinés de la température et des tensions de grille et source-drain. Le régime d'activation thermique est identifié à faible densité de dopage (basse tension de V_g), tandis que le transport à des régimes de densité de porteurs plus élevées est contrôlé par du tunneling direct assisté par le champ électrique ou par l'émission thermionique. On observe une transition vers des processus tunnel de type Fowler-Nordheim à des

tensions plus élevées. Une telle délimitation claire des différents régimes de transport permet à une évaluation précise dans le régime thermionique approprié de la barrière Schottky intrinsèque $\phi_B 0 = 115$ meV. En outre, l'analyse de la tension de transition V_{trans} des régimes de bas dopage vers le régime Fowler-Nordheim déduites pressente une corrélation directe avec l'énergie d'activation d'interface Métal/$MoSe_2$. Cela souligne la nécessité des études plus approfondies à la fois théoriques et expérimentales pour mieux comprendre cette corrélation. Une telle compréhension du transport à travers les interfaces Metal/2D SC-TMDs est cruciale pour une ingénierie de contact dans les FETs à base de TMDs surtout s'il faut envisager la d'implémenter des fonctionnalités spintronique par l'injection de et la détection de spin [Allain15]. Notre approche étant générique, elle peut être étendue aux interfaces entre le métal et d'autres cristaux semi-conducteurs 2D.

Transistor à électron unique à base d'hétérostructures Al-AlOx/MoS_2

L'expertise développée d'une part sur la croissance de nanoparticules auto-assemblés sur le graphene permettant la réalisation des SETs à base h-VdW-DM 2D-0D de Al-AlOx/graphene et d'autre part l'étude détaillée des mécanismes d'injection de charge l'interface métal/semiconducteur 2D dans les FETs à base de TMDs m'ont permis dans la dernière partie de ma thèse de développer des SETs à base Al-AlOx/MoS_2. Nous avons démontré que la croissance d'une fine couche d'Al sur du MoS_2 exfolié sur un substrat de p^+)Si-SiO_2 conduit comme dans le cas du Gr à réseau de nanoparticules auto-assemblés avec des caractéristiques similaires. Démontrant ainsi pour la première fois que comme le Gr le MoS_2 est lui aussi une plateforme propice à l'auto-assemblage des NPs par croissance physique. Nous avons intégré ces hétérostructures d'Al-AlOx/MoS_2 dans les jonctions tunnels par des techniques de lithographie électroniques et avons investigué les propriétés de transport des dispositifs ainsi fabriqués. Nous avons observé à 1.5 K des oscillations de conductance superposées à une croissance exponentielle caractéristique de l'effet de champ sur le canal MoS_2 semiconducteur. Par une analyse détaillée des comportement de transport observé, il résulte que les oscillations de conductance sont l'effet du blocage de Coulomb induit par les NPs. La spectroscopie de conductance révèle des diamants bien définis dans le diagramme de stabilité. Les paramètres électriques du SET extraite des mesures dépendent du niveau de dopage du canal MoS_2 par la tension de grille. Les oscillations de Coulomb sont préservées jusqu'à 50 K. Les mesures quatre points non locales ont révélé une transition de phase métal-isolant dans le canal MoS_2. Ce travail ouvre des portes vers de nouveaux architectures de SET utilisant les hétérostructures à dimensionnalité mixte de van der Waals 2D-0D, contournant ainsi la les difficultés de fabrication habituelle liées à la nécessité de contacter une seule NP. Il démontre ainsi l'importante des hétérostructures pour la nanoélectronique.

Magnétotransport dans les microcristaux Perovskite

Ce volet de mon travail de thèse a consisté à étudier les processus de transport de charge et de spin dans les nanoparticles perovskite de $La_{0.67}Sr_{0.33}MO_3$ (LSMO) quasi parfaitement

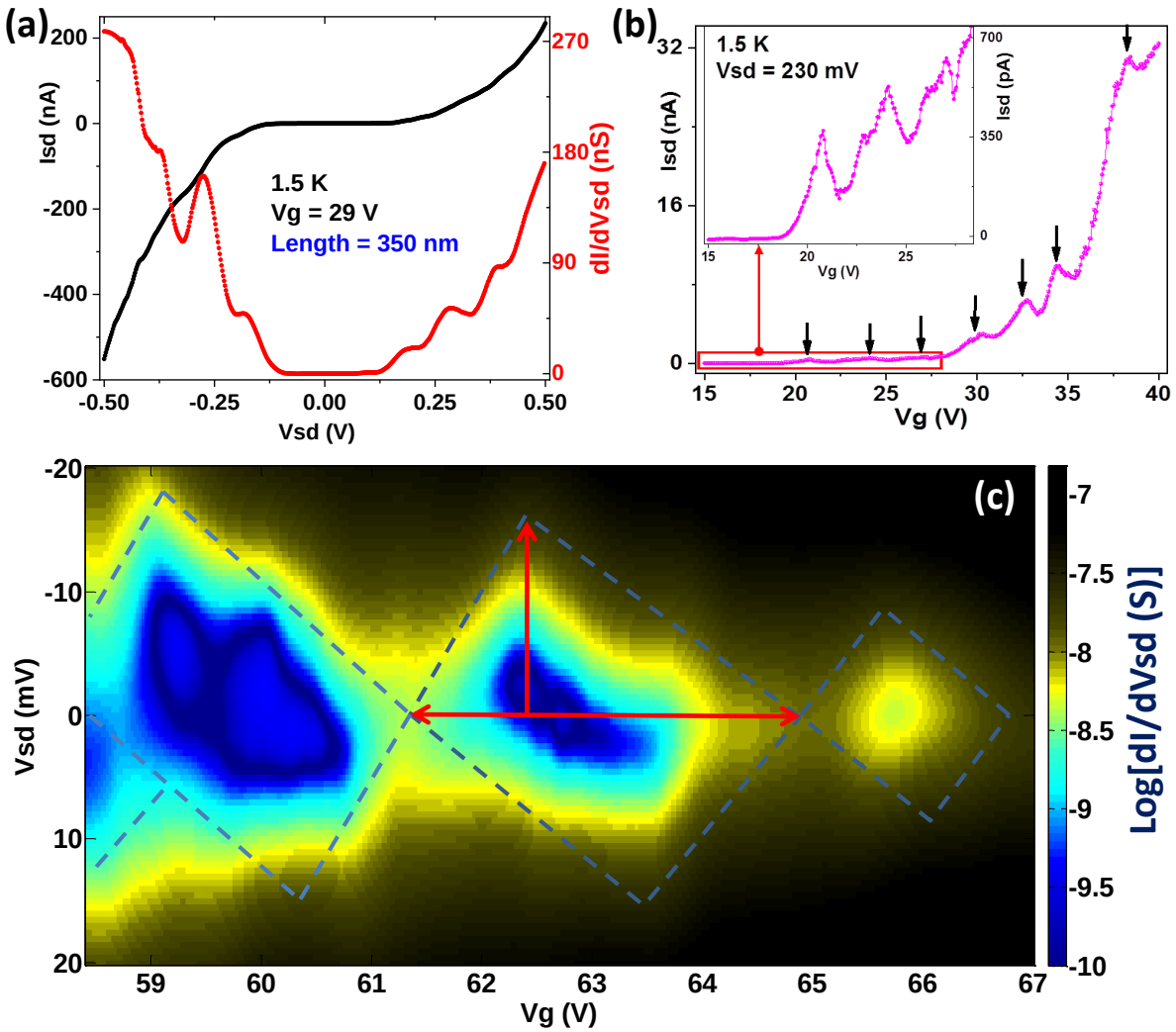

Figure 10.10 – *Mesure de transport à 1.5 K dans les SET à base d'heterostrures d'Al-AlOx/MoS_2 en configuration symétrique (les deux électrodes contiennent les amas d'Al-AlOx). La longueur du canal est de 350 nm. (a) Caractéristique I-Vsd (courbe noire, axe gauche) et conductance différentielle correspondante (courbe rouge, axe droit) mesurée à Vg = 29 V. (b) Courbe de transfert I(Vg) mesurée à Vsd = 230 mV. Les flèches noires renseignent les positions des pics de conductance. La courbe en encart met en évidence la région de basse Vg encadré par le rectangle rouge. (c) Diagramme de stabilité de dI/dVsd (Vsd, Vg) en échelle logarithmique avec les diamants bien discernables illustrés par les lignes en interrompues. L'extension $\Delta Vsd = 16.5 \pm 0.5 mV$ et ΔV_g =3.04 V du diamant centré à Vg = 63 V permettent d'estimer $C_\Sigma = 9.71$ aF, $E_C = e^2/2C_\Sigma = 8.2 \pm 0.3$ meV et $C_g = 0.053 aF$.*

crystallin. Ferromagnétique y compris à température ambiante, le LSMO possède à l'échelle massif une polarisation de spin maximale. Pour cette raison, le LSMO est un candidat idéal pour l'injection ou la détection de spin dans les dispositifs spintronique. Bien que les expériences montrent sans ambiguïtés une densité de courant de diffusion fortement polarisée en spin dans le LSMO volumique [Nadgorny01], le degré de polarisation du courant tunnel de spin demeure controversé [Nadgorny07]. Ce dernier présente habituellement des polarisation de spin de l'ordre de 40% à 60%, certainement limitées par les mecanismes de diffusion de spin à l'interface. Des valeurs de polarization exceptionnellement élevées (entre 80 et 90%) ont été cependant obtenue à basse température sur des échantillons préparés dans les

conditions très précises [Tsymbal11]. Du fait de sa stabilité chimique, le LSMO est adapté aux dispositifs spintroniques hybrides organiques-inorganiques dans lesquels il est courrament ulitisé comme électrodes [Dediu09]. Dans ces dispositifs, l'interface LSMO/organique controle le transport. Par ailleurs, les propriétés des électrodes de LSMO exposées soit à l'environnement ambiant, aux solvant ou aux composés organiques sont difficiles à conciler avec ceux des multicouches épitaxiées crues sous vide dans des conditions très contrôlées. A cause des limites de sensibilité des méthodes expérimentales une analyse quantitative de ces effets d'interface nécessite que l'étude soit menée sur de grande surfaces. Ainsi, la compréhension des effets d'interface sur le transport à l'échelle nanométrique reste un question ouverte [Gambardella14]. Le rapport surface-sur-volume très élevé dans les NPs de $La_{0.67}Sr_{0.33}MnO_3$ rend possible l'étude les propriétés physiques sensibles aux effets de surface ou d'interface donc le magnétisme et le transport dans ces systèmes nanométriques. Notre présentons ici des résultats remarquables de l'étude des propriétés de transport de charge et de spin dans les nanocristaux de LSMO. Ces résultats sont rendue possibles grâce à une combinaison originale d'une part de la synthèse colloïdale de nanocristaux de LSMO d'une très bonne qualité cristalline d'environ 20 nm de taille et de surface dépourvue de ligands de protection et donc exposée à son environnement immédiate et d'autre part d'une géométrie de nanodispositif parfaitement adaptée à une étude magnetotransport robuste à travers un faible nombre de nanoparticules (Fig10.12.(a)).

Les propriétés structuraux des nanocrystaux ont été étudiées par diffraction de rayon X, ce qui a confirmé la structure rhomboédrique propres aux LSMO volumique. De même, les analyses chimiques par spectrométrie plasma à couplage inductif a montré rapports Sr:La de 0.51, c'est à dire proches de la composition la stœchiométrie idéale $La_{0.67}Sr_{0.33}MO_3$ et en accord avec le rapport Sr:La introduit dans le précurseur de synthèse. Les études de microscopie électronique à balayage à haute résolution (MEB) ont montré que la poudre granulaire des particules obtenue par synthèse est principalement constituée de nanocubes de 15 à 30 nm de taille avec le maximum de statistique à 21 nm (Fig10.12.(a)). Afin de mieux comprendre la structure de chaque nanoparticule, les analyses de microscopie électronique à transmission à balayage (METB) avec résolution atomique ont été mené. Elles ont confirmé la structure perovskite et révélé la présence d'un nombre négligeable de défauts. Le degré d'oxydation moyen du Mn a été mesuré par spectroscopie à perte d'énergie à haute résolution ce qui a permis de confirmer un degré d'oxydation de $+3.3 \pm 0.1$ en parfaite accord avec la valeur attendue du ratio La/Sr mesuré par analyse d'élément chimique. En somme, toutes ces analyses physico-chimiques démontrent que le cœur des nanocrystaux présentent la structure et la composition attendue du LSMO massifs non contraint. Ainsi, ces nanocubes peuvent être considérés comme des portions nanométriques du LSMO monocristallin massif.

Étude de magnétométrie

Les courbes de magnétométrie (Fig10.11) confirment que les particules sont ferromagnétiques et suggèrent un comportement magnétique biphasé caractérisé par la superposition

d'une composante de type ferromagnétique et d'une composante de type paramagnétique faite de spins désordonnés. Un tel comportement dans des nanoparticules de taille inférieures à 100 nm est souvent due à une structure "Cœur-Coquille" [Zhang14a] dans laquelle le cœur ferromagnétique de la nanoparticules avec des spins bien organisés est entouré d'une coquille caractérisée par un désordre de spins. Nous avons mené une analyse quantitative (Fig10.11.(b)) basée sur une approximation de l'aimantation à basse température donnée par l'équation10.2 [Coey10].

$$m(B) = \Theta(B)m_F + L(\alpha B)m_P \tag{10.2}$$

Dans cette equation l'aimantation $m(B)$ est la superposition d'une contribution ferromagnétique $\Theta(B)$ du cœur (avec une aimantation de saturation m_F) et une contribution paramagnétique décrite par une fonction Langevin $L(\alpha B)$ avec une valeur de saturation (à champ infinie) m_P. Le pré-facteur $\alpha = \frac{\mu}{k(T+T_0)}$, tient compte de la correction de température effective T_0 qui décrit les interactions entre les moments μ dans le couplage antiferromagnétique attendu dans les manganites dans la phase paramagnétique [Coey10]. Nous avons ajusté les courbes

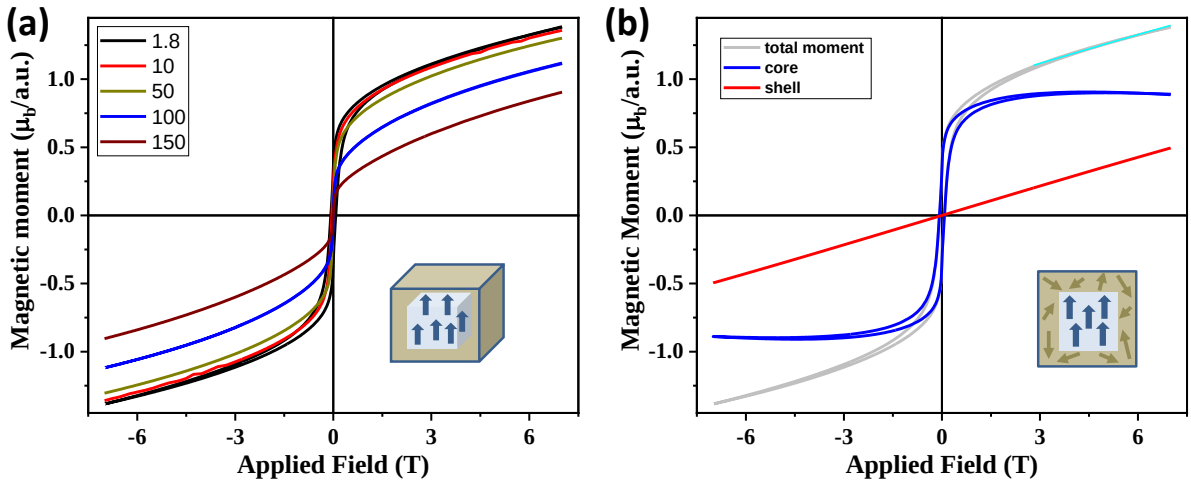

Figure 10.11 *– Propriétés magnétiques des nanocubes LSMO. (a) Courbes de magnétométrie à différentes températures. (b) Décomposition du signal magnétique à 1,8 K en composante de cœur ferromagnétique (courbe bleue) dominante aux champs faibles et une enveloppe de type paramagnétique (courbe rouge) dominante aux champs élevés. Les données expérimentales (courbe grise) ont été ajustées entre 3 et 7 T, (courbe bleu clair). En encart de (a) et (b) nous illustrons les schémas cœur-coquille d'un nanocube avec les moments de cœur alignés et ceux de la coquille désordonnés.*

d'aimantation à champ fort entre 1.8 et 50 K, ce qui a permis d'estimer les valeurs de $T_0 \approx 100$ K et $\mu \approx 10\mu_B$. Ce dernier correspond aux moments magnétique de ~ 3 ions Mn et reflète les interactions entre les ions Mn plus proches voisins. La composante ferromagnétique $\Theta(B)$ est calculée comme étant la différence entre l'aimantation totale mesurée et la valeur obtenue de l'ajustement par la fonction Langevin (Fig10.11.(b)). Il domine l'aimantation à champ faible "champ faible" contrairement au régime de "champ fort" dominé par la composante paramagnétique ce que explique la difficulté à saturer l'aimantation (Fig10.11). La composante ferromagnétique représente environ 25% de l'aimantation de saturation du LSMO massif à basse température ($3.6\mu_B$/f.u.). La brisure de symétrie à la surface du matériau ainsi que le

changement possible du degré d'oxydation du Mn près de la surface des nanoparticules peut perturber le mécanisme de double échange Mn^{3+}-Mn^{4+} et favoriser un couplage antiferromagnétique au detriment du ferromagnétisme. Ceci conduit à ce qu'on appelle communément 'couche magnétique morte' [Boschker11] ou couche antiferromagnétiques ou encore verre de spins [Valencia14] bien connu dans les couches minces de $La_{0.67}Sr_{0.33}MnO_3$. Un tel scénario est en accord avec la structure 'cœur-coquille' considéré pour décrire les nanoparticules de taille inférieur à 100 nm. Dans cet approximation, pour les nanoparticules de taille ~20 nm, la coquille glace de spin s'étendrait jusqu'à 4.0±0.5 nm. Les films minces présentent généralement des couches magnétiques mortes d'environ 2 nm d'épaisseur [Verna10], ou plus importantes lorsqu'elles sont déposées dans les conditions non épithéliales [Borges01]. Cependant, des valeurs aussi faibles que 1 nm, ont été rapportées sur couches minces épitaxiales crûes dans les conditions très optimisées [Valencia07]. Afin de mieux cerner la structure 'cœur-coquille' des nanoparticules des études complémentaires de spectroscopie des pertes d'énergie à haute résolution et de METB à résolution atomique concentrées sur la surface ont été mené. Elles ont révélé que, comme décrit ci-dessus, la charge moyenne de Mn de +3.3 ±0.1 est homogène sur l'ensemble de la particule à l'exception des deux pseudo-cellules unités cubiques externes correspondant à une épaisseur de 0.8 nm à cause principalement des vacances d'oxygène. Ces deux couches superficielles contenant trois plans atomiques de Mn présentent une diminution significative de l'état d'oxydation du Mn ($Mn^{+2.8\pm0.1}$) ce qui est l'origine de la phase paramagnétique superficielles.

Transport de charge et de spin dans les nanocrystaux LSMO

Pour étudier les propriétés de transport des nanoparticules de LSMO, nous avons adopté une géométries de nanodispositif adaptée à une étude de magnetotransport robuste à travers faible nombres de nanoparticules afin de mettre en exergue de rôle des interfaces. Pour ce faire, notre approche a consisté à piéger les NPs dans les nanotranchées à fort rapport d'aspect de 60 à 80 nm de gap. J'ai fabriqué ces nanotranchées par lithographie optique en bénéficiant de la technique de dépôt sous angle développée quelques années plus top dans notre équipe de recherche [Dayen10]. Les nanotranchées ne pouvant accommoder en série que 3 à 4 nanoparticules, les dispositifs ainsi fabriqués confèrent une configuration unique permettant d'adresser précisément les propriétés de transport de charges et de spin à travers ces nanoparticules (Fig10.12.(a)). Nous avons observé des magnétorésistance particulièrement élevées à base température atteignant 90% à 1.5 K (Fig10.12.(a)). Notre analyse détaillé de ces mesures a révélé que la structure Cœur-Coquille est à l'origine de telles observations. La coquille paramagnétique s'est avérée être seule responsable des MR observées. Sur la Fig10.12.(c) reportant la magnetoconductance en fonction de l'aimantation total, ont peut voir que les courbes demeurent relativement plates aux valeurs d'aimantation correspondant au cœur ferromagnétique des particules. La variation de la conductance est observée essentiellement à des valeurs élevées d'aimantation correspondant à l'aimantation de la coquille paramagnétique donc les spin initialement désordonnés sont forcés à s'ordonner sous l'effet du champ magnétique élevé facilitant le transport des charges (Fig10.12.(d)). Les change-

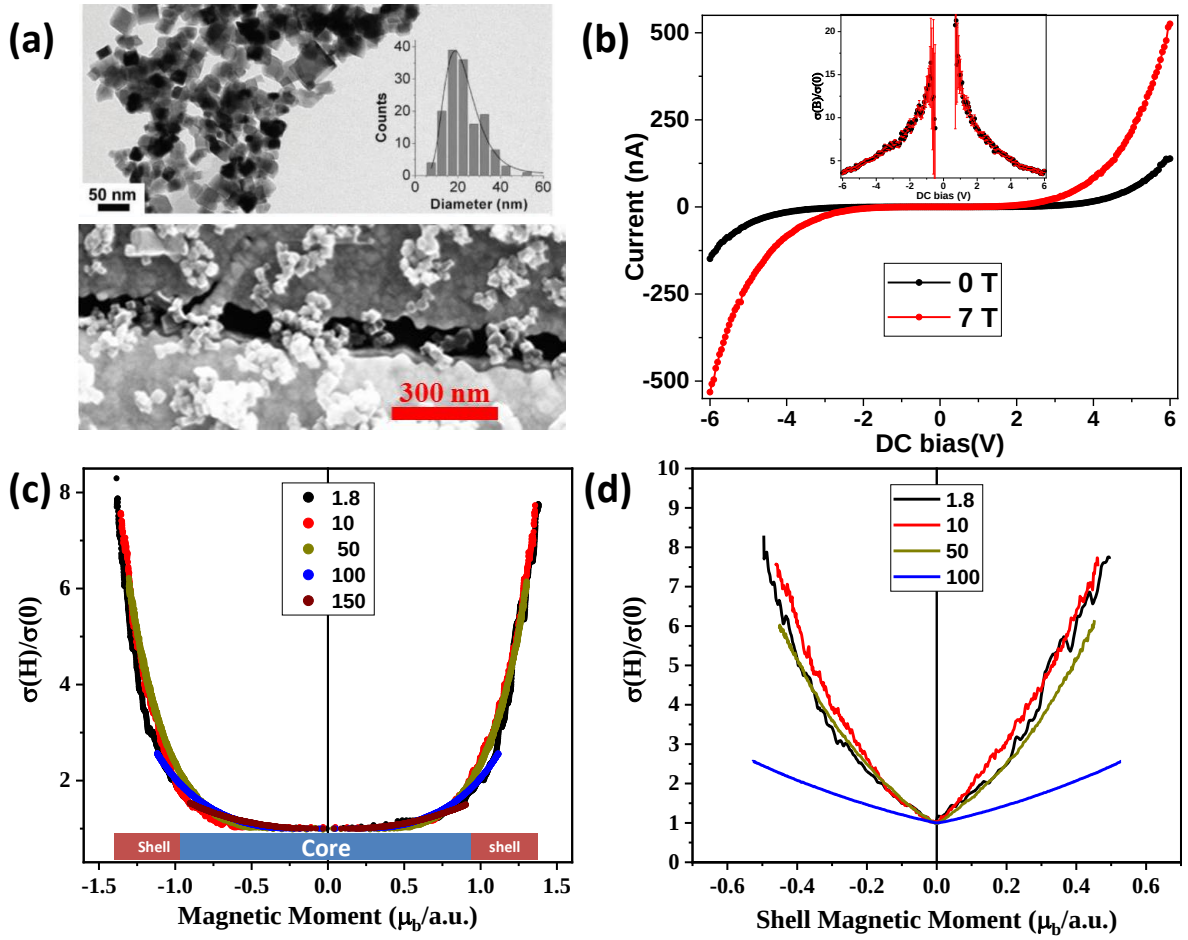

Figure 10.12 *– (a) Images MET des nanocristaux de LMSO. Courbe de statistique de taille en encart. Image MET d'une nanotranchée type avec les nanocristaux piégés par simple drop casting. (b) Caractéristique Isd (Vsd) mesuré à 1.6 K sous 0 T (courbe noire) et 7 T (courbe rouge). En encart : dépendance de la magnetoconductance correspondante en fonction de Vsd. (c) Magnetocnductance normalisée en fonction de l'aimantation, la bande colorée du fond rappelle la contribution de la composante dominante de l'aimantation (bleu : Cœur ferromagnétique, rouge : coquille paramagnétique). (d) Magnetocnductance normalisée en fonction l'aimantation de la coquille $L(\alpha B)m_p$ (voir Équation10.3 et Fig10.11)*

ments de résistances particulièrement élevés observés atteignant un facteur 8 à champ fort et 20 à basse tension source-drain (Fig10.12.(b)) ne peuvent s'expliquer par le simple modèle d'effet tunnel polarisé en spin entre les particules proches voisins. En effet, dans l'hypothèse que les mesures sont réalisées sur un ensemble de nanoparticules avec des aimantations aléatoires avant le champ coercitif, la MR résultante des processus tunnels inter-particules serait données par la formule suivante :

$$MR = \frac{R(B) - R(0)}{R(0)} = \frac{1}{1 + m^2 P^2} \tag{10.3}$$

Où m dénote l'aimantation normée et P la polarisation de spin. Cette équation limite la MR à 50% (ou le double de magnetoconductance). Les interactions entre les particules peuvent introduire quelques déviations de ce simple modèle. Cependant, cela ne saurait expliquer des MR 4 fois supérieurs à la valeur maximale espérée de l'équation.10.3. En outre, l'effet

de blocage de Coulomb et particulièrement les processus tunnels coopératifs (cotunneling en anglais) n'expliquent guère ces fortes valeurs de MR vue qu'elles persistent aux valeurs de tension source drain largement au dessus des valeurs d'énergies de blocage estimées.

En realité, les MR observées dans notre cas s'expliquent en considérant un mécanisme similaire à la magnétorésistance colossale (CMR selon le terme anglais dédié : Colossal magnetoresistance), bien connu dans les manganites à proximité de la température de Curie. La CMR est le changement énorme de la résistance qui se produit lors de du désalignement des moments magnétiques des cations Mn proche voisins impliqués dans le mécanisme de double échange $Mn^{3+} - O - Mn^{4+}$. Lequel désordre de moments réduit de manière considérable la probabilité de transfert de charge qui donne lieu à une importante augmentation de la resistance du materiau. La CMR est donc liée à l'énorme changement de résistance près de la transition magnétique entre les phases désordonnées (généralement paramagnétique) et ordonnées (généralement ferromagnétiques). Ainsi, lors du passage du matériau à l'ordre magnétique au point de transition isolant-métal à environ 360 K pour le LSMO [Coey99] où une variation typique d'un ordre de grandeur de la conductivité est observée sous des champs magnétiques forts caractéristique de la CMR. Dans notre cas, du fait de la structure magnétique cœur-coquille des nanoparticules, les MR observées résultent de l'alignement des moments magnétiques, particulièrement ceux de la couche magnétique morte qui sont forcés à s'aligner suivant la direction du champ lorsque celui-ci atteint des valeurs élevées à basse température, même si le matériau est loin de son point de transition magnétique et justifie les fortes MR observées.

Conclusion

Mon travail de thèse a porté sur l'étude les propriétés de transport de charge et de spin dans les nanoparticules (0D), les matériaux 2D et les hétérosturures de dimensionalité mixte 2D-0D de Van der Waals (h-DM-VdW). Les nanocristaux pérovskite de $La_{0.67}Sr_{0.33}MnO_3$ ont révélé des magnétorésistances exceptionnellement élevées à basse température résultant des moments magnétiques de leur coquille indépendamment de la polarisation de spin du cœur. Ce travail a permis de révéler la façon dont les propriétés de magnétotransport sont influencées à l'échelle manométrique dans ce matériau largement utilisé comme électrode dans les dispositifs spintroniques hybrides. J'ai fabriqué les transistors à effet de champ à base des matériaux bidimensionnel notamment le $MoSe_2$ en utilisant les électrodes de Ti/Au et avons étudié de manière détaillée les mécanismes d'injection de charge à l'interface $MoSe_2$/Ti. En modulant la configuration de bande d'énergie à l'interface $MoSe_2$/Ti nous avons pu mettre en exergue les mécanismes à l'origine de l'injection de charge. Nous avons en outre développé une approche alternative pour fabriquer des composants à électron unique à base d'hétérosturures 2D-0D. Une méthode de croissance est rapportée permettant l'auto-assemblage d'un réseau d'amas d'Al à la surface des matériaux 2D (graphene ou MoS_2). La transparence du graphene et du MoS_2 au champ électrique vertical permet de moduler efficacement l'environnement électrique des amas par le contact de grille ar-

rière donnant lieu aux fonctionalités caractéristique des transistors à un électrons. Les jonctions tunnels Co/AlOx/Al/AlOx/graphene présentent des MR attribuées aux effets magnéto-Coulomb anisotropes. Ce volet de mon travail de thèse démontre les vastes potentialités des hétérostructures à dimensionnalité mixte 2D-0D de Van der Waals pour la nanoélectronique et la spintronique.

List of publications

Paper related to the work of this thesis

- L. D. N. Mouafo, F. Godel, G. Melinte, S. Hajjar-Garreau, H. Majjad, B. Dlubak, O. Ersen, B. Doudin, L. Simon, P. Seneor, J.-F. Dayen, *Anisotropic Magneto-Coulomb properties of 2D-0D heterostructure single electron device*, Adv. Mater. 2018, 30, 1802478

- L. D. N. Mouafo, F. Godel, G. Froehlicher, S. Berciaud, B. Doudin, M. Venkata Kamalakar and J-F. Dayen. *Tuning contact transport mechanisms in high on/off ratio bilayer $MoSe_2$ transistors up to Fowler-Nordheim regime*, 2D Mater. 4 (2017) 015037

- F. Godel, L. D. N. Mouafo, G. Froehlicher, B. Doudin, S. Berciaud, Y. Henry, J-F. Dayen, and D. Halley. *Conductance Oscillations in a Graphene/Nanocluster Hybrid Material: Toward Large-Area Single-Electron Devices*, Adv. Mater., vol. 29, no. 3, p. 1604837, 2017

- Ha. Le. Thi. N'Goc, L. D. N. Mouafo, C. Etrillard, A. Torres-Pardo, J-F Dayen, S. Rano, G. Rousse, C. Laberty-Robert, J. G. Calbet, M. Drillon, C. Sanchez, B. Doudin, and D. Portehault. *Surface-Driven Magnetotransport in Perovskite Nanocrystals*, Adv. Mater. vol. 2017, 1604745

Papers related to other works done during my PhD

- B. Martinez, C. Livache, L.D.N. Mouafo, N. Goubet, S. Keuleyan, H. Cruguel, S. Ithurria, H. Aubin, A. Ouerghi, B. Doudin, E. Lacaze, B. Dubertret, M.G. Silly, R.P.S.M. Lobo, J.-F. Dayen, E. Lhuillier, *HgSe Self-Doped Nanocrystals as a Platform to Investigate the Effects of Vanishing Confinement*, ACS Applied Materials & Interfaces. 9 (2017) 36173-36180

Chapter A

Quantum Capacitance

In field effect devices with the conductive channel consisting of a low DOS systems such as 2D electron gas (2DEG) formed in inversion layer of MOSFETS and GaAs/AlGaAs quantum well or 2D SC-TMDs or graphene (Gr) as it is the case here, the capacitive effect of the metallic gate electrode is not as obvious as in a traditional two metallic planes capacitor. Indeed, an applied gate voltage to the capacitively coupled gate electrode induces an injection of charge carrier in the 2D material resulting to a shift of the chemical potentials of both the gate electrode and the active channel (Fig.A.1). Hence, taking the reference at the Fermi energy of the gate electrode, this shift is given by the Eq.A.1.

$$\mu^{Gr}(n) - \mu^{gate} = eV_g \tag{A.1}$$

The exact position of the chemical potential of the Gr sheet ($\mu^{Gr}(n)$) depends on the density of extra charges that it has accommodated. Two contributions to the shift of the chemical potentials of Gr and the metal gate electrode. First, the classical contribution originating from the applied gate voltage which induces extra charge in both Gr and gate electrode. Second, the quantum contribution resulting from the fact that, the extra charges to be accommodated in the Gr layer, its chemical potential necessarily undergoes a quantum shift. It is worth reminding during the FETs transport experiments in general and Gr FETs in particular, the channel often remains grounded by the source electrode. Therefore, a shift of the chemical potential is not expected in the whole material during the device operation. The shift of $\mu^{Gr}(n)$ is a quantum mechanical effect since the incoming electrons have to occupy available levels higher in energy. The lower states at μ^0 and below being occupied yet by the carrier present in Gr. The requirement for electrons to overcome an additional potential barrier to find available states appears as an additional capacitance (the quantum capacitance) in series

to the gate capacitance.

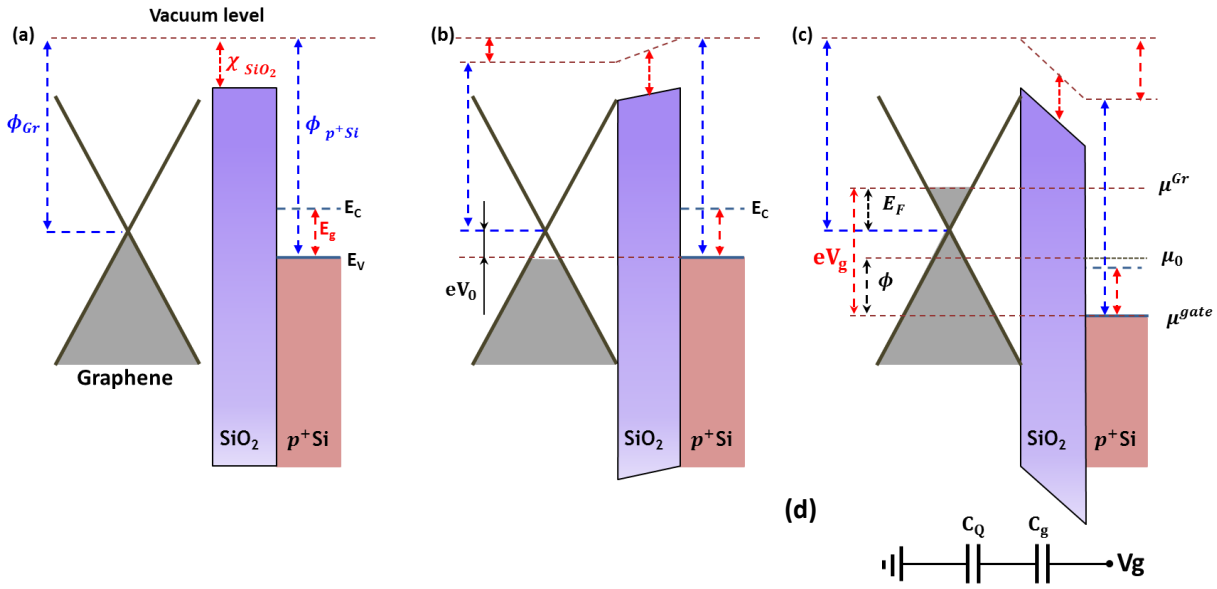

Figure A.1 *– Energy band diagram across the Graphene/SiO_2($p^{++}Si$) heterostructure. (a) The isolated system. Graphene is assumed to be pristine with no doping and its Fermi energy is at the Dirac point. Apart from the energy band filling of graphene in grey arbitrary chosen, other energies are represented on scale using the value from the literature [Xu13, H. Mathieu09]. The graphene work function ($\phi_{Gr} = 4.5eV$, $E_g(\chi)_{SiO_2} = 9(1.1)eV$ and $E_g(\chi)_{Si} = 1.12(4.01)eV$, $p^{++}Si$ is p-type degenerated thus we situated its Fermi energy at valence band maximum Ev. (b) Formation of the heterostructure, no gate voltage applied. Extra holes transferred from $p^{++}Si$ to graphene and its Fermi energy moves downward from the Dirac point and aligns Fermi energy of the metallic gate electrode at equilibrium. The extra charges induce a potential V_0 to graphene. (c) A positive gate voltage is applied inducing a shift of the chemical potential of graphene and p^{++}-Si. To accommodate extra electrons injected, the chemical potential of graphene moves from its equilibrium position μ_0 to a final position μ^{Gr}.*

In the capacitively coupled metallic electrode, the exta-charges are concentrated at the interface and the applied voltage induced shift of the chemical potential is not accompanied with the further shift due to additional energy band filling. Hence, no quantum contribution to the capacitance is to be reported. In Fig.A.1, we represent the evolution of the energy diagram of the $p^{++}Si$-SiO_2/Gr heterostructure. In Fig.A.1(a), Gr and the substrate are isolated and each component of the heterostructure keeps its intrinsic band structure. In Fig.A.1.(b) the Gr flake is in contact with the substrate. Since the work function of Gr is smaller than that of p^{++}-Si, holes are transferred from p^{++}-Si to Gr an electron diffusive in opposite direction, the Gr's Fermi level originally at the Dirac point, moves downward and aligns with the Fermi energy of the gate electrode to establish the equilibrium state. The total Fermi level shift of the Gr is quantified by eV_0, where V_0 is the Gr potential V_0 induced by the presence of the extra-charges at equilibrium. For the sake of simplicity, we have assumed that the position of the Dirac point remains unchanged during the heterostructure formation, which in fact is not obvious. Theoretical calculations based on DFT methods have shown that for a Gr layer in contact with metal, its band structure can be substantially affected and the position of the Dirac importantly modified [Giovannetti08]. An applied positive voltage to $p^{++}Si$ gate electrode enables to inject electrons into the Gr flake and its energy band undergoes important

modification. In Fig.A.1(c), one distinguishes the classical contribution $e\phi$ arising from the potential different between Gr and the gate electrode due to the gate voltage and the quantum contribution due to additional energy barrier that the extra electrons have to overcome to be accommodated in the Gr flake resulting to a shift of its chemical potential from its equilibrium position μ_0 to the final position μ^{Gr}. Following the notation of the Fig.A.1, the Eq.A.1 becomes :

$$\mu^{Gr}(n) - \mu^{gate} = eV_g = E_F^{Gr} + e\phi + eV_0 \tag{A.2}$$

Taking into account the expression of Gr's Fermi energy (Eq.3.2, section.3.1) and using the definition of the electrostatic potential difference $\phi = ne/C_g$, the Eq.A.2 can be rewritten as follow :

$$V_g - V_0 = \frac{E_F^{Gr}}{e} + \frac{ne}{C_g} = \mathrm{sgn}(n)\hbar v_F\sqrt{\pi|n|} + e^2 n/C_g = \frac{ne}{C_{eq}} \tag{A.3}$$

Where C_{eq} is the equivalent capacitor of both the classical capacitor and the quantum capacitor in series (Fig.A.1.(d)). Hence, using the expression $\frac{1}{C_{eq}} = \frac{1}{C_Q} + \frac{1}{C_g}$, we finally get the formula of the he quantum capacitance given by Eq.A.4.

$$C_Q = sgn(n)\frac{e^2}{\hbar v_v\sqrt{\pi}}\sqrt{n} = \frac{e^2}{2}g(E_F) \tag{A.4}$$

This simple derivation based on the band structure arguments provide the precise physical origin of the quantum capacitance. More accurate mathematical derivation of the quantum capacitance can be founded elsewhere [Fang07, Fernández-Rossier07]. In the main test, we discuss the quantitative comparison of the C_Q and C_g for top and back gate configuration.

Chapter B

Thermionic current at metal/semiconductor interface

At the metal/semiconductor interface, the inter-diffusion of charges necessary to establish the equilibrium is materialized by the alignment of the Fermi levels of both materials. It results an interface Schottky energy barrier $q\phi_b = e\phi_m - e\chi$, $e\phi_m$ and $e\chi$ are respectively the metal work function and the semiconductor electron affinity in electron volt. However, a combine effect of the built-in potential V_b due to interface charge depletion/accumulation as well as the image force and the applied electric fields induces a rounding of the conduction band of the semiconductor at the interface and modifies the interface energy barrier energy which becomes $E_a = q\phi_b - (E_c^0 - E_c^\infty)$, E_c^0 and E_c^∞ are respectively the conduction band minimum at the interface and far from the interface. We refer to it as interface activation energy following the nomenclature adopted in the reference [Allain15]. At absolute temperature there are no electrons crossing the interface. At finite temperature however, thermal excitation statistically provides to some electrons sufficient energy to overcome the interface energy barrier. Some, from metal to semiconductor and others in the opposite direction. This process is known as thermionic emission. We provide here the derivation of the electric current expected from such a process. This derivation can be founded in most of the semiconductor text books [Sze81, H. Mathieu09]. We start by presenting the standard 3D model for the current across Metal and bulk semiconductor interface, then we deduce the 2D model adapted to Metal/2D SC-TMDs that are the main interest of this thesis.

B.1 Electric current in thermionic regime

Thermionic regime assumes two main hypothesis : (i) The interface energy barrier is much larger than the thermal energy $E_a \gg K_B T$ such that the current arises essentially from electrons statistically promoted across the barrier by thermal excitation. (ii) The metal/semiconductor interface thermal equilibrium is not affected by the presence of a net current flow. Under these assumptions, the shape of the barrier is not relevant and the current flow depends solely on its height E_a. Therefore, only electrons with sufficient energy crossing perpendicularly the interface in the $x\vec{i}$ direction contribute to the current. The semiconductor to metal current density is given by the Eq.B.1.

$$J_{sc\to m} = \int_{E_F+E_a}^{\infty} q v_x dn \tag{B.1}$$

$E_F + E_a$ is the minimum energy required for thermal emission into the metal. $dn = N(E)F(E)dE$, where $N(E) = \frac{4\pi(2m^*)^{3/2}}{\hbar^3}\sqrt{E-E_c}$ is the 3D DOS and $F(E) = exp[-(E-E_F)/K_BT]$ is the Fermi-Dirac distribution function in Boltzmann approximation since $E - E_F > E_a \gg K_B T$. The energy of electrons is assumed to be essentially kinetic.

$$E = E_c + \frac{1}{2}m^* v^2 = E_F + E_a + \frac{1}{2}m^* v^2 \Rightarrow dE = m^* v dv \quad and \quad \sqrt{E-E_c} = v\sqrt{m^*/2} \tag{B.2}$$

therefore,

$$dn = 2(\frac{m^*}{h})^3 \exp(-\frac{E_a}{K_B T})\exp(-\frac{m^* v^2}{2K_B T})(4\pi v^2 dv) \tag{B.3}$$

Taking $\vec{v} = \vec{v_x} + \vec{v_y} + \vec{v_z}$, $4\pi v^2 dv$ is spherical coordinate equivalent of elementary volume and one can write $dv_x dv_y dv_z = 4\pi v^2 dv$. Hence, the Eq.B.1 becomes.

$$J_{sc\to m} = 2q(\frac{m^*}{h})^3 \exp(-\frac{E_a}{K_B T}) \int_{v_{0x}}^{\infty} v_x \exp(-\frac{m^* v_x^2}{2K_B T})dv_x \int_{-\infty}^{\infty} \exp(-\frac{m^* v_y^2}{2K_B T})dv_y \int_{-\infty}^{\infty} \exp(-\frac{m^* v_z^2}{2K_B T})dv_z \tag{B.4}$$

$$\Rightarrow J_{sc\to m} = 2q(\frac{m^*}{h})^3 \exp(-\frac{E_a}{K_B T})(\frac{K_B T}{m^*})[\exp(-\frac{m^* v_x^2}{2K_B T})]_{v_{0x}}^{\infty} \frac{2\pi K_B T}{m^*} \tag{B.5}$$

$$= 2q(\frac{m^* 2\pi k_B^2 T^2}{h^3})\exp(-\frac{E_a}{K_B T})\exp(-\frac{m^* v_{0x}^2}{2k_B T}) \tag{B.6}$$

Here, v_{0x} is the minimum velocity of the carrier in the conduction band and depends on the built in potential V_b and the applied bias as $\frac{1}{2}v_{0x}^2 = q(V_b - V)$. However, the component related to V_b which the effect is the modification of E_F to E_C distance is already included in the term E_a. Finally,

$$J_{sc\to m} = A^* T^2 \exp(-\frac{E_a}{K_B T})\exp(\frac{qV}{k_B T}) \quad ; \quad A^* = \frac{4\pi q m^* k_B^2}{h^3} \tag{B.7}$$

Where $A^* = \frac{4\pi m^* 2k_B^2}{h^3}$ represents the Richardson constant for a bulk materials. For the electrons crossing the interface from metal to semiconductor, the interface energy barrier hight to overcome is not affected by the dc voltage in thermionic regime. Hence, the metal to semiconductor current density is given by :

$$J_{m\to sc} = A^* T^2 \exp(-\frac{E_a}{K_B T}) \tag{B.8}$$

Hence, the total current density across the Metal/Semiconductor interface is $J = J_{sc\to m} - J_{m\to sc}$ and takes the general form of Eq.B.11.

$$J = A^* T^2 \exp(-\frac{E_a}{K_B T})[\exp(\frac{qV}{K_B T}) - 1] \tag{B.9}$$

This expression quantifies exclusively the current across the interface but does not represent in principle the current flowing trough the device. Indeed after crossing the interface barrier, carriers have to diffuse within the semiconductor to reach the back side Schottky diode where they can be collected. It is therefore needed to quantified the diffusion current before expressing the global current voltage characteristics across the device. The diffusion current is derived by integration the diffusion current density in the SCR. Without going into details, we remind that the final expression is identical to EqB.11 except for the prefactor which defers form $A^* T^2$. However, the two terms are harmonized using the joint conditions for the two currents and the EqB.11 represents the Current-voltage characteristics in a FET [Sze81]. Which is normal since the interface and the SCR are electrically in series.

B.2 Thermionic emission : the 2D model

In 2D materials, quantum confinement freezes the motion of carrier in the $z\boldsymbol{k}$ direction and the motion of carriers is restricted in the x, y directions. Therefore, the derivation of the thermionic current has to be reconsidered taking into account the energy independent 2D DOS $N(E) = 4\pi m^*/h^2$. In these conditions, the Eq.B.3 becomes :

$$\Rightarrow dn = \frac{2m^{*^2}}{h^2} \exp -(\frac{q\phi_F}{K_B T}) \exp(-\frac{m^* v^2}{2K_B T})(2\pi v dv) dE \tag{B.10}$$

Thus by integrating the Eq.B.1 exclusively in x, y plan of the 2D material following similar methodology as in previous section, one obtains :

$$J = A^*_{2D} T^{3/2} \exp(-\frac{E_a}{K_B T})[\exp(\frac{qV}{K_B T}) - 1] \tag{B.11}$$

Where $A^*_{2D} = \frac{(8\pi m^* k_B^3)^{1/2}}{h^2}$ represents the Richardson constant for 2D materials. One sees that the confinement substantially affect the prefactor. The EqB.11 is commonly used formula to analyze the charge transport in 2D-semiconductors based FETs as abundantly detailed in this thesis.

Bibliography

[Ajayan16] P. M. Ajayan, P. Kim, and K. Banerjee. *Two-dimensional van der Waals materials*. Phys. Today **69** (9), 38-44 (2016). 10, 11, 22, 170

[Alferov01] Zhores I. Alferov. *Nobel Lecture: The double heterostructure concept and its applications in physics, electronics, and technology*. Rev. Mod. Phys. **73**, 767–782 (2001). 11

[Allain12] Adrien Allain, Zheng Han, and Vincent Bouchiat. *Electrical control of the superconducting-to-insulating transition in graphene-metal hybrids*. Nature Materials **11** (7), 590–594 (2012). 31, 36, 45, 114, 172

[Allain15] Adrien Allain, Jiahao Kang, Kaustav Banerjee, and Andras Kis. *Electrical contacts to two-dimensional semiconductors* (2015). 43, 44, 118, 122, 123, 126, 129, 178, 193

[Ashcroft76] Neil W Ashcroft and N David Mermin. *Solid state physics*. Holt, Rinehart and Winston, 1976. 20, 38

[Avouris10] Phaedon Avouris. *Graphene: Electronic and Photonic Properties and Devices*. Nano Lett. **10** (11), 4285-4294 (2010). 20, 40

[Baibich88] M. N. Baibich, J. M. Broto, A. Fert, F. Nguyen Van Dau, F. Petroff, P. Etienne, G. Creuzet, A. Friederich, and J. Chazelas. *Giant Magnetoresistance of (001)Fe/(001)Cr Magnetic Superlattices*. Phys. Rev. Lett. **61**, 2472–2475 (1988). 9, 101, 169

[Balcells98] Ll Balcells, J Fontcuberta, B Martinez, and X Obradors. *High-field magnetoresistance at interfaces in manganese perovskites*. Physical Review B **58** (22), R14697 (1998). 146

[Baltic16] Romana Baltic, Marina Pivetta, Fabio Donati, Christian Wäckerlin, Aparajita Singha, Jan Dreiser, Stefano Rusponi, and Harald Brune. *Superlattice of Single Atom Magnets on Graphene*. Nano Letters **16** (12), 7610–7615 (2016). 102

[Beebe06] Jeremy M. Beebe, BongSoo Kim, J. W. Gadzuk, C. Daniel Frisbie, and James G. Kushmerick. *Transition from Direct Tunneling to Field Emission in Metal-Molecule-Metal Junctions*. Phys. Rev. Lett. **97**, 026801 (2006). 48, 125

[Bernand-Mantel08a] Anne Bernand-Mantel. *Transport ctron et effets magn-Coulomb dans une nanoparticule unique*. PhD thesis, (2008). Th de doctorat dirigar Fert, Albert Sciences des mataux Paris 6 2008", note = 2008PA066015,. 59, 87, 89, 106

[Bernand-Mantel08b] Anne Bernand-Mantel. *Transport à un électron et effets magnéto-Coulomb dans une nanoparticule unique*. PhD thesis, Paris 6, (2008). 58

[Bernand-Mantel09] Anne Bernand-Mantel, Pierre Seneor, Karim Bouzehouane, Stéphane Fusil, Cyrile Deranlot, Frédéric Petroff, and Albert Fert. *Anisotropic magneto-Coulomb effects and magnetic single-electron-transistor action in asingle nanoparticle*. Nature Physics **5** (12), 920–924 (2009). 58, 61, 62, 83, 87, 88, 104, 105, 107, 109, 110, 166, 175

[Bernand-Mantel11] A. Bernand-Mantel, P. Seneor, K. Bouzehouane, S. Fusil, C. Deranlot, F. Petroff, and A. Fert. *Anisotropic magneto-Coulomb effect versus spin accumulation in a ferromagnetic single-electron device*. Physical Review B - Condensed Matter and Materials Physics **84** (18), 1–4 (2011). 61, 62, 83, 105, 110, 175

[Binasch89] G. Binasch, P. Grünberg, F. Saurenbach, and W. Zinn. *Enhanced magnetoresistance in layered magnetic structures with antiferromagnetic interlayer exchange*. Phys. Rev. B **39**, 4828–4830 (1989). 9, 101, 169

[Bolotin04] K. I. Bolotin, F. Kuemmeth, A. N. Pasupathy, and D. C. Ralph. *Metal-nanoparticle single-electron transistors fabricated using electromigration*. Applied Physics Letters **84** (16), 3154–3156 (2004). 83, 88, 99, 138

[Borges01] RP Borges, W Guichard, JG Lunney, JMD Coey, and F Ott. *Magnetic and electric dead layers in (La0. 7Sr0. 3) MnO3 thin films*. Journal of Applied Physics **89** (7), 3868–3873 (2001). 150, 182

[Boschker11] H Boschker, Mark Huijben, A Vailionis, J Verbeeck, S v van Aert, M Luysberg, S Bals, G v van Tendeloo, Evert Pieter Houwman, Gertjan Koster, et al. *Optimized fabrication of high-quality La0. 67Sr0. 33MnO3 thin films considering all essential characteristics*. Journal of physics D: applied physics **44** (20), 205001 (2011). 150, 182

[Britnell13] Lıam Britnell, RM Ribeiro, A Eckmann, R Jalil, BD Belle, A Mishchenko, Y-J Kim, RV Gorbachev, T Georgiou, SV Morozov, et al. *Strong light-matter interactions in heterostructures of atomically thin films*. Science **340** (6138), 1311–1314 (2013). 28, 30

[Cao18] *Unconventional superconductivity in magic-angle graphene superlattices*. Nature **556**, 43. 22

[Cao1805] *Correlated insulator behaviour at half-filling in magic-angle graphene superlattices*. Nature **556**, 80 (2005). 22

[Carlsson99] Sven-Bertil Carlsson, Tobias Junno, Lars Montelius, and Lars Samuelson. *Mechanical tuning of tunnel gaps for the assembly of single-electron transistors*. Applied physics letters **75** (10), 1461–1463 (1999). 165

[Castro Neto07] A. H. Castro Neto and Francisco Guinea. *Electron-phonon coupling and Raman spectroscopy in graphene*. Phys. Rev. B **75**, 045404 (2007). 20

[Castro Neto09a] A. H. Castro Neto, F. Guinea, N. M. R. Peres, K. S. Novoselov, and A. K. Geim. *The electronic properties of graphene*. Rev. Mod. Phys. **81**, 109–162 (2009). 18, 19, 20

[Castro Neto09b] A. H. Castro Neto, F. Guinea, N. M. R. Peres, K. S. Novoselov, and A. K. Geim. *The electronic properties of graphene*. Rev. Mod. Phys. **81**, 109–162 (2009). 18, 20, 38, 39, 40, 41, 42

[Chamlagain14] Bhim Chamlagain, Qing Li, Nirmal Jeevi Ghimire, Hsun-jen Chuang, Meeghage Madusanka Perera, Honggen Tu, Yong Xu, Minghu Pan, Di Xaio, Jiaqiang Yan, David Mandrus, Zhixian Zhou, United States, Nanophase Materials Sciences, Oak Ridge, Materials Science, Technology Division, and Computer Engineering. *Mobility Improvement and Temperature Dependence in MoSe2 Field-Effect Transistors on Parylene C Substrate*. ACS nano **8** (5), 5079–5088 (2014). 49, 50, 53, 54, 113, 114, 123

[Chandni16] U. Chandni, K. Watanabe, T. Taniguchi, and J. P. Eisenstein. *Signatures of Phonon and Defect-Assisted Tunneling in Planar Metal-Hexagonal Boron Nitride-Graphene Junctions*. Nano Letters (2016). 29, 31

[Charlier07] Jean-Christophe Charlier, Xavier Blase, and Stephan Roche. *Electronic and transport properties of nanotubes*. Rev. Mod. Phys. **79**, 677–732 (2007). 17

[Chen] Jian Hao Chen, Chaun Jang, Shudong Xiao, Masa Ishigami, and Michael S. Fuhrer. *Intrinsic and extrinsic performance limits of graphene devices on SiO_2, volume = 3, year = 2008*. Nature Nanotechnology (4), 206–209. 41, 42

[Chen13] Jen-Ru Chen, Patrick M Odenthal, Adrian G Swartz, George Charles Floyd, Hua Wen, Kelly Yunqiu Luo, and Roland K Kawakami. *Control of Schottky Barriers in Single Layer MoS2 Transistors with Ferromagnetic Contacts*. Nano Letters page 130612092631002 (2013). 46, 47

[Chen15a] Shao Yu Chen, Changxi Zheng, Michael S. Fuhrer, and Jun Yan. *Helicity-Resolved Raman Scattering of MoS2, MoSe2, WS2, and WSe2Atomic Layers*. Nano Letters (2015). 115, 116

[Chen15b] Xiaolong Chen, Zefei Wu, Shuigang Xu, Lin Wang, Rui Huang, Yu Han, Weiguang Ye, Wei Xiong, Tianyi Han, Gen Long, Yang Wang, Yuheng He, Yuan Cai, Ping Sheng, and Ning Wang. *Probing the electron states and metal-insulator transition mechanisms in molybdenum disulphide vertical heterostructures*. Nature Communications **6**, 1–8 (2015). 52

[Chhowalla13] Manish Chhowalla, Hyeon Suk Shin, Goki Eda, Lain-Jong Li, Kian Ping Loh, and Hua Zhang. *The chemistry of two-dimensional layered transition metal dichalcogenide nanosheets*. Nat. Chem. **5** (4), 263–275 (2013). 22, 23, 25, 26

[Choi17] Wonbong Choi, Nitin Choudhary, Gang Hee Han, Juhong Park, Deji Akinwande, and Young Hee Lee. *Recent development of two-dimensional transition metal dichalcogenides and their applications* (2017). 33, 34

[Coey99] JMD Coey, MV Viret, and S Von Molnar. *Mixed-valence manganites*. Advances in physics **48** (2), 167–293 (1999). 145, 155, 184

[Coey10] John MD Coey. *Magnetism and magnetic materials*. Cambridge University Press, 2010. 149, 181

[Coletti13] C. Coletti, S. Forti, A. Principi, K. V. Emtsev, A. A. Zakharov, K. M. Daniels, B. K. Daas, M. V. S. Chandrashekhar, T. Ouisse, D. Chaussende, A. H. MacDonald, M. Polini, and U. Starke. *Revealing the electronic band structure of trilayer graphene on SiC: An angle-resolved photoemission study*. Phys. Rev. B **88**, 155439 (2013). 21

[Costa00] V. Da Costa, Y. Henry, F. Bardou, M. Romeo, and K. Ounadjela. *Experimental evidence and consequences of rare events in quantum tunneling*. The European Physical Journal B - Condensed Matter and Complex Systems **13** (2), 297–303 (2000). 86

[Costina01] I. Costina and R. Franchy. *Band gap of amorphous and well-ordered Al2O3on Ni3Al(100)*. Applied Physics Letters (2001). 87, 174

[Cowburn95] R. P. Cowburn, S. J. Gray, J. Ferré, J. A. C. Bland, and J. Miltat. *Magnetic switching and inplane uniaxial anisotropy in ultrathin Ag/Fe/Ag(100) epitaxial films*. Journal of Applied Physics **78** (12), 7210-7219 (1995). 112

[Cresti08] Alessandro Cresti, Norbert Nemec, Blanca Biel, Gabriel Niebler, François Triozon, Gianaurelio Cuniberti, and Stephan Roche. *Charge transport in disordered graphene-based low dimensional materials*. Nano Research **1** (5), 361–394 (2008). 17, 18

[Dagotto01] Elbio Dagotto, Takashi Hotta, and Adriana Moreo. *Colossal magnetoresistant materials: the key role of phase separation*. Physics reports **344** (1-3), 1–153 (2001). 150

[Danilov02] Andrey V. Danilov, Dmitrii S. Golubev, and Sergey E. Kubatkin. *Tunneling through a multigrain system: Deducing sample topology from nonlinear conductance*. Physical Review B - Condensed Matter and Materials Physics **65** (125312) (2002). 98, 138, 165, 167

[Dankert14] André Dankert, Lennart Langouche, Mutta Venkata Kamalakar, and Saroj Prasad Dash. *High-performance molybdenum disulfide field-effect transistors with spin tunnel contacts*. ACS Nano (2014). 46, 47, 122, 123

[Dankert17a] André Dankert, Parham Pashaei, M. Venkata Kamalakar, Anand P.S. Gaur, Satyaprakash Sahoo, Ivan Rungger, Awadhesh Narayan, Kapildeb Dolui, Md Anamul Hoque, Ram Shanker Patel, Michel P. De Jong, Ram S. Katiyar, Stefano Sanvito, and Saroj P. Dash. *Spin-Polarized Tunneling through Chemical Vapor Deposited Multilayer Molybdenum Disulfide*. ACS Nano **11** (6), 6389–6395 (2017). 11, 29, 166

[Dankert17b] André Dankert, Parham Pashaei, M. Venkata Kamalakar, Anand P.S. Gaur, Satyaprakash Sahoo, Ivan Rungger, Awadhesh Narayan, Kapildeb Dolui, Md Anamul Hoque, Ram Shanker Patel, Michel P. De Jong, Ram S. Katiyar, Stefano Sanvito, and Saroj P. Dash. *Spin-Polarized Tunneling through Chemical Vapor Deposited Multilayer Molybdenum Disulfide*. ACS Nano **11** (6), 6389–6395 (2017). 29

[Das Sarma11] S. Das Sarma, Shaffique Adam, E. H. Hwang, and Enrico Rossi. *Electronic transport in two-dimensional graphene*. Rev. Mod. Phys. **83**, 407–470 (2011). 20, 21, 30, 39, 40, 41, 42, 52, 93

[Das13a] Saptarshi Das and Joerg Appenzeller. *Screening and interlayer coupling in multilayer* MoS_2. Phys. Status Solidi RRL **7** (4), 268–273 (2013). 114

[Das13b] Saptarshi Das, Hong-Yan Chen, Ashish Verma Penumatcha, and Joerg Appenzeller. *High performance multilayer* MoS_2 *transistors with scandium contacts*. Nano Lett. **13** (1), 100–105 (2013). 45, 46, 47, 48, 49, 50, 118, 122

[Das15] Suprem R. Das, Jiseok Kwon, Abhijith Prakash, Collin J. Delker, Saptarshi Das, and David B. Janes. *Low-frequency noise in MoSe2 field effect transistors*. Applied Physics Letters **106** (8), 083507 (2015). 113

[Dayen10] JF Dayen, V Faramarzi, M Pauly, NT Kemp, M Barbero, BP Pichon, H Majjad, S Begin-Colin, and B Doudin. *Nanotrench for nano and microparticle electrical interconnects*. Nanotechnology **21** (33), 335303 (2010). 151, 182

[Dediu09] VA Dediu. *VA Dediu, LE Hueso, I. Bergenti, and C. Taliani, Nat. Mater. 8, 707 (2009).* Nat. Mater. **8**, 707 (2009). 146, 180

[Dlubak12] Bruno Dlubak, Marie Blandine Martin, Robert S. Weatherup, Heejun Yang, Cyrile Deranlot, Raoul Blume, Robert Schloegl, Albert Fert, Abdelmadjid Anane, Stephan Hofmann, Pierre Seneor, and John Robertson. *Graphene-passivated nickel as an oxidation-resistant electrode for spintronics*. ACS Nano (2012). 88

[Dugay17] J. Dugay, M. Aarts, M. Gimenez-Marqués, T. Kozlova, H. W. Zandbergen, E. Coronado, and H. S.J. Van Der Zant. *Phase transitions in spin-crossover thin films probed by graphene transport measurements*. Nano Letters (2017). 27, 31

[Dulli00] Hani Dulli, P. A. Dowben, S.-H. Liou, and E. W. Plummer. *Surface segregation and restructuring of colossal-magnetoresistant manganese perovskites* $La_{0.65}Sr_{0.35}MnO_3$. Phys. Rev. B **62**, R14629–R14632 (2000). 158

[Eich18] Marius Eich, Riccardo Pisoni, Hiske Overweg, Annika Kurzmann, Yongjin Lee, Peter Rickhaus, Thomas Ihn, Klaus Ensslin, Franti šek Herman, Manfred Sigrist, Kenji Watanabe, and Takashi Taniguchi. *Spin and Valley States in Gate-Defined Bilayer Graphene Quantum Dots*. Phys. Rev. X **8**, 031023 (2018). 138

[Electronics07] Mesoscopic Electronics and Solid State Nanostructures. *Single-Electron Tunneling* pages 247–272 (2007). 95

[Epherre11] Romain Epherre, Etienne Duguet, Stéphane Mornet, Emil Pollert, Stéphanie Louguet, Sébastien Lecommandoux, Christophe Schatz, and Graziella Goglio. *Manganite perovskite nanoparticles for self-controlled magnetic fluid hyperthermia: about the suitability of an aqueous combustion synthesis route*. Journal of Materials Chemistry **21** (12), 4393–4401 (2011). 146

[Fang07] Tian Fang, Aniruddha Konar, Huili Xing, and Debdeep Jena. *Carrier statistics and quantum capacitance of graphene sheets and ribbons*. Applied Physics Letters (2007). 39, 191

[Federspiel15] François Federspiel, Guillaume Froehlicher, Michel Nasilowski, Silvia Pedetti, Ather Mahmood, Bernard Doudin, Serin Park, Jeong O. Lee, David Halley, Benoît Dubertret, Pierre Gilliot, and Stéphane Berciaud. *Distance dependence of the energy transfer rate from a single semiconductor nanostructure to graphene*. Nano Letters **15** (2), 1252–1258 (2015). 35

[Feng17] Yuan Ping Feng, Lei Shen, Ming Yang, Aizhu Wang, Minggang Zeng, Qingyun Wu, Sandhya Chintalapati, and Ching Ray Chang. *Prospects of spintronics based on 2D materials* (2017). 27, 29

[Fernández-Rossier07] J. Fernández-Rossier, J. J. Palacios, and L. Brey. *Electronic structure of gated graphene and graphene ribbons*. Phys. Rev. B **75**, 205441 (2007). 39, 191

[Ferrar07] Andrea C. Ferrar. *Raman spectroscopy of graphene and graphite: Disorder, electron–phonon coupling, doping and nonadiabatic effects*. Solid State Communications **143** (1), 47 - 57 (2007). Exploring graphene. 73

[Feynman60] Richard P Feynman. *There's plenty of room at the bottom*. Engineering and science **23** (5), 22–36 (1960). 9, 169

[Fowler88] A. B. Fowler, J. J. Wainer, and R. A. Webb. *Electronic transport in small strongly localized structures*. IBM Journal of Research and Development **32** (3), 372-383 (1988). 135

[Froehlicher16] Guillaume Froehlicher, M Thomas EBBESEN Professeur, and Université M de Strasbourg Jean-Jacques GREFFET Professeur. *Optical spectroscopy of two-dimensional materials: graphene, transition metal dichalcogenides and van der Waals heterostructures AUTRES MEMBRES DU JURY* (2016). 24, 67

[Fuchs08] Jean-Noël Fuchs and Mark Oliver Goerbig. *Introduction to the physical properties of graphene*. Lecture Notes (2008). 17

[Fulton87] T. A. Fulton and G. J. Dolan. *Observation of single-electron charging effects in small tunnel junctions*. Phys. Rev. Lett. **59**, 109–112 (1987). 10

[Galbiati15] Marta Galbiati, Sergio Tatay, Sophie Delprat, Clément Barraud, Vincent Cros, Eric Jacquet, Fernando Coloma, Fadi Choueikani, Edwige Otero, Philippe Ohresser, et al. *Influence of alkylphosphonic acid grafting on the electronic and magnetic properties of La2/3Sr1/3MnO3 surfaces*. Applied Surface Science **353**, 24–28 (2015). 146

[Gambardella14] A Gambardella, P Graziosi, I Bergenti, M Prezioso, D Pullini, S Milita, Fabio Biscarini, and VA Dediu. *Surface nanostructures in manganite films*. Scientific reports **4**, 5353 (2014). 146, 180

[Giovannetti08] G. Giovannetti, P. A. Khomyakov, G. Brocks, V. M. Karpan, J. van den Brink, and P. J. Kelly. *Doping Graphene with Metal Contacts*. Phys. Rev. Lett. **101**, 026803 (2008). 190

[Glazman88] LI Glazman and KA Matveev. *Inelastic tunneling through thin amorphous films*. Zhurnal Eksperimentalnoi i Teoreticheskoi Fiziki **94** (6), 332–343 (1988). 151

[Godel14] F Godel, M Venkata Kamalakar, B Doudin, Y Henry, D Halley, and J-F Dayen. *Voltage-controlled inversion of tunnel magnetoresistance in epitaxial nickel/graphene/MgO/cobalt junctions*. Applied Physics Letters **105** (15), 152407 (2014). 29

[Godel15] Florian Godel. *Le graphène comme barrière tunnel: propriétés d'injection de charges et de spin*. PhD thesis, Université de Strasbourg, (2015). 74, 75

[Gong14] Cheng Gong, Luigi Colombo, Robert M. Wallace, and Kyeongjae Cho. *The unusual mechanism of partial fermi level pinning at metal-MoS 2 interfaces*. Nano Letters (2014). 135, 164

[Gong17] Cheng Gong, Lin Li, Zhenglu Li, Huiwen Ji, Alex Stern, Yang Xia, Ting Cao, Wei Bao, Chenzhe Wang, Yuan Wang, Z. Q. Qiu, R. J. Cava, Steven G. Louie, Jing Xia, and Xiang Zhang. *Discovery of intrinsic ferromagnetism in two-dimensional van der Waals crystals*. Nature **546** (7657), 265–269 (2017). 11, 170

[Gong18] Chuanhui Gong, Kai Hu, Xuepeng Wang, Peihua Wangyang, Chaoyi Yan, Junwei Chu, Min Liao, Liping Dai, Tianyou Zhai, Chao Wang, Liang Li, and Jie Xiong. *2D Nanomaterial Arrays for Electronics and Optoelectronics*. Advanced Functional Materials **28** (16), 1–23 (2018). 27, 28, 30, 35, 102

[Gorter51] C.J Gorter. *A possible explanation of the increase of the electrical resistance of thin metal films at low temperatures and small field strengths*. Physica **17** (8), 777 - 780 (1951). 10

[Gross00] R Gross, L Alff, B Büchner, BH Freitag, C Höfener, J Klein, Yafeng Lu, W Mader, JB Philipp, MSR Rao, et al. *Physics of grain boundaries in the colossal magnetoresistance manganites*. Journal of Magnetism and Magnetic Materials **211** (1-3), 150–159 (2000). 152

[H. Mathieu09] Henry H. Mathieu and Hervé Fanet (2009). 42, 43, 44, 117, 190, 193

[Hamer18] Matthew Hamer, Endre Tóvári, Mengjian Zhu, Michael D. Thompson, Alexander Mayorov, Jonathon Prance, Yongjin Lee, Richard P. Haley, Zakhar R. Kudrynskyi, Amalia Patanè, Daniel Terry, Zakhar D. Kovalyuk, Klaus Ensslin, Andrey V. Kretinin, Andre Geim, and Roman Gorbachev. *Gate-Defined Quantum Confinement in InSe-Based van der Waals Heterostructures*. Nano Letters (2018). 138

[Han07] Melinda Y. Han, Barbaros Özyilmaz, Yuanbo Zhang, and Philip Kim. *Energy band-gap engineering of graphene nanoribbons*. Physical Review Letters **98** (20), 1–4 (2007). 40

[Hanna91] AE Hanna and M Tinkham. *Variation of the Coulomb staircase in a two-junction system by fractional electron charge*. Physical review B **44** (11), 5919 (1991). 58

[Hasegawa06] Yasumasa Hasegawa, Rikio Konno, Hiroki Nakano, and Mahito Kohmoto. *Zero modes of tight-binding electrons on the honeycomb lattice*. Phys. Rev. B **74**, 033413 (2006). 19

[He15] G. He, K. Ghosh, U. Singisetti, H. Ramamoorthy, R. Somphonsane, G. Bohra, M. Matsunaga, A. Higuchi, N. Aoki, S. Najmaei, Y. Gong, X. Zhang, R. Vajtai, P. M. Ajayan, and J. P. Bird. *Conduction Mechanisms in CVD-Grown Monolayer MoS<inf>2</inf> Transistors: From Variable-Range Hopping to Velocity Saturation*. Nano Letters **15** (8), 5052–5058 (2015). 116, 118

[Hirohata14] Atsufumi Hirohata and Koki Takanashi. *Future perspectives for spintronic devices*. Journal of Physics D: Applied Physics **47** (19), 193001 (2014). 101, 102

[Huang06] M. L. Huang, Y. C. Chang, C. H. Chang, T. D. Lin, J. Kwo, T. B. Wu, and M. Hong. *Energy-band parameters of atomic-layer-deposition Al2O3/InGaAs heterostructure*. Applied Physics Letters (2006). 87, 174

[Huang17] Bevin Huang, Genevieve Clark, Efrén Navarro-Moratalla, Dahlia R. Klein, Ran Cheng, Kyle L. Seyler, DIng Zhong, Emma Schmidgall, Michael A. McGuire, David H. Cobden, Wang Yao, Di Xiao, Pablo Jarillo-Herrero, and Xiaodong Xu. *Layer-dependent ferromagnetism in a van der Waals crystal down to the monolayer limit*. Nature **546** (7657), 270–273 (2017). 11, 170

[Huisman09] Everardus H. Huisman, Constant M. Guédon, Bart J. Van Wees, and Sense Jan Van Der Molen. *Interpretation of transition voltage spectroscopy*. Nano Letters **9** (11), 3909–3913 (2009). 125

[Hwang96] HY Hwang, SW Cheong, NP Ong, and a B Batlogg. *Spin-polarized intergrain tunneling in La 2/3 Sr 1/3 MnO 3*. Physical Review Letters **77** (10), 2041 (1996). 149, 154

[Jariwala13] D. Jariwala, V. K. Sangwan, C.-C. Wu, P. L. Prabhumirashi, M. L. Geier, T. J. Marks, L. J. Lauhon, and M. C. Hersam. *Gate-tunable carbon nanotube-MoS2 heterojunction p-n diode*. Proceedings of the National Academy of Sciences **110** (45), 18076–18080 (2013). 28, 30, 35

[Jariwala16] Deep Jariwala, Tobin J Marks, and Mark C Hersam. *Mixed-dimensional van der Waals heterostructures*. Nature Publishing Group **16** (2016). 11, 12, 15, 26, 27, 30, 35, 102, 171

[Julliere75] M. Julliere. *Tunneling between ferromagnetic films*. Physics Letters A **54** (3), 225 - 226 (1975). 9, 59, 60, 169

[Jung15] Chulseung Jung, Seung Min Kim, Hyunseong Moon, Gyuchull Han, Junyeon Kwon, Young Ki Hong, Inturu Omkaram, Youngki Yoon, Sunkook Kim, and Jozeph Park. *Highly Crystalline CVD-grown Multilayer MoSe2Thin Film Transistor for Fast Photodetector*. Scientific Reports (2015). 115

[Kaasbjerg12] Kristen Kaasbjerg, Kristian S. Thygesen, and Karsten W. Jacobsen. *Phonon-limited mobility in n-type single-layer MoS_2 from first principles*. Phys. Rev. B **85**, 115317 (2012). 49

[Kaasbjerg13] Kristen Kaasbjerg, Kristian S. Thygesen, and Antti-Pekka Jauho. *Acoustic phonon limited mobility in two-dimensional semiconductors: Deformation potential and piezoelectric scattering in monolayer MoS_2 from first principles*. Phys. Rev. B **87**, 235312 (2013). 49

[Kamalakar15] M. Venkata Kamalakar, Christiaan Groenveld, André Dankert, and Saroj P. Dash. *Long distance spin communication in chemical vapour deposited graphene*. Nature Communications (2015). 29

[Kamimura10] Takafumi Kamimura10 and Kazuhiko Matsumoto. *Gate controlled Particle-Wave duality in a single walled carbon nanotube hole-transistor 187 X Gate controlled Particle-Wave duality in a single walled carbon nanotube hole-transistor*. 133

[Kang15] Kibum Kang, Saien Xie, Lujie Huang, Yimo Han, Pinshane Y. Huang, Kin Fai Mak, Cheol Joo Kim, David Muller, and Jiwoong Park. *High-mobility three-atom-thick semiconducting films with wafer-scale homogeneity*. Nature (2015). 34, 35

[Kappera14a] Rajesh Kappera, Damien Voiry, Sibel Ebru Yalcin, Brittany Branch, Gautam Gupta, Aditya D. Mohite, and Manish Chhowalla. *Phase-engineered low-resistance contacts for ultrathin MoS2 transistors*. Nature Materials (2014). 23

[Kappera14b] Rajesh Kappera, Damien Voiry, Sibel Ebru Yalcin, Wesley Jen, Muharrem Acerce, Sol Torrel, Brittany Branch, Sidong Lei, Weibing Chen, Sina Najmaei, Jun Lou, Pulickel M. Ajayan, Gautam Gupta, Aditya D. Mohite, and Manish Chhowalla. *Metallic 1T phase source/drain electrodes for field effect transistors from chemical vapor deposited MoS2*. APL Materials (2014). 23

[Karpan07] V. M. Karpan, G. Giovannetti, P. A. Khomyakov, M. Talanana, A. A. Starikov, M. Zwierzycki, J. van den Brink, G. Brocks, and P. J. Kelly. *Graphite and Graphene as Perfect Spin Filters*. Phys. Rev. Lett. **99**, 176602 (2007). 88

[Karpan08] V. M. Karpan, P. A. Khomyakov, A. A. Starikov, G. Giovannetti, M. Zwierzycki, M. Talanana, G. Brocks, J. van den Brink, and P. J. Kelly. *Theoretical prediction of perfect spin filtering at interfaces between close-packed surfaces of Ni or Co and graphite or graphene*. Phys. Rev. B **78**, 195419 (2008). 88

[Kastner87] M. A. Kastner, R. F. Kwasnick, J. C. Licini, and D. J. Bishop. *Conductance fluctuations near the localized-to-extended transition in narrow Si metal-oxide-semiconductor field-effect transistors*. Phys. Rev. B **36**, 8015–8031 (1987). 91, 133

[Kastner92] M. A. Kastner. *The single-electron transistor*. Rev. Mod. Phys. **64**, 849–858 (1992). 10, 11, 133, 135

[Kessler10] B. M. Kessler, Ç Ö Girit, A. Zettl, and V. Bouchiat. *Tunable superconducting phase transition in metal-decorated graphene sheets*. Physical Review Letters **104** (4), 1–4 (2010). 31, 36

[Kim17] Changsik Kim, Inyong Moon, Daeyeong Lee, Min Sup Choi, Faisal Ahmed, Seunggeol Nam, Yeonchoo Cho, Hyeon-jin Shin, Seongjun Park, and Won Jong Yoo. *Fermi Level Pinning at Electrical Metal Contacts of Monolayer Molybdenum Dichalcogenides* (2017). 135

[Kośmider13] K. Kośmider, J. W. González, and J. Fernández-Rossier. *Large spin splitting in the conduction band of transition metal dichalcogenide monolayers*. Phys. Rev. B **88**, 245436 (2013). 113

[Konstantatos12] Gerasimos Konstantatos, Michela Badioli, Louis Gaudreau, Johann Osmond, Maria Bernechea, F Pelayo Garcia de Arquer, Fabio Gatti, and Frank HL Koppens. *Hybrid graphene-quantum dot phototransistors with ultrahigh gain*. Nat. Nanotechnol. **7** (6), 363–368 (2012). 28, 30, 35

[Kou97] *Mesoscopic Electron Transport*. 1997. 99, 175

[Kouwenhoven97] L. P. Kouwenhoven, T. H. Oosterkamp, M. W. S. Danoesastro, M. Eto, D. G. Austing, T. Honda, and S. Tarucha. *Excitation Spectra of Circular, Few-Electron Quantum Dots*. Science **278** (5344), 1788–1792 (1997). 131, 132, 133, 134

[Kranthi Kumar15] V. Kranthi Kumar, Sukanya Dhar, Tanushree H. Choudhury, S. A. Shivashankar, and Srinivasan Raghavan. *A predictive approach to CVD of crystalline layers of TMDs: The case of MoS<inf>2</inf>*. Nanoscale **7** (17), 7802–7810 (2015). 34

[Krasnozhon14] Daria Krasnozhon, Dominik Lembke, Clemens Nyffeler, Yusuf Leblebici, and Andras Kis. *MoS2transistors operating at gigahertz frequencies*. Nano Letters (2014). 114

[Kufer15] Dominik Kufer, Ivan Nikitskiy, Tania Lasanta, Gabriele Navickaite, Frank H.L. Koppens, and Gerasimos Konstantatos. *Hybrid 2D-0D MoS2-PbS quantum dot photodetectors*. Advanced Materials **27** (1), 176–180 (2015). 35

[Larentis12] Stefano Larentis, Babak Fallahazad, and Emanuel Tutuc. *Field-effect transistors and intrinsic mobility in ultra-thin MoSe2 layers*. Appl. Phys. Lett. **101** (22), 223104 (2012). 113

[Lau12] Chun Ning Lau, Wenzhong Bao, and Jairo Velasco. *Properties of suspended graphene membranes*. Materials Today **15** (6), 238 - 245 (2012). 21

[Lee84] Patrick A. Lee. *Variable-Range Hopping in Finite One-Dimensional Wires*. Phys. Rev. Lett. **53**, 2042–2045 (1984). 133

[Lee12a] Hee Sung Lee, Sung Wook Min, Youn Gyung Chang, Min Kyu Park, Taewook Nam, Hyungjun Kim, Jae Hoon Kim, Sunmin Ryu, and Seongil Im. *MoS 2 nanosheet phototransistors with thickness-modulated optical energy gap (Supplementary)*. Nano Letters **12** (7), 3695–3700 (2012). 73, 74

[Lee12b] Kyung Sig Lee, Rahman Md Anisur, Ki Woong Kim, Won Sun Kim, Tae-Joon Park, Eun Joo Kang, and In Su Lee. *Seed size-dependent formation of Fe3O4/MnO hybrid nanocrystals: selective, magnetically recyclable catalyst systems*. Chemistry of Materials **24** (4), 682–687 (2012). 155, 156

[Li08] Xiaolin Li, Xinran Wang, Li Zhang, Sangwon Lee, and Hongjie Dai. *Chemically Derived, Ultrasmooth Graphene Nanoribbon Semiconductors*. Science **319** (5867), 1229–1232 (2008). 40

[Li11a] Fenghong Li, Yiqiang Zhan, Tsung-Hsun Lee, Xianjie Liu, Akira Chikamatsu, Tzung-Fang Guo, Hong-Ji Lin, JCA Huang, and Mats Fahlman. *Modified surface electronic and magnetic properties of La0. 6Sr0. 4MnO3 thin films for spintronics applications*. The Journal of Physical Chemistry C **115** (34), 16947–16953 (2011). 146

[Li11b] Qiuzi Li, E. H. Hwang, and S. Das Sarma. *Disorder-induced temperature-dependent transport in graphene: Puddles, impurities, activation, and diffusion*. Phys. Rev. B **84** (11), 115442 (2011). 38

[Li13] Song-lin Li, Katsunori Wakabayashi, Yong Xu, Shu Nakaharai, and Katsuyoshi Komatsu. *Thickness-Dependent Interfacial Coulomb Scattering in Atomically Thin Field-E ff ect Transistors* (2013). 50

[Li14] Yilei Li, Jonathan Ludwig, Tony Low, Alexey Chernikov, Xu Cui, Ghidewon Arefe, Young Duck Kim, Arend M. van der Zande, Albert Rigosi, Heather M. Hill, Suk Hyun Kim, James Hone, Zhiqiang Li, Dmitry Smirnov, and Tony F. Heinz. *Valley Splitting and Polarization by the Zeeman Effect in Monolayer* $MoSe_2$. Phys. Rev. Lett. **113**, 266804 (2014). 113

[Li17] Xinming Li, Li Tao, Zefeng Chen, Hui Fang, Xuesong Li, Xinran Wang, Jian Bin Xu, and Hongwei Zhu. *Graphene and related two-dimensional materials: Structure-property relationships for electronics and optoelectronics* (2017). 22, 23, 133

[Liang01] Wenjie Liang, Marc Bockrath, Dolores Bozovic, Jason H. Hafner, M. Tinkham, and Hongkun Park. *Fabry-Perot interference in a nanotube electron waveguide*. Nature (2001). 133

[Liang14] Lizhi Liang, Lei Li, Heng Wu, and Xinhua Zhu. *Research progress on electronic phase separation in low-dimensional perovskite manganite nanostructures*. Nanoscale research letters **9** (1), 325 (2014). 150

[Liang17] Shiheng Liang, Huaiwen Yang, Pierre Renucci, Bingshan Tao, Piotr Laczkowski, Stefan Mc-Murtry, Gang Wang, Xavier Marie, Jean Marie George, Sébastien Petit-Watelot, Abdelhak Djeffal, Stéphane Mangin, Henri Jaffrès, and Yuan Lu. *Electrical spin injection and detection in molybdenum disulfide multilayer channel*. Nature Communications **8**, 1–9 (2017). 29, 166

[Liu09] Zheng Liu, Kazu Suenaga, Peter J. F. Harris, and Sumio Iijima. *Open and Closed Edges of Graphene Layers*. Phys. Rev. Lett. **102**, 015501 (2009). 20

[Liu13] Junku Liu, Qunqing Li, Yuan Zou, Qingkai Qian, Yuanhao Jin, Guanhong Li, Kaili Jiang, and Shoushan Fan. *The Dependence of Graphene Raman D-band on Carrier Density*. Nano Lett. **13** (12), 6170-6175 (2013). 118

[Liu16] Yuan Liu, Nathan O. Weiss, Xidong Duan, Hung-Chieh Cheng, Yu Huang, and Xiangfeng Duan. *Van der Waals heterostructures and devices*. Nature Reviews Materials (2016). 11, 12, 15, 26, 27, 34, 102, 171

[Lopez-Sanchez13] Oriol Lopez-Sanchez, Dominik Lembke, Metin Kayci, Aleksandra Radenovic, and Andras Kis. *Ultrasensitive photodetectors based on monolayer MoS 2*. Nature Nanotechnology **8** (7), 497–501 (2013). 114

[Lu14] Xin Lu, M. Iqbal Bakti Utama, Junhao Lin, Xue Gong, Jun Zhang, Yanyuan Zhao, Sokrates T. Pantelides, Jingxian Wang, Zhili Dong, Zheng Liu, Wu Zhou, and Qihua Xiong. *Large-area synthesis of monolayer and few-layer MoSe2films on SiO2substrates*. Nano Letters (2014). 115

[MacNeill15] David MacNeill, Colin Heikes, Kin Fai Mak, Zachary Anderson, Andor Kormányos, Viktor Zólyomi, Jiwoong Park, and Daniel C. Ralph. *Breaking of Valley Degeneracy by Magnetic Field in Monolayer* $MoSe_2$. Phys. Rev. Lett. **114**, 037401 (2015). 113

[Maidecchi15] Giulia Maidecchi, Chinh Vu Duc, Renato Buzio, Andrea Gerbi, Gianluca Gemme, Maurizio Canepa, and Francesco Bisio. *Electronic Structure of Core-Shell Metal/Oxide Aluminum Nanoparticles*. Journal of Physical Chemistry C **119** (47), 26719–26725 (2015). 77

[Mak10] Kin Fai Mak, Changgu Lee, James Hone, Jie Shan, and Tony F. Heinz. *Atomically Thin* MoS_2*: A New Direct-Gap Semiconductor*. Phys. Rev. Lett. **105**, 136805 (2010). 26, 114

[Makarenko17] Ksenia S. Makarenko, Zhihua Liu, Michel P. de Jong, Floris A. Zwanenburg, Jurriaan Huskens, and Wilfred G. van der Wiel. *Bottom-Up Single-Electron Transistors*. Advanced Materials (2017). 99, 138

[Mann03] David Mann, Ali Javey, Jing Kong, Qian Wang, and Hongjie Dai. *Ballistic Transport in Metallic Nanotubes with Reliable Pd Ohmic Contacts*. Nano Letters (2003). 133

[Martin96] Michael C Martin. *MC Martin, G. Shirane, Y. Endoh, K. Hirota, Y. Moritomo, and Y. Tokura, Phys. Rev. B 53, 14 285 (1996).* Phys. Rev. B **53**, 14 (1996). 149

[Mathieu09] H. Mathieu and H. Fanet. *Physique des semiconducteurs et des composants électroniques: cours et exercices corrigés*. Sciences sup. Dunod, 2009. 20

[Matsumoto96] K. Matsumoto, M. Ishii, K. Segawa, Y. Oka, B. J. Vartanian, and J. S. Harris. *Room temperature operation of a single electron transistor made by the scanning tunneling microscope nanooxidation process for the TiO _x /Ti system*. Applied Physics Letters **68** (1), 34–36 (1996). 88

[Mayorov11] Alexander S. Mayorov, Roman V. Gorbachev, Sergey V. Morozov, Liam Britnell, Rashid Jalil, Leonid A. Ponomarenko, Peter Blake, Kostya S. Novoselov, Kenji Watanabe, Takashi Taniguchi, and A. K. Geim. *Micrometer-Scale Ballistic Transport in Encapsulated Graphene at Room Temperature*. Nano Lett. **11** (2011). 29, 40

[McEuen99] Paul L. McEuen, Marc Bockrath, David H. Cobden, Young-Gui Yoon, and Steven G. Louie. *Disorder, Pseudospins, and Backscattering in Carbon Nanotubes*. Phys. Rev. Lett. **83**, 5098–5101 (1999). 133

[Miró14] Pere Miró, Martha Audiffred, and Thomas Heine. *An atlas of two-dimensional materials*. Chemical Society Reviews **43** (18), 6537–6554 (2014). 18

[Morozov08] S. V. Morozov, K. S. Novoselov, M. I. Katsnelson, F. Schedin, D. C. Elias, J. A. Jaszczak, and A. K. Geim. *Giant Intrinsic Carrier Mobilities in Graphene and Its Bilayer*. Phys. Rev. Lett. **100**, 016602 (2008). 41, 42

[Nadgorny01] B. Nadgorny, I. I. Mazin, M. Osofsky, R. J. Soulen, P. Broussard, R. M. Stroud, D. J. Singh, V. G. Harris, A. Arsenov, and Ya. Mukovskii. *Origin of high transport spin polarization in* $La_{0.7}Sr_{0.3}MnO_3$ *: Direct evidence for minority spin states*. Phys. Rev. B **63**, 184433 (2001). 146, 179

[Nadgorny07] B Nadgorny. *The case against half-metallicity in La 0.7 Sr 0.3 MnO 3*. Journal of Physics: Condensed Matter **19** (31), 315209 (2007). 146, 179

[Nazarov09] Yuli V. Nazarov and Yaroslav M. Blanter. *Quantum Transport: Introduction to Nanoscience*. Cambridge University Press, 2009. 11, 56, 95

[Nicolosi13] Valeria Nicolosi, Manish Chhowalla, Mercouri G. Kanatzidis, Michael S. Strano, and Jonathan N. Coleman. *Liquid Exfoliation of Layered Materials*. Science **340** (6139) (2013). 32, 33

[Novoselov04] Kostya S Novoselov, Andre K Geim, Sergei V Morozov, D Jiang, Y_ Zhang, Sergey V Dubonos, Irina V Grigorieva, and Alexandr A Firsov. *Electric field effect in atomically thin carbon films*. Science **306** (5696), 666–669 (2004). 11, 15, 20, 28, 32, 38, 40, 66, 67, 170

[Novoselov05] KS Novoselov, D Jiang, F Schedin, TJ Booth, VV Khotkevich, SV Morozov, and AK Geim. *Two-dimensional atomic crystals*. Proc. Natl. Acad. Sci. U.S.A. **102** (30), 10451–10453 (2005). 40

[Novoselov16] KS Novoselov, A Mishchenko, A Carvalho, and AH Castro Neto. *2D materials and van der Waals heterostructures*. Science **353** (6298), aac9439 (2016). 11, 26, 27, 30, 34, 35

[Nuryadi11] Ratno Nuryadi. *Master Equation-Based Numerical Simulation in a Single Electron Transistor Using Matlab*. In *Numerical Simulations of Physical and Engineering Processes*. InTech, (2011). 58

[Ono98] Keiji Ono, Hiroshi Shimada, and Youiti Ootuka. *Ferromagnetic single electron transistor*. Solid-State Electronics **42** (7-8), 1407–1411 (1998). 59, 60, 61, 62

[Ootuka01] Youiti Ootuka, Keiji Ono, Hiroshi Shimada, Ryoji Matsuda, and Akinobu Kanda. *Electron transport in ferromagnetic small tunnel junctions*. Materials Science and Engineering B: Solid-State Materials for Advanced Technology **84** (1-2), 114–119 (2001). 60, 61, 62, 88

[Ovchinnikov14] Dmitry Ovchinnikov, Adrien Allain, Ying-Sheng Huang, Dumitru Dumcenco, and Andras Kis. *Electrical transport properties of single-layer WS2*. ACS nano **8** (8), 8174–8181 (2014). 116, 122, 130

[Pan09] Yi Pan, Min Gao, Li Huang, Feng Liu, and H. J. Gao. *Directed self-assembly of monodispersed platinum nanoclusters on graphene Moiŕ template*. Applied Physics Letters **95** (9) (2009). 36, 172

[Pan16] Yuanyuan Pan, Sibai Li, Meng Ye, Ruge Quhe, Zhigang Song, Yangyang Wang, Jiaxin Zheng, Feng Pan, Wanlin Guo, Jinbo Yang, and Jing Lu. *Interfacial Properties of Monolayer $MoSe_2$/Metal Contacts*. The Journal of Physical Chemistry C (2016). 117, 118, 123

[Parui15] Subir Parui, Luca Pietrobon, David Ciudad, Saül Vélez, Xiangnan Sun, Fèlix Casanova, Pablo Stoliar, and Luis E. Hueso. *Gate-controlled energy barrier at a graphene/molecular semiconductor junction*. Advanced Functional Materials (2015). 31

[Pawbake16] Amit S. Pawbake, Mahendra S. Pawar, Sandesh R. Jadkar, and Dattatray J. Late. *Large area chemical vapor deposition of monolayer transition metal dichalcogenides and their temperature dependent Raman spectroscopy studies*. Nanoscale (2016). 115

[Peres07] N M R Peres and Eduardo V Castro. *Algebraic solution of a graphene layer in transverse electric and perpendicular magnetic fields*. Journal of Physics: Condensed Matter **19** (40), 406231 (2007). 18, 20

[Piquemal-Banci17] Maëlis Piquemal-Banci, Regina Galceran, Marie-Blandine Martin, Florian Godel, Abdelmadjid Anane, Frederic Petroff, Bruno Dlubak, and Pierre Seneor. *2D-MTJs: introducing 2D materials in magnetic tunnel junctions*. J. Phys. D: Appl. Phys **50** (2017). 11, 27, 29

[Pisoni18] Riccardo Pisoni, Zijin Lei, Patrick Back, Marius Eich, Hiske Overweg, Yongjin Lee, Kenji Watanabe, Takashi Taniguchi, Thomas Ihn, and Klaus Ensslin. *Gate-tunable quantum dot in a high quality single layer MoS2 van der Waals heterostructure*. Applied Physics Letters **112** (12), 123101 (2018). 29, 136, 138

[Poole83] D.A. Poole, M. Pepper, and H.W. Myron. *Loss of dimensionality, localisation and conductance oscillations in N-type GaAs FET's*. Physica B+C **117-118**, 697 - 699 (1983). 131, 132, 133, 134

[Pradhan08] Aswini K Pradhan, R Bah, RB Konda, R Mundle, H Mustafa, O Bamiduro, Rakhim R Rakhimov, Xiaohui Wei, and David J Sellmyer. *Synthesis and magnetic characterizations of manganite-based composite nanoparticles for biomedical applications*. Journal of Applied Physics **103** (7), 07F704 (2008). 146

[Pradhan14] Nihar R. Pradhan, Daniel Rhodes, Simin Feng, Yan Xin, Shahriar Memaran, Byoung-Hee Moon, Humberto Terrones, Mauricio Terrones, and Luis Balicas. *Field-Effect Transistors Based on Few-Layered α-$MoTe_2$*. ACS Nano **8**, 5911 (2014). 113

[Pradhan15] Nihar R Pradhan, Amber McCreary, Daniel Rhodes, Zhengguang Lu, Simin Feng, Efstratios Manousakis, Dmitry Smirnov, Raju Namburu, Madan Dubey, Angela R Hight Walker, et al. *Metal to insulator quantum-phase transition in few-layered ReS2*. Nano letters **15** (12), 8377–8384 (2015). 53, 54

[Radaelli97] PG Radaelli. *PG Radaelli, G. Iannone, M. Marezio, HY Hwang, S.-W. Cheong, JD Jorgensen, and DN Argyriou, Phys. Rev. B 56, 8265 (1997)*. Phys. Rev. B **56**, 8265 (1997). 147

[Radisavljevic11] B. Radisavljevic, A. Radenovic, J. Brivio, V. Giacometti, and A. Kis. *Single-layer MoS2transistors*. Nature Nanotechnology **6** (3), 147–150 (2011). 28, 49, 50, 170

[Radisavljevic13] Branimir Radisavljevic and Andras Kis. *Mobility engineering and a metal-insulator transition in monolayer MoS 2*. Nature Materials **12** (9), 815–820 (2013). 11, 53, 54, 116, 118

[Raja16] Archana Raja, Andrés Montoya-Castillo, Johanna Zultak, Xiao Xiao Zhang, Ziliang Ye, Cyrielle Roquelet, Daniel A. Chenet, Arend M. Van Der Zande, Pinshane Huang, Steffen Jockusch, James Hone, David R. Reichman, Louis E. Brus, and Tony F. Heinz. *Energy Transfer from Quantum Dots to Graphene and MoS2: The Role of Absorption and Screening in Two-Dimensional Materials*. Nano Letters **16** (4), 2328–2333 (2016). 35

[Rajapitamahuni16] Anil Rajapitamahuni, L Zhang, Mark A Koten, VR Singh, John D Burton, Evgeny Y Tsymbal, Jeffrey E Shield, and Xia Hong. *Giant enhancement of magnetic anisotropy in ultrathin manganite films via nanoscale 1D periodic depth modulation*. Physical review letters **116** (18), 187201 (2016). 146

[Ralph95] D. C. Ralph, C. T. Black, and M. Tinkham. *Spectroscopic Measurements of Discrete Electronic States in Single Metal Particles*. Phys. Rev. Lett. **74**, 3241–3244 (1995). 83, 88

[Ranuárez06] Juan C. Ranuárez, M. J. Deen, and Chih Hung Chen. *A review of gate tunneling current in MOS devices*. Microelectronics Reliability **46** (12), 1939–1956 (2006). 48

[Ribeiro-Soares14] J. Ribeiro-Soares, R. M. Almeida, E. B. Barros, P. T. Araujo, M. S. Dresselhaus, L. G. Cançado, and A. Jorio. *Group theory analysis of phonons in two-dimensional transition metal dichalcogenides*. Phys. Rev. B **90** (11), 115438 (2014). 23, 24, 25

[Robin16] A. Robin, E. Lhuillier, X. Z. Xu, S. Ithurria, H. Aubin, A. Ouerghi, and B. Dubertret. *Engineering the Charge Transfer in all 2D Graphene-Nanoplatelets Heterostructure Photodetectors*. Scientific Reports **6** (1), 24909 (2016). 35

[Schmidt15] Hennrik Schmidt, Francesco Giustiniano, and Goki Eda. *Electronic transport properties of transition metal dichalcogenide field-effect devices: surface and interface effects*, (2015). 22, 25, 26, 49, 50, 52, 53, 54, 142

[Seneor07] Pierre Seneor, Anne Bernand-Mantel, and Frédéric Petroff. *Nanospintronics: When spintronics meets single electron physics*. Journal of Physics Condensed Matter **19** (16) (2007). 10, 11, 55, 56, 58, 61, 78, 83, 88, 102, 107, 110, 175

[Shao16] Jian Shao, Hao Liu, Kai Zhang, Yang Yu, Weichao Yu, Hanxuan Lin, Jiebin Niu, Kai Du, Yunfang Kou, Wengang Wei, et al. *Emerging single-phase state in small manganite nanodisks*. Proceedings of the National Academy of Sciences **113** (33), 9228–9231 (2016). 146, 150

[Shi14] Xiaoling Shi, Guofa Dong, Ming Fang, Fengyun Wang, Hao Lin, Wen-Chun Yen, Kwok Sum Chan, Yu-Lun Chueh, and Johnny C. Ho. *Selective n-type doping in graphene via the aluminium nanoparticle decoration approach*. J. Mater. Chem. C **2**, 5417-5421 (2014). 73

[Shimada98] Hiroshi Shimada, Keiji Ono, and Youiti Ootuka. *Magneto-Coulomb Oscillation in Ferromagnetic Single Electron Transistors*. Journal of the Physical Society of Japan **67** (4), 1359–1370 (1998). 10, 58, 60, 61, 62, 88, 104

[Shklovskii84] Boris Isaakovich Shklovskii and Alex L Efros. *Electronic properties of doped semiconductors*, volume 45. Springer Science, 1984. 51, 52

[Sicot10] M. Sicot, S. Bouvron, O. Zander, U. Rüdiger, Yu S. Dedkov, and M. Fonin. *Nucleation and growth of nickel nanoclusters on graphene Moiŕ on Rh(111)*. Applied Physics Letters **96** (9) (2010). 36

[Simmons63] John G. Simmons. *Generalized Formula for the Electric Tunnel Effect between Similar Electrodes Separated by a Thin Insulating Film*. Journal of Applied Physics (1963). 47, 48, 120

[Singamaneni11] Srikanth Singamaneni, Valery N. Bliznyuk, Christian Binek, and Evgeny Y. Tsymbal. *Magnetic nanoparticles: recent advances in synthesis, self-assembly and applications*. J. Mater. Chem. **21**, 16819-16845 (2011). 102

[Skoropata14] E. Skoropata, R. D. Desautels, C.-C. Chi, H. Ouyang, J. W. Freeland, and J. van Lierop. *Magnetism of iron oxide based core-shell nanoparticles from interface mixing with enhanced spin-orbit coupling*. Phys. Rev. B **89**, 024410 (2014). 156

[Song09] Hyunwook Song, Youngsang Kim, Yun Hee Jang, Heejun Jeong, Mark A. Reed, and Takhee Lee. *Observation of molecular orbital gating*. Nature **462** (7276), 1039–1043 (2009). 48, 122, 125

[Song17] Xiongfei Song, Zhongxun Guo, Qiaochu Zhang, Peng Zhou, Wenzhong Bao, and David Wei Zhang. *Progress of Large-Scale Synthesis and Electronic Device Application of Two-Dimensional Transition Metal Dichalcogenides*, (2017). 33, 34, 35, 45, 49, 50

[Soubelet16] P. Soubelet, A. E. Bruchhausen, A. Fainstein, K. Nogajewski, and C. Faugeras. *Resonance effects in the Raman scattering of monolayer and few-layer* $MoSe_2$. Phys. Rev. B **93**, 155407 (2016). 115

[Splendiani10] Andrea Splendiani, Liang Sun, Yuanbo Zhang, Tianshu Li, Jonghwan Kim, Chi-Yung Chim, Giulia Galli, and Feng Wang. *Emerging Photoluminescence in Monolayer* MoS_2. Nano Lett. **10** (4), 1271–1275 (2010). 25, 26

[Staring92] A. A. M. Staring, H. van Houten, C. W. J. Beenakker, and C. T. Foxon. *Coulomb-blockade oscillations in disordered quantum wires*. Phys. Rev. B **45**, 9222–9236 (1992). 131, 132, 133, 141, 162

[Sze81] S.M. Sze. *Physics of Semiconductor Devices*. Wiley-Interscience publication. John Wiley & Sons, 1981. 43, 44, 45, 47, 48, 120, 122, 193, 195

[Tan07] Y.-W. Tan, Y. Zhang, K. Bolotin, Y. Zhao, S. Adam, E. H. Hwang, S. Das Sarma, H. L. Stormer, and P. Kim. *Measurement of Scattering Rate and Minimum Conductivity in Graphene*. Phys. Rev. Lett. **99**, 246803 (2007). 41

[Tedrow71] Paul M Tedrow and Robert Meservey. *Spin-dependent tunneling into ferromagnetic nickel*. Physical Review Letters **26** (4), 192 (1971). 59

[Terrones10] Mauricio Terrones, Andrés R. Botello-Méndez, Jessica Campos-Delgado, Florentino López-Urías, Yadira I. Vega-Cantú, Fernando J. Rodríguez-Macías, Ana Laura Elías, Emilio Mu noz Sandoval, Abraham G. Cano-Márquez, Jean-Christophe Charlier, and Humberto Terrones. *Graphene and graphite nanoribbons: Morphology, properties, synthesis, defects and applications*. Nano Today **5** (4), 351 - 372 (2010). 18, 21

[Thi N'Goc17] Ha Le Thi N'Goc, Louis Donald Notemgnou Mouafo, Céline Etrillard, Almudena Torres-Pardo, Jean-François Dayen, Simon Rano, Gwenaëlle Rousse, Christel Laberty-Robert, Jose Gonzales Calbet, Marc Drillon, et al. *Surface-Driven Magnetotransport in Perovskite Nanocrystals*. Advanced Materials **29** (9), 1604745 (2017). 147, 149, 157, 159

[Thorat12] ND Thorat, KP Shinde, SH Pawar, KC Barick, CA Betty, and RS Ningthoujam. *Polyvinyl alcohol: an efficient fuel for synthesis of superparamagnetic LSMO nanoparticles for biomedical application*. Dalton Transactions **41** (10), 3060–3071 (2012). 146

[Tian07] Yang Tian, Dairong Chen, Xiuling Jiao, and Yongzheng Duan. *Facile preparation and electrochemical properties of cubic-phase Li 4 Mn 5 O 12 nanowires*. Chemical Communications (20), 2072–2074 (2007). 146

[Tian16] Yingliang Tian, Wencai Liu, Yongqiang Lu, and Shibing Sun. *Molten Salt Synthesis of Strontium-Doped Lanthanum Manganite Nanoparticles with Enhanced Catalytic Performance for Toluene Combustion*. Nano **11** (05), 1650059 (2016). 146

[Tombros07] Nikolaos Tombros, Csaba Jozsa, Mihaita Popinciuc, Harry T. Jonkman, and Bart J. Van Wees. *Electronic spin transport and spin precession in single graphene layers at room temperature*. Nature (2007). 27, 29, 67, 170

[Tongay12] Sefaattin Tongay, Jian Zhou, Can Ataca, Kelvin Lo, Tyler S. Matthews, Jingbo Li, Jeffrey C. Grossman, and Junqiao Wu. *Thermally Driven Crossover from Indirect toward Direct Bandgap in 2D Semiconductors:* $MoSe_2$ *versus* MoS_2. Nano Lett. **12** (11), 5576–5580 (2012). 114

[Tsymbal11] Evgeny Y Tsymbal and J. S. Moodera Zutic, Igor & P. R. Leclair. *Handbook of spin transport and magnetism*. CRC press, 2011. 146, 180

[Valencia07] S Valencia, A Gaupp, W Gudat, Ll Abad, Ll Balcells, and B Martinez. *Surface degradation of magnetic properties in manganite thin films proved with magneto-optical techniques in reflection geometry*. Applied physics letters **90** (25), 252509 (2007). 150, 182

[Valencia14] S Valencia, L Peña, Z Konstantinovic, Ll Balcells, R Galceran, D Schmitz, F Sandiumenge, M Casanove, and B Martínez. *Intrinsic antiferromagnetic/insulating phase at manganite surfaces and interfaces*. Journal of Physics: Condensed Matter **26** (16), 166001 (2014). 150, 182

[Van Der Molen06] S. J. Van Der Molen, N. Tombros, and B. J. Van Wees. *Magneto-Coulomb effect in spin-valve devices*. Physical Review B - Condensed Matter and Materials Physics **73** (22), 1–4 (2006). 61, 104, 105

[van Houten05] H. van Houten, C. W. J. Beenakker, and A. A. M. Staring. *Coulomb-Blockade Oscillations in Semiconductor Nanostructures* (2005). 99, 175

[Verna10] A Verna, Bruce A Davidson, Y Szeto, A Yu Petrov, A Mirone, A Giglia, N Mahne, and S Nannarone. *Measuring magnetic profiles at manganite surfaces with monolayer resolution*. Journal of Magnetism and Magnetic Materials **322** (9-12), 1212–1216 (2010). 150, 182

[Voiry13] Damien Voiry, Hisato Yamaguchi, Junwen Li, Rafael Silva, Diego C. B. Alves, Takeshi Fujita, Mingwei Chen, Tewodros Asefa, Vivek B. Shenoy, Goki Eda, and Manish Chhowalla. *Enhanced catalytic activity in strained chemically exfoliated WS2 nanosheets for hydrogen evolution*. Nature Materials (2013). 23

[Wallace47] Philip Richard Wallace. *The band theory of graphite*. Phys. Rev. **71** (9), 622 (1947). 17

[Wang12] Qing Hua Wang, Kourosh Kalantar-Zadeh, Andras Kis, Jonathan N. Coleman, and Michael S. Strano. *Electronics and optoelectronics of two-dimensional transition metal dichalcogenides*. Nature Nanotechnology **7**, 699 (2012). 15, 22, 27, 32, 33, 40

[Wang16] Ke Wang, Takashi Taniguchi, Kenji Watanabe, and Philip Kim. *Engineering Quantum Confinement in Semiconducting van der Waals Heterostructure* (2016). 29, 31

[Wang17] Hongyue Wang, Emmanuel Lhuillier, Qian Yu, Alexandre Zimmers, Benoit Dubertret, Christian Ulysse, and Hervé Aubin. *Transport in a single self-doped nanocrystal*. ACS nano **11** (2), 1222–1229 (2017). 162

[Wang18a] Ke Wang, Kristiaan De Greve, Luis A. Jauregui, Andrey Sushko, Alexander High, You Zhou, Giovanni Scuri, Takashi Taniguchi, Kenji Watanabe, Mikhail D. Lukin, Hongkun Park, and Philip Kim. *Electrical control of charged carriers and excitons in atomically thin materials*. Nature Nanotechnology (2018). 29, 136, 138

[Wang18b] Qisheng Wang, Yao Wen, Kaiming Cai, Ruiqing Cheng, Lei Yin, Yu Zhang, Jie Li, Zhenxing Wang, Feng Wang, Fengmei Wang, Tofik Ahmed Shifa, Chao Jiang, Hyunsoo Yang, and Jun He. *Nonvolatile infrared memory in MoS₂/PbS van der Waals heterostructures*. Science Advances **4** (4), 1–8 (2018). 31, 36

[Wu06] JH Wu and JG Lin. *Study on the phase separation of La0. 7Sr0. 3MnO3 nanoparticles by electron magnetic resonance*. Journal of Magnetism and Magnetic Materials **304** (1), e7–e9 (2006). 150

[Wu17] Congjun Wu, Fei Wang, Caoyuan Cai, Zhihao Xu, Yang Ma, Fan Huang, Feixiang Jia, and Min Wang. *Integration of graphene/ZnS nanowire film hybrids based photodetector arrays for high-performance image sensors*. 2D Materials **4** (2), 025113 (2017). 30

[Wunderlich06] J. Wunderlich, T. Jungwirth, B. Kaestner, A. C. Irvine, A. B. Shick, N. Stone, K.-Y. Wang, U. Rana, A. D. Giddings, C. T. Foxon, R. P. Campion, D. A. Williams, and B. L. Gallagher. *Coulomb Blockade Anisotropic Magnetoresistance Effect in a* (Ga,Mn)As *Single-Electron Transistor*. Phys. Rev. Lett. **97**, 077201 (2006). 105

[Xia09a] Fengnian Xia, Thomas Mueller, Roksana Golizadeh-Mojarad, Marcus Freitage, Yu Ming Lin, James Tsang, Vasili Perebeinos, and Phaedon Avouris. *Photocurrent imaging and efficient photon detection in a graphene transistor*. Nano Letters **9** (3), 1039–1044 (2009). 29, 39

[Xia09b] Fengnian Xia, Thomas Mueller, Yu Ming Lin, Alberto Valdes-Garcia, and Phaedon Avouris. *Ultrafast graphene photodetector*. Nature Nanotechnology **4** (12), 839–843 (2009). 29

[Xia2010] *Graphene Field-Effect Transistors with High On/Off Current Ratio and Large Transport Band Gap at Room Temperature*. Nano Lett. **10** (2010). 22

[Xu13] Kun Xu, Caifu Zeng, Qin Zhang, Rusen Yan, Peide Ye, Kang Wang, Alan C. Seabaugh, Huili Grace Xing, John S. Suehle, Curt A. Richter, David J. Gund-

lach, and N. V. Nguyen. *Direct measurement of dirac point energy at the graphene/oxide interface*. Nano Letters **13** (1), 131–136 (2013). 190

[Yakimov94] A I Yakimov, V A Markov, A V Dvurechenskii, and O P Pchelyakov. *Conductance oscillations in Ge/Si heterostructures containing quantum dots*. Journal of Physics: Condensed Matter **6** (13), 2573–2582 (1994). 86, 131, 132, 134, 141, 162, 173

[Yakushiji02] K. Yakushiji, S. Mitani, K. Takanashi, and H. Fujimori. *Tunnel magnetoresistance oscillations in current perpendicular to plane geometry of CoAlO granular thin films*. Journal of Applied Physics **91** (10 I), 7038–7040 (2002). 61, 62, 78

[Yakushiji05] Kay Yakushiji, Franck Ernult, Hiroshi Imamura, Kazutaka Yamane, Seiji Mitani, Koki Takanashi, Saburo Takahashi, Sadamichi Maekawa, and Hiroyasu Fujimori. *Enhanced spin accumulation and novel magnetotransport in nanoparticles*. Nature Materials **4** (1), 57–61 (2005). 61, 62, 78

[Yang17] Heejun Yang, Sung Wng Kim, Manish Chhowalla, and Young Hee Lee. *Structural and quantum-state phase transition in van der Waals layered materials*. Nature Physics (2017). 22, 25, 53, 54, 114

[Yin11] Zongyou Yin, Hai Li, Hong Li, Lin Jiang, Yumeng Shi, Yinghui Sun, Gang Lu, Qing Zhang, Xiaodong Chen, and Hua Zhang. *Single-Layer MoS 2 Phototransistors*. ACS nano **6** (1), 74–80 (2011). 29

[Yu16] Zhihao Yu, Zhun Yong Ong, Yiming Pan, Yang Cui, Run Xin, Yi Shi, Baigeng Wang, Yun Wu, Tangsheng Chen, Yong Wei Zhang, Gang Zhang, and Xinran Wang. *Realization of Room-Temperature Phonon-Limited Carrier Transport in Monolayer MoS_2 by Dielectric and Carrier Screening*. Advanced Materials **28** (3), 547–552 (2016). 49, 50

[Zeng12] Hualing Zeng, Junfeng Dai, Wang Yao, Di Xiao, and Xiaodong Cui. *Valley polarization in MoS 2 monolayers by optical pumping*. Nature Nanotechnology **7** (8), 490–493 (2012). 25, 26, 113

[Zeng13] Hualing Zeng, Gui-Bin Liu, Junfeng Dai, Yajun Yan, Bairen Zhu, Ruicong He, Lu Xie, Shijie Xu, Xianhui Chen, Wang Yao, et al. *Optical signature of symmetry variations and spin-valley coupling in atomically thin tungsten dichalcogenides*. Sci. Rep. **3** (2013). 25, 113

[Zhang05a] Yuanbo Zhang, Joshua P. Small, William V. Pontius, and Philip Kim. *Fabrication and electric-field-dependent transport measurements of mesoscopic graphite devices*. Applied Physics Letters **86** (7), 1–3 (2005). 32

[Zhang05b] Yuanbo Zhang, Yan-Wen Tan, Horst L. Stormer, and Philip Kim. *Experimental observation of the quantum Hall effect and Berry's phase in graphene*. Nature **438**, 201 (2005). 20

[Zhang09] Yuanbo Zhang, Tsung-Ta Tang, Caglar Girit, Zhao Hao, Michael C. Martin, Alex Zettl, Michael F. Crommie, Y. Ron Shen, and Feng Wang. *Direct observation of a widely tunable bandgap in bilayer graphene*. Nature **459** (7248), 820 (2009). 40

[Zhang14a] T Zhang, XP Wang, QF Fang, and XG Li. *Magnetic and charge ordering in nanosized manganites*. Applied Physics Reviews **1** (3), 031302 (2014). 149, 150, 181

[Zhang14b] Yi Zhang, Tay Rong Chang, Bo Zhou, Yong Tao Cui, Hao Yan, Zhongkai Liu, Felix Schmitt, James Lee, Rob Moore, Yulin Chen, Hsin Lin, Horng Tay Jeng, Sung Kwan Mo, Zahid Hussain, Arun Bansil, and Zhi Xun Shen. *Direct observation of the transition from indirect to direct bandgap in atomically thin epitaxial $MoSe_2$*. Nature Nanotechnology (2014). 25, 113

[Zhang15a] Enze Zhang, Yibo Jin, Xiang Yuan, Weiyi Wang, Cheng Zhang, Lei Tang, Shanshan Liu, Peng Zhou, Weida Hu, and Faxian Xiu. *ReS_2-Based Field-Effect Transistors and Photodetectors*. Adv. Func. Mater. **25** (26), 4076–4082 (2015). 122

[Zhang15b] Xin Zhang, Xiao-Fen Qiao, Wei Shi, Jiang-Bin Wu, De-Sheng Jiang, and Ping-Heng Tan. *Phonon and Raman scattering of two-dimensional transition metal dichalcogenides from monolayer, multilayer to bulk material*. Chem. Soc. Rev. **44**, 2757 (2015). 115

[Zhong16] Hongxia Zhong, Ruge Quhe, Yangyang Wang, Zeyuan Ni, Meng Ye, Zhigang Song, Yuanyuan Pan, Jinbo Yang, Li Yang, Ming Lei, Junjie Shi, and Jing Lu. *Interfacial Properties of Monolayer and Bilayer MoS 2 Contacts with Metals: Beyond the Energy Band Calculations*. Scientific Reports **6** (October 2015), 1–16 (2016). 118

[Zhu09] Wenjuan Zhu, Vasili Perebeinos, Marcus Freitag, and Phaedon Avouris. *Carrier scattering, mobilities, and electrostatic potential in monolayer, bilayer, and trilayer graphene*. Phys. Rev. B **80**, 235402 (2009). 42

[Zhu16] Yinyan Zhu, Kai Du, Jiebin Niu, Lingfang Lin, Wengang Wei, Hao Liu, Hanxuan Lin, Kai Zhang, Tieying Yang, Yunfang Kou, et al. *Chemical ordering suppresses large-scale electronic phase separation in doped manganites*. Nature communications **7**, 11260 (2016). 146

[Zota16] Cezar B. Zota and E. Lind. *Size-effects in indium gallium arsenide nanowire field-effect transistors*. Applied Physics Letters **109** (6), 063505 (2016). 133

[Zwanenburg09] F. A. Zwanenburg, D. W. Van Der Mast, H. B. Heersche, L. P. Kouwenhoven, and E. P A M Bakkers. *Electric field control of magnetoresistance in InP nanowires with ferromagnetic contacts*. Nano Letters **9** (7), 2704–2709 (2009). 109, 112

[Zwanenburg13] Floris A. Zwanenburg, Andrew S. Dzurak, Andrea Morello, Michelle Y. Simmons, Lloyd C. L. Hollenberg, Gerhard Klimeck, Sven Rogge, Susan N. Coppersmith, and Mark A. Eriksson. *Silicon quantum electronics*. Rev. Mod. Phys. **85**, 961–1019 (2013). 131, 132, 133

UNIVERSITÉ DE STRASBOURG

Louis Donald MOUAFO NOTEMGNOU

ECOLE DOCTORALE pcp

Two dimensional materials, nanoparticles and their heterostructures for nanoelectronics and spintronics

Résumé

Cette thèse porte sur l'étude du transport de charge et de spin dans les nanostructures 0D et 2D ainsi que les hétérosturures 2D-0D de Van der Waals (hVdW). Les nanocristaux pérovskite de $La_{0.67}Sr_{0.33}MnO_3$ ont révélé des magnétorésistances (MR) exceptionnelles à basse température résultant de l'aimantation de leur coquille indépendamment du cœur ferromagnétique. Les transistors à effet de champ à base de $MoSe_2$ ont permis d'élucider les mécanismes d'injection de charge à l'interface metal/semiconducteur 2D. Une méthode de fabrication des hVdW adaptés à l'électronique à un électron est rapportée et basée sur la croissance d'amas d'Al auto-assemblés à la surface du graphene et du MoS_2. La transparence des matériaux 2D au champ électrique permet de moduler efficacement l'état électrique des amas par la tension de grille arrière donnant lieu aux fonctionalités de logique à un électron. Les dispositifs à base de graphene présentent des MR attribuées aux effets magnéto-Coulomb anisotropiques.

Mots-clés: Transport de charge, transistor à effet de champ, nanoparticule cœur-coquille, blocage de Coulomb, transistor à électron unique, effet magnéto-Coulomb, transport de spin, graphène, dichalcogénures de métaux de transition, hétérostructures de van der Waals, magnétisme, magnétorésistance, pérovskites.

Abstract

This thesis investigates the charge and spin transport processes in 0D and 2D nanostructures and 2D-0D Van der Waals heterostructures (VdWh). The La0.67Sr0.33MnO3 perovskite nanocrystals reveal exceptional magnetoresistances (MR) at low temperature driven by their paramagnetic shell magnetization independently of their ferromagnetic core. A detailed study of MoSe2 field effect transistors enables to elucidate a complete map of the charge injection mechanisms at the metal/MoSe2 interface. An alternative approach is reported for fabricating 2D-0D VdWh suitable for single electron electronics involving the growth of self-assembled Al nanoclusters over the graphene and MoS2 surfaces. The transparency the 2D materials to the vertical electric field enables efficient modulation of the electric state of the supported Al clusters resulting to single electron logic functionalities. The devices consisting of graphene exhibit MR attributed to the magneto-Coulomb effect.

Keywords: Charge transport, Field effect transistor, core-shell nanoparticle, Coulomb blockade, Single electron transistor, magneto-Coulomb effect, spin transport, graphene, transition metal dichalcogenide, van der Waals heterostructures, Magnetism, magnetoresistance, perovskites.